Carbon based materials for electrochemical and chemical energy conversion and storage

Wei Wang

UNIVERSITÉ DE STRASBOURG

ÉCOLE DOCTORALE DES SCIENCES CHIMIQUES (ED 222)

ICPEES, UMR 7515 CNRS

THÈSE

présentée par :

Wei WANG

soutenue le : **06 décembre 2019**

pour obtenir le grade de : **Docteur de l'université de Strasbourg**

Discipline/ Spécialité : Chimie/Chimie

Matériaux à base de carbone pour la conversion et le stockage d'énergie électrochimique et chimique

Carbon based Materials for Electrochemical and Chemical Energy Conversion and Storage

THÈSE dirigée par :

M. PHAM-HUU Cuong — Directeur de Recherche, Université de Strasbourg

RAPPORTEURS :

M. de JONG Krijn P. — Professeur, Universiteit Utrecht

M. KHODAKOV Andrei — Directeur de Recherche, Université de Lille 1

EXAMINATEUR :

M. LOUIS Benoît — Directeur de Recherche, Université de Strasbourg

---

MEMBRE INVITE :

M. GIAMBASTIANI Giuliano — Directeur de Recherche, Italian National Research Council

Acknowledgement

My PhD thesis has been performed at the Institute of Chemistry and Processes for Energy, Environment and Health (ICPEES, UMR 7515) of the CNRS, University of Strasbourg. Looking back on my entire PhD study, many people have been involved in encouraging and guiding me during such a period. Without their kind help, I would never have made this exciting experience. I would like to take this opportunity to give my heartfelt thanks to all of them. I would like also to express my great thanks to the China Scholarship Council for the financial funding during my stay in ICPEES.

First of all, I would like to express my sincere gratitude to my advisor, Dr. Cuong Pham-Huu for providing me the chance to study in his laboratory. Thanks for his guidance, patience, and support during my whole PhD research. As the advisor, he is always ready to help me and guide me in the right scientific direction. He always encourages and inspires me to think and solve problems independently on different research projects. Without his selfless help and strong support in both research and daily life, I could not smoothly complete my research in a correct and scientifically pertinent manner. I largely took advantage from his experience throughout the work and learned how to be a humorous and high productive researcher, which will inevitably benefit the rest of my life. I would like to express him with my gratefulness and thankfulness for supporting me on this special day.

I would like also express my gratefulness to Dr. Giuliano Giambastiani from both Institute of Chemistry of OrganoMetallic Compounds (ICCOM) and Institute of Chemistry and Processes for Energy, Environment and Health (ICPEES, UMR 7515) for his valuable guidance and encouragement during my PhD study and also for his great help during the thesis writing.

I also want to express my warmest welcome and deepest gratitude to Prof. Krijn Pieter de Jong from Debye Institute for Nanomaterials Science (DINS) at Utrecht University and Dr. Andrei Khodakov from the Unité de Catalyse et Chimie du Solide (UMR 8181) at University of Lille-1 for accepting to act as advisory committee members of my thesis. I would also like to express my sincere gratitude to Dr. Benoît

Louis from Institute of Chemistry and Processes for Energy, Environment and Health (ICPEES, UMR 7515) at the University of Strasbourg for accepting to be one jury member for my PhD defense without any hesitation.

Special thanks are due to Dr. Housseinou Ba, Dr. Cuong Duong-Viet, Dr. Sergey Pronkin for their guidance and assistance in my research and also to Dr. Jean-Mario Nhut and Fabrice Vigneron for their support in the design and installation of the reaction systems. I learned how to be a focused, efficient researcher, and how to design and implement programs properly from them. Many thanks to all of them for their advice, and encouragement in both research and daily life, which make me feel confident to fulfill my PhD research. It is not sufficient to express my gratitude with these words.

I would like to thank Prof. Ovidiu Ersen, Dr. Walid Baaziz in the Institut de Physique et Chimie des Matériaux de Strasbourg (IPCMS, UMR 7504) at the University of Strasbourg and Dr. Yuefeng Liu in the Dalian Institute of Chemical Physics at University of Chinese Academy of Sciences for their help in TEM analysis.

I also express my gratitude to all the administrative staffs: Véronique Verkruysse, Agnès Orb, Catherine Kientz, Silviya Markova, Michèle Thomas and technical referees: Dr. Dominique Begin, Dr. Ksenia Parkhomenko, Thierry Romero, Sécou Sall, Dr. Thierry Dintzer, Alain Rach, Christophe Mélart, and Christophe Sutter at ICPEES for their valuable guidance and unwavering support.

I am also indebted to Anurag Mohanty, Dr. Zhenxin Xu, Dr. Ahmed Essyed, Dr. Lai Truong-Phuoc, Dr. Franck Ulm, Hamza El Marouazi, Ahmed Ait Khouya for their kind help, advice, encouragement and discussions in accomplishing this work. And also, I would like to thank all my friends in ICPEES and other friends in Strasbourg that I cannot list all here for the precious friendship and spiritual support.

Finally, I really appreciate the sacrifices that my family made for my study abroad. Thanks for their silent pay and support throughout these years. I would like also to express the profound gratitude to my beloved girlfriend for her selfless support on my research during these years. I also extend great thanks to all the relatives of my family for their help and support to my family and to my study.

Content

Résumé

1. Introduction

La conversion et le stockage de l'énergie ont toujours été les deux problèmes critiques de la société humaine, en particulier dans un contexte économique changeant et en pleine expansion. L'offre totale d'énergie primaire dans le monde a été multipliée par 2,5 entre 1971 et 2017 (passant de 5,519 Mtoe à 13,972 Mtoe), tandis que la consommation finale totale a été multipliée par 2,3. De nos jours, les combustibles fossiles, tels que le charbon, le pétrole et le gaz naturel, dominent toujours l'approvisionnement énergétique global dans le monde (représentant environ 81% de la production totale d'énergie en 2017) [1]. Toutefois, l'exploitation massive de combustibles fossiles entraînera une grave pollution de l'environnement et une crise énergétique à l'avenir [2, 3]. La double pression exercée par l'épuisement des combustibles fossiles et la dégradation de l'environnement a contraint les industriels et les gouvernements à explorer sans cesse les énergies renouvelables (RE) afin de réduire la part des sources d'énergie fossile dans l'approvisionnement énergétique et de réduire les émissions de CO_2 pour notre développement durable à venir. Les sources d'énergie renouvelables (RES), telles que l'énergie solaire et éolienne, ont fait l'objet d'une attention considérable au cours des dernières années [4-6]. Cependant, la nature fluctuante et intermittente de ces RES empêche la production d'énergie renouvelable de résoudre l'équilibre entre l'offre et la demande d'énergie, ce qui influe considérablement sur la sécurité et la stabilité du réseau énergétique, en particulier dans un scénario énergétique futur intégrant les RES à grande échelle [5-7]. Par conséquent, les systèmes de stockage d'énergie présentent un grand intérêt pour atténuer ces problèmes et permettre aux sources d'énergie renouvelables de devenir des sources primaires fiables d'approvisionnement en énergie. Les systèmes de stockage d'énergie peuvent offrir des avantages substantiels pour l'intégrité du système d'alimentation en termes de nivellement de la charge, de qualité de l'alimentation et de réserve en veille. Avec les systèmes de stockage d'énergie, l'électricité pourrait être produite à des moments de faible demande, à faible coût de production ou à partir de sources d'énergie renouvelables intermittentes, et utilisée en période de forte demande, de coûts de production élevés ou en l'absence d'autres moyens de production [7]. Le développement des systèmes de stockage tant électrochimique, supercondensateurs, que chimique, procédé de conversion d'électricité en gaz, permet de répondre efficacement aux

problèmes liés au développement des énergies renouvelables, intermitence par nature, et leurs stockage [6, 8].

1.1 Stockage électrochimique

La plupart des énergies renouvelables étant produites sous forme d'électricité, à l'exception des biocarburants, il est donc très intéressant de développer une plateforme de stockage d'énergie électrochimique fiable [9]. Les super-condensateurs (SCs), également appelés condensateurs électrochimiques (ECs) ou ultra-condensateurs, ont suscité un intérêt considérable ces dernières années. Faisant partie des dispositifs de stockage d'énergie électrochimiques les plus répandus, les SCs ont une large gamme d'applications en raison de leurs caractéristiques exceptionnelles, telles que la densité de puissance élevée, la durée de vie extrêmement longue et la densité d'énergie désirée réalisable, ce qui conviennent pour combler le fossé puissance/énergie entre les batteries (caractérisées par une densité d'énergie élevée mais à faible densité de puissance) et les condensateurs conventionnels (caractérisées par une densité de puissance élevée mais par une densité d'énergie faible) [9-11]. Sur la base du mécanisme de stockage d'énergie, les SCs peuvent être divisés en deux catégories: les condensateurs à double couche électrique (EDLCs), dans lesquels la capacité est dérivée des charges électrostatiques pures accumulées à l'interface électrode-électrolyte, et les pseudocondensateurs, où le stockage d'énergie repose sur des réactions réversibles d'oxydo-réduction ou de transfert rapide de charges faradiques de l'espèce électroactive à la surface de l'électrode [12-14]. En général, les pseudocondensateurs ont une capacité plus élevée que les EDLCs, mais souffrent généralement d'une densité de puissance et d'une stabilité plus faibles en raison de la faible conductivité électrique et de l'effondrement de la structure lors du test de cyclage [14].

Les matériaux carbonés, tels que les charbons actifs (AC), les nanotubes de carbone (CNTs) et le graphène, ont toujours été considérés comme les principaux candidats aux composites pour électrodes à haute performance en raison de leurs propriétés remarquables en matière de conductivité électrique, de leur grande surface, leur excellente stabilité chimique et thermique et leur respect vis-à-vis de l'environnement [12, 15]. Parmi eux, les ACs sont bien connus pour leur structure de pores interconnectés, leur taille de pore adaptable et leur grande surface spécifique (SSA) (pouvant dépasser 3,000 $m^2 \cdot g^{-1}$), qui sont des facteurs critiques pour les SC

hautes performances [14, 16]. Les AC peuvent généralement être produits à partir de diverses sources de carbone naturelles, telles que la biomasse renouvelable, par carbonisation avec des étapes d'activation physiques et/ou chimiques ultérieures, ce qui leur assure un coût bien inférieur aux autres matériaux à base de carbone [17, 18]. Les électrodes ACs stockent généralement la charge électrostatiquement par adsorption réversible des ions électrolytes sur les matériaux électroactifs. La génération de charge d'électrode de surface implique une dissociation de surface et une adsorption ionique à la fois des défauts de l'électrolyte et du réseau cristallin [15, 19].

1.2 Stockage chimique: procédé de Power-to-Gas

Avec l'intégration à grande échelle d'énergies renouvelables, il est essentiel de développer une stratégie de stockage d'énergie avec une capacité de stockage importante et une flexibilité dans le futur mix énergétique. Parmi les différents systèmes de stockage d'énergie, les processus Power-to-Gas (PtG) utilisant H_2 produit par électrolyse de l'eau à partir des sources renouvelables pour l'hydrogénation du CO_2 (méthanation de CO_2) afin de produire du gaz naturel de synthèse (SNG) ont été considérés comme l'une des stratégies les plus prometteuses pour le scénario énergétique futur avec une plus grande part de RE [20-22]. Cette stratégie de stockage d'énergie chimique peut transformer et stocker efficacement le surplus d'électricité provenant de sources d'énergie renouvelables intermittentes en gaz vecteurs d'énergie stockables facilement à grande échelle et à long terme, à savoir H_2 et CH_4, qui peuvent ensuite être utilisés pour le chauffage domestique ou comme matière première dans l'industrie chimique, et même être reconvertis pour produire de l'électricité à faible émission de carbone. Par conséquent, cette chaîne technique peut faciliter la distribution d'énergie entre différents systèmes d'approvisionnement en énergie en connectant le réseau électrique au réseau de distribution de gaz existant et en équilibrant efficacement l'offre et la demande en énergie dans le temps. De plus, le coût global de stockage et de transformation peut être considérablement réduit [5, 23, 24]. Le processus de méthanation du CO_2 peut améliorer considérablement la compatibilité de ce système de stockage d'énergie avec l'infrastructure du réseau de gaz existante, car il augmente considérablement la densité énergétique des gaz (35-40 $MJ \cdot m^{-3}$ pour le CH_4 contre 12,75 $MJ \cdot m^{-3}$ pour H_2) et l'injection de CH_4 dans les infrastructures de réseau de gaz naturel ne pose pas de problème par rapport à celle de H_2 en ce qui concerne les

questions de sécurité et d'efficacité [23, 25]. D'autre part, ce processus réduit efficacement les émissions de CO_2, permet de le recycler dans le monde et répond parfaitement aux exigences du développement durable.

La réaction de méthanation peut être catalysée par différents métaux, notamment le Ru, le Rh, le Pd, le Co et le Ni, déposés sur différents supports, tels que Al_2O_3, CeO_2, ZrO_2, avec ou sans promoteurs [26-28]. En raison de leur prix peu élevé, de leur activité et de leur sélectivité élevées, les catalyseurs à base de nickel sont les plus utilisés parmi les divers catalyseurs [6, 29]. Cette réaction est une réaction hautement exothermique; par conséquent, une température élevée limitera la conversion du CO_2 et la sélectivité pour le CH_4 [30]. De plus, au cours du processus de réaction, une grande quantité de chaleur sera libérée par la réaction elle-même, formant des points chauds locaux dans le catalyseur. Cela provoquera une dérive de température à l'intérieur du réacteur, entraînant la formation de sous-produits, tels que le CO, et la désactivation du catalyseur par frittage de phase active, et donc la compromission de la sécurité de l'installation [31-33]. Par conséquent, l'utilisation de supports à haute conductivité thermique pour transférer la chaleur libérée de façon homogène sur l'ensemble du lit catalytique, associée à un chauffage optimisé pour le contrôle en temps voulu de la température de réaction, serait d'un grand intérêt pour l'ensemble du processus catalytique. Des récents rapports ont souligné l'utilisation efficace de catalyseurs structurés avec des substrats à haute conductivité thermique ou de nouveaux types de réacteurs pour une telle réaction afin d'éviter les problèmes liés à l'emballement de la température [6, 34-36]. Cependant, même si de tels phénomènes pouvaient être réduits, les catalyseurs présentaient une performance modérée à une température de réaction moyenne et une capacité de traitement en masse limitée. En outre, la plupart de ces conceptions sont relativement complexes et coûteuses, et certaines d'entre elles en sont encore au stade du développement.

Le chauffage par induction électromagnétique (IH) a fait l'objet d'une attention soutenue récemment en tant que méthode de chauffage à la pointe de la technologie. Il s'agit d'une technologie de chauffage prometteuse en raison de ses avantages incomparables en matière de rendement élevé et de contrôle précis, contrairement aux techniques de chauffage conventionnelles, telles que le chauffage par résistance et le chauffage par flamme, dans lesquelles une forte inertie thermique et une zone de chauffage difficillement contrôlable existent toujours [37, 38]. En mode IH, la chaleur sera générée à l'intérieur du catalyseur ou du suscepteur directement (induite par le

champ magnétique alternatif haute fréquence externe) dans la région bien prédéfinie, ce qui entraîne un chauffage rapide, une consommation d'énergie réduite et une efficacité de fonctionnement globale accrue [38-40]. La température au niveau du lit de catalyseur est contrôlée presque en temps réel par un pyromètre laser, garantissant ainsi une réponse extrêmement rapide aux écarts de température survenant au niveau du lit de catalyseur. La capacité de régulation rapide d'IH permet de contrôler et d'équilibrer les changements de température brusques et indésirables sur le lit catalytique [41]. De ce fait, les fluctuations de température, fréquemment rencontrées dans les systèmes réels, peuvent être contrôlées avec précision (**Schéma 1**).

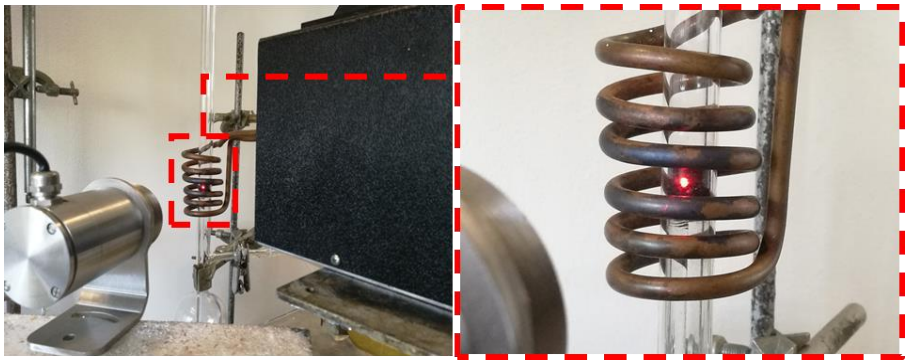

Schéma 1. Images du catalyseur Ni/OCF placé dans le réacteur tubulaire en quartz inséré dans la bobine du dispositif de chauffage inductif avec le pyromètre laser [41].

Dans la présente thèse, nous nous concentrons principalement sur le développement de matériaux à base de carbone durable pour le stockage efficace de l'énergie électrochimique, en particulier des supercondensateurs, et l'utilisation de l'induction électromagnétique pour le chauffage des catalyseurs au nickel supportés pour la conversion et le stockage de l'énergie chimique, principalement sur la méthanation du CO_2. Dans la première partie, deux structures de carbone dérivées de la biomasse différentes (mousse de carbone hiérarchique provenant de déchets de figues et feuille nanométrique de carbone de type graphène dérivée du saccharose) ont été synthétisées et étudiées pour les applications en supercondensateurs utilisant une configuration de cellule à trois électrodes. Des performances électrochimiques exceptionnelles ont été obtenues. Ensuite, dans la deuxième partie, des catalyseurs au nickel supportés sur feutre de carbone macroscopique, ainsi que sur des poudres à base d'Al_2O_3 ont été étudiées pour la méthanation du CO_2 avec des performances améliorées en utilisant le mode de chauffage par IH.

2. Résultats et discussions

2.1 Matériaux à base de carbone pour le stockage d'énergie électrochimique supercondensateur

2.1.1 Mousse de carbone biosourcée pour les supercondensateurs hautes performances

La première partie décrit l'obtention d'une structure de carbone poreuse biosourcée de type mousse provenant de déchets de matières premières à base de figues, utilisant l'activation chimique du KOH. Les effets de la quantité de KOH, de la température de calcination et du précurseur de carbone sur le produit final ont été étudiés. Le matériau carboné poreux hiérarchisé ainsi obtenu présente une SSA supérieure à 2,000 $m^2 \cdot g^{-1}$ avec une très forte porosité interconnectée, comme le montre la **Fig. 1**, ce qui permettrait d'améliorer de manière significative la conductivité électronique globale ainsi que le taux de diffusion des ions.

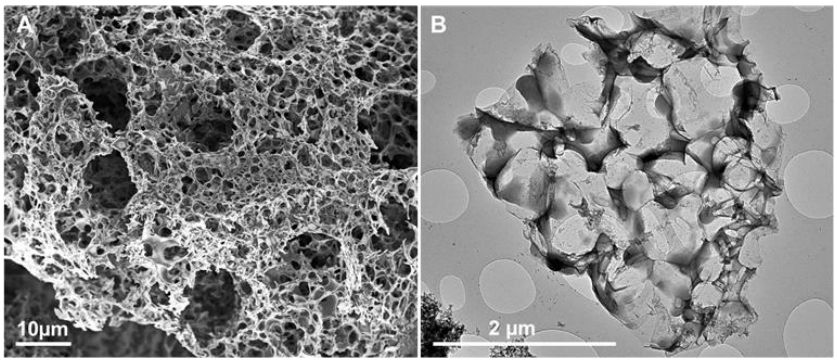

Fig. 1. (A) Images SEM et (B) TEM du matériau carboné $^{3Act.}$C-Fig$_{IN}$ 900 ºC [42].

L'échantillon de $^{3Act.}$C-FigIN 900 ºC optimisé a démontré d'excellents performances électrochimiques en tant que supercondensateur. Les courbes de charge/décharge à différentes densités de courant sont présentées sur la **Fig. 2A**, et toutes les courbes collectées présentent une forme presque linéaire et symétrique, indiquant le bon comportement du condensateur et l'excellente réversibilité électrochimique. Le meilleur échantillon présente une capacité spécifique supérieure dans l'électrolyte aqueux de 340 et 217 $F \cdot g^{-1}$ pour une densité de courant de 0,5 et 20 $A \cdot g^{-1}$, respectivement, et avec une grande stabilité (**Fig. 2B**).

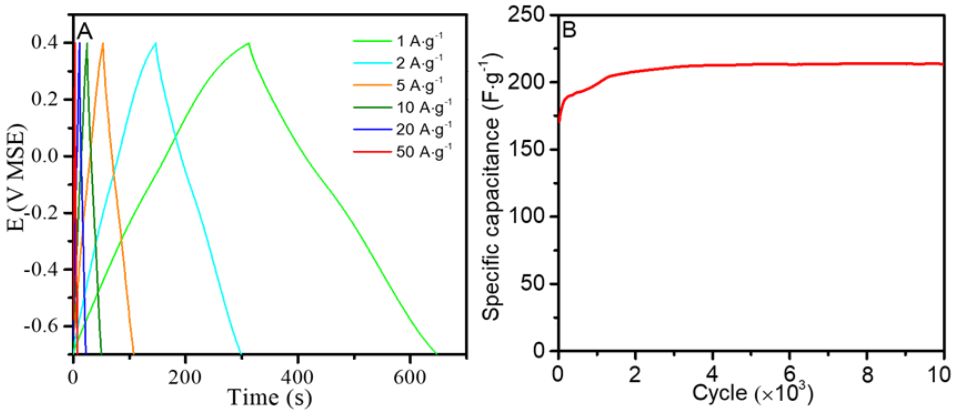

Fig. 2. (A) Courbes charge/décharge pour différentes densités de courant et (B) Les performances de stabilité à une densité de courant de 20 $A \cdot g^{-1}$ pour le $^{3Act.}$C-Fig$_{IN}$ 900 ^{o}C dans une solution à 0,5 M d'H_2SO_4 à 25 °C [42].

2.1.2 Structures de carbone avec morphologie type graphène pour supercondensateurs hautes performances

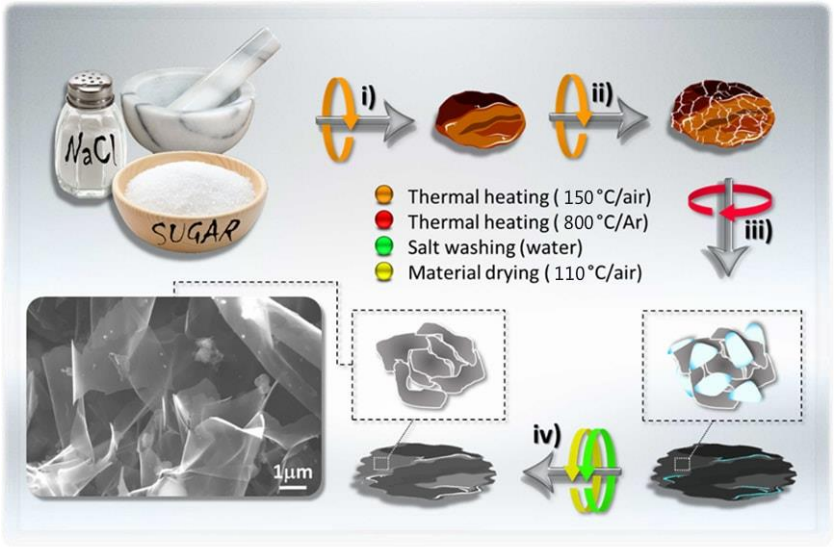

Schéma 2. Étapes séquentielles (i → iv) pour la préparation de matériaux *StS*x/y à partir de mélanges physiques (wt./wt.) de saccharose finement broyé/sel de table et de la capacité de surface spécifique de l'échantillon *StS*1/1 pour différentes densités de courant dans une solution à 0,5 M d'H_2SO_4 [43]

Dans cette contribution, un mélange physique de saccharose ($C_{12}H_{22}O_{11}$) et de sel de table (NaCl) dans un rapport pondéral variable est utilisé comme source de carbone renouvelable et comme agent modèle sacrificiel [43]. Des structures de carbone

robustes, ressemblant à du graphène avec des cellules très ouvertes, composées de quelques couches, ont aini pu être produites par une procédure d'activation chimique simple, comme illustré dans le **Schéma 2**. L'influence de la source de carbone/sel sur la structure finale du carbone et les performances électrochimiques a également été étudiée.

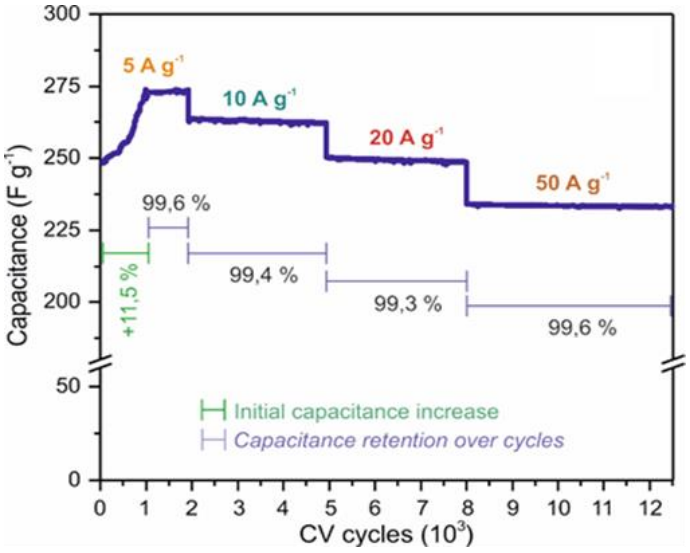

Fig. 3. Stabilité de *StS*$_{1/1}$ sur des milliers de cycles et rétention de la capacité à différentes densités de courant dans une configuration de cellule à trois électrodes avec 0,5 M H_2SO_4 [43].

L'imprégnation par la solution de KOH permet d'optimiser l'effet template de NaCl, favorisant ainsi la génération couches de C ressemblant à des "pelures d'oignon" autour du noyau inorganique. Après avoir éliminé le NaCl, des nanofeuilles de carbone de morphologie similaire à celle du graphène ont été obtenues. Le carbone tel que préparé affichait une SSA élevée de 896 $m^2 \cdot g^{-1}$ avec une meilleure surface accessible aux ions et une faible résistance au transport des ions, qui sont les caractéristiques clés des supercondensateurs électrochimiques efficaces à double couche. Par conséquent, l'échantillon optimisé StS$_{1/1}$ présentait une capacité spécifique supérieure de 312 et 234 $F \cdot g^{-1}$ à 0,5 et 50 $A \cdot g^{-1}$ dans un électrolyte à 0,5 M d'H_2SO_4, respectivement, ainsi qu'une excellente stabilité de cycles et rétention de capacité (**Fig. 3**). À notre connaissance, ces performances exceptionnelles sont comparables aux systèmes à base de carbone à la pointe de la technologie.

2.2 Catalyseur à base de nickel pour la conversion et le stockage d'énergie chimique

2.2.1 Méthanation du CO_2 en mode de fonctionnement dynamique utilisant un feutre de carbone décoré de nanoparticules de nickel (Ni/OCF) combiné à un chauffage par induction

La méthanation du CO_2 est une approche efficace pour la conversion et le stockage de l'énergie chimique des excédente électricité renouvelable. C'est une technologie dite «deux en un», qui permet de produire du gaz de synthèse tout en atténuant la concentration de CO_2 dans l'atmosphère. Dans cette contribution, un catalyseur efficace et robuste a été synthétisé et utilisé pour la méthanation du CO_2 alimenté par IH dans des conditions à la fois stationnaires et dynamiques. Un feutre de carbone de forme macroscopique a été utilisé à la fois comme suscepteur et comme support du catalyseur (**Fig. 4A**). Après traitement thermique à la vapeur d'acide, les propriétés de surface et de texture de la CF ont été considérablement modifiées (**Fig. 4B**), ce qui a inévitablement accru la dispersion des nanoparticules de nickel (Ni NPs) sur un tel disque en feutre de carbone oxydé (OCF), comme illustré à la **Fig. 4C-D**. Les résultats du microscope électronique à transmission (TEM) ont indiqué que l'on obtenait une dispersion élevée de NPs de Ni sur le OCF avec une taille de particule moyenne d'environ 4 ± 1 nm.

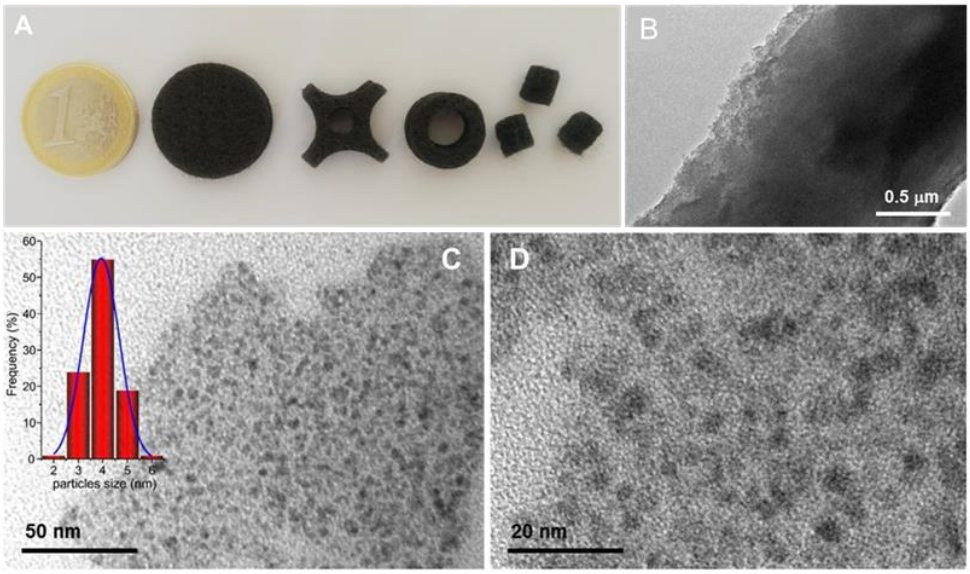

Fig. 4. (A) Exemples de différentes formes macroscopiques CF, (B) Image TEM de l'OCF, Micrographies TEM à faible (C) et moyen (D) grossissement de Ni/OCF [41].

La conductivité électrique et thermique inhérente au CF a été utilisée avec succès pour transférer l'énergie électromagnétique en chaleur sur l'ensemble du lit de catalyseur. Contrairement au chauffage thermique classique, l'IH permet à l'énergie électromagnétique d'être directement convertie en chaleur par le suscepteur (OCF) et les Ni NPs et non par des transferts du four au réacteur puis au catalyseur durant lequel une importante perte de chaleur a eu lieu. Plus important encore, le contrôle rapide de la température dans le lit de catalyseur, par un pyromètre laser en temps réel, garantissant ainsi une réponse extrêmement rapide de tout écart de température survenant dans le lit du catalyseur permettant au système électromagnétique d'enclencher la correction afin d'éviter un emballement en température dans le lit catalytique (**Schéma 1**). Le catalyseur Ni/OCF chauffé par IH a permis d'obtenir une conversion du CO_2 (X_{CO2}) de l'ordre de 74% et une sélectivité en CH_4 (S_{CH4}) proche de 97% à 320 °C, ce qui montre une excellente maîtrise de la stabilité du catalyseur dans des conditions de fonctionnement dynamiques forcées, comme indiqué sur la **Fig. 5**.

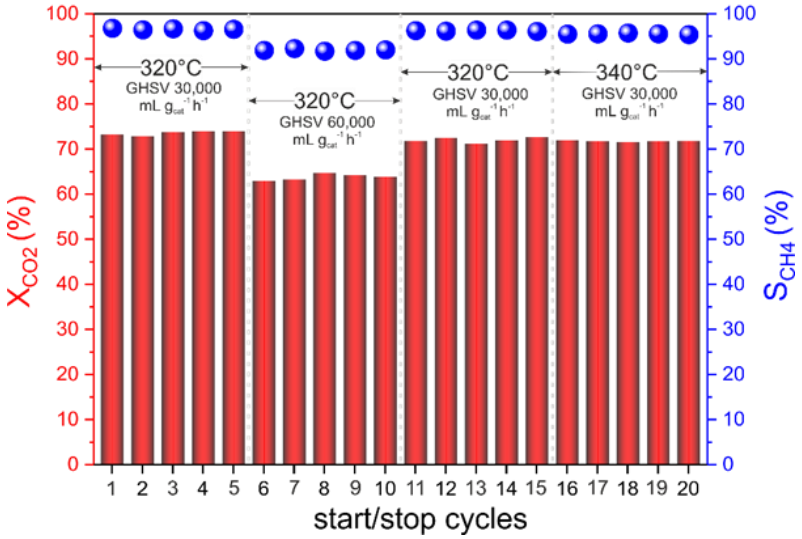

Fig. 5. Performances du catalyseur Ni/OCF mimant les modes de conditions de fonctionnement dynamiques sous la forme de cycles de démarrage/arrêt successifs exécutés dans différentes conditions [41].

2.2.2 Le chauffage par induction améliore les performances de méthanation du CO_2 à basse température sur un catalyseur Ni/Al_2O_3

Cette dernière partie sur la méthanation du CO_2, montre les performances obtenues pour différentes charges de Ni déposées sur de la poudre d'Al_2O_3. Les catalyseurs ainsi

synthétisés permettent de moduler la conductivité électrique du catalyseur vis-à-vis du chauffage par IH. Seuls les catalyseurs ayant une teneur en nickel suffisante pourraient être chauffés jusqu'à la température de réaction souhaitée sans suscepteur.

Le catalyseur avec une teneur en Ni de 40% en poids présente des performances catalytiques exceptionnelles à une température relativement basse, < 250 °C, comme le montre la **Fig. 6A**. La conversion du CO_2 présente une amélioration significative lorsque la température de la réaction est augmentée de 150 à 210 °C, indiquant que l'activité catalytique du catalyseur dépend fortement de la température de réaction, généralement attribuée au contrôle cinétique [44]. Au-delà de 210 °C, la conversion du CO_2 augmente lentement en raison de l'exothermicité de la réaction de méthanation et de la limitation thermodynamique dans les conditions d'essai [30, 44]. Dans le même temps, bien que l'augmentation du GHSV (STP) de 20 $L \cdot g_{cat.}^{-1} \cdot h^{-1}$ à 30 $L \cdot g_{cat.}^{-1} \cdot h^{-1}$ ait entraîné une diminution de la conversion du CO_2, la chaleur totale libérée par la réaction a été augmentée [33]. Par conséquent, le système a besoin d'une puissance plus basse pour maintenir la température de réaction (**Fig. 6B**). À l'état d'équilibre à 230 °C, la conversion du CO_2 est respectivement de 85% et 82%, avec une sélectivité en CH_4 proche de 100%. Pour autant que nous sachions, ces performances exceptionnelles n'ont jamais été atteintes de tous les systèmes de catalyseurs à base de nickel supporté sur alumine recensés dans la littérature.

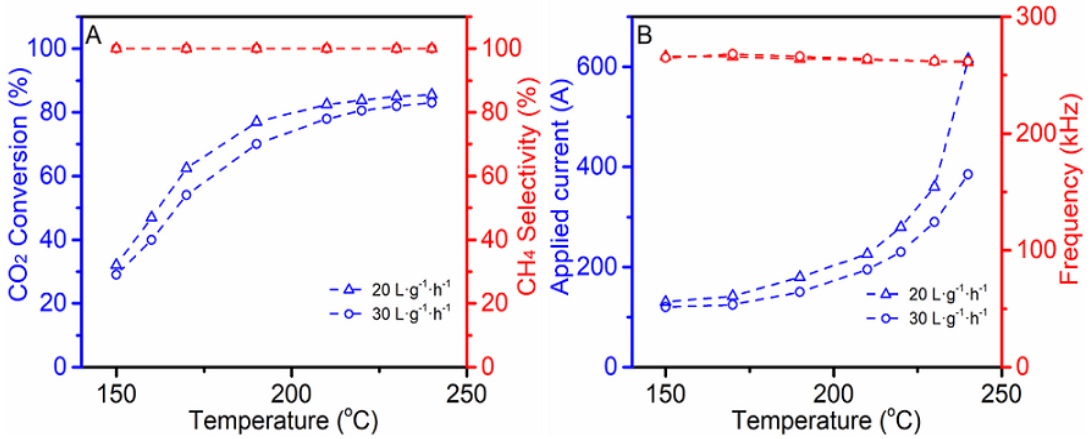

Fig. 6. (A) Conversion du CO_2 et sélectivité du CH_4 obtenues sur catalyseur $40Ni/Al_2O_3$, (B) Le courant et la fréquence appliqués obtenus en fonction de la température sous différents GHSV.

Les performances catalytiques et les phénomènes d'emballement en température ont également été étudiés sous chauffage thermique conventionnel avec l'utilisation d'un four externe (**Fig. 7**). À basse température de réaction (≤ 220 °C), la conversion du CO_2 était bien inférieure à celle obtenue en mode IH à la même température de réaction et la température du lit de catalyseur reste similaire à celle du four (**Fig. 7A**). Cependant, lorsque la température de réaction a été augmentée à 230 °C (température du four), une forte augmentation de la température a été enregistrée à l'intérieur du lit de catalyseur avec une conversion de CO_2 similaire de 87% à l'état stable par rapport à celle obtenue avec l'approche IH. Cela peut fournir un moyen de prédire la température locale des Ni nanoparticules (NPs) sur le support en Al_2O_3 pendant le processus de réaction chauffé en mode IH.

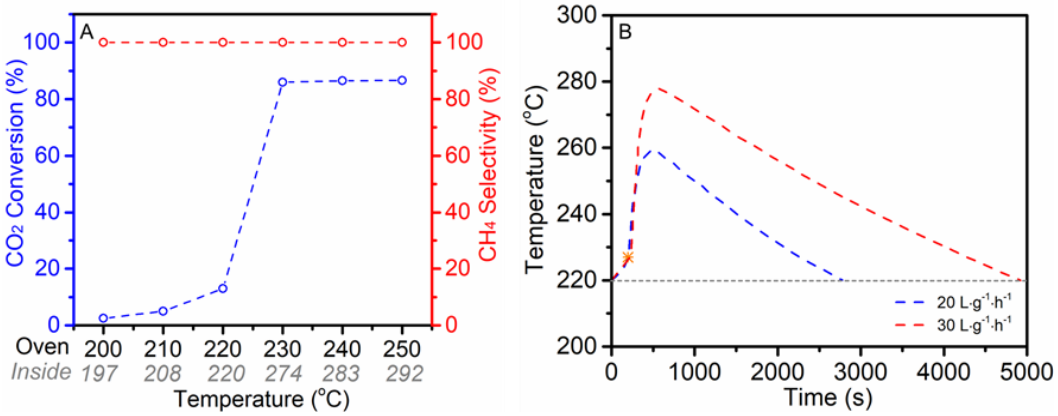

Fig. 7. (A) Performances en méthanation du CO_2 sous chauffage thermique conventionnel par un four externe à GHSV (STP) de 20 $L \cdot g_{cat.}^{-1} \cdot h^{-1}$, (B) phénomènes d'emballement thermique à l'intérieur du lit de catalyseur. Conditions de réaction: 0,4 g de catalyseur, rapport H_2/CO_2 (v/v) de 4, 1 atm.

À une température initiale de réaction de 220 °C, on a observé une grave dérive de température quelques minutes après l'introduction des réactifs dans le réacteur, soit 40 °C et 60 °C sous une GHSV de 20 $L \cdot g_{cat.}^{-1} \cdot h^{-1}$ et 30 $L \cdot g_{cat.}^{-1} \cdot h^{-1}$, respectivement (**Fig. 7B**). Des résultats similaires ont également été rapportés dans des études récentes sur la méthanation du CO_2 [33, 45, 46]. L'augmentation du débit de réactif entraînait généralement une augmentation de la vitesse de réaction et par conséquent une accumulation importante de chaleur libérée en raison de la nature exothermique de la réaction, contribuant ainsi à la formation de points chauds et à un échauffement

important [33, 35]. Il convient de noter qu'il faut près de 30 et 60 minutes au système pour revenir à la température de réaction initiale définie, ce qui reflète la faible capacité de régulation de la température en utilisant le mode de chauffage classique où plusieurs étapes de transfert de la chaleur du four au catalyseur sont nécessaires. En revanche, lors de l'évaluation du même catalyseur en mode IH, la fluctuation maximale de température est inférieure à 5 °C, ce qui se produit lors d'une conversion élevée du CO_2, puis tend rapidement à se stabiliser à la température cible en quelques minutes grâce à la réponse extrêmement rapide en terme de température du système IH.

3. Conclusions et perspectives

3.1 Conclusion générale

Dans cette thèse, des efforts importants ont été déployés pour la conception de matériaux en carbone pour les SCs hautes performances et l'exploration de systèmes pour la méthanation de CO_2 efficaces en mode IH. Deux matériaux de carbone différents, la structure de mousse de carbone à partir de déchets de figues et les nanofeuilles de carbone de type graphène dérivées du saccharose avec des performances électrochimiques exceptionnelles, ont été fabriqués et entièrement étudiés en tant que matériaux pour électrodes de supercondensateurs dans une configuration de cellule à trois électrodes. Parallèlement, un catalyseur de nickel macroscopique sur support carbone a été mis au point pour la méthanation du CO_2 avec une performance catalytique améliorée alimentée par IH. De plus, la capacité de régulation rapide de l'installation IH et les phénomènes d'emballement de la température à l'intérieur du lit de catalyseur soumis à un chauffage thermique conventionnel ont également été étudiés à l'aide d'un catalyseur au nickel propulsé par Al_2O_3 pour la méthanation du CO_2 dans la dernière partie de cette thèse. Sur la base de toutes les expériences et réalisations, plusieurs conclusions peuvent être résumées sous différentes perspectives:

1. L'activation chimique KOH est une approche efficace pour fabriquer des matériaux en carbone à haute porosité à partir de sources de carbone naturelles avec des performances électrochimiques exceptionnelles. NaCl peut être efficacement utilisé comme agent structurant sacrificiel pour la synthèse de nanofeuilles de carbone de type graphène à cellules ouvertes. Le précurseur du carbone, la température de calcination et la quantité de KOH ont une influence significative sur la morphologie et les

propriétés texturales de la structure finale du carbone, et ont donc une incidence sur ses performances électrochimiques.

2. Les structures de carbone finales obtenues, à la fois sous forme de mousse de carbone et sous forme de nanofeuillets de carbone de type graphène, présentent une capacité supérieure dans une configuration de cellule à trois électrodes dans des conditions de test, indiquant que ces matériaux carbonés sont des candidats appropriés pour les supercondensateurs à haute capacité.

3. Le traitement thermique à la vapeur d'acide est une méthode efficace pour modifier à la fois les propriétés spécifiques et texturales des matériaux à base de carbone, en l'occurrence des feutres de carbone sous forme macroscopique, ce qui permet de préparer des matériaux carbonés avec des propriétés physico-chimiques intéressantes pour des applications en catalyse.

4. Le feutre de carbone macroscopique ainsi synthétisé s'avère être un suscepteur idéal permettant de transformer efficacement l'énergie électromagnétique en chaleur avec une perte de charge négligeable. Le catalyseur macroscopique synthétisé à base de nickel (Ni/OCF) présentait une activité catalytique pour la réaction de méthanation du CO_2 fortement accrue avec une excellente stabilité dans des conditions de fonctionnement à l'état stationnaire et dynamique sous chauffage par induction électromagnétique (IH).

5. Tous les catalyseurs obtenus présentent des performances catalytiques nettement améliorées pour la méthanation du CO_2 en mode IH par rapport à un chauffage classique par effet Joule, indiquant les avantages considérables de l'approche IH, attribués à la surchauffe locale des espèces métalliques à base de nickel. Cependant, la détermination directe de la température de surface des particules métalliques reste un défi de taille et nécessite des études complémentaires.

6. La capacité de régulation rapide de la puissance du système IH permet de contrôler et d'équilibrer dans un temps très court les changements de température non désirés et soudains au niveau du lit de catalyseur. Par conséquent, le système peut fonctionner dans des conditions dynamiques et l'emballement en température à l'intérieur du lit de catalyseur peut être considérablement réduit par rapport au chauffage classique par un four électrique.

3.2 Perspectives

Les travaux de cette thèse permettent d'apporter des solutions intéressantes aux exigences actuelles en matière de conversion et de stockage de l'énergie. A l'aune des résultats obtenus les perspectives suivantes peuvent être proposées pour la suite:

(i) la poursuite des études sur l'activation chimique à base de KOH sur d'autres formes de carbone afin de produire des matériaux carbonés avec des propriétés physico-chimiques adaptées pour des applications en électrochimiques ou en tant que supports pour des catalyseurs hétérogènes.

(ii) la poursuite des travaux déjà réalisés sur l'influence du chauffage inductif pour générer des points chauds locaux sur la surface des particules métalliques pour le développement des procédés catalytiques opérant à basse température pour la réaction de méthanation du CO_2.

(iii) l'utilisation du chauffage inductif pour d'autres réactions exothermiques telles que la synthèse de Fischer-Tropsch ou l'oxydation sélective où un control précis de la température au sein du lit catalytique permettrait de réduire les gradients de température en vue de prévenir les problèmes de perte en sélectivité ou de désactivation du catalyseur.

Reference

[1] IEA (International Energy Agency), *World Energy Balances 2019 Overview*, https://webstore.iea.org/world-energy-balances-2019.

[2] N. Abas, A. Kalair, N. Khan. *Futures*, 2015, 69: 31-49.

[3] B. K. Bose. *IEEE Ind. Electron. Mag.*, 2010, 4(1): 6-17.

[4] O. Ellabban, H. Abu-Rub, F. Blaabjerg. *Renew. Sust. Energy Rev.*, 2014, 39: 748-764.

[5] M. Bailera, P. Lisbona, L. M. Romeo, S. Espatolero. *Renew. Sust. Energy Rev.*, 2017, 69: 292-312.

[6] M. Götz, J. Lefebvre, F. Mörs, A. M. Koch, F. Graf, S. Bajohr, R. Reimert, T. Kolb. *Renew. Energy.*, 2016, 85: 1371-1390.

[7] H. Chen, T. N. Cong, W. Yang, C. Tan, Y. Li, Y. Ding. *Prog. Nat. Sci.*, 2019,19(3): 291-312.

[8] L. Dai, D. W. Chang, J.-B. Baek, W. Lu. *Small*, 2012, 8: 1130-1166.

[9] W. Raza, F. Ali, N. Raza, Y. Luo, K. H. Kim, J. Yang, S. Kumar, A. Mehmood, E. E. Kwon. *Nano Energy*, 2018, 52: 441-473.

[10] L. L. Zhang, X. S. Zhao. *Chem. Soc. Rev.*, 2009, 38: 2520-2531.

[11] M. Conte. *Fuel Cells*, 2010, 10: 806-818.

[12] H. Jiang, P. S. Lee, C. Li. *Energy Environ. Sci.*, 2013, 6: 41-53.

[13] Y. Wang, Y. Song, Y. Xia. *Chem. Soc. Rev.*, 2016, 45: 5925-5950.

[14] Y. Zhai, Y. Dou, D. Zhao, P. F. Fulvio, R. T. Mayes, S. Dai. *Adv. Mater.*, 2011, 23: 4828-4850.

[15] J. Yan, Q. Wang, T. Wei, Z. Fan. *Adv. Energy Mater.*, 2014, 4: 1300816-1300858.

[16] L. Borchardt, M. Oschatz, S. Kaskel. *Mater. Horiz.*, 2014, 1: 157-168.

[17] A. M. Abioye, F. N. Ani. *Renew. Sust. Energy Rev.*, 2015, 52: 1282-1293.

[18] Q. Wang, J. Yan, Z. Fan. *Energy Environ. Sci.*, 2016, 9: 729-762.

[19] P. Simon, Y. Gogotsi. *Nat. Mater.*, 2008, 7: 320-329.

[20] S. Clegg, P. Mancarella. *IEEE Trans. Sustain. Energy*, 2015, 6: 1234-1244.

[21] A. Lewandowska-Bernat, U. Desideri. *Energy Procedia*, 2017, 105: 4569-4574.

[22] S. McDonagh, R. O'Shea, D. M. Wall, J. P. Deane, J. D. Murphy. *Appl. Energy*, 2018, 215: 444-456.

[23] G. Guandalini, S. Campanari, M.C. Romano. *Appl. Energy*, 2015, 147: 117-130.

[24] M. Qadrdan, M. Abeysekera, M. Chaudry, J. Wu, N. Jenkins. *Int. J. Hydrogen*

Energy, 2015, 40: 5763-5775.

[25] J. Ma, Q. Li, M. Kühn, N. Nakaten. *Renew. Sust. Energy Rev.*, 2018, 97: 478-496.

[26] W. Wang, S. Wang, X. Ma, J. Gong. *Chem. Soc. Rev.*, 2011, 40: 3703-3727.

[27] M. A. A. Aziz, A. A. Jalil, S. Triwahyono, A. Ahmad. *Green Chem.*, 2015, 17: 2647-2663.

[28] M. Younas, L. Loong Kong, M. J. Bashir, H. Nadeem, A. Shehzad, S. Sethupathi. *Energy Fuels*, 2016, 30: 8815-8831.

[29] C. H. Bartholomew. *Appl. Catal. A-Gen.*, 2001, 212: 17-60.

[30] J. Gao, Y. Wang, Y. Ping, D. Hu, G. Xu, F. Gu, F. Su. *Rsc Adv.*, 2012, 2: 2358-2368.

[31] A. Fache, F. Marias, V. Guerré, S. Palmade. *Chem. Eng. Sci.*, 2018, 192: 1124-1137.

[32] S. Ewald, M. Kolbeck, T. Kratky, M. Wolf, O. Hinrichsen. *Appl. Catal. A-Gen.*, 2019, 570: 376-386.

[33] C. Schüler, M. Wolf, O. Hinrichsen. *J. CO_2 Util.*, 2018, 25: 158–169.

[34] S. Danaci, L. Protasova, J. Lefevere, L. Bedel, R. Guilet, P. Marty. *Catal. Today*, 2016, 273: 234-243.

[35] A. Vita, C. Italiano, L. Pino, P. Frontera, M. Ferraro, V. Antonucci. *Appl. Catal. B. Environ.*, 2018, 226: 384-395.

[36] S. Rönsch, J. Schneider, S. Matthischke, M. Schlüter, M. Götz, J. Lefebvre, P. Prabhakaran, S. Bajohr. *Fuel*, 2016, 166: 276-296.

[37] O. Lucía, P. Maussion, E. J. Dede, J. M. Burdío. *IEEE Trans. Ind. Electron.*, 2013, 61: 2509-2520.

[38] W. Wang, G. Tuci, C. Duong-Viet, Y. Liu, A. Rossin, L. Luconi, J.-M. Nhut, L. Nguyen-Dinh, C. Pham-Huu, G. Giambastiani. *ACS Catal.*, 2019, 9(9): 7921-7935.

[39] S. Ceylan, L. Coutable, J. Wegner, A. Kirschning. *Chem. Eur. J.*, 2011, 17: 1884-1893.

[40] J. Leclercq, F. Giraud, D. Bianchi, K. Fiaty, F. Gaillard. *Appl. Catal. B. Environ.*, 2014, 146: 131-137.

[41] W. Wang, C. Duong-Viet, Z. Xu, H. Ba, G. Tuci, G. Giambastiani, Y. Liu, T. Truong-Huu, J.-M. Nhut, C. Pham-Huu. *Catal. Today*, 2019, in press. DOI: 10.1016/j.cattod.2019.02.050.

[42] H. Ba, W. Wang, S. Pronkin, T. Romero, W. Baaziz, L. Nguyen-Dinh, W. Chu, O. Ersen, C. Pham-Huu. *Adv. Sustainable Syst.*, 2018, 2: 1700123.

[43] H. Ba, W. Wang, G. Tuci, S. N. Pronkin, C. Weinberg, L. Nguyen-Dinh, G. Giambastiani, C. Pham-Huu. *Mater. Today Energy*, 2018, 10: 118-125.

[44] G. Garbarino, C. Wang, T. Cavattoni, E. Finocchio, P. Riani, M. Flytzani-Stephanopoulos, G. Busca. *Appl. Catal. B. Environ.*, 2019, 248: 286-297.

[45] S. Ratchahat, M. Sudoh, Y. Suzuki, W. Kawasaki, R. Watanabe, C. Fukuhara. *J. CO_2 Util.*, 2018, 24: 210-219.

[46] D. Schlereth, O. Hinrichsen. *Chem. Eng. Res. Des.*, 2014, 92: 702-712.

Chapter 1

Introduction about electrochemical and chemical energy conversion and storage

The rapid increase of population and the relentless move forward to a well-being society is closely linked with an ever-increasing energy demand worldwide. It has been reported by the International Energy Agency (IEA) that between 1971 and 2017, the world total primary energy supply (TPES) increased by more than 2.5 times (from 5,519 Mtoe to 13,972 Mtoe), while the total final consumption (TFC) was multiplied by 2.3. At present, fossil fuels, such as coal, oil and natural gas, still dominate the overall energy supply around the world (accounting for about 81% of the total primary energy supply in 2017, **Fig. 1-1**) [1]. However, the massive worldwide consumption of fossil fuels, on one hand, may result in energy crisis in the future (due to the shortages and associated high prices), and on the other hand, will cause serious environment problems [2, 3]. Indeed, fossil fuels are mainly composed of hydrocarbons, and their combustion inevitably produces a large amount of CO_2, which is known as one of the main greenhouse gases (GHGs) that contribute to the dramatic environmental and climate effects. The amount of global CO_2 emissions from fuel combustion has more than doubled since the early seventies and increased by around 40% since 2000 (up to 32.31 $GtCO_2$ in 2016) [4]. As a consequence, CO_2 concentration in the atmosphere has continuously and dramatically increased during the past centuries, from approximately 277 ppm (parts per million) at the beginning of the industrial era in 1750, to about 405 ppm in 2017 and even higher concentrations (410 ppm) recorded in June 2019 [5-8]. As anticipated above, such high CO_2 concentrations has been considered as one of the main drivers for global warming [9, 10], causing in turn a series of serious drawbacks invariably influencing the global ecological systems, hence resulting into extreme weather events (such as droughts, floods and heat waves), and sea level rise [11-13].

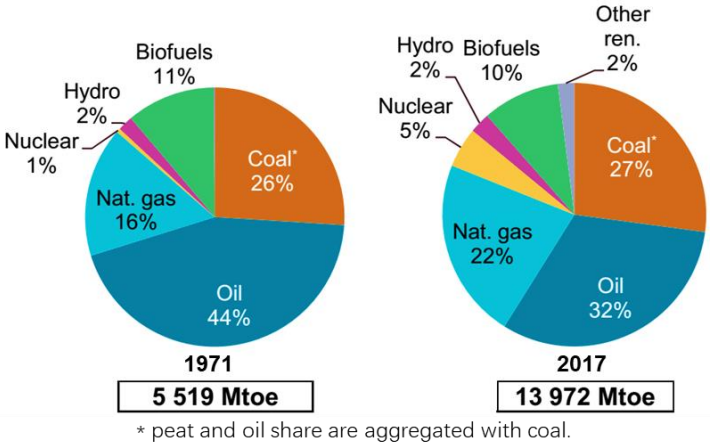

Fig. 1-1. World total primary energy supply by fuel [1].

The dual pressure from fossil fuel depletion and environmental deterioration has forced industries and governments to continuously explore alternative energy sources for a sustainable development. Great efforts have been devoted to preventing the global warming trend based on a combination of carbon capture, storage and utilization (CCS/CCU), the integration of renewable energy (RE) from diverse renewable energy sources (RES) and the energy efficiency improvement [14-16]. In recent decades there has been a tremendous expansion of RE from various RES to decrease the shares of fossil fuels in the energy mix and the GHGs emissions (**Fig. 1-2**). In 2017, the RES contributed to 13.5% of the TPES, and 24.5% of the global electricity production [17]. RES, such as solar, hydro and wind power, have been fully exploited for the production of renewable electricity with reduced or even zero carbon emissions and they have been expected to face a large increase in terms of power supply in the future [18, 19]. The production price of RE becomes more and more competitive compared to those of the fossil sources according to the report by Bloomberg New Energy Finance [20]. In the 2030 climate & energy framework, the European Commission has set several key targets of at least a 32% share of RE in final energy consumption, including an upward revision clause for 2023 with at least 40% GHG emissions cut compared to 1990 levels as well as an improvement in energy efficiency of at least 32.5% by 2030 in order to achieve a more competitive, secure and sustainable energy system and to meet its long-term 2050 greenhouse gas reduction target (achieving a climate neutral) [21, 22].

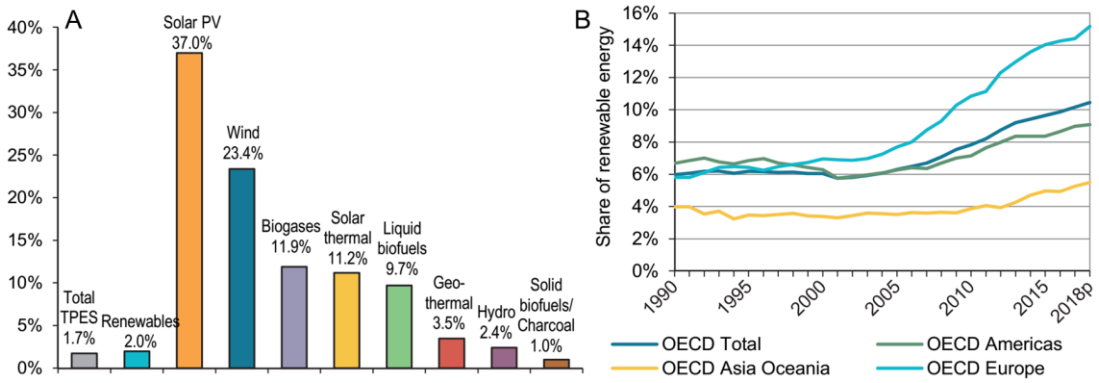

Fig. 1-2. (A) Average annual growth rates of world renewables supply from 1990 to 2017, (B) OECD regional shares of RE supply in TPES [17].

RE has some indisputable advantages over the traditional fossil fuels, but at the same time, it also presents new challenges in terms of energy distribution and storage. Indeed, one issue generally related to the electricity generation from RES is the classical discrepancy between their spatial localization and the place of energy demand. This requires significant investments to build up or reinforce the electricity transmission network as to deliver the generated power from RES into the grid [23, 24]. It is worthy to note that electricity transport is a costly process and should be avoided as much as possible in order to reduce the overall costs of the process. Moreover, the intermittent nature of RES will result in fluctuating and unpredictable power output, which limits their widely expansion to a large extent [25]. Problems with fluctuating electricity production from RES may be not obvious in a power grid with low share of RE since they can be balanced by conventional power generation [26]. However, in a future energy scenario with large scale integration of RES, the variable and not entirely predictable power output along with the mismatch between RE peak power output and power demand will likely pose severe challenges to accurately predict the energy supply-demand, as a consequence render difficult the electric grid management [27, 28].

To this aim, energy storage systems are of high interest as they can help to mitigate (in part at least) some of the problems listed above; hence they can largely contribute to foster the utilization of RES to become reliable primary sources for energy supply. Indeed, energy storage systems can provide substantial benefits to the power system integrity in terms of load levelling, power quality and standby reserve. With energy storage systems, electricity can be produced and stored when it is not required, including from intermittent RES, and can be used at times of high demand [25]. In addition, storing energy also allows transmission and distribution to operate at full capacity, decreasing the demand for newer or upgraded lines and increasing plant efficiencies [25, 29, 30].

1.1 Electrochemical energy storage

As most RE is supplied in the form of electricity, the development of reliable electrochemical storage systems is receiving a great interest from the scientific community [31]. Supercapacitors (SCs), also called electrochemical capacitors (ECs) or ultracapacitors, have triggered tremendous attention in recent years as one of the leading electrochemical energy storage devices [31, 32]. As an important type of

electrochemical energy storage devices, SCs have a wide range of applications due to their exceptional features, such as high power density (> 10 $kW \cdot kg^{-1}$), ultra-long cycle life (> 10^5), low maintenance, outstanding stability and great potential to deliver high energy density, which are suitable for bridging the power/energy gap between batteries (featured by high energy density but low power density) and conventional capacitors (featured by high power density but low energy density) [33-35], as illustrated in **Fig. 1-3**. Even through the energy storage within such devices is limited, SCs are still considered as the most promising energy storage devices for various applications in ubiquitous electrical products (*i.e.* portable electronic devices, hybrid electric vehicles, trains, uninterruptible power supplies) to provide large current and high specific power within short durations [25, 31, 36].

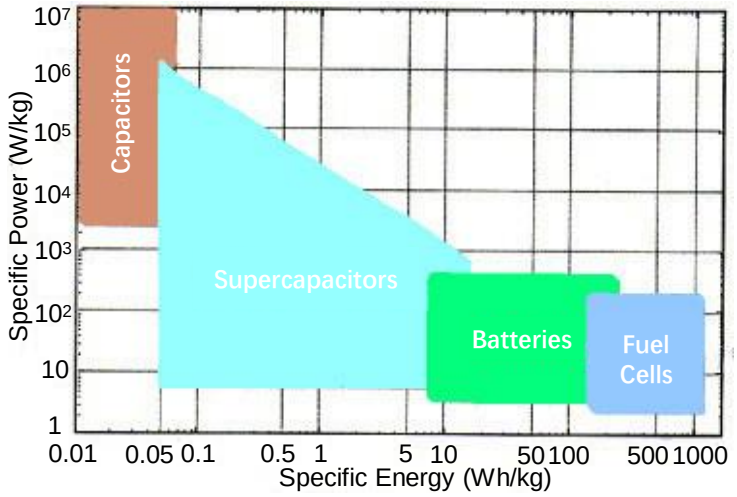

Fig. 1-3. Schematic comparison of the Ragone plot of different electrochemical energy conversion and storage devices [33].

1.1.1 Energy storage mechanism in supercapacitors

Based on the energy storage mechanism, SCs can be basically divided into two categories: the electrical double layer capacitors (EDLCs) and pseudo-capacitors (PCs). In EDLCs, the capacitance arises from the pure electrostatic charges accumulated at the electrode-electrolyte interface [34, 35, 37]. On the other hand, within PCs, the energy storage relies on fast and highly reversible oxidation/reduction (redox) or Faradic charge transfer reactions of electroactive species on the surface or near-surface of the electrode, along with the electric double layer storage mechanism, such as transition

metal oxides and conductive polymers [34, 35, 37, 38].

The energy storage mechanism in EDLCs is in much the same way as that in the traditional capacitors, through charge separation. However, EDLCs can store much more energy (several orders of magnitude) compared to conventional capacitors [31, 39]. This property is issued from the large interfacial area and the atomic range of charge separation distance. This energy storage mechanism allows very fast energy uptake and delivery and a high stability of EDLCs during millions of charge/discharge cycles [40]. The most widely studied materials with EDLC energy storage mechanism are carbon materials. Such energy storage process is non-Faradic in nature [33, 41]. Typically, the EDLCs can be constructed when two charged electric conductors, such as porous carbon rod, are inserted into a liquid ionic solution, as shown in **Fig. 1-4**. Charge separation occurs electrostatically at each liquid-solid interface, solvated ions (positive or negative ionic charges) within the electrolyte accumulate at the surface of the solid electrode by an equal but opposite charge at the solid electrode surface to meet electroneutrality, leading to the formation of the so called electric double layer (EDL) [41, 42]. During the charging process, cations within the electrolyte will be attracted towards the negative electrode while anions move in the opposite direction (Fig. 1-4A). Reverse processes will take place during the discharge process (Fig. 1-4B). In the whole process, however, no actual charge transfer occurs directly across the electrode-electrolyte interface, and no net ion exchanges occur between the electrode and the electrolyte [41, 43]. The accumulation of charges, the limit of which is influenced by the potential difference in the solid-liquid interface, gives rise to the double layer capacitance on each rod [44]. In fact, charge separation takes place once one carbon rod is brought in contact with the liquid solution, forming the conventionally called ideally polarized electrode [41].

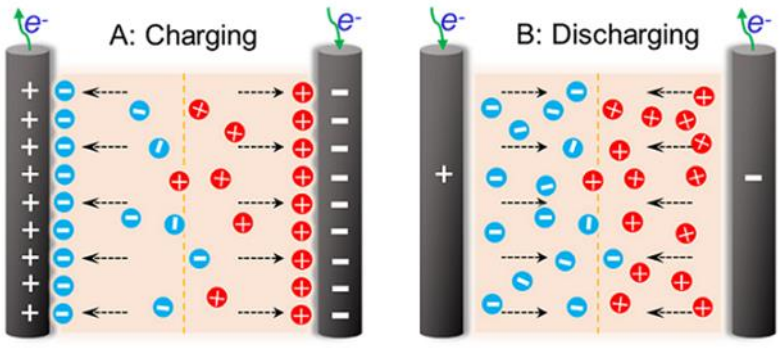

Fig. 1-4. Principle of a single-cell EDLC.

Fig. 1-4 illustrates one single-cell EDLC constructed by two carbon rods. The process effectively creates two EDLCs at each carbon rods that connected in series by the electrolyte, and stay charged after the circuit is opened [39, 42, 43]. On each electrode-electrolyte interface, the charging-discharging process can be expressed as follows [43, 45]:

Near the positive electrode:

$$E_{s1} + A^- \underset{\text{discharge}}{\overset{\text{charge}}{\rightleftharpoons}} E_{s1}^+ // A^- + e^- \qquad \text{Eq. (1)}$$

Near the negative electrode:

$$E_{s2} + C^+ + e^- \underset{\text{discharge}}{\overset{\text{charge}}{\rightleftharpoons}} E_{s2}^- // C^+ \qquad \text{Eq. (2)}$$

Therefore, the overall charging discharging process can be expressed as:

$$E_{s1} + E_{s2} + A^- + C^+ \underset{\text{discharge}}{\overset{\text{charge}}{\rightleftharpoons}} E_{s1}^+ // A^- + E_{s2}^- // C^+ \qquad \text{Eq. (3)}$$

Where, E_{s1} and E_{s2} are referred to as the electrode surface, the A^- and C^+ represent the anion and cation charges within the electrolyte, and the "//" represents the electrode-electrolyte interface.

The energy storage in PCs is completely different from that in EDLCs since it is via fast reversible redox reactions occur at or near the surface of the electroactive materials (Faradic in origin), which is analogous to that in batteries, especially rechargeable batteries. The Faradic process involves the charge passing across the double layer, as that in batteries, resulting in Faradic current passing through the capacitor. However, they are quite different in origin from the perspective of kinetic process, since reactions that take place within PCs are not limited by solid-state diffusion [46]. As defined by Conway, pseudocapacitance arises on account of an intermediate situation where Faradic charge transfer occurs, however, owing to special thermodynamic conditions, the extent of charge acceptance (quantity of passed charge), Q, is a continuous function of the potential change, dV, resulting in the derivate, dQ/dV, arises with properties equivalent to a measurable capacitance [38]. Materials for energy

storage undergoing such mechanism have been fully investigated in the late decades and they basically are metal oxides, such as RuO_2 [47], MnO_2 [48] and Nb_2O_5 [49]. Until now three different types of reversible redox mechanisms that give rise to pseudocapacitance have been clearly identified and well explained by Conway [38, 44] and Augustyn [46, 50], as illustrated in **Fig. 1-5**. From a thermodynamic perspective, pseudocapacitance originates whenever some property, y, proportional to the passed charge, is related to potential by an equation of this type:

$$\frac{y}{1-y} = K \exp\left(\frac{VF}{RT}\right) \qquad \text{Eq. (4)}$$

Here, the quantity y can be an extent of fractional coverage of an electrode surface, an extent of fractional absorption into some intercalation host, or some extent of conversion of an oxidized species (or vice versa) to a reduced species in a redox system in solution, as well explained by Conway in 1999 [38]. K is the equilibrium constant, V is the potential, F is the Faraday's constant, R and T is ideal gas constant and temperature, respectively.

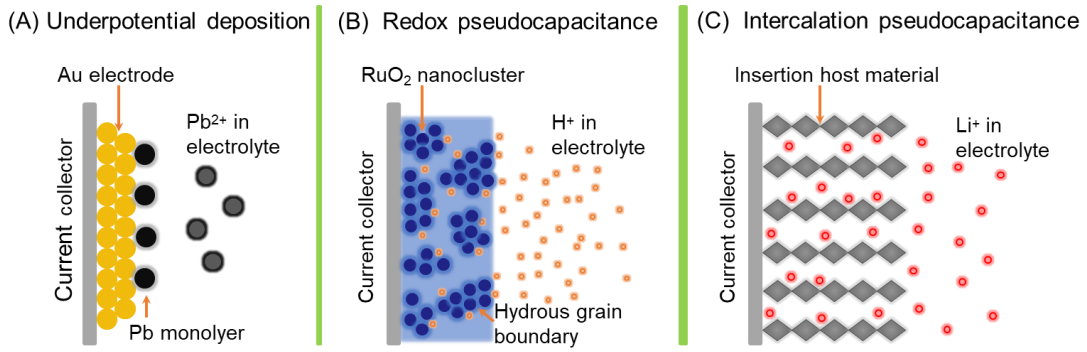

Fig. 1-5. Different types of reversible redox mechanisms that give rise to pseudocapacitance [46].

PCs can be considered (to some extent) as a complementary form of EDLCs and the energy storage inside PCs always accompany the EDLC behavior. These SCs generally display similar but distinguishable cyclic voltammetry (CV) and galvanostatic charge-discharge (GCD) curves, which are completely different from that of batteries [51, 52], as demonstrated in **Fig. 1-6**. Among the three above mentioned reversible redox mechanisms that give rise to pseudocapacitance, intercalation

pseudocapacitance in recent years has greatly broadened the family members of pseudocapacitive materials. However, in most of the cases, electrode materials with intercalation pseudocapacitance demonstrate non-negligible CV peaks (as shown in Fig. 1-6) which make it confused for researchers to distinguish this with a similar process that occurs in batteries [46, 51]. Recent results on the different electrochemical behavior of $LiCoO_2$ in bulk and at nano-scale have led to a further classification of the pseudocapacitive materials into intrinsic and extrinsic pseudocapacitive materials [46, 53, 54]. However, Brousse and Long et al. strongly recommended to determine pseudocapacitive materials by considering the original definition and their basic electrochemical signatures [55]. Based on their opinion, the "extrinsic pseudocapacitance" should instead be expressed as "capacity", and some so-called "extrinsic pseudocapacitive" materials (*i.e.* nickel hydroxides), should be classified as battery-type materials. For better understanding and distinguishing the intercalation pseudocapacitive charge-storage mechanism from that of battery materials, kinetic analysis has been fully investigated [50, 56-59]. And it has been proposed that the current obeys a power-law relationship with the sweep rate as [56]:

$$i(\mathrm{v}) = av^b \qquad \text{Eq. (5)}$$

Where i is the current obtained at a specific sweep rate v, a and b are adjustable values. The diffusion-controlled contribution and capacitive contribution for charge storage can be quantitatively determined by the value of b [58]. For capacitive process, the value of b approaching to 1, such as MnO_2 indicating the pseudocapacitive behavior in origin, whilst for battery signatures materials, such as $LiFeO_4$, the value of b is 0.5 [37, 51, 54]. Although this quantitative kinetics analysis method has been extensively utilized to evaluate and prove the kinetics performance of various electrode materials, it should not be solely method used to determine the electrochemical signatures of the materials, other electrochemical methods (*i.e.* electrochemical impedance spectroscopy (EIS)) should also be taken into consideration [46, 51, 59]. Until recently, "The first question a researcher should ask when doing electrochemical data analyses on a new nanomaterial is whether the material is battery-like or capacitor-like" has clearly and comprehensively explained by Gogotsi and Penner [60] based on the above-mentioned work.

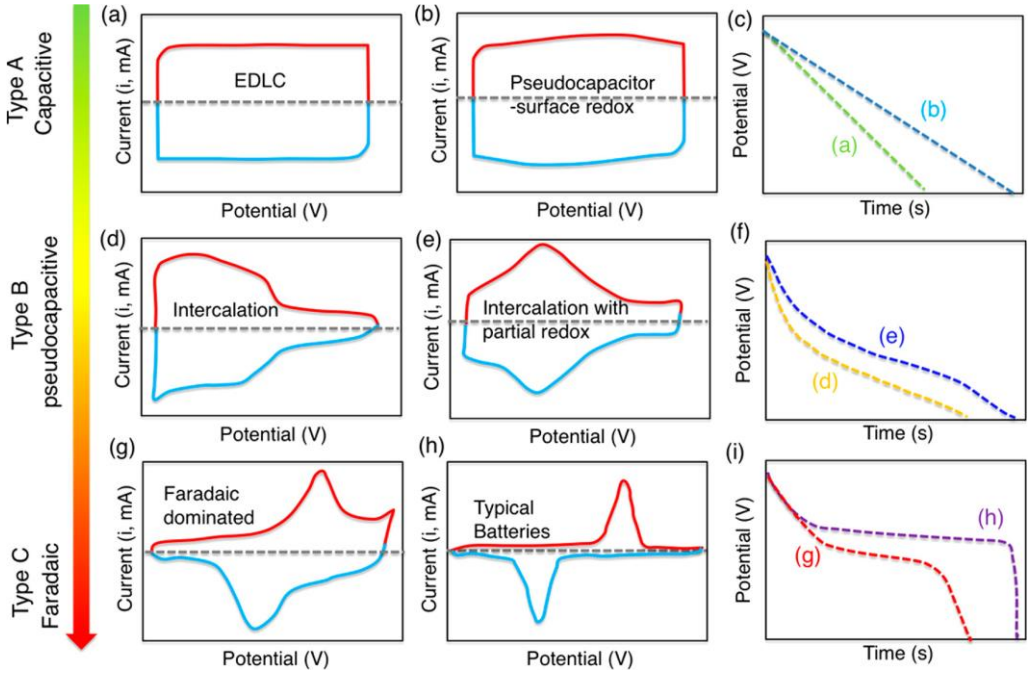

Fig. 1-6. Schematic cyclic voltammograms (a, b, d, e, g, h) and corresponding galvanostatic discharge (c, f, i) curves of different types energy-storage materials [60].

Generally, PCs have higher capacitance compared with that of EDLCs and rather faster charge-discharge rates than batteries since the pseudocapacitance is originating from fast Faradaic reaction and the related electrochemical processes taking place only on the surface or subsurface of the electrode materials with no solid-diffusion limitation. On this point PCs have been considered to bridge the gap between EDLCs and batteries [37, 46, 51]. However, this type of capacitors regularly suffers from lower power density and undesirable mechanical stability due to the poor electrical conductivity, the limited Faradic processes involved and the structure swelling and shrinking during the charge and discharge cycles [34, 43, 61, 62].

In summary, the energy storage processes in SCs are typically occur on the surface of the electrode material with the charging and discharging on the order of seconds and minutes, which is totally different from that in battery. In batteries, additional steps take place on the electrode, such as cation diffusion within a crystalline framework, chemical interconversions of the chemical electrode reagents with substantial phase changes, subsequently resulting in a relatively slow rate of energy storage and delivery [39, 46, 63]. Although the overall energy change can be conducted in a relatively reversible thermodynamic way, the charge and discharge processes in a battery often involve irreversibility in interconversion of the electroactive materials, thus leading to the energy dissipation through resistive losses and the poor cycle life [38, 46].

1.1.2 Models development for electrical double layer interface

From the above discussion it is obvious that even though the energy storage mechanism is different in EDLCs, PCs, and batteries [36, 60, 64], the construction of EDL is necessary and widely involved in the electrochemical processes taking place in these energy storage devices. This leads to various detailed investigation of the EDL near the electrode-electrolyte interface for a good understanding of the surface chemistry between capacitor components in order to improve the interfacial interactions to fabricate well-defined structures to enhance the energy storage performance [38, 65-68]. Several theories or models concerning on this solid electrode interphase (SEI) have been developed over the past few decades [38, 66, 69, 70].

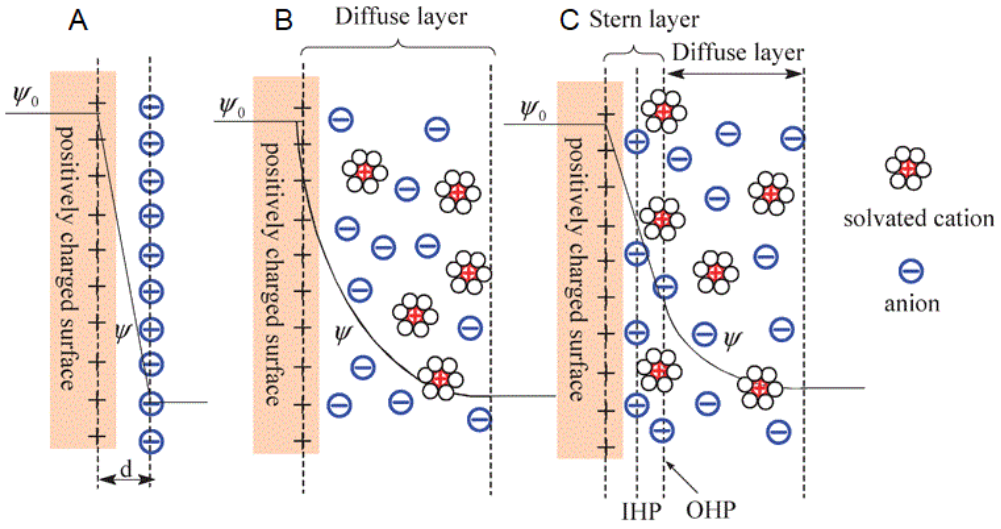

Fig. 1-7. Schematics of different EDL models at a positively charged surface: (A) the Helmholtz model, (B) the Gouy-Chapman model, and (C) the Stern model with the inner Helmholtz plane (IHP) and outer Helmholtz plane (OHP). The OHP is the boundary of the Stern layer and the plane where the diffuse layer begins. ψ_0 and ψ are the potentials at the electrode surface and the electrode-electrolyte interface, respectively [40].

The first concept of electric double layer was introduced by von Helmholtz in 1853 for investigating the spatial charge distribution of colloidal particles [71] and was subsequently adapted to the case of metal/electrolyte solution interface [72]. As schematically illustrated in **Fig. 1-7A**, the Helmholtz EDL model reveals that charged electrode immersed in electrolyte solution will attract counterions to its surface forming

two compact layers of charges with opposite polarity at the electrode/electrolyte interface, which are separated by small distance (d, order of few Å). This model is identical to that of conventional dielectric capacitors, and the specific capacitance (C_H, $F \cdot m^{-2}$) based on Helmholtz model can be determined by the following formula [38, 66, 73-75]:

$$C_H = \frac{\partial \delta}{\partial \psi} = \frac{\varepsilon_r \varepsilon_0}{d} \qquad \text{Eq. (6)}$$

Where δ is the surface charge density, ψ is the potential drop across the double layer, ε_r is the electrolyte relative permittivity, ε_0 is the vacuum permittivity (8.85419×10^{-12} $F \cdot m^{-1}$), and d is the effective thickness of the double layer [34, 74-76]. This is the simplest model to describe the charge distribution near the interface. However, the differential capacitance predicted with this model is constant at the interface, which contradicts the observed experimental results that the measured capacitance varies with potential and the electrolyte concentration. Its major problem lies in the surface distribution of charges in the electrolyte side as ions in the solution cannot remain static in a compact array due to their interactions and thermal fluctuations [38, 66, 73, 75].

The Helmholtz EDL model was further refined by Gouy in 1910 [77] and Chapman in 1913 [78] with the consideration of electrolyte ions thermal fluctuation inside the electrolyte. According to this model, electrolyte ions are attracted or repelled by electrostatic force near the interfacial region depending on their polarity, and meanwhile, these ions have a tendency to diffuse into the electrolyte near the interfacial region due to random thermal motion instead of rigidly attached to the electrode surface (hypothesized in Helmholtz model), thus forming the diffuse layer inside the electrolyte with a net charge density equal and opposite to the excess or deficit charge on the electrode surface [38, 61, 69, 74-76], as illustrated in **Fig. 1-7B**. The full mathematical formulation of the diffuse layer model was established based on the combination of Poisson's equation and Boltzmann's energy distribution function [38, 73-75]. And the interface differential capacitance can be calculated as [66, 69, 74, 75]:

$$C_D = \frac{d\sigma_M}{d\psi_0} = \left(\frac{2\varepsilon_r \varepsilon_0 n z^2 e^2}{k_B T}\right)^{1/2} Cosh\left(\frac{ze\psi_0}{2k_B T}\right) = \frac{\varepsilon_r \varepsilon_0}{L_D} Cosh\left(\frac{ze\psi_0}{2k_B T}\right) \qquad \text{Eq. (7)}$$

L_D is the Debye length is defined by the following equation for a z : z electrolyte:

$$L_D = \left(\frac{\varepsilon_r \varepsilon_0 k_B T}{2nz^2 e^2}\right)^{1/2} \quad \text{Eq. (8)}$$

Where σ_M is the surface charge density on the metallic side, ψ_0 is the potential at the electrode surface, n is the concentration of cations or anions at thermodynamic equilibrium in the solution, z is the valence of electrolytic ions, e is the elementary charge, k_B is the Boltzmann constant ($k_B = 1.381\times10^{-23}$ $m^2\cdot kg\cdot K^{-1}\cdot s^{-2}$), T is the absolute temperature, the L_D is referred to the thickness of the diffuse layer.

From Eq. (8) we can see that if the concentration of the electrolyte solution is increased, the diffuse layer will become compact, and the differential capacitance increases, whilst the increase of the applied potential on the electrode will also increase the capacitance (Eq. (7)). Therefore, this model makes a better approach to the reality than the Helmholtz model. However, this model assumes that ions are point charges, and as a consequence of that ions can be infinitely close to the interface, which leads to an overestimated capacitance, except for low potential levels in dilute electrolytes. For highly charged surfaces and multivalent ions, the predicted capacitance is a great disappointment [38, 40, 61, 73-75].

In 1924, Stern distinguished the interfacial region into two different ions distribution regions by combing the Helmholtz model and the Gouy-Chapman model [79]: the internal Stern layer (compact layer, or Helmholtz layer), in which ions are specifically adsorbed to the electrode surface, referring to the distance of closest approach of ions, and the connected diffuse layer as defined in Gouy-Chapman model [38, 40, 73, 74, 80], as illustrated in **Fig. 1-7C**. Therefore, the overall capacitance of the EDL (C_S) under such model can be considered as the combination of the Helmholtz layer capacitance (C_H) and the diffuse capacitance (C_D) in series, which can be expressed as [38, 40, 66, 73, 76]:

$$\frac{1}{C_S} = \frac{1}{C_H} + \frac{1}{C_D} \quad \text{Eq. (9)}$$

In this model, the ions are recognized as having finite size, including the annular thickness of ions' hydration shells. Therefore, their approach to the electrode surface

can be limited [38, 40, 61, 75]. Consequently, the overestimated capacitance that arises in the Gouy-Chapman treatment is effectively avoided. This Gouy-Chapman-Stern EDL theory gives results close to the experimental values in most of the situations, therefore, it has been widely adopted as basis of general interpretations of electrode interface phenomena in the development of EDLCs [38, 69, 75, 81].

Based on several meticulous works, Grahame further modified the Stern model [82]. In this model, he underlined the specific adsorption of ions on the electrode surface and explicitly distinguished three ion distribution regions: the inner Helmholtz plane (IHP), which is formed by the locus of the centers of specifically adsorbed ions at the electrode surface; the out Helmholtz plane (OHP), which is constructed by the centers of the non-specifically adsorbed counterions (the hydrated or solvated ions) and the diffusion layer as described above (as shown in Fig. 1-7C) [38, 40, 75, 76]. This theory is essential for clarifying the integral electrochemical processes occurring at the EDL interface and it provides a better understanding of how EDL capacitance is affected by the nature of electrolyte, such as ions size and polarizability [76].

1.1.3 Capacitance, Energy and Power of supercapacitors

As depicted in Fig. 1-4, one working supercapacitor requires two electrodes, one of which is charged negatively with respect to the other. As each of the electrode represents one capacitor, the overall capacitance (C_{cell}) of such a system can be determined by the series equivalent circuit consisting of anode capacitance (C_A) and cathode capacitance (C_C) according to the following equation [39, 40]:

$$\frac{1}{C_{Cell}} = \frac{1}{C_A} + \frac{1}{C_C} \qquad \text{Eq. (10)}$$

For a symmetric SC, $C_A = C_C$, the overall capacitance C_{cell} will be half of either one's capacitance, while for an asymmetric SC, $C_A \neq C_C$, C_{cell} is mainly dominated by the electrode with a smaller capacitance [43, 83]. In general, the capacitance and stored charge essentially depend on the electrode materials and the used electrolyte.

There are two characteristic parameters for evaluating one supercapacitor: the energy density (E) and power density (P), which can be expressed as a quantity per unit weight or per unit volume [32, 36, 40, 43, 81, 83]. In general, when one supercapacitor is charged, the maximum (theoretical) energy density stored within it is given by the

following equation:

$$E = \frac{1}{2} \times C \times V^2 = \frac{1}{2} \times Q \times V \qquad \text{Eq. (11)}$$

and the maximum (theoretical) power density that the cell is able to deliver can be calculated as follows:

$$P = \frac{V^2}{4R_{ESR}} \qquad \text{Eq. (12)}$$

where C is the capacitance of the cell, which is limited by the electrode and electrolyte combination, V denotes the nominal cell voltage range which is greatly influenced by the used electrolyte, Q is the stored total charges, R_{ESR} is the equivalent series resistance of the capacitor components. R_{ESR} generally comprises many types of resistance including the intrinsic electronic resistance of the active materials and the current collector, the contact resistance between the current collector and active materials, the electrolyte ions diffusion resistance in the electrolyte and the electrode pores as well as the resistance caused by the binder and separator [36, 40, 43, 81, 83].

The biggest challenge that supercapacitors are facing today is to increase their energy density to reach 10 $W \cdot h \cdot kg^{-1}$ or more, moving closer to batteries whilst cutting the cost [84]. From the above equations, it can be clearly seen that C, V and R_{ESR} are three important variables determining the supercapacitor performance. Because the energy storage and deliver processes involved in EDLCs are merely charge adsorption and desorption, the related R_{ESR} is low, therefore, EDLCs have a relatively high power density [38]. The energy and power stored in a SC can be continuously increased in proportion to the square of the cell voltage. Therefore, the increase of cell voltage should be more effective than improve the capacitance or decrease the equivalent series resistance for raising the ECs energy and power density [37, 83]. By adjusting the electrolyte, such as using organic electrolytes, the cell potential range can be greatly improved, from about 1 V generally for aqueous electrolyte to 3 - 3.5 V for organic electrolytes, meanwhile the potential-depend charge accumulation, Q, should also increase, thus the energy stored in the EDLC can be increased by nearly an order of magnitude [43, 85]. By developing asymmetric hybrid supercapacitor through packaging different types electrode materials, such as one with EDLC capacitance and

the other one with pseudocapacitance, inside the same cell, the operating voltage (V) of the full cell could be maximized during the charge and discharge process, and also both Faradaic and non-Faradaic processes will lead to much more charge store (Q), consequently increasing the energy and power density of the device [32, 36, 83, 86].

1.1.4 Activated carbon electrode material for supercapacitor

Electrode materials, as described above, are one of the critical factors that mainly determine the overall device performance. Therefore, many researches have been focusing on the development of novel materials with advanced nanotechnologies and engineering skills [34-37, 43, 46, 52, 61, 68, 75, 83-86]. Carbon materials, which have always been considered as the main candidate for high performance electrode composite, have received tremendous attention in the past decades due to their outstanding properties regarding their excellent electrical conductivity, achievable high surface area, outstanding chemical and thermal stability, controllable pore size, environmental friendliness and average low cost [34, 35, 38-40, 87, 88].

As an important member of the carbon material family, activated carbons (ACs), are well-known for the rich pore structure and achievable large specific surface area (SSA) (even up to 3000 $m^2 \cdot g^{-1}$), which are critical factors for high electrochemical performance. Together with their moderate cost and generally straightforward preparation approach, ACs have been the most commonly used electrode materials [34-36, 40, 61, 75, 87-89]. ACs based electrode generally store charge electrostatically through reversible adsorption of electrolyte ions onto the electroactive materials. The surface electrode charge generation involves surface dissociation and ion adsorption form both the electrolyte and crystal lattice defects [85, 88]. Even the pure carbon based SCs suffer from low energy density, typically on the order of 3 - 5 $W \cdot h \cdot kg^{-1}$. However, due to their tailorable structures and surface properties they still represent attractive materials for the development of potential achievable high energy density SCs in the last decade [34, 35, 40, 61, 75, 87-89].

ACs can be generally produced from various kinds of natural precursors, such as renewable biomass or synthetic carbon-rich organic precursors, through carbonization under an inert atmosphere, with subsequent physical and/or chemical activation steps to increase the specific surface area, enhance and adjust the pore volume and pore size distribution [61, 75, 85, 87-90]. Physical activation usually refers to the thermal

treatment of the as obtained carbons under oxidizing conditions, such as in the presence of CO_2, air or steam at a desired temperature. On the other hand, chemical activation takes place by thermal heating the carbon precursors in the presence of chemical activating agents, such as KOH, NaOH, $ZnCl_2$, K_2CO_3, H_3PO_4. The carbonization and activation processes are generally carried out simultaneously at lower temperatures with shorter activation time than that of physical activation and the resulting materials exhibit higher carbon yield and porosity [39, 40, 61, 88, 90, 91]. Among the activation agents, KOH is the most widely used. During the activation process, KOH etches the carbon framework producing CO_2 which leads to the formation of pores inside the carbon matrix, hence the obtained porous activated carbon materials can be widely used in energy storage field [88, 90, 91-93].

A high porosity carbon (AC4T800t2) with total pore volume of 1.448 $cm^3 \cdot g^{-1}$ and large SSA of 2457 $m^2 \cdot g^{-1}$ has been synthesized by KOH activation of coal raw materials [92]. The sample exhibited high specific capacitance (279 $F \cdot g^{-1}$ at a scan rate of 200 $mV \cdot s^{-1}$) but show relative low energy density (< 5 $W \cdot h \cdot kg^{-1}$). Another kind of oxygen-rich activated carbon (OAC) derived from bituminous coal have been reported by Zhang et al. [93] The OAC with oxygen content (up to 12%), moderately large specific surface area (1950 $m^2 \cdot g^{-1}$) and total pore volume (1.1 $cm^3 \cdot g^{-1}$), presented a high specific capacitance of 270 $F \cdot g^{-1}$ at a high current density (20 $A \cdot g^{-1}$) in 3 M KOH electrolyte. The extractable energy density of OAC based supercapacitor could reach up to 7.6 $W \cdot h \cdot kg^{-1}$ with a power density close to 10 $kW \cdot kg^{-1}$, indicating a great potential of such material in EDLC capacitors. The authors attributed the improved performance to the high oxygen content, high specific surface area, suitable pore size distribution and good electrical conductivity of the material. Recently, ultrathin carbon nanonets (UCN) derived from fluorene with remarkable cell capacitance of 211 $F \cdot g^{-1}$ at 100 $A \cdot g^{-1}$ has been first reported by He et al. (**Fig. 1-8)** [94]. The optimized material exhibited improved energy density of 10.9 $W \cdot h \cdot kg^{-1}$ but at a relatively lower corresponding power density of 26.3 $W \cdot kg^{-1}$. The restricted energy density should be due to the limitation of the operation voltage in aqueous solution (1 V), as discussed before [Eq. (11) and (12)]. Wei et al. have very recently described the synthesis of crumpled carbon nanonets (CCNN) from anthracene oil by calcium carbonate template strategy coupled with in-situ KOH activation [95]. The product does not show very high specific surface area (1822 $m^2 \cdot g^{-1}$), but it shows high total pore volume up to 4.11 $cm^3 \cdot g^{-1}$. And it exhibits remarkable energy density of 113.1 $W \cdot h \cdot kg^{-1}$ at 0.05 $A \cdot g^{-1}$ with a good cycle

stability in ionic liquid electrolyte (1-butyl-3-methylimidazolium hexafluorophosphate, with extend voltage window of 3.5 V). However, these types of derived carbons are produced from fossil fuel-based precursors which are expensive and nonrenewable.

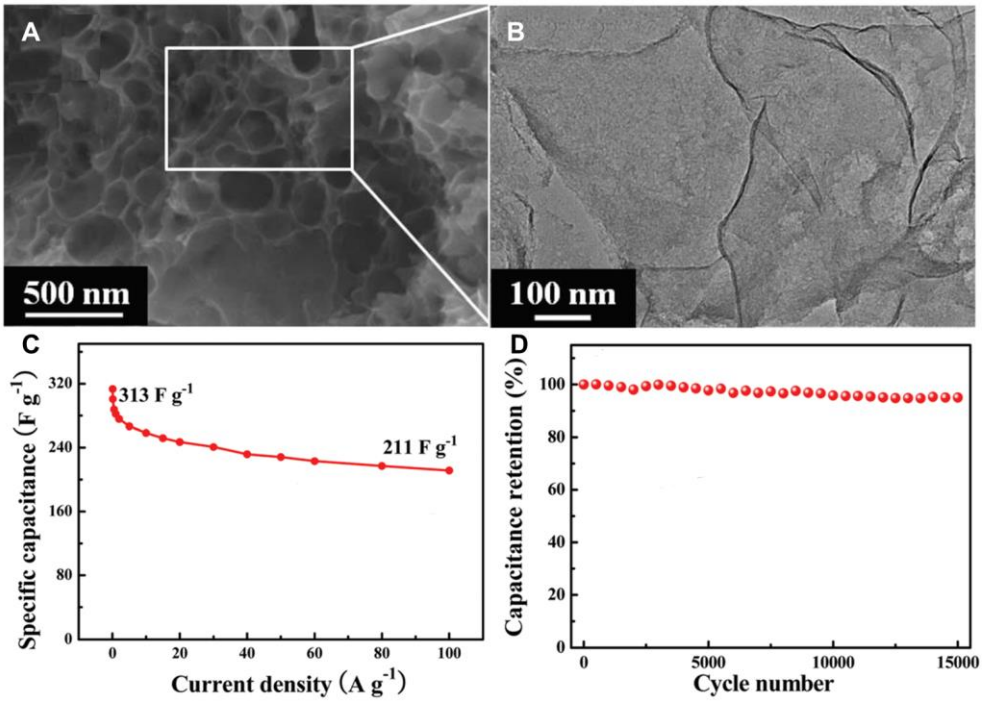

Fig. 1-8. (A) FESEM and (B) TEM images of $UCN_{3\text{-}10}$, (C) Specific capacitance of $UCN_{3\text{-}10}$ electrode at different current densities, (D) Cycling stability of the $UCN_{3\text{-}10}$ electrode [94].

In recent year, many efforts have been devoted to developing sustainable and high-performance electrode materials from biomass and its derivatives due to their large availability and low cost [31, 34, 37, 75, 89-91]. Natural biomass resources generally contain plenty of hetero-elements, such as O, N and S, which can be directly used as carbon precursor to produce heteroatom doped carbon structures. These heteroatoms can increase the wettability of the electrode under aqueous electrolytes, which will facilitate the electrolytic ions transfer in microporous and mesoporous channels thus improving the availability of surface area and enhancing the ultimate electrochemical performance of the porous carbons [31, 37, 40, 96]. And they can effectively induce pseudocapacitance with the EDL capacitance while maintaining the excellent intrinsic characteristics of carbon materials at the same time and producing high capacitance electrode [87]. Compared with the post heteroatom doping process, the use of light hetero-elements rich carbon precursors represents a more cost-effective and sustainable

way to the production of high-performance electrode materials [97, 98].

A three-dimensional (3D) honeycomb-like porous carbon (HLPC) with relatively large specific surface area (up to 2725 $m^2 \cdot g^{-1}$) has been prepared by Liang et al. though a simple carbonization of pomelo peel followed by KOH activation approach [99]. The as-synthesized HLPC displayed an interconnected porous carbon structure (numerous micropores (0.7-2.0 nm) and some mesopores (2.0-3.3 nm)) with nitrogen and oxygen-containing groups on the surface. This carbon structure exhibited a high specific capacitance of 342 $F \cdot g^{-1}$ and 171 $F \cdot cm^{-3}$ at 0.2 $A \cdot g^{-1}$ in 6 M KOH solution with a considerable capacitance retention of 62% at 20 $A \cdot g^{-1}$. A symmetric SC device based on the above mentioned HLPC material has delivered a maximum energy density of ~ 9.4 $W \cdot h \cdot kg^{-1}$ at a power density of 96 $W \cdot kg^{-1}$ in KOH electrolyte, which is almost up to the target of 10 $W \cdot h \cdot kg^{-1}$ [84]. This result makes this HLPC material an excellent candidate for its use in a high-performance electrochemical energy system. However, the corresponding power density is relatively lower compared with the traditional characteristics of the high-power density of a supercapacitor, this restricted power density could be attributed to the ineffective connection of different channels. Similar chemical activation approach has also been adopted in the treatment of bean shells by Xu et al. to produce hierarchical porous carbon materials with worm-like micropores in combination with mesopores as well as sulfur and nitrogen doping for EDLCs, lithium ion batteries and sodium ion batteries [100]. Meanwhile, O-N-S co-doped hierarchical porous carbons (HPCs) from ant powder have been reported by Zhao et al. using one-step carbonization and activation process [101], as illustrated in **Fig. 1-9**. The HPCs possessed a large specific surface area (2650 $m^2 \cdot g^{-1}$) and high total pore volume (1.4 $cm^3 \cdot g^{-1}$) with suitable pore size distribution (average pore width of 2.1 nm) as well as interconnected macro-, meso- and micropores. These properties ensure an ultra-high specific capacitance of 576 $F \cdot g^{-1}$ in aqueous solution (6 M KOH) at 1 $A \cdot g^{-1}$ in a three-electrode system. The fabricated symmetric supercapacitor delivered a notable energy density of 67 $W \cdot h \cdot kg^{-1}$ at a power density as high as 18 $kW \cdot kg^{-1}$ in ionic liquid electrolyte (1-ethyl-3-methylimidazolium tetrafluoroborate, $EMIMBF_4$, with voltage window of 3.6 V), indicating the great promise of these HPCs for high-performance electrochemical energy storage. However, Zhai et al. have pointed out that organic groups involved with oxygen and nitrogen are not stable during long cycling. In addition, in organic electrolyte, these heteroatoms could cause decomposition of the electrolyte and thereby show negative affection to cycle life [34]. Recently, 3-D

hierarchical porous carbons (PCs) obtained by carbonization and subsequent chemical activation of soybean roots (SRs) with superior electrochemical performance have been reveal by Guo et al. [102]. Their large SSA (2143 $m^2 \cdot g^{-1}$), unique 3D hierarchical structure composed of abundant micropores and some mesopores and high content of surface oxygen (8.4 wt.%) endowed the optimized sample (SRPC-4K) with outstanding electrochemical properties with superior rate capability of 276 $F \cdot g^{-1}$ at 20 $A \cdot g^{-1}$ in a symmetric two-electrode supercapacitor (6M KOH electrolyte). Most importantly, a superior energy density of 100.5 $W \cdot h \cdot kg^{-1}$ was gained at a power density of 4.4 $kW \cdot kg^{-1}$ in neat EMIMB4, and a maintenance of 40.7 $W \cdot h \cdot kg^{-1}$ at an ultrahigh power density of 63 $kW \cdot kg^{-1}$, which are the state-of-the-art level and give to such a material great potentialities for its exploitation in SCs.

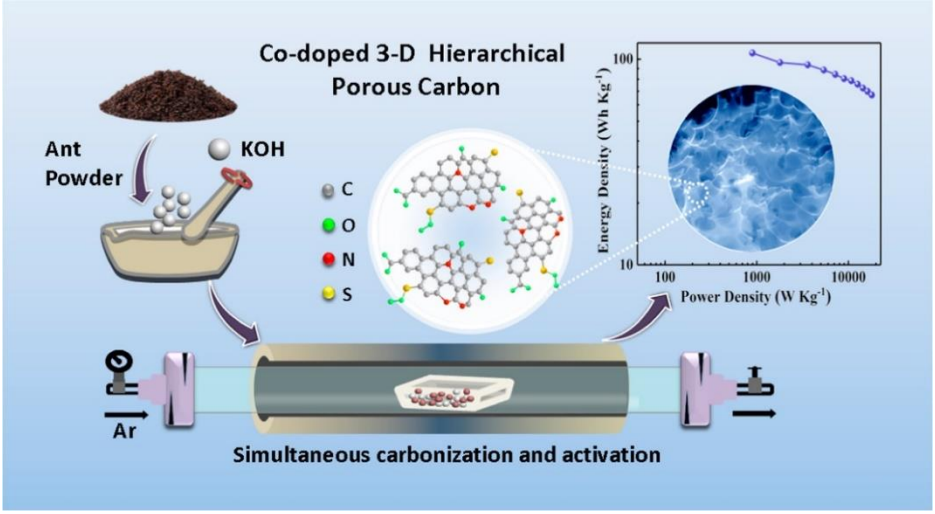

Fig. 1-9. Schematic illustration of the production processes for the 3-D HPCs [101].

Carbon precursors and the activation processes have a greatly influence on the morphology, porous structure and surface structure of final carbon materials [91, 103]. Recently, porous graphene-like nanosheets (PGNSs) have been prepared by a simultaneous activation - graphitization (SAG) route starting from renewable biomass waste coconut shell [104]. The PGNSs with specific surface area of 1874 $m^2 \cdot g^{-1}$ and total pore volume of 1.21 $cm^3 \cdot g^{-1}$ exhibited an excellent capacitance of 276 $F \cdot g^{-1}$ and 196 $F \cdot g^{-1}$ in aqueous solution (6 M KOH) and organic electrolyte (1 M Et_4NBF_4-PC) at 1 $A \cdot g^{-1}$. Notably, this material has shown a remarkable energy density of 7.3 $W \cdot h \cdot kg^{-1}$ and 54.7 $W \cdot h \cdot kg^{-1}$ at a power density of 7.1 $kW \cdot kg^{-1}$ and 10 $kW \cdot kg^{-1}$ in aqueous solution (voltage window 1 V) and organic electrolyte (extended voltage window 3.0

V), respectively. Such an excellent performance has been attributed to several factors: the good electron conductivity that promotes the electron transport; the porous structure facilitates the rapid ions diffusion by providing interconnected and low-resistance channels, and the in parallel or in series contacted porous graphene-like nanosheets that greatly short ion diffusion channels and facilitate the permeation of the electrolyte between the carbon layers. Another kind of 3-D framework porous carbon nanosheets (PCNSs) have been reported by Chen et al. through chemical activation of dry elm samara (**Fig. 1-10a** and **b**) [105]. The PCNS-6 with specific surface area of 1947 $m^2 \cdot g^{-1}$ and total pore volume of 1.33 $cm^3 \cdot g^{-1}$ displayed a state-of-the-art capacitance of 470 $F \cdot g^{-1}$ and 310 $F \cdot g^{-1}$ in aqueous solution (6 M KOH) at 1 $A \cdot g^{-1}$ in a three- and two-electrode system, respectively, together with an energy density as high as 22.22 $W \cdot h \cdot kg^{-1}$ at a high power density of 20 $kW \cdot kg^{-1}$ in the aqueous electrolyte. By using ionic liquid electrolyte (1-ethyl-3-methylimidazolium tetrafluoroborate, $EMIMBF_4$), the PCNS-6 based supercapacitor could achieve an energy density up to 25.4 $W \cdot h \cdot kg^{-1}$ at a power density of 15 $kW \cdot kg^{-1}$. In addition, other different morphology porous structure, such as 3-D flower-like and hierarchical porous carbon material (FHPC) has also been reported (**Fig. 1-10 c** and **d**) [106].

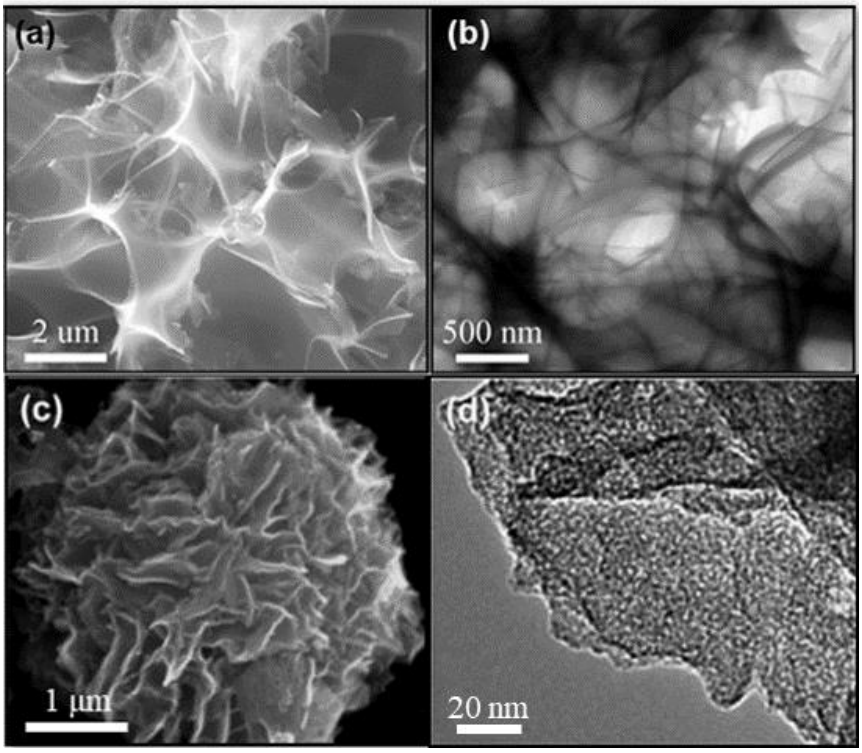

Fig. 1-10. SEM and TEM images of (a, b) PCNS-6, (c, d) FHPC [105, 106].

1.2 Chemical energy conversion and storage

Recently, many large-scale energy storage technologies have been developed, such as flywheels, compressed air, pumped hydro and thermal energy storage systems [25, 29, 30]. However, these storage strategies are either short-term approaches with limited storage capability and high cost or limited deployment issues (*i.e.* problems related to sites availability or negative influence on environment). Therefore, they are not necessarily applicable to flexible larger-scale systems, and their efficiency may be suboptimal [25, 26, 107, 108]. Thus, long-term energy storage systems for large-scale integration of RES and suitable to provide effective balance for the energy grid are needed. In the context of large-scale RE storage, catalytic processes allowing the conversion of the surplus electricity deriving from RES into chemical compounds represents a highly challenging alternative to any other energy storage approach. Chemical compounds can be further transported through existing infrastructures which could also contribute to the reduction of the overall process costs. All the processes fall in the general power-to-X concept as summarized in **Fig. 1-11** [14, 28, 109].

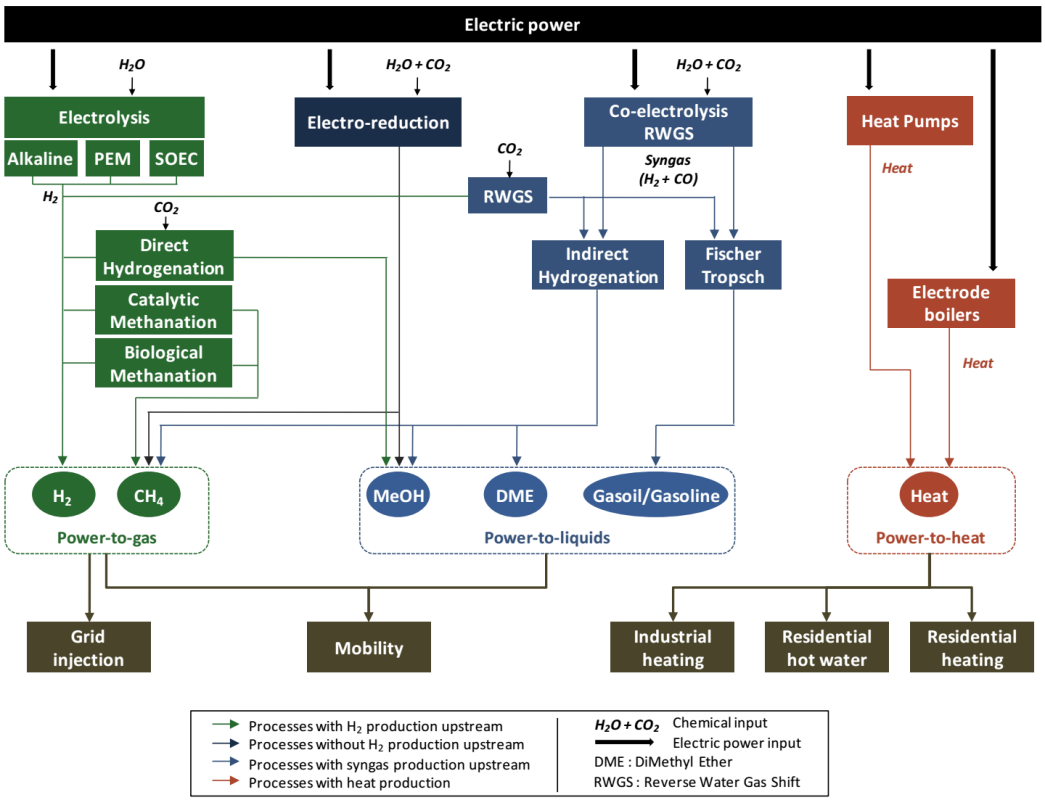

Fig. 1-11. Flow-chart diagram of the conversion of renewable electricity into chemical compounds [109].

1.2.1 Power-to-Gas

Power-to-Gas (PtG) processes have been proposed as a very promising storage technology. The combination of renewable H_2 (through water electrolysis) with the subsequence hydrogenation of CO_2 for the production of synthetic natural gas (SNG) (CO_2 methanation reaction) has been considered as one of the most promising strategies for the future energy mix with larger share of RE from diverse RES [110-112]. This strategy can effectively transform the surplus electric energy obtained from intermittent RES into easily long-term and large-scale storable and transportable chemical energy carrier gases, *i.e.* H_2 and CH_4, which could be further used for powering clean energy vehicles, for domestic heating, or as raw materials for chemical industry. They can even be reconverted back to low-carbon electricity whenever it is necessary (with associated loss in terms of energy efficiency), as shown in **Fig. 1-12** [113]. Therefore, this process paves the way towards an enormous storage capacity for excess energy with high electricity generation from RES in excess of demand and provides the large integration of fluctuating RE in the energy mix, including the provision of balancing power [27, 114]. The development of PtG systems is still in its infancy worldwide but it is expected to become a major player in the near future with optimization processes.

The primary step of PtG is the conversion of the excess electrical energy from RES into H_2 via water electrolysis process. Such a process has been widely investigated with different electrolysis technologies, generally including alkaline electrolysis (AEL), polymer electrolyte membrane electrolysis (PEMEL), and solid oxide electrolysis (SOEL) in recent years, and their advantages and drawbacks have been overviewed in several reports [114, 115]. The as-produced H_2 can be subsequently stored in compressed gas tanks (CHG, compressed hydrogen gas), cryogenic compressed liquid hydrogen tanks, metal hydride (MH) tanks or even underground caverns [26, 115]. The H_2 can thus be used as fuel for fuel cells in the fields of transport or to produce back electricity for remote installations. During the last decades, great efforts have been devoted to increase the hydrogen-based economy mostly in the field of transportation or as a complement chemical product for domestic heating through its injection into the

gas infrastructure. However, despite such efforts it has been a consensus that the hydrogen deployment remains limited in terms of market which is mostly due to the lack of hydrogen transport infrastructures and market interest [116].

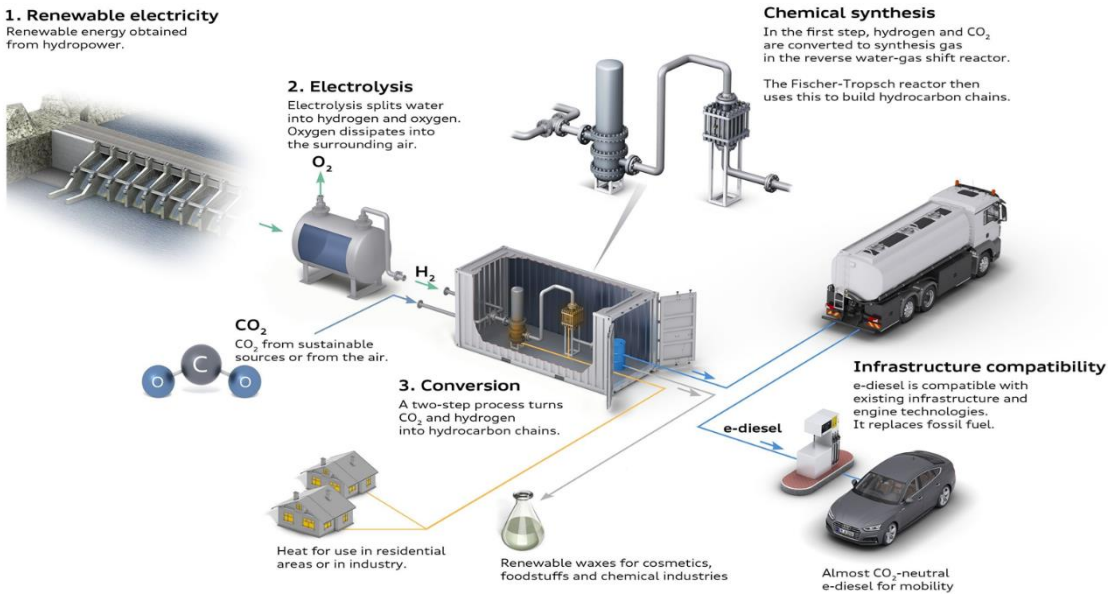

Fig. 1-12. Scheme of PtG technical chains with CO_2 recycling [113].

The produced H_2 from RES can be directly used to generate SNG through the CO_2 methanation reaction to achieve free- or zero-carbon emission, which can be effectively linked with the CCS/CCU chains and the national natural gas grid [112, 115, 117]. Such a process can also be employed for biogas upgrading by converting the co-generated CO_2 into methane, resulting in greatly increase of CH_4 production for Biomass-to-Gas (BtG). About 1.3×10^9 m^3 of biomethane was produced in 2013 in Europe, which corresponds to about 12 TWh/a of chemical energy that can be stored in the form of methane (based on an average concentration of CO_2 of ca. 45%) [115, 118].

The methanation reaction greatly improve the compatibility of such an energy storage system with the existing gas grid infrastructures since it greatly increases the energy density of the gas (35-40 $MJ \cdot m^{-3}$ for CH_4 vs. 12.75 $MJ \cdot m^{-3}$ for H_2) while reducing safety issues compared with the injection of H_2 [14, 107, 119]. In addition, this process contributes to the mitigation of CO_2 emissions, fulfilling well with the

urgency of a clean energy and a sustainable development [108, 120, 121]. Therefore, this technical chain can effectively balance the energy supply and demand with time and facilitate the energy distribution among different energy supply systems by connecting the electricity network with the existing gas distribution grids in a single energy system. Moreover, the overall capability and cost for storage and transformation have been greatly decreased [24, 107, 117, 119]. These advantages make this high flexible technology one of the most promising ones for energy storage. However, further optimizations are still needed in order to optimize the operational costs [26, 117].

1.2.2 CO_2 methanation

In the PtG technology chains, methanation can be achieved by both low temperature biological and medium to high temperature catalytic methanation process. The former produce methane mainly by acetolactic methanogenesis and hydrogenotrophic methanogenesis, and the process generally operated at moderate temperature under anaerobic conditions and mostly under atmospheric pressure. It generally shows high tolerance against pollutant substances in the feed gases. However, the overall process has greater mass transfer resistance with slow kinetics as well as low flexibility when compared with the latter [115, 122]. Herein, we will mainly focus on the catalytic methanation process.

Catalytic CO_2 methanation, also well-known as Sabatier reaction, remains the most advantageous reaction with respect to thermodynamics, since the reaction is considerably simpler and faster than other reactions which form hydrocarbons or alcohols [123, 124]. Therefore, such reaction has already attracted tremendous attention from researchers around the world. The National Aeronautics Space Administration (NASA) is also interested in the application of such process for its use in future manned space colonization on Mars [125]. CO_2 methanation (Eq. (13)) likely involves several other reactions, such as the reverse water gas shift reaction (RWGS, Eq. (14)), forming CO by-product, and the subsequent CO methanation (Eq. (15)):

$$CO_2 + 4H_2 \rightarrow CH_4 + 2H_2O \qquad \Delta H^o_{298K} = -165\ kJ \cdot mol^{-1} \qquad \text{Eq. (13)}$$

$$CO_2 + H_2 \rightarrow CO + H_2O \qquad \Delta H^o_{298K} = +41\ kJ \cdot mol^{-1} \qquad \text{Eq. (14)}$$

$$CO + 3H_2 \rightarrow CH_4 + H_2O \qquad \Delta H^o_{298K} = -206\, kJ \cdot mol^{-1} \qquad \text{Eq. (15)}$$

It is generally known that the Eq. (13) and Eq. (15) are exothermic reactions with thermodynamically limitation at high temperature, whilst the Eq. (14) is endothermic reaction, therefore, it is quite desirable to conduct this reaction at low reaction temperature to achieve high CO_2 conversion and CH_4 selectivity.

1.2.3 Metal-based heterogeneous catalysts

The reduction of the fully oxidized carbon (+ 4) to methane (- 4) is an eight-electron process with high kinetic barrier due to the chemical inertness and thermodynamic stability of CO_2 molecule, which usually requires effective catalysts to achieve desirable reaction rate with high CH_4 selectivity [126, 127]. Generally, this reaction can be catalyzed by various metals, including Ni, Rh, Ru, Co and Pd, working as active phases, supported on diverse of carriers, such as Al_2O_3, SiO_2, CeO_2, ZrO_2 and SiC with or without promoters, for instance Mn, Ce, K, Ca, Mg [127-130]. Among these catalysts, nickel-based catalysts are the most widely studied due to their low cost and achievable high activity and selectivity. Herein, we start from an overview of the Ni-based catalysts followed by the noble metal catalysts together with a brief introduction about the reaction mechanism since this is still under debate.

Ni-based catalysts

Ni-based catalysts are the most widely investigated materials for CO_2 methanation due to their low cost, achievable high activity and selectivity. Ni-based catalysts generally involve various metal oxides carriers or promoters to pursue achievable high catalytic performance. The supports, the promoters or second active metal as well as the nickel loading and catalyst preparation method have great influence on the overall catalytic performance [127-130].

The effect of supports on the catalytic performance is basically related to their different surface and textural properties, such as surface basicity, specific surface area and pore size distribution, which normally have a great influence on the dispersion and stabilization of the active phases as well as on the adsorption of the reactants on the catalyst surface, thereby affecting the overall catalytic performance and even influence the reaction mechanism [129-131]. The interaction between the active phase and the

support is also claimed to prevents the undesired metal nanoparticles (NPs) sintering during the course of the reaction. Therefore, the investigation of such a reaction on different carriers supported catalysts is of high interest in the design of highly effective catalytic systems [129, 132]. Tada et al. studied the effect of different supports on CO_2 methanation performance and their results indicated that the activity followed the order: $Ni/CeO_2 > Ni/\alpha\text{-}Al_2O_3 > Ni/TiO_2 > Ni/MgO$ under the same test conditions [133]. Ni supported on CeO_2 exhibited remarkable catalytic performance, several times higher than that supported on MgO at a reaction temperature ≤ 350 °C. This result was basically ascribed to the CeO_2 surface coverage of CO_2-derived species as well as to the partial reduction of CeO_2 surface. The electronic interactions between metal phase and support was also discussed. However, their explanations about the CO_2 reduction to CO based on the XRD, H_2-TPR and external CO methanation results were not completely convincing, especially in the lower temperature range where high conversion and selectivity occurred. Thus, in-situ study on this point should be conducted to confirm their assumption. Le et al. also found that Ni/CeO_2 possessed the best catalytic performance among other ZrO_2, SiO_2, TiO_2 and $\gamma\text{-}Al_2O_3$ supported Ni catalysts, especially at low reaction temperature range (150 - 250 °C) [134]. The optimized catalyst exhibited superior performance for both CO_2 and CO methanation due to the high Ni dispersion and strong CO_2 adsorption. However, in their test, a large percentage of diluted gas (49 v.% He) with excess H_2 (50 v.%) was used, which could modify somehow the catalytic performance. Indeed, it is generally known that with the increase of H_2 to CO_2 ratio, the CO_2 conversion can be artificially improved. Meanwhile, this is relatively uneconomical since H_2 also accounts for a portion of the overall production cost. In addition, the high diluted reactant mixture also significantly reduces the local hot spot generation inside the catalyst bed which artificially improves the catalytic performance compared to undiluted feed.

A high-loaded Ni-Al mixed oxide catalyst (ca. 70 wt.%) has been employed for CO_2 methanation by Abelló et al. [135] Although the high nickel loading is theoretically thought to be counterproductive for the nickel-based catalysts performance, their activated catalyst exhibited high CO_2 conversion with CH_4 selectivity very close to 100%. This was originated by the formation of small metallic nickel crystallites (ca. 6 nm) highly dispersed over NiO-alumina upon partial reduction of the mixed oxide. The utilization of another excellent support, mesostructured silica nanoparticles (MSN), with surface defect sites has been reported by Aziz et al. [136]. The catalytic

performance of Ni/MSN has been studied and compared with that on the other catalysts with Ni supported on MCM-41 (mobile crystalline material), HY (protonated Y zeolite), SiO_2 and γ-Al_2O_3. The Ni/MSN exhibited the highest activity with 64.1% CO_2 conversion and 99.9% CH_4 selectivity at 300 °C. The high activity of such catalyst was attributed to the presence of both intra- and inter-particle porosity which, on one side, led to the accessible high concentration of basic sites, on the other side, decreased the mass transfer resistance and facilitated the transport of both reactant and product molecules during the reaction. The methanation activity increased with the increase of the concentration of basic sites as they were favorable for the increase of CO_2 adsorption at the catalyst surface. The Ni/MSN catalyst also displayed superior stability and remarkable resistance to coke formation with no deactivation up to 200 h [136]. They further investigated the catalytic process with different metal (Rh, Ru, Ni, Ir, Fe, Cu) promoted MSN [137]. The methane formation rate on Ni/MSN could up to 0.2539 $mol_{CH4} \cdot mol_{Metal}^{-1} \cdot s^{-1}$, which was comparable to that on the Rh/MSN and Ru/MSN catalysts, *i.e.* 0.2842 and 0.2971 $mol_{CH4} \cdot mol_{Metal}^{-1} \cdot s^{-1}$, respectively. But on an area basis, the Ni/MSN was the most active catalyst among all the studied catalysts, while Ir/MSN was the poorest one (as shown in **Fig. 1-13A**) [137]. The authors also proposed that surface defect sites or oxygen vacancies in MSN were considered to be responsible for the formation of surface carbon species (bridged carbonyl and linear carbonyl), which were supposed to interact with the atomic hydrogen dissociated at the metal sites as to form methane, as illustrated in **Fig. 1-13B** [136, 137].

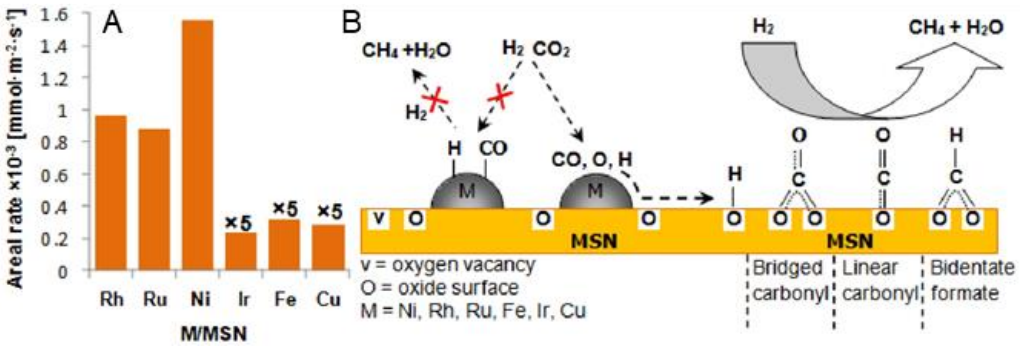

Fig. 1-13. (A) Catalytic performance and (B) Plausible mechanism of CO_2 methanation on different metal-promoted MSN catalysts [137].

Catalysts composites based on metal oxides have also received great attention from the scientific community interested in the field of methanation reaction [138-140].

Lin et al. reported the application of mesoporous Ni/Al_2O_3-ZrO_2 catalysts synthesized by a single-step epoxide-driven sol-gel method for enhanced low temperature CO_2 methanation [139]. They pointed out that the incorporation of ZrO_2 into Ni/Al_2O_3 could form Al_2O_3-ZrO_2 solid solution, which weakened the interaction of Ni-Al_2O_3 and facilitated the reduction and dispersion of NiO. Therefore, moderate increase in ZrO_2 loading could promote the formation of active metal Ni sites while increasing at the same time the surface oxygen vacancies, which were considered to be the main players for the improved low-temperature catalytic activity and CH_4 selectivity. However, excessive addition of ZrO_2 could cover abundantly the surface of NiO and Al_2O_3 support, thereby, decreasing the overall catalytic performance. The formation of solid solution could also promote the catalytic stability. The final optimized catalyst (20Ni/Al_2O_3-ZrO_2-1.0) exhibited 77% CO_2 conversion with almost 100% CH_4 selectivity at a reaction temperature of 300 ºC. Similar results have also been obtained by Zhan et al. [140]. They revealed that the presence of ZrO_2 in the Ni/γ-Al_2O_3 catalyst effectively suppressed the formation of $NiAl_2O_4$ by forming a γ-(Al, Zr)$_2O_3$ solid solution, thereby, weakening the NiO-Al_2O_3 interaction and enhancing the dispersion of Ni species. The improved catalytic performance was attributed to the largest amount of solid solution and the small sizes of Ni metal particles. A series of $Ce_xZr_{1-x}O_2$ (CZ) supported nickel catalysts have been prepared by ammonia evaporation (AE) [141]. Some Ni species could well incorporate into CeO_2 lattice of CZ support, resulting in the imbalance of electric charge and lattice distortion of CeO_2. The optimized Ni/CZ-AE showed enhanced catalytic performance at 275 ºC with 55% CO_2 conversion and 99.8% CH_4 selectivity. The authors also revealed that the CH_4 formation processed via a CO free mechanism *i.e*, formation of carbonates and formate species which were further hydrogenated and decomposed directly to release CH_4. Various other carriers have also been studied which show promising results but remain outside the scope of the current discussion.

The effect of adding promoters or a second metal on the ultimate catalytic performance of a given catalyst have also been matter of investigation. Generally, the addition of a promoter can greatly affect the surrounding environment of the active sites, decrease the reduction temperature, enhance the dispersion of active sites, provide more surface basicity or oxygen vacancy, which have been considered to be beneficial for the methanation activity [142-144]. Alkaline-earth metal and rare earth elements can not only work as structural promoters by increasing the dispersion of the active phase and

stabilizing the dispersed metallic phase against sintering, but they can also act as chemical promoters by modifying the surface basicity of the catalyst and regulating the electron property of the metallic active sites [142, 143]. Guo et al. checked the role of different alkaline-earth metal oxides (MgO, CaO, SrO and BaO) on CO_2 methanation over modified Ni/SiO_2 catalyst [143]. The authors pointed out that MgO addition inhibited the catalytic property of the Ni/SiO_2 catalyst due to the low reducibility of the nickel species, while SrO promoted the catalytic activity and enhanced the catalyst stability due to the inhibition of Ni sintering. CaO addition affected negligibly the performance of the $Ni/CaO/SiO_2$ catalyst. However, Xu et al. reported that the Ca doping in Ni-Al composite could greatly enhance the surface basicity of the material. Indeed, it was claimed to foster the chemisorption and activation of CO_2, thus, leading to a decrease of the apparent activation energy of CO_2 from 75.2 to 53.6 $kJ \cdot mol^{-1}$ and the significantly promoted low-temperature catalytic activity [144]. A series of rare earth (La, Ce, Sm and Pr) doped Ni-based catalysts for CO_2 methanation have been fabricated through a facile one-pot evaporation procedure by Xu. et al. [127]. The nickel species were highly dispersed among the mesoporous framework with strong metal-framework interactions. It has been found that rare earth dopants could significantly enhance the surface basicity and/or electron property of the catalysts, thus enhancing the chemisorption and activation of CO_2 molecule. As a result, the apparent activation energies of CO_2 could be obviously decreased and the low-temperature catalytic activity was greatly intensified over rare earth promoted catalysts. Similar effects have also been observed on La-doped $Ni/\gamma\text{-}Al_2O_3$ and Ni/Mg-Al catalysts [145, 146].

On the other hand, the addition of second active metal phase can effectively modify the metal-support interaction. Indeed, it can increase the dispersion and stabilization of the nickel phase, which is largely beneficial for the enhancement of catalyst activity and stability since nickel is also more vulnerable to coking and sintering in such exothermal reaction [147-149]. Co-Ni bimetal doped ordered mesoporous Al_2O_3 materials have been designed for enhanced CO_2 methanation [148]. The Co and Ni species were homogenously distributed in the Al_2O_3 matrix with strong interactions between metal and the mesoporous framework. By this way, the severely thermal sintering of the metallic Co-Ni active centers could be successfully inhibited during the catalyst reduction and activity evaluation processes. Similar results have also been reported by Zhu et al. in their study on active oxygen material $Ce_xZr_{1-x}O_2$-supported Ni-Co bimetallic nanosized catalysts for methanation [149]. Xu et al. further

revealed that the synergistic effect between the Ni and Co bimetallic active centers greatly enhanced the low-temperature activity by coordinating the activation of H_2 and CO_2, prominently decreasing the activation energy toward CO_2 methanation [148]. Ocampo et al. studied the influence of noble metals (Rh, Ru) addition on the catalytic performance of Ni/$Ce_xZr_{1-x}O_2$ (Ni-CZ) catalyst [138]. The addition of noble metal in nickel catalysts could lead to higher Ni dispersion with improved redox properties and restrict Ni oxidation via hydrogen atom spillover effect during the methanation process. This resulted in a raise of both activity and catalyst life-time without modifying the support intrinsic activity. The catalyst deactivation was mostly due to nickel particles sintering rather than carbon deposits. The utilization of other metals such as Fe, Mo has also been reported elsewhere [147, 150].

The nickel loading and the preparation of the catalyst also have great impact on both the interaction of nickel with the support and the nature of nickel species, which further affect the overall properties of the catalysts and the catalytic behaviors during methanation process [151, 152]. It is generally known that the metal species tend to be highly dispersed across the carrier at low loadings, whereas the metal particles tend to aggregate, forming large particle sizes, at high loadings [129]. Therefore, a moderate increase of nickel loading should increase the active sites, leading to the gradual improvement of the catalytic activity. Lin et al. found that as the Ni loading increased from 10 to 20 wt.% in the Ni/Al_2O_3-ZrO_2 catalyst, the optimal reaction temperature further decreased from 340 to 300 ^oC, accompanied with a slight increase of the catalytic activity (77%), revealing that the increasing Ni loading further improved the low-temperature CO_2 methanation activity. However, the growth momentum of CO_2 conversion was restrained for the 30 wt.% loading catalyst, which presented a slight decline in the optimal catalytic activity compared to the 20 wt.% loading catalyst, attributing probably to the aggregation of nickel nanoparticles at high nickel loading [139]. Similar results have also reported by Garbarino et al. and Rahmani et al. [145, 153]. The calcination of the pre-synthesized catalyst could also significantly affect the properties of the final catalyst, thereby affecting its ultimate catalytic performance. Rahmani et al. revealed that with the increase of the calcination temperature, the interaction between the NiO and the support could be greatly increased, while the surface area of the catalyst and the dispersion of the Ni were decreased. As a consequence, the overall catalytic performance was greatly decreased, especially in the low temperature range [153]. CeO_2 with different SSA were used for preparing nickel-

based catalysts with fixed theoretical nickel loading but different nickel dispersions (different particle size) by wet impregnation. The Ni/CeO_2(230) catalyst with the largest SSA exhibited enhanced dispersion of nickel species with relatively smaller particle size, thus displayed the best catalytic performance compared with other catalysts [134]. $Ni_aCe_{1-a}O_x$ ($0.3 \leq a \leq 0.9$) catalysts with different Ni contents prepared by co-precipitation have also been investigated by the authors. Although the nickel loading was quite high (75 wt.%) in the $Ni_{0.9}Ce_{0.1}O_x$ catalyst, the nickel crystallite sizes were close to that on the Ni/CeO_2 with 10 wt.% nickel loading prepared by impregnation method [134]. This is probably due to the fact that part of the nickel was involved in the construction of the catalyst composite structure (with strong interaction with CeO_2), which could be evidenced by the high reduction temperature of the NiO to some extent. This consequently resulted in the significantly decrease of the effective nickel active species on the surface of the catalyst. Meanwhile, Zhang et al. pointed out that urea hydrolysis method was a more efficient approach for the Ni-based catalyst preparation compared with co-precipitation method. The Ni-based catalyst obtained by the former approach displayed higher Ni dispersion, larger CO_2 adsorption capacity and thereby better catalytic performance [146]. Liu et al. fully investigated the influence of the nickel loading and the preparation method on the Ni/TiO_2 catalyst for CO_2 methanation [154]. Results clearly demonstrated that the particle size of the Ni increased with the increase of nickel loading, as shown in **Fig. 1-14(a-d)**. Two reduction peaks appeared at much lower temperature with significantly higher I_L/I_H ratio for the catalyst prepared by impregnation method [$Ni(15\%)/TiO_2$-IMP] compared with that synthesized via a deposition-precipitation approach [$Ni(15\%)/TiO_2$-DP]. This suggested the presence of relatively larger particles sizes of NiO with lower dispersion on the surface of TiO_2 and weaker interaction between NiO and TiO_2 in the $Ni(15\%)/TiO_2$-IMP sample (**Fig. 1-14c** and **1-14e**). The good dispersion of Ni NPs with large unsaturation on the $Ni(15\%)/TiO_2$-DP facilitated a high exposure of active sites, which accelerated the formation of surface-dissociated hydrogen and the subsequent hydrogenation removal of surface nickel carbonyl species. This accounted for the enhanced low-temperature catalytic performance, as shown in **Fig. 1-14g** and **h)**. Garbarino et al. studied the effect of Ni loading and the nature of the active species on Ni/Al_2O_3 catalyst in CO_2 methanation [155]. They concluded that moderate Ni loading could resulted in small Ni particles after pre-reduction, which were very selective to methanation without CO formation, while the high Ni loadings always leaded to large Ni particles, which on the

contrary benefited the CO production. Cubic Ni crystal structure was observed on the spent catalyst with no carbonaceous species, tending to exclude the formation of carbon species in significant amounts thus suggesting that the methanation "via carbide" mechanism could not be predominant. The authors then suggested that fast methanation occurred at the expense of CO intermediate on the corners of nanoparticles interacting with Al_2O_3, likely with a "via oxygenate" mechanism. According to the results discussed above one can notice the relatively large influence of the support nature on the methanation performance.

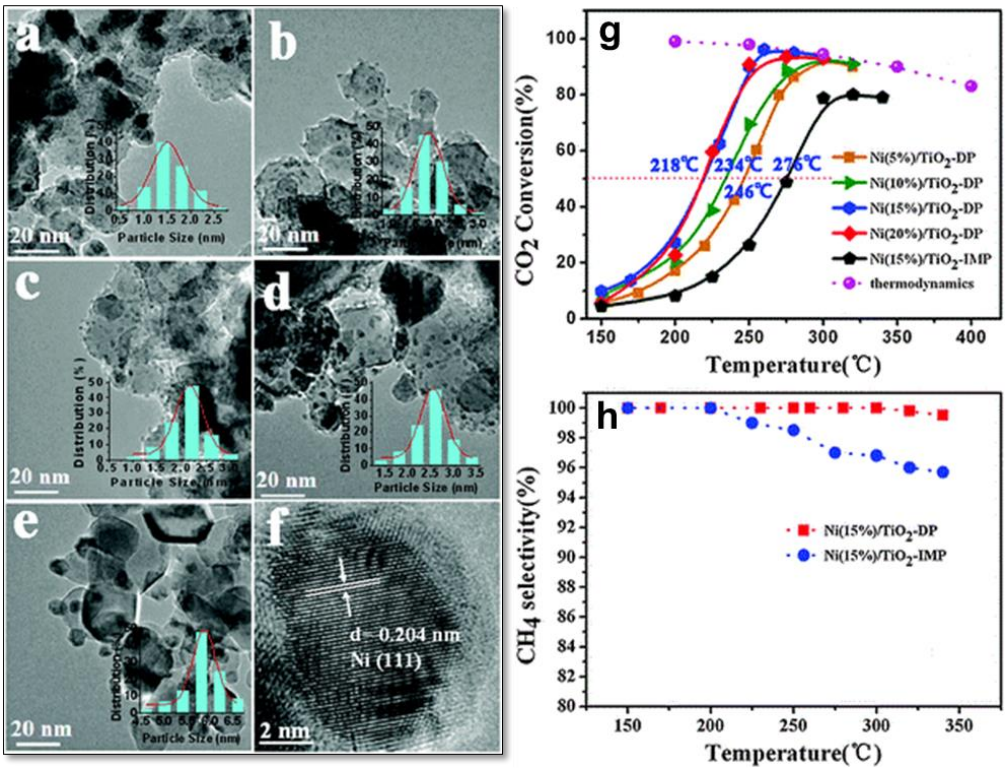

Fig. 1-14. TEM images of Ni/TiO_2 with particle size distribution of Ni after reduction at 450 °C for 4 h: (a) $Ni(5\%)/TiO_2$-DP, (b) $Ni(10\%)/TiO_2$-DP, (c) $Ni(15\%)/TiO_2$-DP, (d) $Ni(20\%)/TiO_2$-DP, (e) $Ni(15\%)/TiO_2$-IMP, (f) HRTEM for $Ni(15\%)/TiO_2$-IMP, and their catalytic performance: (g) CO_2 conversion, (h) CH_4 selectivity [154].

Noble metal-based catalysts

Supported Rh catalysts generally possess excellent catalytic activity for CO_2 methanation at relatively low temperature. Rh/TiO_2 has been reported as one of the most active catalyst for CO_2 methanation, being up to (approximately) one order of magnitude more active than Rh/SiO_2 and Rh/Al_2O_3 [156]. The enhanced activity of

Rh/TiO_2 catalyst has been contributed to the electronic interaction between the metal and the support [157, 158]. The possible strong metal-support interaction (SMSI) caused by the reduction process together with the interaction of Ti^{3+} ions at the edge of TiO_2 with the CO adsorbed on Rh should also be taken into account [156, 159]. These interactions have been considered to be beneficial for the breaking of C=O bond, thus resulting in an increase of the overall activity [160, 161]. The effect of Rh particle size on CO_2 methanation performance has been studied by Karelovic et al. using $Rh/\gamma\text{-}Al_2O_3$ catalysts with different Rh particle size prepared by varying the Rh loading [159, 162]. The authors found that the methane production rate, the apparent activation energy and reaction orders with respect to H_2 and CO_2 were highly sensitive to Rh particle size in the temperature range from 85 to 165 °C [159]. Since small Rh particles have less active sites and bind $CO_{(adsorbed)}$ intermediate more strongly than large metal clusters, the methane formation rate (per surface Rh atoms) increased as Rh particle size increased up to ca. 7 nm. Accordingly, the activation energies for the catalysts with small cluster size (2 nm) could up to 28.7 $kJ \cdot mol^{-1}$, which was much higher than that of the catalysts with larger particles (> 7nm, 17 $kJ \cdot mol^{-1}$). Beyond this size, these changes were not appreciable. In addition, the metal particle size displays almost no noticeable influence on the hydrogenation to methane at temperatures between 185 and 200 °C [162]. The reaction order with respect to CO_2 is near zero for large clusters, whereas it decreased to -0.36 for small size clusters. On the basis of kinetic analysis, it was concluded that the dissociation of $CO_{(adsorption)}$ was assisted by the presence of H species and that a likely surface intermediate is Rh carbonyl hydrides. Activation energy for CO dissociation was found to be similar to that of the overall reaction which suggested the importance of CO bond dissociation in the reaction path [159, 162]. Jacquemin et al. fully investigated the reaction mechanism for CO_2 methanation at low temperature on $Rh/\gamma\text{-}Al_2O_3$ catalyst [163]. They pointed out that the dissociation of $CO_{2(g)}$ to $CO_{(adsorbed)}$ and $O_{(adsorbed)}$ on the catalyst surface seems to be responsible for the oxidation of the Rh catalysts, while the oxidation state of the Rh played a critical role in the distribution of the adsorbed species. By further study the reaction mechanism and comparison of CO_2 and CO methanation process in the presence/absence of O_2, Beuls et al. found that the presence of O_2, in low proportion, had a positive effect on the catalytic performance for CO_2 methanation. However, if the amount of O_2 was too high, a negative effect was observed. The positive effect could be due to the fact that oxygen favored the oxidation of Rh and consequently the formation of more reactive species (gem-dicarbonyl), while

the negative effect was explained by a deep oxidation of Rh [164]. It is interesting to mention that Swalus et al. adopted a well-known catalyst (Ni/AC) in H_2 activation as H_2 storage source to enhance the H_2 supply at the surface of Rh/γ-Al_2O_3 (an active catalyst recognized in CO_2 adsorption and dissociation for CO_2 methanation). A significant synergistic effect was observed in the activity of the mechanical mixing catalyst due to the increase of H_2 adsorption and promotion of carbon hydride formation [165]. The production of methane over the mixed catalyst was higher compared to that observed with the two catalysts taken separately. The migration of activated hydrogen species from 1 wt.% Ni/AC catalysts toward 1 wt.% Rh/γ-Al_2O_3 was thought to be responsible for the augmentation of the catalytic performance. This hydrogen could then react with CO_2 species to form methane but also to preserve Rh particles in an adequate reduced state which is essential for carrying out the CO_2 hydrogenation [165].

Hydrogenation of CO_2 toward methane has also been extensively studied using supported Ru catalysts [166-168]. TiO_2 supported Ru catalyst with uniform Ru particle size has been prepared by the barrel-sputtering method and employed for such reaction by Abe et al. [169]. It was found that the onset temperature decreased linearly with the particle diameter in the range of 2.5 - 6 nm, while the turnover number (TON_{CH4}) demonstrated a mirror trend. An onset temperature of 60 ºC for CH_4 generation was observed with Ru/TiO_2(B) catalyst, which produced 100% yield of CH_4 at 160 ºC as well as a methanation reaction rate of 0.04 $\mu mol \cdot min^{-1} \cdot g^{-1}$ at room temperature. Xu et al. investigated the structure-activity relationship in CO_2 methanation by synthesizing Ru/rutile TiO_2 catalysts with almost similar particle size. They reported that the extent of encapsulation of Ru particles by TiO_x layers and the amount of hydroxyl groups on the TiO_2 surface were the two factors could be responsible for the enhanced activity of Ru/rutile TiO_2 catalyst in CO_2 hydrogenation [170]. Recently, Wang et al. highlighted the promotion effect of oxygen vacancies on CO_2 methanation [171] by comparing the catalytic processes of Ru/CeO_2 (with oxygen vacancy) and Ru/α-Al_2O_3 (without oxygen vacancy) catalysts. The authors revealed that CO_2 methanation underwent formate route at the Ru/CeO_2 catalyst surface with the jointly participation of Ce^{3+}, surface hydroxyl, and oxygen vacancy, whilst the CO_2 methanation on Ru/α-Al_2O_3 underwent CO route over Ru surface with the absence of oxygen vacancy, hence demonstrating active site dependent catalytic mechanism toward CO_2 methanation. Catalytic evaluation and oscillating reaction test further proved that the oxygen vacancy catalyzed the rate-determining step with a much lower activation temperature, namely

125 °C over Ru/CeO_2 versus 250 °C on $Ru/\alpha\text{-}Al_2O_3$. Tada et al. evidenced that the moderate addition of CeO_2 in Ru/Al_2O_3 could enlarge the specific surface area of the catalyst as well as the reaction rate between the formats intermediates with H_2 [172].

Other noble metal-based catalysts have also been investigated for such reaction [173-175]. The results reported indicated that noble metals could be used as efficient catalyst for CO_2 methanation. However, due to the high price, the noble-metal based catalysts are generally favored for mechanistic and kinetic investigations, which have been widely debated in the literature without reaching a clear consensus form the scientific community yet [126, 132, 176].

Structured catalyst and reactor design

Since methanation reaction is a highly exothermic process, the effective heat removal from the catalyst bed is an essential issue for the large-scale production of SNG. It has been widely reported that heat released by the reaction easily accumulated inside the catalyst bed, forming hot spots and thus causing serious temperature runaway, which will consequently lead to the formation of by-products as well as the catalyst deactivation by either sintering or formation of carbon deposits [151, 177, 178]. It has been reported that for a GHSV of 5000 h^{-1} and a complete CO_2 conversion, approximately 2 MW heat per m^3 of catalyst bed are required to be removed from the reactor [114]. Therefore, it is necessary to propose new reactor technologies suitable for coping with an efficient reactor heat removal and design catalysts that are active and stable for operating within a large temperature range. The heat removal is also necessary to prevent undesired temperature runaway within the catalyst bed which could pose problems for the thermodynamic limitation of the process and for the security of the plant. Great efforts have been taken to prevent sudden and serious temperature runaway, including diluted the reactants with excess of inert gas or by mixing the catalyst with other inactive substrates which could enhance the heat transfer from the catalyst bed to the reactor wall and the reactant gas phase.

Recently, different configurations of structured catalysts have been developed to enhance the heat transfer whilst keeping excellent catalytic performance [178-180]. Macro-porous metal structure (stainless steel, 316L) coated with Ni/Al_2O_3 powder have been fabricated by Danaci et al. through innovative and highly reproducible robocasting technique-three dimensional fibre deposition (3DFD) and applied for the CO_2 methanation [180]. Enhanced catalytic activity and stability have been observed

compared with that of a powder Ni/Al_2O_3 catalyst. The author attributed this to the improved heat transfer properties of the 3DFD structured catalyst, which could avoid formation of local hot spots and prevent temperature increase inside the catalyst bed. However, they did not provide sufficient evidence, such as temperature changes in the catalyst bed, etc. Meanwhile, Vita et al. reported the effective synthesis of structured catalyst by solution combustion synthesis (SCS) method through two processes [178]. Powder Ni/GDC (gadolinium-doped ceria) catalyst was first synthesized by SCS, followed by in situ deposition of the Ni/GDC coating layer on the cordierite monolith (500 cpsi) with the same approach. Very uniform, thin (10 - 40 μm) and high thermal and mechanical resistance catalytic layers could be in situ deposited on the macroscopic substance. The structured catalyst possessed high surface-to-volume ratio, good interface mass transfer and low pressure drops, therefore, it exhibited high CH_4 productivity (10.7 $L_{CH4}\cdot g^{-1}\cdot h^{-1}$ at 400 ºC with a high GHSV) and promising long-term stability (over 200 h of time-on-stream). Honeycomb-type structured Ni/CeO_2 catalyst have been reported by Fukuhara et al. by wash-coating powder Ni/CeO_2 catalyst on aluminum substrate [181]. The optimized catalyst maintained high activity and stability under high feeding flow rate, which was attributed to the enhanced heat and mass transfer ability of the metallic structured catalyst. In the following work [182], the effect of different configurations on the catalytic performance of a structured catalyst and the temperature runaway have been studied by Ratchahat et al. (as shown in **Fig. 1-15**). High CO_2 conversion (> 90%) and CH_4 selectivity (> 99.5%) as well as superior stability (no obvious conversion drop over 76 h time-on-stream test) were obtained at a setting temperature of 300 ºC under a flow rate of 3,000 $mL\cdot min^{-1}$ and a feed ratio of P_{CO2}/P_{H2} of 0.12/0.88. It is interesting to note that under high feed rate conditions, a moderate hot spot over the multi-stacked catalyst was observed which was advantageous for re-boosting CO_2 conversion to high level during the test by virtue of high heat transfer on the structured catalyst. As far as we know, such catalyst is at the frontier of state-of-the-art. However, the overall temperature increase was still high as the observed maximum temperature inside the catalyst was 540 ºC, which was much higher than the set temperature, *i.e.* 300 ºC, and thus, still posing a challenge for its exploitation in industrial plants, especially under dynamic operation situations where reagent loads are discontinuously supplied. Other structured supports, such as metallic plates [183], foils [184] and foams [185] have also been employed for the fabrication of structured catalysts.

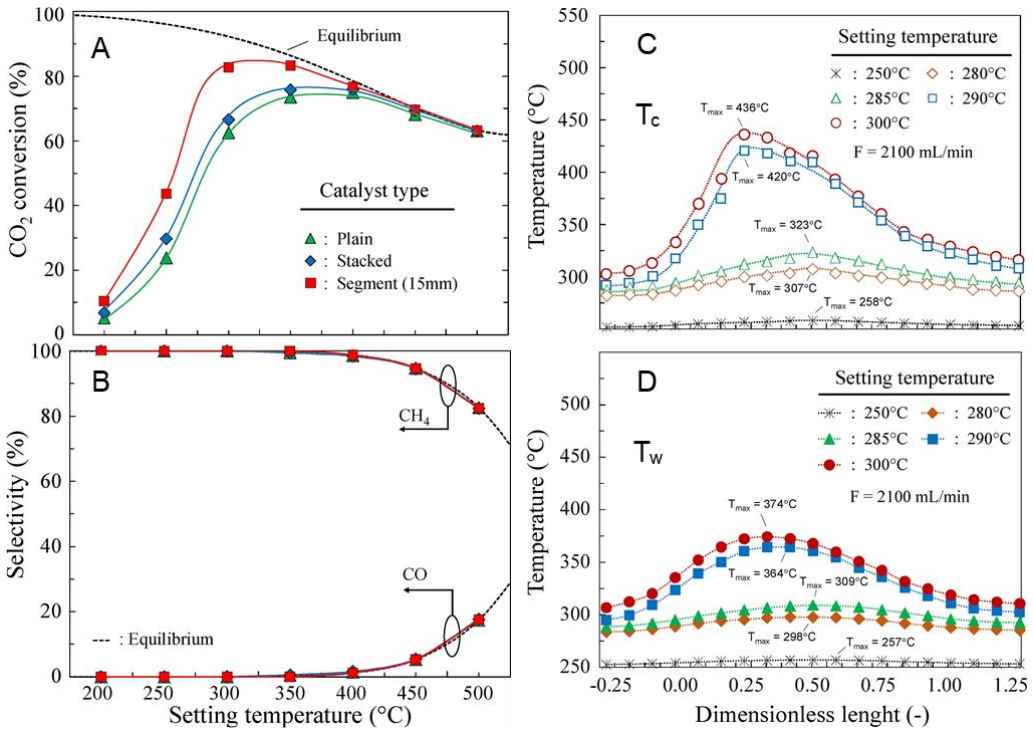

Fig. 1-15. Methanation performance of various structured catalysts (A, B) and the temperature profiles of the multi-stacked catalyst at (C) the center (Tc) and (D) the wall (Tw) [182].

On the other side, microchannel reactors with excellent thermal control have also been developed for this reaction [186, 187]. However, they suffer the limited low capacity for large scale treatment of the reactants. Other different types of reactors have also been designed, including adiabatic fixed-bed reactors, fluidized-bed reactors and three-phase reactors, and investigated under both steady-state and dynamic conditions to achieve effective heat management. Their advantages and disadvantages have been fully reviewed in the literature [114, 188]. Although the temperature can be controlled in part, the overall CO_2 methanation activity is generally low with limited mass processing ability. In addition, most of these reactor designs are relatively complex, and expensive, and some of them are still under development stage. So far, the methanation usually performed in packed-bed reactors due to its economic efficiency [131].

Based on the above discussion, an innovative reaction system for CO_2 methanation should be the combination of a suitable designed reactor and constructed catalyst system with a superior and effective heat management capacity as well as a suitable mass processing ability of the raw material. Structured catalyst systems can provide superior heat transfer capacity. Moreover, their generally macroscopic structure greatly

decreases the pressure drop in the reaction zone, which makes it available for treating a large amount of raw materials. These facts indicate that structured catalyst systems are suitable candidates for industry in the near future. However, the main problem which needs to be tackled remains the problem linked with heat management inside the catalyst bed in order to operate the catalyst as close as possible to the kinetic regime. In addition, PtG operation also depends on the supply of the reactants, *i.e.* CO_2 and H_2. If the renewable H_2 production is not sufficient, the methanation reactor will be switched to a shutdown mode. Under these conditions, the catalyst will undergo successive start-up and shut-down steps which require highly stable materials to face with sudden and intermittent reaction temperature changes. In such dynamic operation process the rapid temperature change, increase and decrease, of the reactor also play an important role to reduce the delay and to prevent damage on the catalyst by sudden temperature runaway. It is also worthy to note that the problems linked with the reactor heat management could become worse if the process is operated at total pressure higher than atmospheric one. Indeed, under high pressure the apparent density of reagents increases and therefore also causes a large increase in the heat released by the reaction which needs to be removal from the catalyst bed to avoid temperature runaway. Such problems are frequently encountered with exothermic processes operated at medium to high pressure, *i.e.* Fischer-Tropsch synthesis.

1.3 Induction heating for heat management in catalytic processes

Heterogeneous catalytic process involves systems in which catalysts and reactants are from different physical phases (mostly consists of reactions between gaseous or liquid reactants and a solid catalyst) to generate desired products [189, 190]. As an important industrial process, heterogeneous catalysis is involved in about 80% of the different catalytic chemical procedures to produce compounds and commodities [191]. The catalytic process normally needs an external energy input to spur the reaction start with desired catalyst as to decrease the overall reaction activation energy and speed up the reaction rate [189, 192]. Advances in catalysis, process design, and reactor engineering hold the task of demonstrating how energy losses, scale-up issues, by-product formation, and costly equipment can be minimized while saving the process intensification principles [193]. Making innovations in catalysis does not mean squeezing a few percent units from a consolidated protocol but rather guarantee a

quantum leap in the process efficiency in terms of time, energy costs, employment of raw materials, easy process scale-up and environmental impact.

The electromagnetic induction heating (IH) or radiofrequency (rf) heating of magnetic nanoparticles (NPs) or electrically conductive susceptors has been exploited for a wide range of applications [194-197]. IH can provide unique features compared with classical heating systems based on heat convection, conduction and/or radiation (*i.e.* flame and resistance heating). Thus, IH is a powerful tool that can be exploited to achieve specific and highly challenging tasks not easily addressed otherwise. IH takes advantage of the electromagnetic properties of a magnetically susceptible medium (susceptor) exposed to a varying magnetic field (H) produced by an alternating current (ac) generator. The capacity of IH to target heat directly where it is needed through the electromagnetic energy adsorption/conversion on dedicated materials (noncontact heating technology) is not just an alternative heating approach but rather a powerful tool that allows overcoming the heat transfer limits encountered in classical "contact" heating reactors. With IH, high temperatures can be reached more quickly on the target sample (catalyst) without the need of heating the catalyst support (if any), liquid/gaseous carriers and reagents, or even the entire reactor. The heat originated by induction is generated directly in the catalyst and it is not required to cross the whole reactor, from its outer walls up to the catalyst core. Accordingly, IH occurs almost instantaneously on the target sample without appreciable thermal inertia and heating efficiency considerably higher than those provided by conduction/convection/radiation schemes. Furthermore, heat loss (dissipation phenomena) and "heat waste" mainly due to the prolonged exposure of reagents and products to large temperature gradients into the reactor can be deeply mitigated [198, 199]. As a matter of fact, catalyst fouling problems for a wide variety of inductively heated processes are significantly reduced compared to protocols using conventional heating systems and catalysts show markedly increased lifetimes [200, 201]. Such a contactless heating technology makes any transformation safer, cleaner and more reproducible. Overall, a careful reactor design (coil) and an appropriate susceptor choice optimize the inductor power required for running a catalytic process up to the bounds of its inherent kinetics while ensuring an optimal energy balance [197, 202-204].

Indeed, many of these key features have been summarized in the "cold catalysis" concept that illustrates how challenging catalytic transformations can be conveniently accomplished using IH-based energy-saving protocols [205]. This concept looks even

beyond the high benefits coming from the implementation of IH in catalysis and it aims at the development of protocols where the energy required for a given process to occur (heat) can be provided directly where it is needed and where the target susceptor simultaneously holds the role of catalyzing the process. In this part, a brief description of induction heating theory will be presented along with the application of IH in some gaseous and liquid-phase catalytic processes.

1.3.1 Brief description of induction heating theory

When a work piece (electrically conductive) is immersed in an alternating magnetic field, RF energy is directly targeted to the material and locally transformed into heat with only minor energy losses due to convection, conduction or thermal radiation. There are three electromagnetic dissipation phenomena responsible for RF energy conversion into heat, whose occurrence depends on the susceptor nature: 1) the *hysteresis heating* in the case of ferromagnetic (FM) materials, cycling through their magnetic hysteresis loops [206, 207]; 2) the magnetic field heating mechanism by relaxation losses (*Néel relaxation mechanism*) taking place in superparamagnetic (SPM) nanoparticles [208, 209], and 3) the *Joule heating* due to eddy currents (or Foucault currents) occurring on electrically conductive samples [210, 211].

FM particles possesses distinctive magnetization (M/H) profiles that allow the conversion of RF magnetic field into heat by means of hysteresis losses. These samples are characterized by (1) the remnant magnetization (M_r, **Fig. 1-16a**), namely the magnetization retained by the material in its magnetically saturated state (M_s) after removal of the external magnetic field (H = 0) and (2) the coercive field (H_c, Fig. 1-16a), which is the magnetic field required to demagnetize the sample. M_r and H_c define the area subtended by the FM material hysteresis (Fig. 1-16a) that is proportional to the amount of heat dissipated during the sample magnetization reversal. The greater the hysteresis area, the higher the energy absorbed per mass unit and subsequently the heat produced. For superparamagnetic (SPM) particles, they lack the hysteresis contribution to the heat production (**Fig. 1-16b**) and dissipate the electromagnetic energy through the Néel relaxation mechanism [208]. The latter describes the rotation of the individual magnetic moments in single-domain NPs (single giant magnetic moment) toward an applied external magnetic field. Such a rotation moves away the magnetic moment from the crystal "easy axis" with subsequent heat release into the system [212].

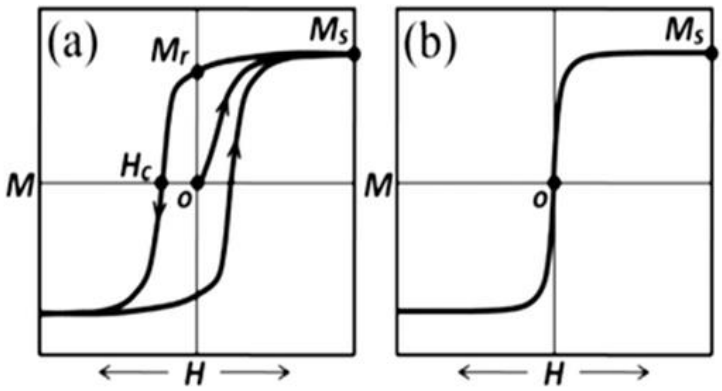

Fig. 1-16. Schematic illustration of (a) a typical hysteresis loop of an array of FM NPs and (b) a typical curve for a SPM sample. Reproduced from Ref. [213] with permission from The Royal Society of Chemistry.

In addition to hysteresis loss and Néel relaxation phenomena, eddy currents induced by an AC magnetic field, that flow through the resistance of an electrically conductive susceptor, dissipate energy by Joule effect [214]. At odds with the other heat contributions, eddy currents generated by an AC magnetic field do not contribute to the homogeneous warm-up of the conductor but they concentrate heat to the surface of the susceptor mainly [215, 216].

All of these heat contributions outline the hyperthermal efficiency or specific absorption rate (SAR) of a given sample, *i.e.* its own capacity to act as heat mediator once immerged in an ac magnetic field [217]. As mentioned above, the preparation of nanostructures joining high magnetic heating efficiency (SAR) with excellent catalytic performance for a given process represents nowadays the most challenging task in the field of inductively-heated catalytic processes.

Two further distinctive features of magnetic susceptor/catalysts applied to inductively heated catalytic processes are: The Curie Temperature (T_C) and the blocking temperature (T_B). These T values mark the material phase transition from FM to paramagnetic (PM) and from FM to SPM, respectively. Overall, they indicate the temperature limits beyond which a given FM sample loses its permanent magnetism and related hysteresis loss contribution to its heating.

1.3.2 Inductive Heating for gas-phase catalytic synthesis processes

Magnetic IH can beneficially be combined with the portfolio of classical heating devices due to the above-mentioned advantages. The IH technical setup has been widely

employed for the controllable synthesis of various materials, *i.e.* lager scale produce of SiC nanowires [218], catalyst-free synthesis of SiC/SiO_2 nanocables and nanosprings [219], nanostructured Mo_2C thin films [220], and catalytic chemical vapor deposition (CVD) of nanocarbon materials, *i.e.* rapid growth of carbon nanotubes [221-223] and high quality graphene [224]. The utilization of such a technology in the CVD process is much cost-effective since the heat is generated inside the substrate or the catalyst directly, which can greatly reduce the heat transfer intermediary steps, then leading to the decrease of energy consumption and the overall reaction time [221, 222, 224, 225]. Moreover, such kind of heating process has consequences on the growth mechanism and morphology of the carbon nanostructures, its fast start up/shut down capability provide a good possibility for the growth mechanism investigation [222, 225, 226].

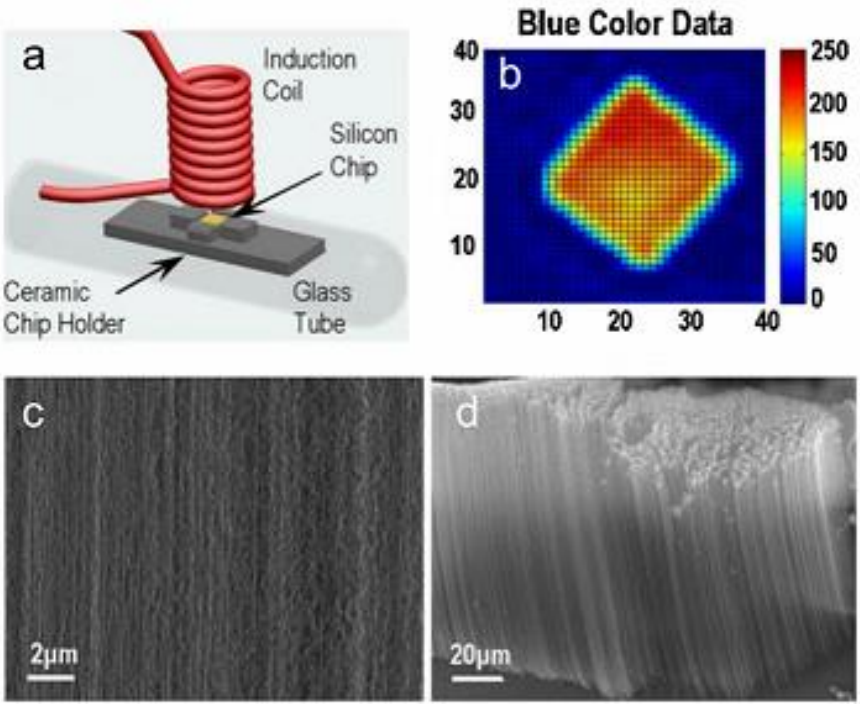

Fig. 1-17. (a) Schematic representation of the CNTs synthesis and the IH configuration. (b) Temperature estimation during heating process. (c, d) SEM micrographs of the vertically-aligned CNTs synthesized through IH [221].

Aligned carbon nanotubes with growth rates as high as 200 $\mu m \cdot min^{-1}$ in less than 1 min have been achieved by Sosnowchik using an IH system (**Fig. 1-17**). The rapid heating up and cooling down ability of the system allowed the obtained product with high purity which benefited the growth rate and mechanism analysis. Comparative analysis of the synthesized multiwalled carbon nanotubes (CNTs) by external electrical

furnace and RF inductive heating assistant CVD method on Fe:Co:$CaCO_3$ catalyst has been investigated by Biris et al. [225]. Results strongly proved that IH generated qualitatively superior CNTs with smaller external diameter and more homogeneous diameter distribution as well as wide aspect ratio range and high graphitization degree compared with those synthesized by an external heating device (oven). Such superiority was attributed to the advantage of the inductive heating: the fast heating rate effectively eliminates the dimensional growth of the active phase which usually caused by the surface diffusion on the support at high temperature. The resulting smaller catalyst nanoparticles contribute to the smaller CNTs diameter [227, 228]. Meanwhile, the high frequency current resulted in localized temperature spikes in metallic species together with the adsorption of the heat released by the exothermic reaction of carbon graphitization process leading to higher local temperature of the metallic catalyst which can be responsible for the higher growth rate of smaller diameter CNTs [229, 230]. At the same time, Li et al. [231] reported the synthesis of high purity (around 95%), smaller diameter (from 0.8 to 1 nm) and hundreds range of aspect ratio single-walled carbon nanotubes (SWCNTs) using a simple self-designed IH instrument at lower temperature compared with what have been reported before [232-234]. They revealed that the etching effect of weakly bonded carbon atoms and amorphous carbon by atomic hydrogen and OH radical were responsible for small diameter and high purity of the final product. Furthermore, they pointed out that such a low temperature synthesis provided applicable strategy for the direct growth of SWCNTs on semiconductor devices. Similar results have also been obtained by Okamoto [223].

IH has also been employed for controllable catalytic synthesis of high-quality graphene on copper substrate, where in general high synthesis temperature and short growth time as well as fast growth termination are required to obtained high-quality monolayer graphene. However, the thermal inertia of conventional CVD setup greatly prolongs the overall processing time, resulting in the decrease of the whole productivity and energy efficiency [235, 236]. Meanwhile, the breakdown of the remained carbon source during the cooling process could lead to the further growth of the graphene layers on the substrate and even the formation of impurities, which can greatly influence the following investigation and application [226, 237]. In this situation, IH can achieve quite high temperature values upon suitable design of the reaction system, and most importantly it can start/stop the growth process almost immediately throughout the reaction. In order to provide uniform perpendicular magnetic field to the surface of the

two-dimensional Cu conductor for good heating uniformity, Helmholtz-like geometry configuration IH setup has been constructed by Tao et al. [224] and Piner et. al [238] (as demonstrated in **Fig. 1-18a**). This configuration can deliver as much as possible of the induced magnetic field lines pass through the obversed side of Cu substrate, which greatly improve the electrical efficiency with much lower frequency as well as the potential to control temperature profile over the surface of the foils. Such transverse flux concept has also been investigated and discussed by Blinov et al. for rolling mills [239]. Large-area high quality monolayer graphene film with remarkable field effect mobility (FETs) (~ 14 000 $cm^2 \cdot V^{-1} \cdot s^{-1}$ under ambient conditions on conventional SiO_2/Si substrate) have been rapidly synthesized on magnetic fields inductively heated 125 μm Cu foils with a frequency of 240 kHz (**Fig. 1-18b-f**). The achieved outstanding graphene field-effect transistor (GFETs) properties were partly attributed to the improved inductively heated CVD synthetic approach in both the RF coupling efficiency and the thermal stability and uniformity. Several other considerations about the design of the RF induction heating, *i.e.* gas pressure and the thickness of the substrate, for uniform and high-quality graphene synthesis have also been discussed.

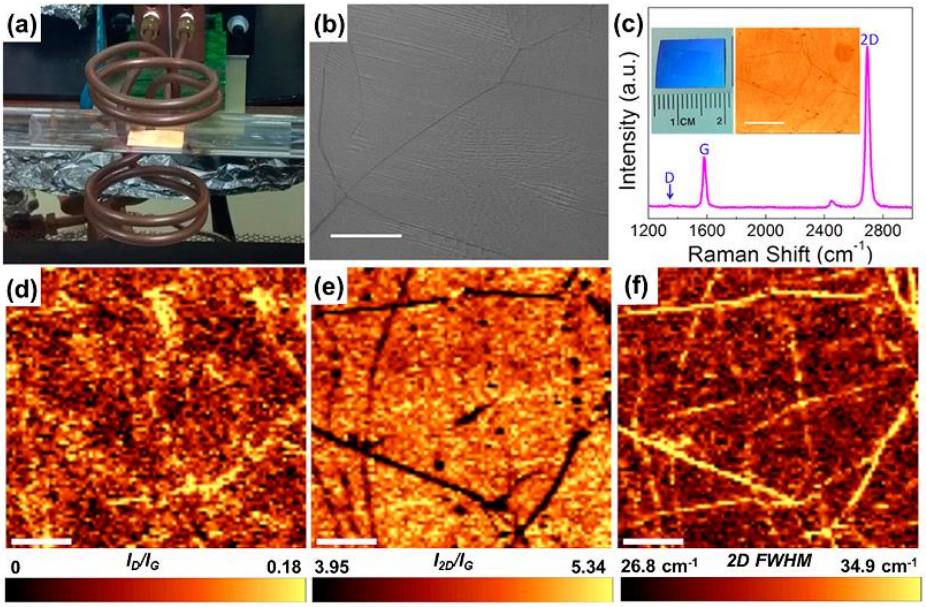

Fig. 1-18. (a) Photograph of the copper and rf coil. (b) SEM image (scale bar is 3 μm) of as-grown monolayer graphene. (c) Raman spectrum of obtained graphene. Insets are photograph and optical microscopic image (scale bar is 20 μm) of transferred graphene on SiO_2/Si substrate. (d-f) Raman mapping of transferred graphene film. Scale bars are 6 μm [238].

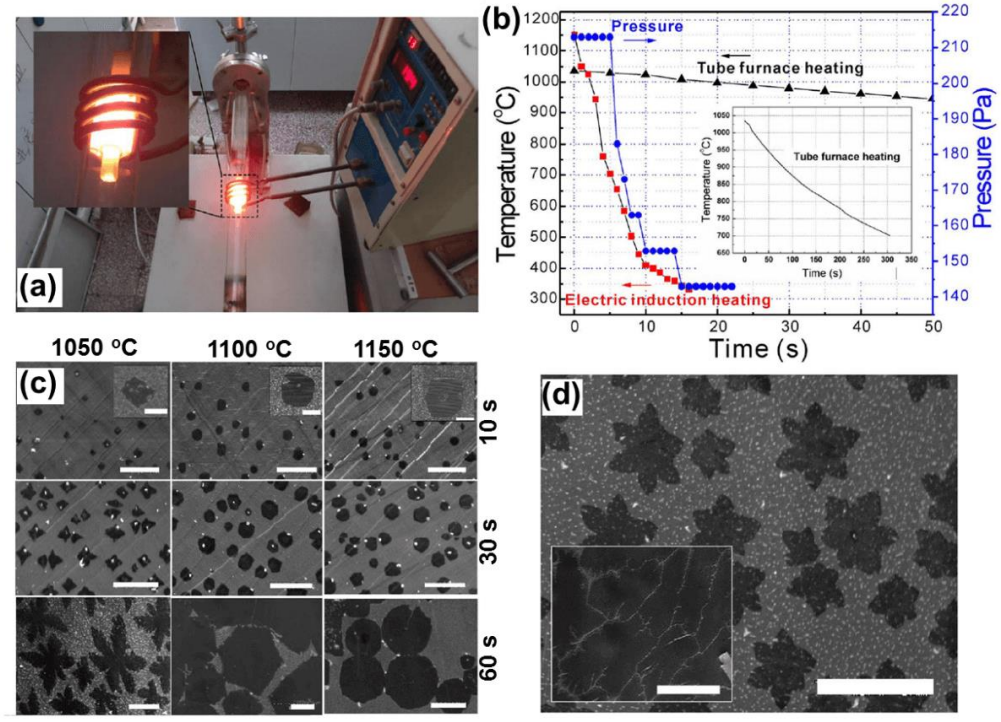

Fig. 1-19. (a) photo image of the electromagnetic induction CVD system, in which the selected tungsten (W) coil/W plate/Cu foils are heated. (b) Rapid-cooling performance of the inductive heated CVD system and its comparison with tube furnace-based system cooled by exposing to ambient environment (inset). (c) SEM images of graphene domains grown on Cu at different growth temperature and times. (d) SEM image of graphene grown at 1035 °C for 1 min by using IH and tube furnace heating (inset). Scale bar: 10 μm [226].

It is worthy to note that rapid heating/quenching CVD system has been developed by Wu et al. [226] based on the accurate selective heating and fast heating/cooling capacities of electromagnetic IH technique (as displayed in **Fig. 1-19a** and **b**). The localized heating and rapid quenching abilities of the induction CVD system allows the initiation and termination of graphene growth rapidly, making it possible for the authors to controllably synthesize single crystalline graphene domains with varying shapes (circular, hexagonal, and dendritic, **Fig. 1-19c**) for the first time and to directly observe their shape evolution with growth time. Formation of different shapes of graphene domains have been fully investigated and explained form the perspective of both growth mechanisms and thermodynamics. The authors have disclosed that the graphene nucleation only occurs during the initial stage depending mostly on the surface state of

Cu catalyst, and the domain density and lateral size are independent of the growth temperatures because of the surface-limiting effect in contrast to what have been reported by Kim et al. [240]. The obtained CVD graphene layer with similar or even higher quality (thickness less than 1 nm evidenced by atomic force microscope (AFM) with high crystallinity confirmed by selective area electron diffraction (SAED)) than that produced with classical thermal heating in rather short time (as demonstrated in **Fig. 1-19c** and **d**), this was attributed to the advantages of the induction CVD system [226, 238]. Such research provides feasible and essential insights into the growth kinetics and mechanisms of single crystal graphene by using IH technical setup.

Such an advanced technology has recently been used in other gas-phase chemical processes to eliminate the thermal inertia phenomena typically encountered with more conventional thermal heating systems. Among the studied transformations, IH has been successfully used for the catalytic combustion of volatile organic compounds (VOCs) [241], CO_2 methanation [242] and steam methane reforming (SMR) [204], where strong exothermic or endothermic processes are involved. In these situations, temperature gradient can be easily formed inside the catalyst bed. Temperature runaway caused by heat acceleration together with temperature compensation required for insufficient temperature supply are the issues that need to be solved urgently.

Generally, VOCs reaction is kinetically controlled and the reaction rate increases exponentially with temperature at low region due to the exothermic property of the reaction. Therefore, the effective control of the reaction temperature is essential for better understanding of such reaction [243]. Recently, Leclercq et al. [241] have reported for the first time the potentialities of the inductively heated fast-response catalytic systems for the rapid abatement of isopropyl alcohol (IPA) in air with accurately regulation of the catalytic temperature. Catalyst (SnO_2) were deposited as thin films on a stainless-steel support selected as susceptor which could be fast and homogenously heated, up to several hundred degrees per minute with IH. The fast on/off heat switching at the catalytic bed along with the ability of IH to ensure very rapid heating/cooling rates of the catalyst/susceptor, turned out to be a fundamental tool for an efficient and fast VOCs oxidation treatment on-demand, as shown in **Fig. 1-20**. Results indicated that 50% IPA conversion could be achieved at about 80 ^{o}C on 1 wt.% Pt/Al_2O_3 catalyst and a total diminution of high amounts of IPA around 1 vol.% in air to CO_2 and H_2O was accomplished in less than 30 s on the SnO_2/SS catalyst. This result provides a clear-cut evidence of the great potentiality of inductively heated catalytic

systems for practical applications in the air treatment from organic volatile pollutants. Indeed, the released heat by the reaction can be effectively used as heating source by the thermal conductive stainless-steel since the concentration of contaminants is high. Heat loss in this process is particularly important when considering the energy efficiency since generally the contaminants in the VOCs combustion process only accounted for few hundred ppm (< 1000 ppm) of the total gas flow. Thus, the possibility to target the heat only to the catalyst by IH allows a significant reduction of heat dissipated in the flue gas. The same team has reported on the use of IH for the fast toluene vapors conversion into CO_2 and H_2O using a model reactor system joining in series a toluene adsorbent (e.g. Al_2O_3) and an efficient catalytic system for the complete low temperature VOC oxidation (1% Pt on ceramic Yttria-stabilized zirconia-Pt/YSZ) [244]. Catalyst and toluene adsorbent were finally arranged on a stainless-steel susceptor for the RF heating. IH was used to rapidly heat both the catalytic system and VOC adsorbent at the optimal working temperatures. Hence, catalyst was located within the IH coils while toluene adsorbent was intentionally housed outside the coils. Thus, two different temperatures were optimally and rapidly managed with a unique IH source: a lower temperature for the optimal toluene desorption from the Al_2O_3 adsorbent and a higher temperature for its complete oxidation. Such a scheme proposes a valuable example of continuum VOC adsorption/decomposition system where contaminants desorption rate and their fast catalytic oxidation is controlled by IH.

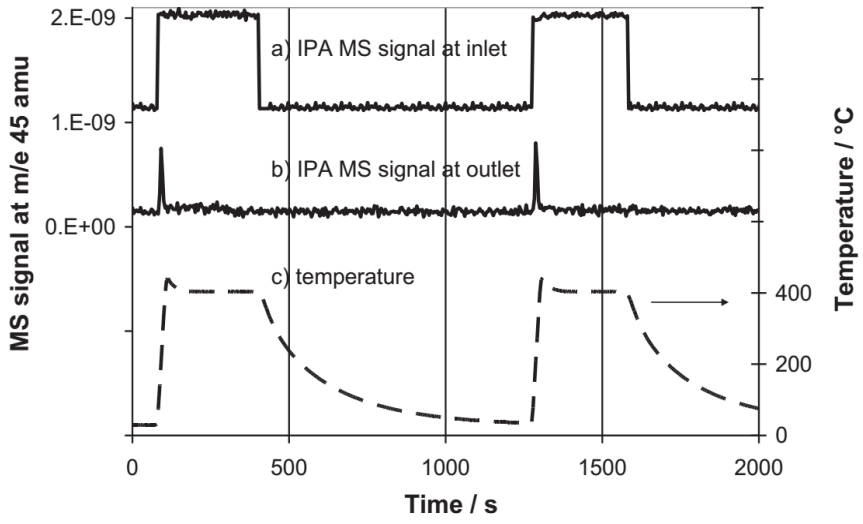

Fig. 1-20. IPA combustion monitored by mass spectrometry and the temperature response (heating rate of 800 $^{o}C \cdot min^{-1}$ and natural cooling rate) vs time [241].

Another area with potential application of IH technology is the Sabatier reaction. During this strong exothermic reaction, large temperature gradient and temperature runaway can be easily present inside the catalyst bed with conventional heating technology especially when pure reactants flows are used [182, 245]. The utilization of IH in such a field has already shown obvious advantages in the improvement of catalytic activity and energy efficiency [242]. Structure controllable iron carbide nanoparticles (ICNPs) with enhanced magnetic behavior and heating property have been fully developed by Bordet et al. (**Fig. 1-21a**) [242] and used as heating media of a composite catalyst for CO_2 methanation within induction heated continuous-flow reactor. The ICNPs could fast transform the electromagnetic energy into heat and the released heat was used to activate the Ru NPs (**Fig. 1-21b**). The ICNPs-RuSiRAlOx catalyst exhibited exceptional performance at relatively low amplitude (< 30 mT) (**Fig. 1-21c**). Such low amplitude operation condition should significantly benefit the remarkable stability of the catalyst as no deactivation was detected with 150 h time on stream test at 28 mT. However, according to the architecture of the catalyst (Fig. 6b), the thermal migration and sintering of the iron and ruthenium phases with time could represent a negative issue for the long-term catalyst stability even though the authors pointed out the slightly growth of Ru NPs led to gradually increase of CO_2 conversion. Despite outstanding catalytic outcomes, the methanation set-up described above foresees a "static" electromagnetic environment of the catalytic system (f = 300 MHz and fixed magnetic field strengths comprised between 20 and 64 mT) without any temperature control in "real-time" at the catalytic bed. This aspect is even more relevant in the case of highly exothermic processes where a discontinuous reagents supply can be responsible of sudden temperature deviations at the active sites with the occurrence of severe and potentially irreversible catalyst deactivation phenomena. Furthermore, the total catalytic activity and energy efficiency need to be further improved with optimized catalyst, reactor and IH device design.

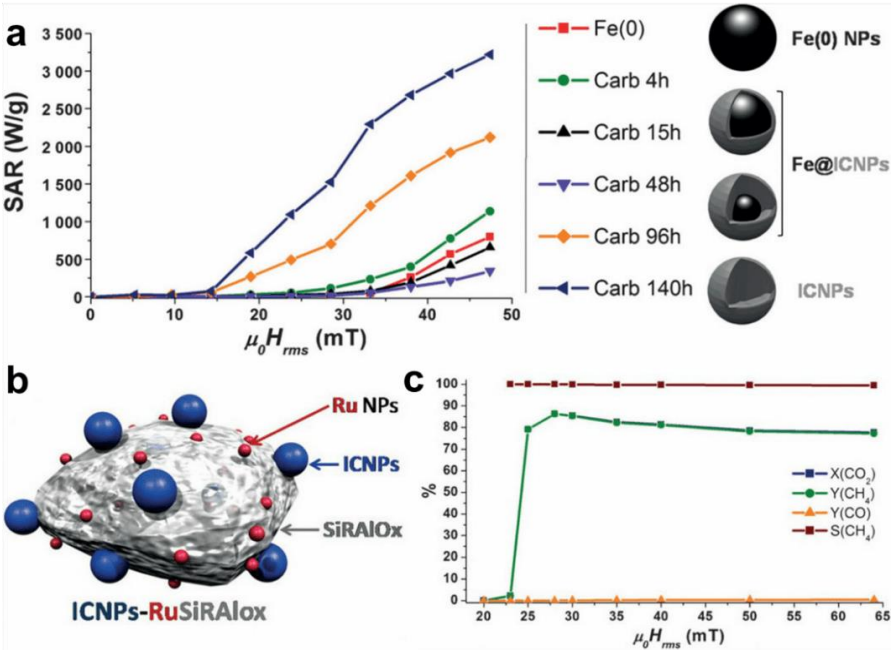

Fig. 1-21. (a) Heating power measurements at 100 kHz for ICNPs resulting from different carbonization times; (b) schematic representation of the catalytic system; (c) catalytic performance of the Ru-based catalyst [242].

On the other hand, for highly endothermic reactions, such as dry and steam methane reforming, which are thermodynamically favored at temperatures higher than 700 °C in industrial plants, unsatisfactory catalytic performance resulted from the insufficient heat supply due to the temperature gradient need to be enhanced by timely energy supplementation. Mortensen and co-workers [246] reported that Ni-Co alloy with high Tc are a suitable active catalyst for induction heated steam methane reforming (SMR). Co (with Tc = 1115 °C) rather than Ni (with Tc = 354 °C) could adjust the alloy catalyst to be heated up to the desired temperature range (~ 800 °C) and provide sufficient heat to enable such endothermic reaction. Hysteresis heating is directly evidenced as the primary heating mechanism in Ni-Co SMR catalyst and they revealed that the dual role of the Ni-Co NPs (both susceptor and catalytic phase) effectively facilitated the intimate contact between the catalytic active site and the heat source and consequently resulting in more than 90% of the methane conversion at the corresponding equilibrium temperature (700 - 800 °C) on the surface of $NiCo/MgAl_2O_4$ catalyst (**Fig. 1-22**). In the following optimized work, Vinum et al. [204] demonstrated the application of well-defined Co-Ni NPs with increased hysteresis opening directly for SMR process with IH. The tailored dual-function CoNi NPs displayed outstanding catalytic activity and stability with 90 - 95% conversion of methane at an equilibrium

temperature of 715 °C. More importantly, during more than 300 h stability test, there was no significant decrease of the activity with any structure change and carbon formation on the catalyst. The authors pointed that the conversion rate of the reactant is limited by the inherent chemical reactivity for induction heated reformers, while the heat transport limitation take responsibility for that in the traditional externally fired reformers. This highlighted the excellent heat transfer from the induction field to the magnetic susceptor and active catalyst. It happens that there is a similar case, Varsano et al. [247] took full use of the self-generated heat inside the $Ni_{60}Co_{40}$ alloy catalyst induced by external radiofrequency alternating magnetic field to maintain the endothermic dry reforming of methane (DRM), effectively avoiding heat dissipation and increasing the overall energy efficiency. The fast heating of the system to high temperature (200 °C·min^{-1}) in rather short time by IH could limit the formation of carbon that generally occurs at lower temperature. While the directly and homogeneously inside heating of the catalyst could efficiently avoid the temperature gradient formation in the reactor, and the optimized catalytic system demonstrated comparable catalytic performance. Similar research results have also been reported by Pérez-Camacho and co-workers [248] in their systemically investigation on biogas reforming with IH technology.

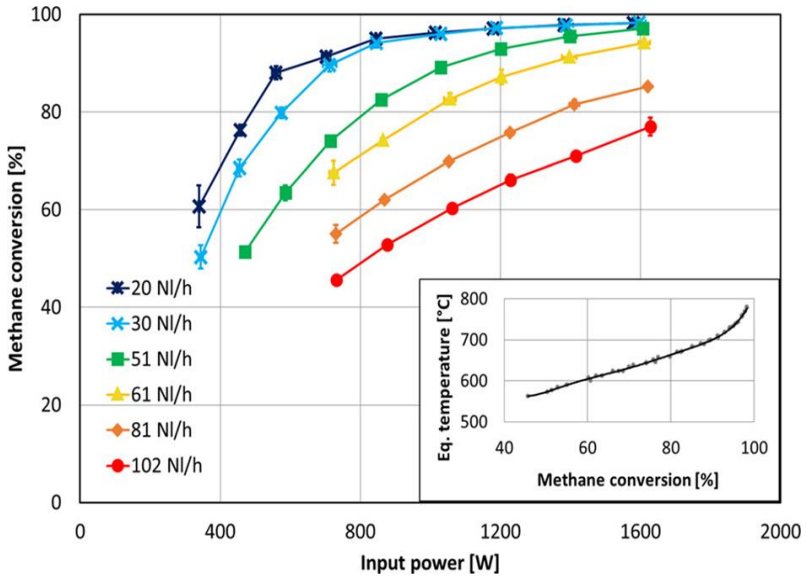

Fig. 1-22. CH_4 conversion and equilibrium temperature (insets) for steam reforming reaction over a 12.6 wt.%/9.0 wt.% NiCo/$MgAl_2O_4$ catalyst as a function of power input to the induction heater and at different total flow rates series [246].

1.3.3 Inductive heating for liquid-phase catalytic synthesis processes

Due to the contactless nature of IH and its fast and uniformity "self-heating" (direct heat generation inside the workpiece) capacity, IH technology has also been beneficially combined with the portfolio of heating devices for assisting catalytic organic synthesis reactions through the direct heating of magnetic nanoparticles (heating media) housed in liquid to enhanced the whole catalytic performance in recent years [249, 250]. Much attention has been paid to the design of structured magnetic NPs since the thermal energy input is based on its self-generation directly. In general, active phases can be doped or immobilized on magnetic nanoparticles or inertly coated magnetic nanoparticles to form core-shell structures. After reaction they can be easily removed through a magnet and regenerated immediately with simple washing, thus ensuring the high process efficiency and easy workup [250-252]. Researcher have shown that IH holds great potentialities in various synthesis processes [250, 253].

Kirschning et al. first exploited the application of magnetic material as heatable media combined with IH for various synthetic processes in flow chemistry [249, 254-256]. The SPM NPs have been synthesized through coating magnetic Fe_3O_4/Fe_2O_3 NPs with a silica shell followed by impregnation with Pd or Au as catalytic active sites (Fe_2O_3/Fe_3O_4@SiO_2-MagSilica®) for various heterogeneous reactions including catalytic transformations, transfer hydrogenations, heterocyclic condensations, and so on, in an inductively heated continuous microfluidic fixed-bed reactor operated at middle frequency field (25 kHz)(**Fig. 1-23**) [249, 257]. The silica shell could avoid the magnetic NPs from coupling, thereby effectively preserving their SPM properties. Besides, the silica-shell in MagSilica® increases the NPs surface area and creates a versatile platform to its surface engineering *via* exohedral chemical functionalization and/or metal NPs decoration. The MagSilica-Au(0) composite was successfully scrutinized for the catalytic O_2-promoted oxidation of allylic and benzylic alcohols, and the MagSilica-Pd(0) was tested in a fixed-bed reactor as catalyst for the Suzuki-Miyaura and Heck cross-coupling reactions. Both these engineered nanoarchitectures demonstrated to undergo rapid heating upon radiofrequency excitation, thus allowing heat to be directly transferred from the SPM iron-oxide core to the neighboring transition metal and catalytically active sites. When used in mesofluidic reactors, both catalyst composites gave from good to almost complete substrates conversion in a single pass as a function of the applied reactor temperature and flow-rate. Local higher

temperature of the SPM NPs than the measured bulk temperature should be formed under IH, and this was also responsible for their good performance. However, this has not been totally evidenced because so far, the determination of NPs' temperature is still a challenging task [255, 258]. The fast heating capability of IH allows the reactants be heated up directly and rapidly inside the continuous reactor compared with conventional conductive heating [254]. It has been concluded that the IH technical setup is consider to be more suitable (comparable rate acceleration, much simpler and less safety issues) for performing synthetic process with great future prospects under flow conditions compared with corresponding microwave devices [256].

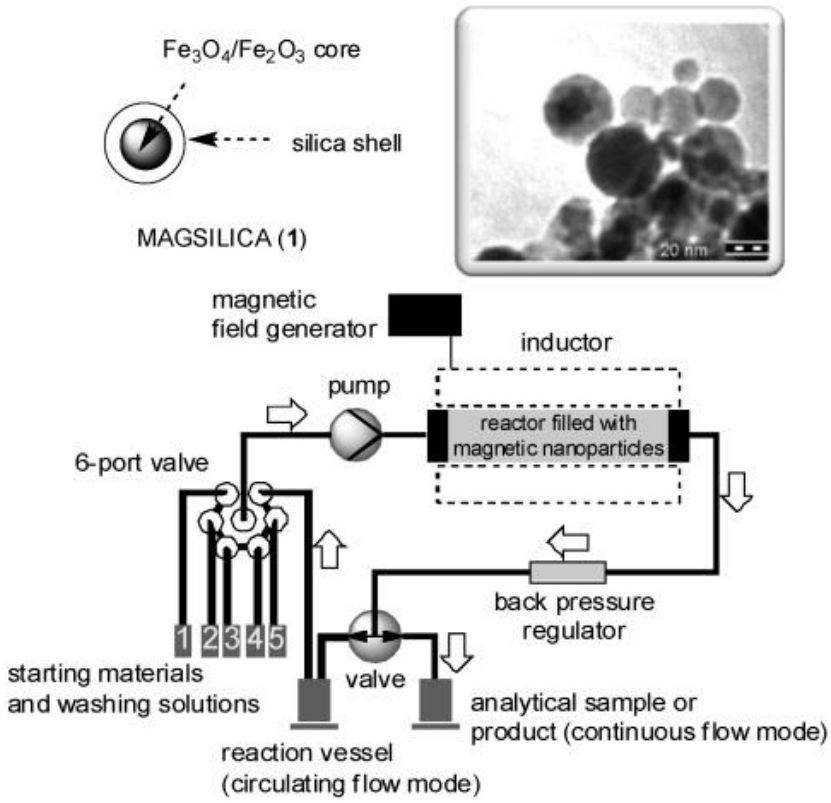

Fig. 1-23. Superparamagnetic core-shell NPs 1 (schematic drawing of 1 and TEM micrographs) and experimental setup for either circular or continuous operation [254].

In the extend study, mixtures of SPM NPs with solid metal oxides, such as CrO_2 and NiO_2, were used for various metal oxide mediated oxidation organic reactions. Those SPM NPs worked as the initial heating source by IH, while the metal oxides were heated up through heating exchange with the adjacent heating centers. The IH technical setup exhibited much better time/yield ratio in the flow mode compared to the batch mode. Alternatively, conductive steel beads and copper wire have also been utilized as

heating media (through induced eddy current) for organic synthesis in rapidly varying magnetic field. Enhanced with IH technology, the fixed-bed materials displayed great potential for several transformations [254, 255]. However, the surface temperature of individual NPs or copper wire is still unpredictable and need to be further investigated since the temperature is one critical parameter in organic synthesis process. It should be noticed that the idea of employing RF-heatable nanocarriers for the heat transfer to catalytically active metal NPs is the forerunner concept that has opened the way to a great number of recent achievements in the field of inductively heated catalytic transformations under flow conditions.

Magnetic core-shell $NiFe_2O_4$@TiO_2 NPs have also been employed by Rebrov and co-workers as an acid catalyst for the continuous flow and inductively-heated direct amide synthesis [259-261]. The core-shell structure is quite stable even after calcination at relatively high temperature. Results indicated that RF heating could significantly increase the apparent reaction rate (by 60%) due to the uniform heating capacity with reduced temperature gradients. Moreover, the catalyst deactivation rate was decreased by inhibiting the coke deposition to some extent compared with conversional heating schemes (**Fig. 1-24**). By further comparing the catalytic performance of the core-double shell structure catalyst (TiO_2@SiO_2@$NiFe_2O_4$) with just core-shell structure catalyst (TiO_2@$NiFe_2O_4$), they revealed that the introduction of an intermediate silica layer could effectively suppress the electronic interaction between the magnetic core (nickel ferrite) and TiO_2 shell, preventing the magnetic core dissolution and increasing its magnetization ability during the reaction, which in turns allows to maintain the heating effect and the catalytic performance of the system.

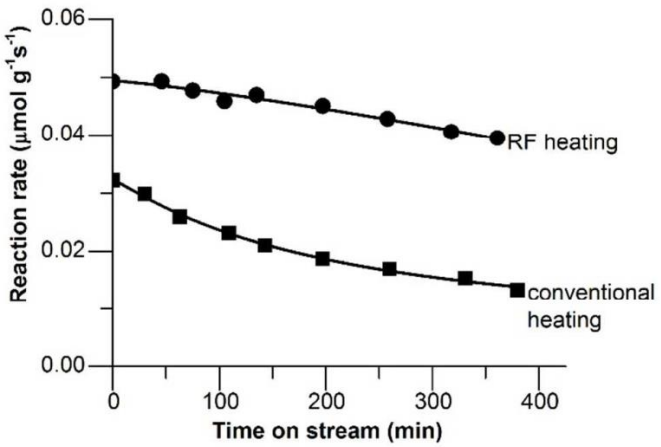

Fig. 1-24. Reaction rate of amide synthesis over the T-32-500 catalyst in conventionally and RF-heated flow reactors as a function of time on stream [260].

Very recently, Asensio and Chaudret have proposed an elegant and highly efficient protocol for the inductively heated hydrodeoxygenation (HDO) of acetophenone derivatives and biomass derived molecules under remarkably mild operative conditions [262]. They prepared hybrid functional materials based on the combination of magnetic susceptors with excellent heating power ($Fe_{2.2}C$ NPs) and Ru NPs featuring by high catalytic activity in HDO ($Fe_{2.2}C$@Ru NPs) [242]. This ideal combination has allowed the authors to run high-temperature catalysis in solution, ensuring excellent catalyst activity and high products selectivity already in the presence of low catalyst loadings and low hydrogen pressures. The use of magnetic nanoparticles (NPs) as a local transducer for the radiofrequency conversion into heat (through hysteresis loss) was found to improve the energy efficiency of the process. Indeed, the heat is directly and homogeneously transferred to the active sites without the need of heating the reactor walls, hence allowing very high local temperatures to be reached at the catalyst surface. This reactor configuration is well emphasized by these authors with the figurative concept of "hot spots" in a "cold environment". Indeed, the heating targeted to the catalytic bed (hence, where it is needed for the process to occur) can reach temperatures well-above those of the solvent boiling point. This can be explained on the basis of the fact that heat transfer from the susceptor to the solvent is slowed down by the formation of a "vapor shell" around the catalyst particles [263]. Overall, the proposed IH configuration allows the creation of local "hot spots" at the catalyst bed surrounded by a vapor phase where higher temperatures and gas pressures (ideal for running the HDO process) may be reached.

These above-mentioned results have opened an interesting development of the IH mode for operating various chemical syntheses with magnetic materials both in laboratory and industrial processes. The capacity of IH to drive heat directly where it is needed through the selective radiofrequency absorption onto dedicated materials (magnetic or electrically conductive), turned out to be an enabling technology capable to push several catalytic transformations beyond the reactor heat transfer limits, to the bounds of the process kinetics. Moreover, the removal of several heat transfer restrictions typically encountered in classical contact heating schemes has largely contributed to the improvement of process energetic as well as the reduction of side-products classically indicated as "heat wastes". Overall, the transition from a contact-to-contactless heat management in catalysis based on IH technology are manifold: more favorable energy balance, process intensification, reactor setup simplification, reduced

safety issues, minor operational costs and increased process productivity. With suitable design of the magnetic NPs and the reactor, the IH technical reactor should help the chemists to perform syntheses and workups much more efficiency in the near future.

1.4 Scope and outline of this thesis

As mentioned above, energy conversion and storage have always been the two critical issues for human society, especially under relentless development of renewable energy (RE). Development of new electrical devices, such as supercapacitors, for electrochemical storage of RE (with fast charge and discharge process), and integrated chemical energy conversion and storage strategies, such as Power-to-Gas (PtG) technical chain, are promising solutions to cope with the increasing of RE contribution in the energy mix and for the development of energy with lower carbon footprint. In the present thesis, we will focus on the development of sustainable carbon materials for electrochemical energy storage (supercapacitors) and supported nickel catalyst for chemical energy conversion and storage (catalytic CO_2 methanation) assisted by induction heating technology with high energy targeting and low heat waste.

Chapter 2 summarizes the detailed procedures for the development of new porous biomass-derived carbon structures for potential supercapacitor application. This chapter also reports on the preparation of mesoporous supported nickel-based catalysts for catalytic CO_2 methanation operated under induction heating technology. Different characterization technologies used within this thesis will also be detailed in this chapter.

Chapter 3 describes the synthetic procedure for two totally different biomass-derived carbon structures, *i.e.* a hierarchical porous carbon foam and a graphene-like carbon nanosheet, for supercapacitor application. Their textural properties as well as the superior electrochemical performance have been fully investigated and discussed. The synthesized carbon materials exhibited great potential as supercapacitor candidates.

Chapter 4 reports the catalytic methanation of CO_2 on different mesoporous nickel-based catalysts: Ni NPs decorated on a macroscopic oxidized carbon felt (Ni/OCF), and a powdered alumina supported nickel catalyst (Ni/Al_2O_3). The catalytic performance of all the catalysts has been fully investigated using both induction heating and conventional Joule heating modes. The structure-activity relationship and the explanation of the enhanced catalytic performance have been thoroughly investigated

and discussed with a special emphasize on the advantage of using a non-contact inductive heating (IH) mode on the catalyst temperature control and heat supply.

Finally, **Chapter 5** summarizes the general conclusions on the basis of the works presented above along with different perspectives for further developments of the presented catalytic systems and schemes.

Reference

[1] IEA (International Energy Agency). *World energy balances 2019 overview.* https://webstore.iea.org/world-energy-balances-2019.

[2] D. Pimentel, L. Hurd, A. C. Bellotti, M. J. Forster, I. N. Oka, O. D. Sholes, R. J. Whitman. *Science*, 1973, 182(4111): 443-449.

[3] N. Abas, A. Kalair, N. Khan. *Futures*, 2015, 69: 31-49.

[4] IEA (International Energy Agency). *CO_2 emission from fuel combustion 2018 overview.* https://webstore.iea.org/co2-emissions-from-fuel-combustion-2018.

[5] C. Le Quéré, R. M. Andrew, P. Friedlingstein, et al. *Earth Syst. Sci. Data*, 2018, 10(4): 2141-2194.

[6] National Oceanic and Atmospheric Administration (NOAA). *NEWS & FEATURES: Carbon dioxide.* https://www.noaa.gov/news/carbon-dioxide-levels-breach-another-threshold-at-mauna-loa.

[7] National Oceanic and Atmospheric Administration (NOAA). *NEWS & FEATURES: State of the Climate.* https://www.noaa.gov/news/2017-was-one-of-three-warmest-years-on-record-international-report-confirms.

[8] National Oceanic and Atmospheric Administration (NOAA)/Earth System Research Laboratory. https://www.esrl.noaa.gov/gmd/ccgg/trends/global.html.

[9] T. R. Karl, K. E. Trenberth. *Science*, 2013, 302(5651): 1719-1723.

[10] S. J. Davis, K. Caldeira, H. D. Matthews. *Science*, 2010, 329(5997): 1330-1333.

[11] C. Rosenzweig, A. Iglesias, X. B. Yang, P. R. Epstein, E. Chivian. *Global Chang. Hum. Health*, 2001, 2(2): 90-104.

[12] S. Rahmstorf, D. Coumou. *Proc. Natl. Acad. Sci. U.S.A.*, 2011, 108(44): 17905-17909.

[13] E. M. Fischer, R. Knutti. *Nat. Clim. Chang.*, 2015, 5(6): 560-564.

[14] H. Blanco, A. Faaij. *Renew. Sust. Energy Rev.*, 2018, 81: 1049-1086.

[15] P. Markewitz, W. Kuckshinrichs, W. Leitner, J. Linssen, P. Zapp, R. Bongartz, A. Schreiber, T. E. Müller. *Energy Environ. Sci.*, 2012, 5(6): 7281-7305.

[16] R. M. Cuéllar-Franca, A. Azapagic. *J CO_2 Util.*, 2015, 9: 82-102.

[17] IEA (International Energy Agency). *Renewables Information 2019 Overview.* https://webstore.iea.org/renewables-information-2019.

[18] H. Lund. *Energy*, 2007, 32(6): 912-919.

[19] O. Ellabban, H. Abu-Rub, F. Blaabjerg. *Renew. Sust. Energy Rev.*, 2014, 39: 748-

764.

[20] Bloomberg New Energy Finance (BNEF). https://about.bnef.com/blog/wind-solar-boost-cost-competitiveness-versus-fossil-fuels/.

[21] European Commission. *2030 Climate & Energy framework*. https://ec.europa.eu/clima/policies/strategies/2030_en.

[22] European Commission. *Our Vision for A Clean Planet for All*. 2018, https://ec.europa.eu/clima/sites/clima/files/docs/pages/vision_1_emissions_en.pdf.

[23] G. Stoeglehner, N. Niemetz, K. H. Kettl. *Energy, Sust. Soc.*, 2011, 1(1): 2.

[24] M. Qadrdan, M. Abeysekera, M. Chaudry, J. Wu, N. Jenkins. *Int. J. Hydrogen Energy*, 2015, 40(17): 5763-5775.

[25] H. Chen, T. N. Cong, W. Yang, C. Tan, Y. Li, Y. Ding. *Prog. Nat. Sci.*, 2009, 19(3): 291-312.

[26] G. Gahleitner. *Int. J. Hydrogen Energy*, 2013, 38(5): 2039-2061.

[27] M. Jentsch, T. Trost, M. Sterner. *Energy Procedia*, 2014, 46: 254-261.

[28] A. Varone, M. Ferrari. *Renew. Sust. Energy Rev.*, 2015, 45: 207-218.

[29] S. Hameer, J. L. van Niekerk. *Int. J. Energy Res.*, 2015, 39(9): 1179-1195.

[30] I. Hadjipaschalis, A. Poullikkas, V. Efthimiou. *Renew. Sust. Energy Rev.*, 2009, 13(6-7): 1513-1522.

[31] W. Raza, F. Ali, N. Raza, Y. Luo, K. H. Kim, J. Yang, S. Kumar, A. Mehmood, E. E. Kwon. *Nano Energy*, 2018, 52: 441-473.

[32] M. Conte. *Fuel Cells*, 2010, 10(5): 806-818.

[33] R. Kötz, M. J. E. A. Carlen. *Electrochim. Acta*, 2000, 45(15-16): 2483-2498.

[34] Y. Zhai, Y. Dou, D. Zhao, P. F. Fulvio, R. T. Mayes, S. Dai. *Adv. Mater.*, 2011, 23(42): 4828-4850.

[35] H. Jiang, P. S. Lee, C. Li. *Energy Environ. Sci.*, 2013, 6(1): 41-53.

[36] Y. Shao, M. F. El-Kady, J. Sun, Y. Li, Q. Zhang, M. Zhu, H. Wang, B. Dunn, R. B. Kaner. *Chem. Rev.*, 2018, 118(18): 9233-9280.

[37] Y. Wang, Y. Song, Y. Xia. *Chem. Soc. Rev.*, 2016, 45(21): 5925-5950.

[38] B. E. Conway. *Springer US*, 1999. ISBN: 978-0-306-45736-4. DOI: 10.1007/978-1-4757-3058-6.

[39] A. G. Pandolfo, A. F. Hollenkamp. *J. Power Sources*, 2006, 157(1): 11-27.

[40] L. L. Zhang, X. S. Zhao. *Chem. Soc. Rev.*, 2009, 38(9): 2520-2531.

[41] A. K. Shukla, S. Sampath, K. Vijayamohanan. *Curr. Sci.*, 2000, 79(12): 1656-

1661.

[42] J. R. Miller, P. Simon. *Science*, 2008, 321(5889): 651-652.

[43] G. Wang, L. Zhang, J. Zhang. *Chem. Soc. Rev.*, 2012, 41(2): 797-828.

[44] B. E. Conway, V. Birss, J. Wojtowicz. *J. Power Sources*, 1997, 66(1-2): 1-14.

[45] J. P. Zheng, J. Huang, T. R. Jow. *J. Electrochem. Soc.*, 1997, 144(6): 2026-2031.

[46] V. Augustyn, P. Simon, B. Dunn. *Energy Environ. Sci.*, 2014, 7(5): 1597-1614.

[47] S. Trasatti, G. Buzzanca. *J. Electroanal. Chem. Interfacial Electrochem.*, 1971, 29(2): A1-A5.

[48] V. Subramanian, H. Zhu, R. Vajtai, P. M. Ajayan, B. Wei. *J. Phys. Chem. B*, 2005, 109(43): 20207-20214.

[49] J. W. Kim, V. Augustyn, B. Dunn. *Adv. Energy Mater.*, 2012, 2(1): 141-148.

[50] V. Augustyn, J. Come, M. A. Lowe, J. W. Kim, P. L. Taberna, S. H. Tolbert, H. D. Abruña, P. Simon, B. Dunn. *Nat. Mater.*, 2013, 12(6): 518-522.

[51] Y. Jiang, J. Liu. *Energy Environ. Mater.*, 2019, 2(1): 30-37.

[52] H. S. Nan, X. Y. Hu, H. W. Tian. *Mat. Sci. Semicon. Proc.*, 2019, 94: 35-50.

[53] M. Okubo, E. Hosono, J. Kim, M. Enomoto, N. Kojima, T. Kudo, H. Zhou, I. Honma. *J. Am. Chem. Soc.*, 2007, 129(23): 7444-7452.

[54] P. Simon, Y. Gogotsi, B. Dunn. *Science*, 2014, 343(6176): 1210-1211.

[55] T. Brousse, D. Bélanger, J. W. Long. *J. Electrochem. Soc.*, 2015, 162(5): A5185-A5189.

[56] H. Lindström, S. Södergren, A. Solbrand, H. Rensmo, J. Hjelm, A. Hagfeldt, S. E. Lindquist. *J. Phys. Chem. B*, 1997, 101(39): 7717-7722.

[57] T. C. Liu, W. G. Pell, B. E. Conway, S. L. Roberson. *J. Electrochem. Soc.*, 1998, 145(6): 1882-1888.

[58] J. Wang, J. Polleux, J. Lim, B. Dunn. *J. Phys. Chem. C*, 2007, 111(40): 14925-14931.

[59] J. Xie, P. Yang, Y. Wang, T. Qi, Y. Lei, C. M. Li. *J. Power Sources*, 2018, 401: 213-223.

[60] Y. Gogotsi, R. M. Penner. *ACS Nano*, 2018, 12(3): 2081-2083.

[61] A. González, E. Goikolea, J. A. Barrena, R. Mysyk. *Renew. Sust. Energy Rev.*, 2016, 58: 1189-1206.

[62] S. R. Bishop, D. Marrocchelli, C. Chatzichristodoulou, N. H. Perry, M. B. Mogensen, H. L. Tuller, E. D. Wachsman. *Annu. Rev. Mater. Res.*, 2014, 44: 6.1-6.35.

[63] P. V. Braun, J. Cho, J. H. Pikul, W. P. King, H. Zhang. *Curr. Opin. Solid State Mater. Sci.*, 2012, 16(4): 186-198.

[64] B. E. Conway. *J. Electrochem. Soc.*, 1991, 138(6): 1539-1548.

[65] J. A. Davis, R. O. James, J. O. Leckie. *J. Colloid Interface Sci.*, 1978, 63(3): 480-499.

[66] F. Béguin, E. Frackowiak, M. Lu (Series Editor). Wiley-VCH, 2013. ISBN: 978-3-527-32883-3.

[67] J. M. Griffin, A. C. Forse, W. Y. Tsai, P. L. Taberna, P. Simon, C. P. Grey. *Nat. Mater.*, 2015, 14(8): 812-819.

[68] D. P. Dubal, O. Ayyad, V. Ruiz, P. Gomez-Romero. *Chem. Soc. Rev.*, 2015, 44(7): 1777-1790.

[69] A. J. Bard, L. R. Faulkner. *John Wiley & Sons: New York*, 2001, ISBN: 978-0-471-04372-0.

[70] J. H. Masliyah, S. Bhattacharjee. *John Wiley & Sons*, 2006. ISBN: 978-0471-78882-9. DOI:10.1002/0471799742.

[71] H. V. Helmholtz. *Ann. Phys. Chem.*, 1853, 165(7): 353-377.

[72] H. V. Helmholtz. *Ann. Phys. Chem.*, 1879, 243(7): 337-382.

[73] F. Belhachemi, S. Rael, B. Davat. *Thirty-Fifth IAS Annual Meeting and World Conference on Industrial Applications of Electrical Energy, IEEE*, 2000, 5: 3069-3076. DOI: 10.1109/IAS.2000.882604.

[74] H. Wang, H., L. Pilon. *J. Phys. Chem. C*, 2011, 115(33): 16711-16719.

[75] A. Tyagi, R. K. Gupta. *Nanomaterials: A Guide to Fabrication and Applications*, Chapter 11, CRC Press, 2016, 54: 261-281. DOI: 10.1201/b19168-11.

[76] J. Kang, J. Wen, S. H. Jayaram, A. Yu, X. Wang. *Electrochim. Acta*, 2014, 115: 587-598.

[77] M. Gouy. *J. Phys. Theor. Appl.*, 1910, 9(1): 457-468.

[78] D. L. Chapman. *London, Edinburgh, Dublin Philos. Mag. J. Sci.*, 1913, 25(148): 475-481.

[79] O. Stern. *Z. Elektrochem. Angew. Phys. Chem.*, 1924, 30(21-22): 508-516.

[80] L. Zhang, X. Hu, Z. Wang, F. Sun, D. G. Dorrell. *Renew. Sust. Energy Rev.*, 2018, 81: 1868-1878.

[81] R. Burt, G. Birkett, X. S. Zhao. *Phys. Chem. Chem. Phys.*, 2014, 16(14): 6519-6538.

[82] D. C. Grahame. *Chem. Rev.*, 1947, 41: 441-501.

[83] C. Zhong, Y. Deng, W. Hu, J. Qiao, L. Zhang, J. Zhang. *Chem. Soc. Rev.*, 2015, 44(21): 7484-7539.

[84] A. Burke. *Electrochim. Acta*, 2007, 53(3): 1083-1091.

[85] P. Simon, Y. Gogotsi. *Nat. Mater.*, 2008, 7: 320-329.

[86] A. Muzaffar, M. B. Ahamed, K. Deshmukh, J. Thirumalai. *Renew. Sust. Energy Rev.*, 2019, 101: 123-145.

[87] L. Hao, X. Li, L. Zhi. *Adv. Mater.*, 2013, 25(28): 3899-3904.

[88] J. Yan, Q. Wang, T. Wei, Z. Fan. *Adv. Energy Mater.*, 2014, 4(4): 1300816-1300858.

[89] Q. Wang, J. Yan, Z. Fan. *Energy Environ. Sci.*, 2016, 9(3): 729-762.

[90] A. M. Abioye, F. N. Ani. *Renew. Sust. Energy Rev.*, 2015, 52: 1282-1293.

[91] Z. Gao, Y. Zhang, N. Song, X. Li. *Mater. Res. Lett.*, 2017, 5(2): 69-88.

[92] Z. Peng, Z. Guo, W. Chu, M. Wei. *RSC Adv.*, 2016, 6(48): 42019-42028.

[93] C. Zhang, D. Long, B. Xing, W. Qiao, R. Zhang, L. Zhan, X. Liang, L. Ling. *Electrochem. Commun.*, 2008, 10(11): 1809-1811.

[94] X. He, X. Xie, J. Wang, X. Ma, Y. Xie, J. Gu, N. Xiao, J. Qiu. *Nanoscale*, 2019, 11(14): 6610-6619.

[95] F. Wei, X. He, H. Zhang, Z. Liu, N. Xiao, J. Qiu. *J. Power Sources*, 2019, 428: 8-12.

[96] G. Lin, R. Ma, Y. Zhou, Q. Liu, X. Dong, J. Wang. *Electrochim. Acta*, 2018, 261: 49-57.

[97] H. Jin, X. Wang, Z. Gu, J. Polin. *J. Power Sources*, 2013, 236: 285-292.

[98] Y. Li, G. Wang, T. Wei, Z. Fan, P. Yan. *Nano Energy*, 2016, 19: 165-175.

[99] Q. Liang, L. Ye, Z. H. Huang, Q. Xu, Y. Bai, F. Kang, Q. H. Yang. *Nanoscale*, 2014, 6(22): 13831-13837.

[100] G. Xu, J. Han, B. Ding, P. Nie, J. Pan, H. Dou, H. Li, X. Zhang. *Green Chem.*, 2015, 17(3): 1668-1674.

[101] G. Zhao, C. Chen, D. Yu, L. Sun, C. Yang, H. Zhang, Y. Sun, F. Besenbacher, M. Yu. *Nano Energy*, 2018, 47: 547-555.

[102] N. Guo, M. Li, Y. Wang, X. Sun, F. Wang, R. Yang. *ACS Appl. Mater. Interfaces*, 2016, 8(49): 33626-33634.

[103] W. Chen, R. B. Rakhi, M. N. Hedhili, H. N. Alshareef. *J. Mater. Chem. A*, 2014, 2(15): 5236-5243.

[104] L. Sun, C. Tian, M. Li, X. Meng, L. Wang, R. Wang, J. Yin, H. Fu. *J. Mater.*

Chem. A, 2013, 1(21): 6462-6470.

[105] C. Chen, D. Yu, G. Zhao, B. Du, W. Tang, L. Sun, Y. Sun, F. Besenbacher, M. Yu. *Nano Energy*, 2016, 27: 377-389.

[106] Q. Wang, J. Yan, Y. Wang, T. Wei, M. Zhang, X. Jing, Z. Fan. *Carbon*, 2014, 67: 119-127.

[107] G. Guandalini, S. Campanari, M. C. Romano. *Appl. Energy*, 2015, 147: 117-130.

[108] P. Collet, E. Flottes, A. Favre, L. Raynal, H. Pierre, S. Capela, C. Peregrina. *Appl. Energy*, 2017, 192: 282-295.

[109] J. De Bucy, O. Lacroix, L. Jammes. *ENEA Consulting, Paris, France*. 2016.

[110] S. Clegg, P. Mancarella. *IEEE Trans. Sustain. Energy*, 2015, 6(4): 1234-1244.

[111] A. Lewandowska-Bernat, U. Desideri. *Energy Procedia*, 2017, 105: 4569-4574.

[112] S. McDonagh, R. O'Shea, D. M. Wall, J. P. Deane, J. D. Murphy. *Appl. Energy*, 2018, 215: 444-456.

[113] Audi e-diesel plant Laufenburg. Audi MediaCenter. https://www.audi-mediacenter.com/en/photos/detail/audi-e-diesel-plant-laufenburg-55305.

[114] A. Buttler, H. Spliethoff. *Renew. Sust. Energy Rev.*, 2018, 82: 2440-2454.

[115] M. Götz, J. Lefebvre, F. Mörs, A. M. Koch, F. Graf, S. Bajohr, R. Reimert, T. Kolb. *Renew. Energy*, 2016, 85: 1371-1390.

[116] M. Ball, M. Weeda. *Int. J. Hydrogen Energy*, 2015, 40(25): 7903-7919.

[117] M. Bailera, P. Lisbona, L. M. Romeo, S. Espatolero. *Renew. Sust. Energy Rev.*, 2017, 69: 292-312.

[118] European Technology and Innovation Platform (ETIP) Bioenergy. http://www.etipbioenergy.eu/?option=com_content&view=article&id=276.

[119] J. Ma, Q. Li, M. Kühn, N. Nakaten. *Renew. Sust. Energy Rev.*, 2018, 97: 478-496.

[120] S. Schiebahn, T. Grube, M. Robinius, V. Tietze, B. Kumar, D. Stolten. *Int. J. Hydrogen Energy*, 2015, 40(12): 4285-4294.

[121] K. Hashimoto, M. Yamasaki, S. Meguro, T. Sasaki, H. Katagiri, K. Izumiya, N. Kumagai, H. Habazaki, E. Akiyama, K. Asami. *Corros. Sci.*, 2002, 44(2): 371-386.

[122] K. Ghaib, K. Nitz, F. Z. Ben-Fares. *ChemBioEng Rev.*, 2016, 3(6): 266-275.

[123] P. Sabatier, J. B. Senderens. *CR Acad. Sci.*, 1902, 134: 689-691.

[124] T. Inui, T. Takeguchi. *Catal. Today*, 1991, 10(1): 95-106.

[125] P. J. Lunde, F. L. Kester. *Ind. Eng. Chem. Process Des. Dev.*, 1974, 13: 27-33.

[126] W. Wang, S. Wang, X. Ma, J. Gong. *Chem. Soc. Rev.*, 2011, 40(7): 3703-3727.

[127] L. Xu, F. Wang, M. Chen, D. Nie, X. Lian, Z. Lu, H. Chen, K. Zhang, P. Ge. *Int. J. Hydrogen Energy*, 2017, 42(23): 15523-15539.

[128] G. A. Mills, F. W. Steffgen. Catalytic methanation. *Catal. Rev.*, 1974, 8(1): 159-210.

[129] M. A. A. Aziz, A. A. Jalil, S. Triwahyono, A. Ahmad. *Green Chem.*, 2015, 17(5): 2647-2663.

[130] P. Frontera, A. Macario, M. Ferraro, P. Antonucci. *Catalysts*, 2017, 7(2): 59-86.

[131] W. Wei, G. Jinlong. *Front. Chem. Sci. Eng.*, 2011, 5(1): 2-10.

[132] J. H. Kwak, L. Kovarik, J. Szanyi. *ACS Catal.*, 2013, 3(9): 2094-2100.

[133] S. Tada, T. Shimizu, H. Kameyama, T. Haneda, R. Kikuchi. *Int. J. Hydrogen Energy*, 2012, 37(7): 5527-5531.

[134] T. A. Le, M. S. Kim, S. H. Lee, T. W. Kim, E. D. Park. *Catal. Today*, 2017, 293: 89-96.

[135] S. Abelló, C. Berrueco, D. Montané. *Fuel*, 2013, 113: 598-609.

[136] M. A. A. Aziz, A. A. Jalil, S. Triwahyono, R. R. Mukti, Y. H. Taufiq-Yap, M. R. Sazegar. *Appl. Catal. B: Environ.*, 2014, 147: 359-368.

[137] M. A. A. Aziz, A. A. Jalil, S. Triwahyono, S. M. Sidik. *Appl. Catal. A: Gen.*, 2014, 486: 115-122.

[138] F. Ocampo, B. Louis, L. Kiwi-Minsker, A. C. Roger. *Appl. Catal. A: Gen.*, 2011, 392(1-2): 36-44.

[139] J. Lin, C. Ma, Q. Wang, Y. Xu, G. Ma, J. Wang, H. Wang, C. Dong, C. Zhang, M. Ding. *Appl. Catal. B: Environ.*, 2019, 243: 262-272.

[140] Y. Zhan, Y. Wang, D. Gu, C. Chen, L. Jiang, K. Takehira. *Appl. Surf. Sci.*, 2018, 459: 74-79.

[141] J. Ashok, M. L. Ang, S. Kawi. *Catal. Today*, 2017, 281: 304-311.

[142] H. Liu, X. Zou, X. Wang, X. Lu, W. Ding. *J. Nat. Gas Chem.*, 2012, 21(6): 703-707.

[143] M. Guo, G. Lu. *RSC Adv.*, 2014, 4(102): 58171-58177.

[144] L. Xu, H. Yang, M. Chen, F. Wang, D. Nie, L. Qi, X. Lian, H. Chen, M. Wu. *J. CO_2 Util.*, 2017, 21: 200-210.

[145] G. Garbarino, C. Wang, T. Cavattoni, E. Finocchio, P. Riani, M. Flytzani-Stephanopoulos, G. Busca. *Appl. Catal. B Environ.*, 2019, 248: 286-297.

[146] L. Zhang, L. Bian, Z. Zhu, Z. Li. *Int. J. Hydrogen Energy*, 2018, 43: 2197-2206.

[147] R. Razzaq, H. Zhu, L. Jiang, U. Muhammad, C. Li, S. Zhang. *Ind. Eng. Chem. Res.*, 2013, 52(6): 2247-2256.

[148] L. Xu, X. Lian, M. Chen, Y. Cui, F. Wang, W. Li, B. Huang. *Int. J. Hydrogen Energy*, 2018, 43(36): 17172-17184.

[149] H. Zhu, R. Razzaq, C. Li, Y. Muhmmad, S. Zhang. *AIChE J.*, 2013, 59(7): 2567-2576.

[150] G. Wang, S. Xu, L. Jiang, C. Wang. *Int. J. Hydrogen Energy*, 2016, 41(30): 12910-12919.

[151] S. Ewald, M. Kolbeck, T. Kratky, M. Wolf, O. Hinrichsen. *Appl. Catal. A: Gen.*, 2019, 570: 376-386.

[152] X. Jia, X. Zhang, N. Rui, X. Hu, C. J. Liu. *Appl. Catal. B: Environ.*, 2019, 244: 159-169.

[153] S. Rahmani, M. Rezaei, F. Meshkani. *J. Ind. Eng. Chem.*, 2014, 20: 1346-1352.

[154] J. Liu, C. Li, F. Wang, S. He, H. Chen, Y. Zhao, M. Wei, D. G. Evans, X. Duan. *Catal. Sci. Technol.*, 2013, 3(10): 2627-2633.

[155] G. Garbarino, P. Riani, L. Magistri, G. Busca. *Int. J. Hydrogen Energy*, 2014, 39(22): 11557-11565.

[156] F. Solymosi, A. Erdöhelyi, T. Bánsági. *J. Catal.*, 1981, 68(2): 371-382.

[157] Z. L. Zhang, A. Kladi, X. E. Verykios. *J. Catal.*, 1994, 148(2): 737-747.

[158] F. Solymosi, I. Tombácz, J. Koszta. *J. Catal.*, 1985, 95(2): 578-586.

[159] A. Karelovic, P. Ruiz. *J. Catal.*, 2013, 301: 141-153.

[160] A. T. Bell. *J. Mol. Catal. A: Chem.*, 1995, 100(1-3): 1-11.

[161] K. J. Williams, A. B. Boffa, M. Salmeron, A. T. Bell, G. A. Somorjai. *Catal. Lett.*,1991, 9(5-6): 415-426.

[162] A. Karelovic, P. Ruiz. *Appl. Catal. B: Environ.*, 2012, 113: 237-249.

[163] M. Jacquemin, A. Beuls, P. Ruiz. *Catal. Today*, 2010, 157(1-4): 462-466.

[164] A. Beuls, C. Swalus, M. Jacquemin, G. Heyen, A. Karelovic, P. Ruiz. *Appl. Catal. B: Environ.*, 2012, 113: 2-10.

[165] C. Swalus, M. Jacquemin, C. Poleunis, P. Bertrand, P. Ruiz. *Appl. Catal. B: Environ.*, 2012, 125: 41-50.

[166] S. Akamaru, T. Shimazaki, M. Kubo, T. Abe. *Appl. Catal. A: Gen.*, 2014, 470: 405-411.

[167] S. Eckle, M. Augustin, H. G. Anfang, R. J. Behm. *Catal. Today*, 2012, 181(1): 40-51.

[168] S. Ma, W. Song, B. Liu, H. Zheng, J. Deng, W. Zhong, J. Liu, X. Q. Gong, Z. Zhao. *Catal. Sci. Technol.*, 2016, 6(15): 6128-6136.

[169] T. Abe, M. Tanizawa, K. Watanabe, A. Taguchi. *Energy Environ. Sci.*, 2009, 2(3): 315-321.

[170] J. Xu, X. Su, H. Duan, B. Hou, Q. Lin, X. Liu, X. Pan, G. Pei, H. Geng, Y. Huang, T. Zhang. *J. Catal.*, 2016, 333: 227-237.

[171] F. Wang, S. He, H. Chen, B. Wang, L. Zheng, M. Wei, D. G. Evans, X. Duan. *J. Am. Chem. Soc.*, 2016, 138(19): 6298-6305.

[172] S. Tada, O. J. Ochieng, R. Kikuchi, T. Haneda, H. Kameyama. *Int. J. Hydrogen Energy*, 2014, 39(19): 10090-10100.

[173] J. N. Park, E. W. McFarland. *J. Catal.*, 2009, 266(1): 92-97.

[174] J. Martins, N. Batail, S. Silva, S. Rafik-Clément, A. Karelovic, D. P. Debecker, A. Chaumonnot, D. Uzio. *Catal. Commun.*, 2015, 58: 11-15.

[175] A. H. Zamani, R. Ali, W. A. Bakar. *J. Ind. Eng. Chem.*, 2015, 29: 238-248.

[176] D. Theleritis, S. Souentie, A. Siokou, A. Katsaounis, C. G. Vayenas. *ACS Catal.*, 2012, 2(5): 770-780.

[177] C. H. Bartholomew. *Appl. Catal. A: Gen.*, 2001, 212(1-2): 17-60.

[178] A. Vita, C. Italiano, L. Pino, P. Frontera, M. Ferraro, V. Antonucci. *Appl. Catal. B: Environ.*, 2018, 226: 384-395.

[179] C. Y. Zhao. *Int. J. Heat Mass Transf.*, 2012, 55(13-14), 3618-3632.

[180] S. Danaci, L. Protasova, J. Lefevere, L. Bedel, R. Guilet, P. Marty. *Catal. Today*, 2016, 273: 234-243.

[181] C. Fukuhara, K. Hayakawa, Y. Suzuki, W. Kawasaki, R. Watanabe. *Appl. Catal. A: Gen.*, 2017, 532: 12-18.

[182] S. Ratchahat, M. Sudoh, Y. Suzuki, W. Kawasaki, R. Watanabe, C. Fukuhara. *J. CO_2 Util.*, 2018, 24: 210-219.

[183] Z. Liu, B. Chu, X. Zhai, Y. Jin, Y. Cheng. *Fuel*, 2012, 95: 599-605.

[184] O. Görke, P. Pfeifer, K. Schubert. *Catal. Today*, 2005, 110(1-2): 132-139.

[185] Y. Li, Q. Zhang, R. Chai, G. Zhao, Y. Liu, Y. Lu, F. Cao. *AIChE J.*, 2015, 61(12): 4323-4331.

[186] K. P. Brooks, J. Hu, H. Zhu, R. J. Kee. *Chem. Eng. Sci.*, 2007, 62(4): 1161-1170.

[187] Y. Men, G. Kolb, R. Zapf, V. Hessel, H. Loewe. *Catal. Today*, 2007, 125: 81-87.

[188] S. Rönsch, J. Schneider, S. Matthischke, M. Schlüter, M. Götz, J. Lefebvre, P. Prabhakaran, S. Bajohr. *Fuel*, 2016, 166: 276-296.

[189] H. Knözinger, K. Kochloefl. *Ullmann's Encyclopedia of Industrial Chemistry, Wiley-VCH*, 2000, DOI: 10.1002/14356007.a05_313.

[190] N. Mizuno, M. Misono. *Chem. Rev.*, 1998, 98(1): 199-218.

[191] J. J. Bravo-Suárez, R. V. Chaudhari, B. Subramaniam. Novel materials for catalysis and fuels processing. ACS Symposium Series, American Chemical Society: Washington, DC, 2013, 3-68. DOI: 10.1021/bk-2013-1132.ch001.

[192] M. V. Twigg. *CRC Press*, 1989, ISBN: 978-0723-40857-4, DOI: 10.1201/9781315138862.

[193] A. Stankiewicz, J. A. Moulijn. *Ind. Eng. Chem. Res.*, 2002, 41(8): 1920-1924.

[194] B. P. Timko, K. Whitehead, W. Gao, D. S. Kohane, O. Farokhzad, D. Anderson, R. Langer. *Annu. Rev. Mater. Res.*, 2011, 41: 1-20.

[195] Z. Hedayatnasab, F. Abnisa, W. M. A. W. Daud. *Mater. Des.*, 2017, 123: 174-196.

[196] W. Wang, G. Tuci, C. Duong-Viet, Y. Liu, A. Rossin, L. Luconi, J. M. Nhut, L. Nguyen-Dinh, C. Pham-Huu, G. Giambastiani. *ACS Catal*., 2019, 9: 7921-7935.

[197] O. Lucía, P. Maussion, E. J. Dede, J. M. Burdío. *IEEE Trans. Ind. Electron.*, 2013, 61(5): 2509-2520.

[198] A. Ovenston, J. R. Walls. *J. Chem. Soc., Faraday Trans. 1*, 1983, 79: 1073-1084.

[199] P. D. Muley, C. Henkel, K. K. Abdollahi, D. Boldor. *Energy Fuels*, 2015, 29(11): 7375-7385.

[200] J. Bursavich, M. Abu-Laban, P. D. Muley, D. Boldor, D. J. Hayes. *Energy Convers. Manage.*, 2019, 183: 689-697.

[201] M. Abu-Laban, P. D. Muley, D. J. Hayes, D. Boldor. *Catal. Today*, 2017, 291: 3-12.

[202] T. K. Houlding, E. V. Rebrov. *Green Process. Synth.*, 2012, 1(1): 19-31.

[203] W. Wang, C. Duong-Viet, Z. Xu, H. Ba, G. Tuci, G. Giambastiani, Y. Liu, T. Truong-Huu, J. M. Nhut, C. Pham-Huu. *Catal. Today*, 2019, in press, DOI: 10.1016/j.cattod.2019.02.050.

[204] M. G. Vinum, M. R. Almind, J. S. Engbæk, S. B. Vendelbo, M. F. Hansen, C. Frandsen, J. Bendix, P. M. Mortensen. *Angew. Chem. Int. Ed.*, 2018, 57(33): 10569-10573.

[205] A. Meffre, B. Mehdaoui, V. Connord, J. Carrey, P. F. Fazzini, S. Lachaize, M. Respaud, B. Chaudret. *Nano Lett.*, 2015, 15(5): 3241-3248.

[206] S. Ruta, R. Chantrell, O. Hovorka. *Sci. Rep.*, 2015, 5, 9090.

[207] R. Hergt, S. Dutz, M. Röder. *J. Phys.: Condens. Matter*, 2008, 20(38): 385214.

[208] X. Zhang, S. Chen, H. M. Wang, S. L. Hsieh, C. H. Wu, H. H. Chou, S. Hsieh. *Biomed. Eng.*, 2010, 22(05): 393-399.

[209] J. Pearce, A. Giustini, R. Stigliano, P. J. Hoopes. *J. Nanotechnol. Eng. Med.*, 2013, 4(1): 011005.

[210] A. J. Moses. *Wiley Encyclopedia of Electrical and Electronics Engineerin,* Wiley: 2016, pp 1-22.

[211] C. Appino, O. De La Barrière, F. Fiorillo, M. Lobue, F. Mazaleyrat, C. Ragusa. *J. Appl. Phys.*, 2013, 113(17): 17A322.

[212] D. Lisjak, A. Mertelj. *Prog. Mater. Sci.*, 2018, 95: 286-328.

[213] N. A. Frey, S. Peng, K. Cheng, S. Sun. *Chem. Soc. Rev.*, 2009, 38(9): 2532-2542.

[214] R. S. Ruffini, R. J. Madeira. *Mater. Sci. Forum*, 1992, 102-104: 383-392.

[215] J. Corcoran, P. B. Nagy. *J. Nondestruct. Eval.*, 2016, 35(4): 58.

[216] A. Skumiel, M. Kaczmarek-Klinowska, M. Timko, M. Molcan, M. Rajnak. *Int. J. Thermophys.*, 2013, 34(4): 655-666.

[217] J. Carrey, B. Mehdaoui, M. Respaud. *J. Appl. Phys.*, 2011, 109(8): 083921.

[218] W. M. Zhou, B. Yang, Z. X. Yang, F. Zhu, L. J. Yan, Y. F. Zhang. *Appl. Surf. Sci.*, 2006, 252(14): 5143-5148.

[219] W. M. Zhou, Z. X. Yang, F. Zhu, Y. F. Zhang. *Physica E*, 2006, 31(1): 9-12.

[220] H. Y. Chen, L. Chen, Y. Lu, Q. Hong, H. C. Chua, S. B. Tang, J. Lin. *Catal. Today*, 2004, 96(3): 161-164.

[221] B. D. Sosnowchik, L. Lin. *Appl. Phys. Lett.*, 2006, 89(19): 193112.

[222] D. Lupu, A. R. Biriş, A. Jianu, C. Bunescu, E. Burkel, E. Indrea, G. Mihăilescu, S. Pruneanu, L. Olenic, I. Mişan. *Carbon*, 2004, 42(3): 503-507.

[223] A. Okamoto, H. Shinohara. *Carbon*, 2005, 43(2): 431-436.

[224] L. Tao, J. Lee, H. Li, R. D. Piner, R. S. Ruoff, D. Akinwande. *Appl. Phys. Lett.*, 2013, 103(18): 183115.

[225] A. R. Biris, A. S. Biris, D. Lupu, S. Trigwell, E. Dervishi, Z. Rahman, P. Marginean. *Chem. Phys. Lett.*, 2006, 429(1-3): 204-208.

[226] C. Wu, F. Li, W. Chen, C. P. Veeramalai, P. C. Ooi, T. Guo. *Sci. Rep.*, 2015, 5: 9034.

[227] V. I. Zaikovskii, V. V. Chesnokov, R. A. Buyanov. Kinet. *Catal.*, 2001, 42(6): 813-820.

[228] S. Sato, A. Kawabata, M. Nihei, Y. Awano. *Chem. Phys. Lett.*, 2003, 382(3-4):

361-366.

[229] L. Tapaszto, K. Kertész, Z. Vértesy, Z. E. Horvath, A. A. Koos, Z. Osváth, Z. Osváth, Z. Sárközi, A. Darabont, L. P. Biró. *Carbon*, 2005, 43(5): 970-977.

[230] C. Singh, M. S. P. Shaffer, A. H. Windle. *Carbon*, 2003, 41(2): 359-368.

[231] Z. Li, B. Zhao, P. Liu, B. Zhao, D. Chen, Y. Zhang. *Physica E*, 2008, 40(3): 452-456.

[232] T. Guo, P. Nikolaev, A. Thess, D. T. Colbert, R. E. Smalley. *Chem. Phys. Lett.*, 1995, 243(1-2): 49-54.

[233] J. F. Colomer, C. Stephan, S. Lefrant, G. Van Tendeloo, I. Willems, Z. Konya, A. Fonseca, C. Laurent, J. B. Nagy. *Chem. Phys. Lett.*, 2000, 317(1-2): 83-89.

[234] J. Qiu, Y. Li, Y. Wang, T. Wang, Z. Zhao, Y. Zhou, F. Li, H. Cheng. *Carbon*, 2003, 41(11): 2170-2173.

[235] Y. Zhang, L. Zhang, C. Zhou. *Acc. Chem. Res.*, 2013, 46(10): 2329-2339.

[236] X. Li, W. Cai, J. An, S. Kim, J. Nah, D. Yang, R. Piner, A. Velamakanni, I. Jung, E. Tutuc, S. K. Banerjee, L. Colombo, R. S. Ruoff. *Science*, 2009, 324(5932): 1312-1314.

[237] R. Muñoz, C. Gómez-Aleixandre. *Chem. Vap. Deposition*, 2013, 19: 297-322.

[238] P. Piner, H. Li, X. Kong, L. Tao, I. N. Kholmanov, H. Ji, W. H. Lee, J. W. Suk, J. Ye, Y. Hao, S. Chen, C. W. Magnuson, A. F. Ismach, D. Akinwande, R. S. Ruoff. *ACS Nano*, 2013, 7(9): 7495-7499.

[239] K. Blinov, A. Nikanorov, B. Nacke, M. Klöpzig. *COMPEL- Int. J. Comput. Math. Electr. Electron. Eng.*, 2011, 30(5): 1539-1549.

[240] H. Kim, C. Mattevi, M. R. Calvo, J. C. Oberg, L. Artiglia, S. Agnoli, C. F. Hirjibehedin, M. Chhowalla, E. Saiz. *ACS Nano*, 2012, 6(4): 3614-3623.

[241] J. Leclercq, F. Giraud, D. Bianchi, K. Fiaty, F. Gaillard. *Appl. Catal. B: Environ.*, 2014, 146: 131-137.

[242] A. Bordet, L. M. Lacroix, P. F. Fazzini, J. Carrey, K. Soulantica, B. Chaudret. *Angew. Chem. Int. Ed.*, 2016, 55(51): 15894-15898.

[243] H. Huang, Y. Xu, Q. Feng, D. Y. C. Leung. *Catal. Sci. Technol.*, 2015, 5(5): 2649-2669.

[244] J. Leclercq. Université Claude Bernard - Lyon I, Doctoral dissertation, Catal., 2013, Français. ⟨NNT : 2013LYO10265⟩. ⟨tel-01070795⟩.

[245] D. Schlereth, O. Hinrichsen. *Chem. Eng. Res. Des.*, 2014, 92(4): 702-712.

[246] P. M. Mortensen, J. S. Engbæk, S. B. Vendelbo, M. F. Hansen, M. Østberg. *Ind. Eng. Chem. Res.*, 2017, 56(47): 14006-14013.

[247] F. Varsano, M. Bellusci, A. L. Barbera, M. Petrecca, M. Albino, C. Sangregorio. *Int. J. Hydrogen Energy*, 2019, 44(38): 21037-21044.

[248] M. N. Pérez-Camacho, J. Abu-Dahrieh, D. Rooney, K. Sun. *Catal. Today*, 2015, 242: 129-138.

[249] S. Ceylan, C. Friese, C. Lammel, K. Mazac, A. Kirschning. *Angew. Chem. Int. Ed.*, 2008, 47(46): 8950-8953.

[250] J. Wegner, S. Ceylan, A. Kirschning. *Adv. Syn. Catal.*, 2012, 354(1): 17-57.

[251] R. N. Grass, E. K. Athanassiou, W. J. Stark. *Angew. Chem. Int. Ed.*, 2007, 46(26): 4909-4912.

[252] H. Yoon, S. Ko, J. Jang. *Chem. Commun.*, 2007, (14): 1468-1470.

[253] J. Wegner, S. Ceylan, A. Kirschning. *Chem. Commun.*, 2011, 47(16): 4583-4592.

[254] S. Ceylan, L. Coutable, J. Wegner, A. Kirschning. *Chem. Eur. J.*, 2011, 17(6): 1884-1893.

[255] S. Ceylan, T. Klande, C. Vogt, C. Friese, A. Kirschning. *Synlett*, 2010, 13: 2009-2013.

[256] J. Wegner, S. Ceylan, C. Friese, A. Kirschning. *Eur. J. Org. Chem.*, 2010, 2010(23): 4372-4375.

[257] S. R. Chaudhuri, J. Hartwig, L. Kupracz, T. Kodanek, J. Wegner, A. Kirschning. *Adv. Syn. Catal.*, 2014, 356(17): 3530-3538.

[258] C. Niether, S. Faure, A. Bordet, J. Deseure, M. Chatenet, J. Carrey, B. Chaudret, A. Rouet. *Nat. Energy*, 2018, 3(6): 476-483.

[259] T. K. Houlding, P. Gao, V. Degirmenci, K. Tchabanenko, E. V. Rebrov. *Mater. Sci. Eng.*, 2015, 193: 175-180.

[260] Y. Liu, P. Gao, N. Cherkasov, E. V. Rebrov. *RSC Adv.*, 2016, 6: 100997-101007.

[261] Y. Liu, N. Cherkasov, P. Gao, J. Fernández, M. R. Lees, E. V. Rebrov. *J. Catal.*, 2017, 355: 120-130.

[262] J. M. Asensio, A. B. Miguel, P. F. Fazzini, P. W. N. M. van Leeuwen, B. Chaudret. *Angew. Chem. Int. Ed.*, 2019, 131: 1-6.

[263] A. Riedinger, P. Guardia, A. Curcio, M. A. Garcia, R. Cingolani, L. Manna, T. Pellegrino. *Nano Lett.*, 2013, 13(6): 2399-2406.

Chapter 2

Material synthesis, characterization and performance evaluation

2.1 Material synthesis

2.1.1 Carbon materials synthesis

Hierarchical carbon foam structure from waste fig fruit

The waste fig-fruits were firstly separated into different desired parts and pre-thermal treated at 250 °C in air for 2 h in order to remove the water and moisture. The as-treated samples were grinded into power followed by impregnation with an aqueous solution of KOH to obtain samples with different KOH content. After dried in the oven at 130 °C, the mixture was further annealed in argon flow (100 $mL \cdot min^{-1}$) at different temperature, *i.e.* 700 and 900 °C for 2 h. The as-synthesized samples were washed with diluted hydrochloric acid (HCl, 6M) followed by deionized water until neutral pH was reached. The final products were totally dried in the oven at 110°C overnight before further characterization and electrochemical evaluation tests. These obtained samples were referred to as $^{XAct.}$C-Fig$_Y$ 700 °C and $^{XAct.}$C-Fig$_Y$ 900 °C, respectively (X is the KOH/Carbon weight ratio and Y is the corresponding used part of the fig fruit, *i.e.* inner part, peel and the whole fruit) [1-3]. The synthesis process is illustrated in **Fig. 2-1**.

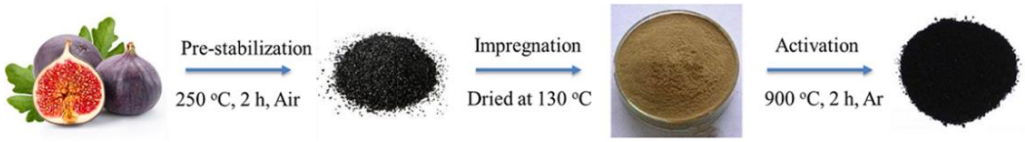

Fig. 2-1. Schematic of synthesis procedures of hierarchical carbon structure from waste fig fruit.

Graphene-like nanosheet carbon structure from sucrose

Sucrose ($C_{12}H_{22}O_{11}$) and table salt (NaCl) were purchased from local foodstuff commercial providers and used as received without any further purification/treatment. All aqueous solutions and material washings were prepared/performed using ultrapure Milli-Q water. Unless otherwise stated, all other chemicals, solvents and gases were purchased from commercial suppliers and used as received without further purification.

The synthetic procedure of graphene-like nanosheet structure starting from the mixture of sucrose/salt with modified chemical activation is outlined in **Fig. 2-2**. Physical mixtures of the two raw components (sucrose-to-salt, $StS_{x/y}$, at variable x/y composition = 1/1, 1/0, 1/2, 1/5, 2/1 and 5/1 wt./wt.) are finely grinded together in a pestle and mortar before undergoing a first thermal heating in air at 150 °C where sugar

polycondensation starts. Afterwards, the reddish-brown composite was crushed in a fine powder and impregnated with a concentrated KOH solution (~15 M) prepared by dissolving an amount of the inorganic base equal to that of the starting sugar/salt mixture (wt./wt.) in water. The oven dried mixture was calcinated at 800 °C for 1 h under Ar flow (100 mL·min^{-1}). The as-obtained composites are thoroughly washed with deionized water till neutrality of the discharged aqueous phases [4-6]. The as-prepared C-samples were then dried at 110 °C overnight before following use.

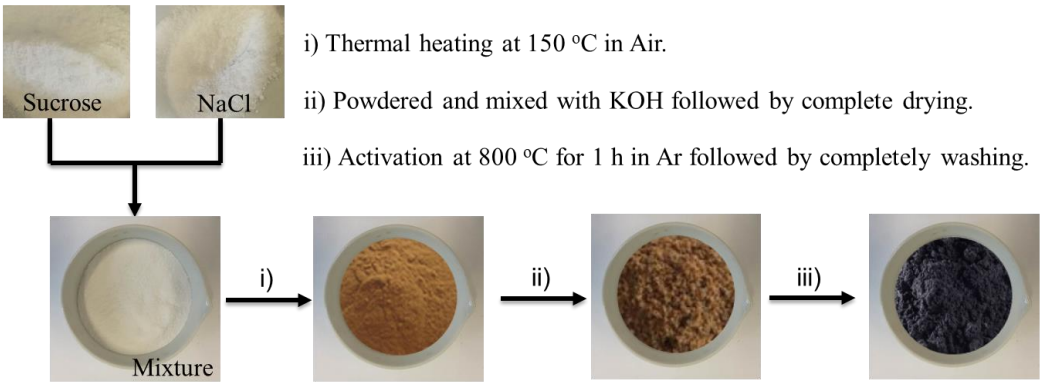

Fig. 2-2. Schematic of synthesis procedures of graphene-like nanocarbon sheets structure from sucrose.

2.1.2 Ni-based methanation catalysts preparation

Macroscopic carbon felt supported nickel catalyst (Ni/OCF)

Commercial soft polyacrylonitrile (PAN)-based carbon felt (CF) was purchased from Carbone Lorraine Ltd. [RVC 4002 Carbon felt (d = 100 kg·m^{-3}; 96% carbon content; Specific Surface Area (SSA): 2.0 ± 1 m^2·g^{-1}] in the form of a black carpet with a thickness of 12 mm. It can be easily adapted into various macroscopic shapes including cylinders, disks or others as a function of its downstream application (as shown in **Fig. 2-3**). The as-received CF sample was cut into disks of external diameter of 24 mm before being oxidized upon treatment with gaseous nitric acid (68 wt.% HNO_3) [7-9]. In a typical oxidation procedure, CF disk was located inside a tubular quartz reactor heated to 250 °C by an external electrical furnace. Nitric acid vapors obtained by heating concentrated nitric acid (68 wt.% HNO_3) at 125 °C were then allowed to pass through the tubular reactor for 4 h. Afterwards, the oxidized carbon felt (OCF) was thoroughly washed with distilled water and dried in an oven at 110 °C to constant weight prior any use.

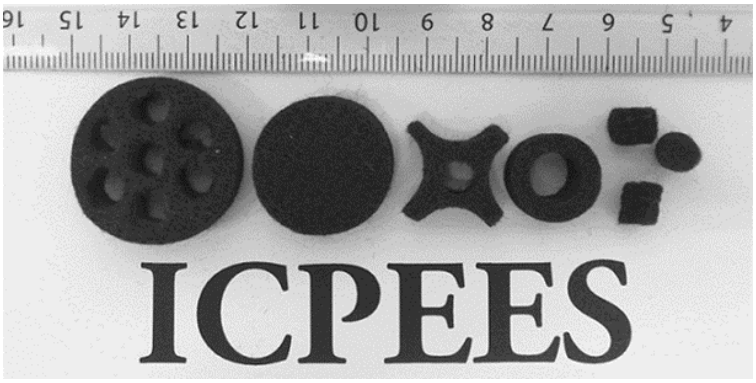

Fig. 2-3. Carbon felt with different macroscopic shapes.

Nickel NPs were deposited on OCF by incipient wetness impregnation approach, using an aqueous solution of nickel nitrate [$Ni(NO_3)_2 \cdot 6H_2O$] as to get a theoretical metal loading close to 10 wt.%. The oven-dried sample was calcined in air at 300 °C for 1 h to convert the nickel nitrate into its oxide counterpart. Afterwards, NiO_X/OCF underwent an in-situ reduction step at 350 °C for 1 h under H_2 (100 $mL \cdot min^{-1}$) [9, 10].

Powder alumina supported nickel catalyst (Ni/Al_2O_3)

Nickel-based catalysts were prepared by incipient wetness impregnation method. Typically, γ-Al_2O_3 (Ketjen CK-300B, Akzo Nobel) in the form of extruded trilobs (~ 1 mm ~ 4 mm) was finely crushed and a fraction between 40-80 µm was retained for the catalyst preparation. An aqueous solution with desired amount of nickel nitrate precursor ($Ni(NO_3)_2 \cdot 6H_2O$) was deposited onto the Al_2O_3 powder. The oven-dried catalyst precursor was then calcinated in air at 350 ºC for 2 h to convert the nickel salt into the corresponding oxide. According to the impregnation technique, the nickel loading in the final composites was varied between 10 to 40 wt.%. and relative samples were quoted as follows: *x*Ni/Al_2O_3 (x = 10, 20, 30, 40 with x stands for the Ni wt.%). All oxide precursors were then reduced just before running the catalytic tests.

2.2 Material characterization

2.2.1 Textural properties determination

The liquid N_2 adsorption-desorption was conducted for determining the textural properties of the samples on a Micromeritics sorptometer (Micromeritics, Norcross, GA, USA). The samples were generally degassed under vacuum for 6 h at 250 °C to

remove the moisture. The adsorption-desorption measurement was carried out using liquid N_2 as adsorbent at -196 ºC. The specific surface areas (SSA) were calculated from N_2 physisorption isotherms by Brunauer-Emmett-Teller (BET) method and the pore size distribution (PSD) was calculated from the desorption branch of the isotherm using Barrett-Joyner-Halenda (BJH) approach.

2.2.2 Temperature programmed characterization

The hydrogen temperature programmed reduction (H_2-TPR) process for the catalyst was performed on a chemisorption analyzer (Micromeritics, AutoChem II, USA) coupled with a thermal conductivity detector (TCD) for analyzing the H_2 uptake during the reduction process. Typically, 50 mg sample was loaded in one quartz U tube, and the system was increased to 100 ºC and kept at this temperature for 30 min until the baseline was stable, then the reduction gas of 10% H_2/Ar with a total gas flow rate of 30 mL·min^{-1} was introduced into the U tube passing through the catalyst bed. The temperature of system was increased from 100 ºC to 800 ºC with a heating rate of 5 ºC·min^{-1} and the H_2 uptake amount during the reduction was directly analyzed on-line.

The temperature programmed oxidation (TPO) measurement of the catalyst was conducted on the same chemisorption analyzer coupled with a mass spectrometer (Pfeiffer-Balzer Omnistar). 30 mg sample was loaded in one quartz U tube, and the system was increased to 50 ºC under He and kept at this temperature for 60 min, then the oxidation gas with 20 v% O_2/He with a total gas flow rate of 20 mL·min^{-1} was introduced into the U tube passing through the catalyst bed until the baseline was stable. The system temperature was increased from 100 ºC to 800 ºC with a heating rate of 5 ºC·min^{-1}, the resulting gases were analyzed on-line by MS. The m/z signal of 44 (CO_2) was monitored with a time interval of 0.1 s.

The Thermal gravimetric analysis (TGA) analysis was run in the 50 - 800 °C temperature range (heating rate of 5 °C·min^{-1}) using a TGA Q5000 instrument operating under an air flow with N_2 working as the balance gas.

2.2.3 Surface morphology and property investigation

The scanning electron microscopy (SEM) was carried out on a Zeiss 2600F with a resolution of 5 nm. The sample was deposited onto a double face graphite tape in order to avoid charging effect during the analysis.

The transmission electron microscopy (TEM) analysis was carried out on a JEOL 2100F working at 200 kV accelerated voltage, equipped with a probe corrector for spherical aberrations, and a point-to-point resolution of 0.2 nm. The sample was dispersed in ethanol assisted by ultrasonication process for 5 min and a drop of the solution was deposited on a copper covered with a holey carbon membrane for observation.

The Raman analysis was carried out using a LabRAM ARAMIS confocal microscope spectrometer equipped with CCD detector. Spectra were recorded over the range of 200 - 3200 cm^{-1} using the 532 nm/100 mW emission of a YAG laser source with laser quantum MPC600 PSU to excite the samples.

The power X-ray diffraction (XRD) *measurements* were carried out on a Bruker D-8 Advance diffractometer equipped with a Vantec detector (Cu Kα radiation) working at 40 kV and 40 mA. The powdered sample was packed onto a glass slide and analyzed using a continuous mode with a 2θ scanning range from 10° to 90°.

2.3 Performance evaluation

2.3.1 Electrochemical performance test

Fabricate of carbon electrode (working electrode)

Certain amount of carbon powder was ultrasonically dispersed in *i*-propanol to obtain 2 $mg \cdot mL^{-1}$ slurry. 0.5 vol. % of 5% Nafion® solution was added into slurry as a binder. 100 µL of the slurry was pipetted on the top surface of glassy carbon rod (d = 5 mm, HTW Hochtemperatur-Werkstoffe GmbH, Germany) and dried in air at 60 °C, as illustrated in **Fig. 2-4**. Glassy carbon with the deposit of 0.2 mg of carbon sample was used as a working electrode in a three-electrode cell configuration [3, 6].

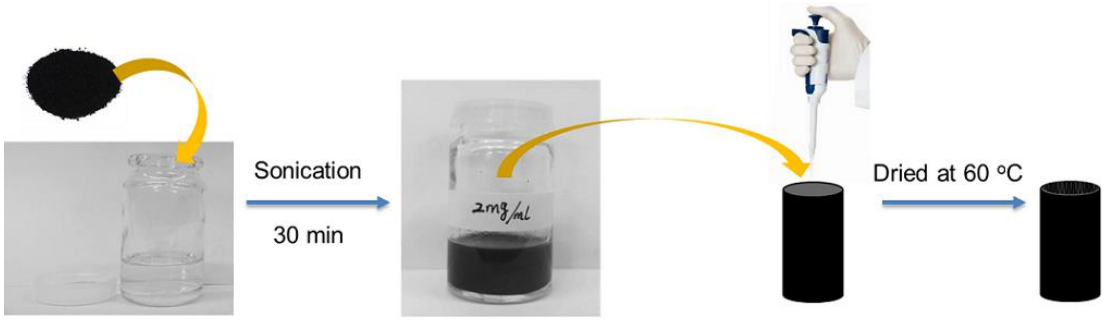

Fig. 2-4. Illustration of fabricating the working electrode.

Supercapacitor performance test

All electrochemical measurements were performed in 0.5 M H_2SO_4 aqueous solution using a three-electrode glass cell with separate electrode compartments (as shown in **Fig. 2-5**) [3, 6]. A high surface area Pt wire was used as a counter electrode (CE) and mercury sulfate electrode (MSE, Schott Instruments) was used as a reference electrode (RE). For the sake of comparison with other data from the literature, all potentials reported in the thesis are conventionally referred to the reversible hydrogen electrode (0.00 V RHE = 0.680 V MSE). The acidic electrolyte was purged with a N_2 flow for at least 20 min before running each experiment. In addition, the N_2 flow was constantly maintained throughout all measurements. Potentiostat Bio-Logic SP300 (Grenoble, France) was used for all electrochemical measurements. Cyclic voltammetry (CV), galvanostatic cycling with potential limiting (GCPL) and electrochemical impedance spectroscopy (EIS) were recorded.

Fig. 2-5. Three-electrode glass cell system.

By integration of the CV curve at a scan rate of 20 $mV \cdot s^{-1}$, the specific capacitance (C, $F \cdot g^{-1}$) can be initially calculated using the following equation [11, 12]:

$$C = \frac{1}{mv(V_b - V_a)} \int_{V_a}^{V_b} IdV \qquad \text{Eq. (16)}$$

where C is the specific capacitance ($F \cdot g^{-1}$); m is the mass of the material loaded on the working electrode (g); v is the scan rate ($V \cdot s^{-1}$); I is the discharge current (A); V_a and V_b are the low and high potential limit of the cyclic voltammetry tests.

By using the discharge portion of the charge-discharge (CD) curves during the GCPL test, the specific capacitance values can also be calculated through the following formula [12-14]:

$$C = \frac{I\Delta t}{m\Delta V} \qquad \text{Eq. (17)}$$

Here, I is the constant discharge current (A); Δt is the discharge time (s); ΔV is the working potential window of the electrode.

The energy and power of the carbon materials can be measured during the galvanostatic cycling, and calculated according to the following equations [11, 15]:

$$\mathrm{E} = \mathrm{I} \int V(t)dt \qquad \text{Eq. (18)}$$

$$\mathrm{P} = \frac{E}{\Delta t} \qquad \text{Eq. (19)}$$

2.3.2 Catalytic methanation performance evaluation

A fixed-bed quartz reactor with a continuous flow was used to evaluate the CO_2 methanation activity at atmospheric pressure. Typically, the catalyst precursor was first in-situ reduced at 350 °C in pure H_2 (100 $mL \cdot min^{-1}$) for 1h prior the reaction, while for Ni/Al_2O_3 catalyst, the catalyst was reduced in an external electric furnace at 350 °C in pure H_2 (100 $mL \cdot min^{-1}$) for 3 h with a heating rate of 5 $^{o}C \cdot min^{-1}$, then the reduced catalyst was fast moved inside the quartz reactor for the reaction test. For conventional thermal heating process, the quartz tube reactor containing the reduced catalyst was housed inside an electric furnace and the temperature was detected with a thermocouple. For inductive heating process, the reduced catalyst was placed in the centre of the reactor and the reaction temperature was controlled by an advanced induction heating system (EASYHEAT LI 3542 with a power factor of 0.85) equipped with a laser to monitor the catalyst bed temperature, no external susceptor was used during the test process. A mixture gas with desired H_2/CO_2 ratio (v./v.) was continuously passed

through the catalyst bed providing an approximate gas hurly space velocity (GHSV). Gases at the reactor outlet are passed through a trap filled with silicon carbide pellets where water are further condensed before reaching the gas chromatograph, then the effluent gas from the reactor was analysed on-line by a CP-3800 gas chromatograph (GC) equipped with a thermal conductivity detector (TCD) and flame ionization detector (FID) detectors (fitted with a packed CP-Carbobond and DB-1 column). All exit lines were maintained at 110 °C by heating tapes to avoid condensation of water remained in the feed. The CO_2 conversion (X_{CO2}) and CH_4 selectivity (S_{CH4}) were calculated according to the following equations:

CO_2 conversion:

$$X_{CO2}\,(\%) = \frac{F_{CO2,in} - F_{CO2,out}}{F_{CO2,in}} \times 100 \qquad \text{Eq. (20)}$$

CH_4 selectivity:

$$S_{CH4}(\%) = \frac{F_{CH4,out}}{F_{CH4,out} + F_{CO,out}} \times 100 \qquad \text{Eq. (21)}$$

Where $F_{i(in/out)}$ ($mL \cdot min^{-1}$) is the flow rate of each corresponding component in the feed or effluent.

Reference

[1] Q. Liang, L. Ye, Z. H. Huang, Q. Xu, Y. Bai, F. Kang, Q. H. Yang. *Nanoscale*, 2014, 6(22): 13831-13837.

[2] A. Elmouwahidi, Z. Zapata-Benabithe, F. Carrasco-Marín, C. Moreno-Castilla. *Bioresource Technol.*, 2012, 111: 185-190.

[3] H. Ba, W. Wang, S. Pronkin, T. Romero, W. Baaziz, L. Nguyen-Dinh, W. Chu, O. Ersen, C. Pham-Huu. *Adv. Sustainable Syst.*, 2018, 2(2): 1700123.

[4] R. Shi, C. Han, H. Li, L. Xu, T. Zhang, J. Li, Z. Lin, C. P. Wong, F. Kang, B. Li. *J. Mater. Chem. A,* 2018, 6(35): 17057-17066.

[5] L. Chen, Z. Wang, C. He, N. Zhao, C. Shi, E. Liu, J. Li. *ACS Appl. Mater. Interfaces,* 2013, 5(19): 9537-9545.

[6] H. Ba, W. Wang, G. Tuci, S. Pronkin, C. Weinberg, L. Nguyen-Dinh, G. Giambastiani, C. Pham-Huu. *Mater. Today Energy,* 2018, 10: 118-125.

[7] Z. Xu, C. Duong-Viet, H. Ba, B. Li, T. Truong-Huu, L. Nguyen-Dinh, C. Pham-Huu. *Catalysts*, 2018, 8(4), 145.

[8] C. Duong-Viet, Y. Liu, H. Ba, L. Truong-Phuoc, W. Baaziz, L. Nguyen-Dinh, J. M. Nhut, C. Pham-Huu. *Appl. Catal. B: Environ.*, 2016, 191: 29-41.

[9] W. Wang, C. Duong-Viet, Z. Xu, H. Ba, G. Tuci, G. Giambastiani, Y. Liu, T. Truong-Huu, J. M. Nhut, C. Pham-Huu. *Catal. Today*, 2019, in press. https://doi.org/10.1016/j.cattod.2019.02.050.

[10] P. Azadi, R. Farnood, E. Meier. *J. Phys. Chem. A*, 2009, 114(11): 3962-3968.

[11] Y. Shao, M. F. El-Kady, J. Sun, Y. Li, Q. Zhang, M. Zhu, H. Wang, B. Dunn, R. B. Kaner. *Chem. Rev.*, 2018, 118(18): 9233-9280.

[12] X. Peng, H. Cao, Z. Qin, C. Zheng, M. Zhao, P. Liu, B. Xu, X. Zhou, Z. Liu, J. Guo. *Electrochim. Acta*, 2019, 305: 56-63.

[13] N. P. Wickramaratne, J. Xu, M. Wang, L. Zhu, L. Dai, M. Jaroniec. *Chem. Mater.*, 2014, 26(9): 2820-2828.

[14] X. Liu, L. Zhou, Y. Zhao, L. Bian, X. Feng, Q. Pu. *ACS Appl. Mater. Interfaces*, 2013, 5(20): 10280-10287.

[15] Y. Wang, Y. Song, Y. Xia. *Chem. Soc. Rev.*, 2016, 45(21): 5925-5950.

Chapter 3

Biomass-derived carbon structures for high performance supercapacitors

Chapter 3.1

Bio-sourced foam-like activated carbon materials as high performance supercapacitor

Abstract

Bio-inspired and cost-effective strategy for the synthesis of highly porous carbon foam structure originating from waste fig fruit raw materials using KOH chemical activation has been described. The as-synthesized porous carbon sample exhibits a specific surface area more than 2000 $m^2 \cdot g^{-1}$, along with relatively high porosity constructed by interconnected micro-, meso- and macro-pores. Such sample ultimately displays superior specific capacitance of 340 $F \cdot g^{-1}$ and 217 $F \cdot g^{-1}$ at a current density of 0.5 $A \cdot g^{-1}$ and 20 $A \cdot g^{-1}$ in aqueous electrolyte respectively. In addition, the sample also exhibits an extremely high stability during long term cycling tests with more than 99% capacitance retention after 10,000 cycles.

Keywords

Electrochemical energy storage; Supercapacitors; Bio-inspired structured materials; Hierarchical carbon materials; High energy density.

This chapter is based on the following publication:

H. Ba, W. Wang, S. Pronkin, T. Romero, W. Baaziz, L. Nguyen-Dinh, W. Chu, O. Ersen, C. Pham-Huu. *Adv. Sustainable Syst.*, 2018, 2(2): 1700123.

3.1.1 Introduction

The climate change induced by the Green House Gas (GHG) urges the different industrialized countries to move towards the development of renewable energy in order to reduce the emission amount of the GHG in atmosphere [1-4]. The renewable energy (RE) development is also pushing ahead since the Fukushima accident where several countries worldwide have decided to reduce the contribution of their nuclear energy supply by renewable ones. The development of renewable energy goes along with the ability to produce high performance systems for electrical energy storage (EES) which display high reversibility along with high energy and high-power output. In fact, RE produces electricity which cannot be stored as such and thus needs to be converted into other forms of energy which can be easily reused when needed [5-9].

Among the different systems for EES, electrochemical supercapacitors (SCs), which store energy by adsorption of electrolyte ions on the porous electrode surface, are considered to be a viable system [10, 11]. The SCs displays relatively high power density, rapid charging/discharging, long life time along with low maintenance and operation cost which renders them as interesting candidates in the fields of energy storage from renewable energy systems compared to batteries [12-15]. The main concerns are the relatively low energy density of commercialized SCs, *i.e.* 5 $Wh \cdot kg^{-1}$ which is far lower than that of batteries, *i.e.* lead acid batteries (40 $Wh \cdot kg^{-1}$) [16-18]. It is thus of high interest to develop new porous systems with high accessibility and high energy density along with long-term stability for new generation of SCs regarding the growing demand of energy storage due to the extensive development of renewable energy. Within the SCs the capacitance is directly dependent on the electrode SSA and, as a consequence the most developed system is based on activated carbon which possesses high specific surface area [19]. Recent work has shown that the specific capacitance is not only influenced by the electrode SSA but also by other factors such as the accessibility and the wettability of the support porosity [20]. Gao et al. [21] has shown that the combination of hierarchical porous carbon and highly efficient ionic liquid electrolyte allows one to obtain high performance SCs. It is generally accepted that carbon-based composites with hierarchical pores and high accessibility will significantly contribute to the development of advanced SCs which can fulfil all the requirements described above. Zhang et al. [22] have reported the use of porous 2D-layered carbon-metal oxide composite for generating supercapacitor with superior rate

performance thanks to the high accessibility of the composite. Research groups have also recently focused attention on the development of layered transition metal carbides and nitrides as high-performance solid-state supercapacitors [23-25]. Such materials display high capacitance and energy density along with an extremely high stability as a function of cycling test.

Carbon-based supports with hierarchical structure and medium to high SSA are also attracting a large field of investigation since the last decade. Carbon nanomaterials, *i.e.* carbon nanotubes/nanofibers and graphene, display relatively high specific surface area as well as high electrical conductivity which render them potential candidates for SCs application. However, the difficulty to produce large quantity with low cost prevents them for large development. Recent review by Wang and co-workers has highlighted the development of biomass-derived carbon materials with different porous structures as electrodes for electrochemical energy storage [26]. These carbon-based materials can be efficiently synthesized from different biomass sources through appropriate thermal treatment and subsequently used as support for pseudo-supercapacitors [27-34].

Potassium hydroxide (KOH) and potassium carbonate (K_2CO_3) are the most widely used activating agents to produce activated carbon with high surface area and large porosity [35, 36]. Different lignocellulosic biomass materials have been prepared with specific surface area (SSA) ranged from 700 to 1200 $m^2 \cdot g^{-1}$ in the above-mentioned reports. Graphene-based composites with high SSA have been synthesized by Ruoff and co-workers and graphene-like structure from biomass reported by Shi et al. for use as SC in different electrolyte medias [37, 38]. The graphene-based material was thermally treated in the presence of KOH which produce microporous holey carbon with extremely high specific surface area, *i.e.* > 3000 $m^2 \cdot g^{-1}$. The as-synthesized materials display high capacitance along with high current and power density close to that obtained on lead batteries along with high capacitance retention up to thousands of cycles. However, the re-stacking of graphene upon drying due to the van der Waals forces could be an issue for the large-scale development of such system. Wei et al. [39] have synthesized 3D interconnected porous nitrogen-doped carbon aerogels with high SSA, also through KOH activation process, for high-rate supercapacitors. The system displays an energy density of 23 $Wh \cdot kg^{-1}$ at power density of 263 $W \cdot kg^{-1}$ along with high capacitance retention of 91% over 10,000 cycles. Similar results have also been reported by Song et al. [40] on 3D nitrogen-doped carbonaceous nanofibers aerogels

with a SSA of 1324 $m^2 \cdot g^{-1}$, large pore volume (0.66 $cm^3 \cdot g^{-1}$) and high degree of doping which display a specific capacitance of 250 $F \cdot g^{-1}$ at 1 $A \cdot g^{-1}$ and retains high value of 138 $F \cdot g^{-1}$ at 10 $A \cdot g^{-1}$. Hierarchical silicon carbide, pure or decorated with oxygenated functional groups, also displays extremely high supercapacitance, *i.e.* 253 $F \cdot g^{-1}$ for pure SiC and 301 $F \cdot g^{-1}$ for the same doped with oxygenated functional groups [41, 42].

The aim of the present article is to report the synthesis of 3D carbon foam structure with high specific surface area, > 2000 $m^2 \cdot g^{-1}$, derived from waste fig fruit by chemical activation in the presence of KOH for supercapacitors application. The material displays hierarchical porous structure with high porosity interconnected by thin carbon sheet structure, which could significantly improve the overall electronic conductivity as well as a high ion diffusion rate especially at high charging/discharging level. The synthesized materials are completely characterized in order to get full insight about their structure properties. This allow one to make a structure-performance correlation, which will facilitate the design of high-performance electrode. The as-synthesized composite displays superior specific capacitance along with an extremely high stability during long term charge/discharge cycling. Compared with other synthetic nanostructured carbon materials, such as nanotubes, nanofibers and graphene-based materials, such bio-massed derived carbon foam material has an advantage of lower cost and more facile scale-up while demonstrating similar if not superior electrochemical performance [43, 44].

3.1.2 Results and discussion

The microstructures of the carbon materials derived from fig-fruit after annealing at different temperatures are presented in **Fig. 1**. Low magnification SEM micrographs evidence the hierarchical 3D morphology of the annealed carbon materials. The SEM micrographs of the fig-fruit just annealed at 250 °C are also presented for comparison (**Fig. 1a-b**). The dry material displays a smooth surface with low porosity according to the SEM analysis. The materials after annealing at 900 °C without KOH and with different KOH/carbon ratio display a significant change in terms of microstructure as shown by the SEM analysis (**Fig. S1-S3**).

Thermal treatment in the presence of KOH leads to the formation of hierarchical foam carbon material with interconnected and open pores (**Fig. 1c-f**). It is worthy to note that thermal annealing at 900 °C induces the formation of large pores as evidenced

by the SEM results (Fig. 1e-f) compared to that obtained at lower annealing temperature, *i.e.* 700 °C (Fig. 1c-d). Meanwhile, the high annealing temperature is also at the origin of the formation of a large amount of micro- and small mesopores inside the sample matrix as shown by the textural property analysis below. High resolution SEM analysis of the carbon structure derived from the pyrolysis of the inner part of the fruit at 900 °C is also presented in **Fig. 1j** and **k**. According to the SEM results, we can see clearly that the sample is extremely porous with micro- and mesopores connecting from each other through a network of macropores. The sheet-like morphology with an extremely thin dimension of the sample also significantly contributes to the accessibility of the sample surface during operation, leading to short ion diffusion path with improved charge/discharge behavior. The hierarchical and interconnected nanostructure in the synthesized sample is of high interest for ion diffusion during the charge/discharge process along with improved electronic conductivity.

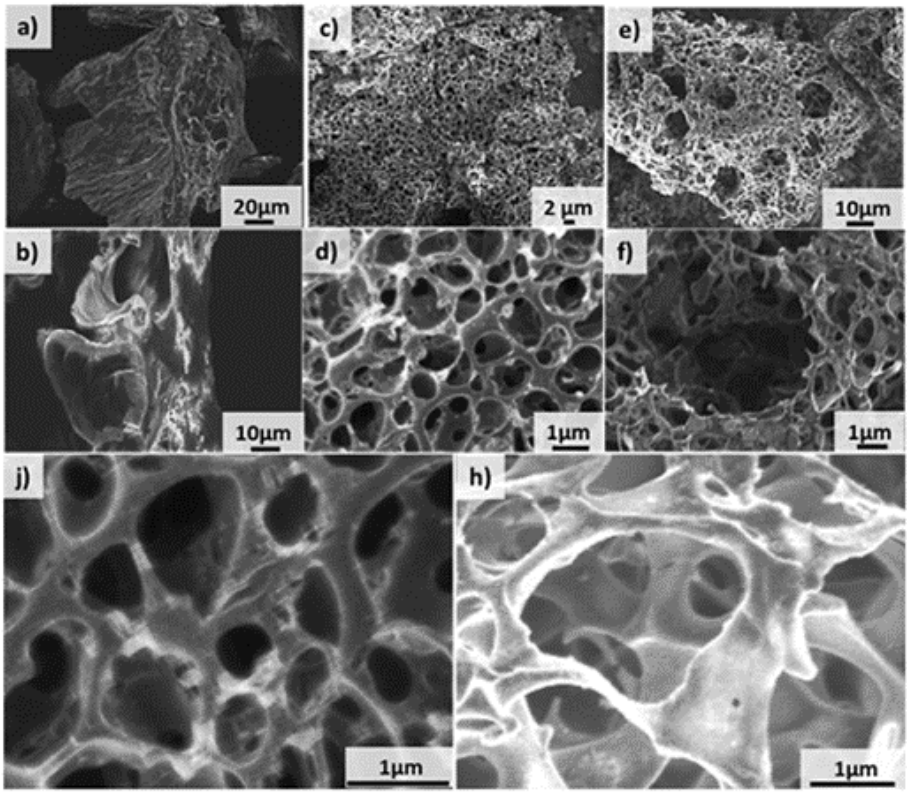

Fig. 1. SEM micrographs of the hierarchical carbon materials derived from waste fig fruit at various temperatures. (a, b) Inner part after stabilization at 250 °C in air. (c, d) and (e, f) Inner part after chemical activation at 700 °C and 900 °C respectively. (j, k) High resolution SEM micrographs showing the interconnected porous foam-like structure of the inner fruit after chemical activation at 900 °C.

The SEM micrographs of the different regions of the fruit, *i.e.* peel and all part of the fig, are also presented in Fig. S2, which confirms the large difference in term of microstructure between the samples. The resulted activated carbon synthesized from the inner part of the fruit displays hierarchical porous and well-connected structure (Fig. 1j-k) while the peel and the total part of the fruit only lead to the formation of dense carbon structure with a low number of pores (Fig. S2a-d). Such difference in terms of porosity could be directly linked to the starting structure of the raw materials and confirms the strong influence of the raw material on the final products.

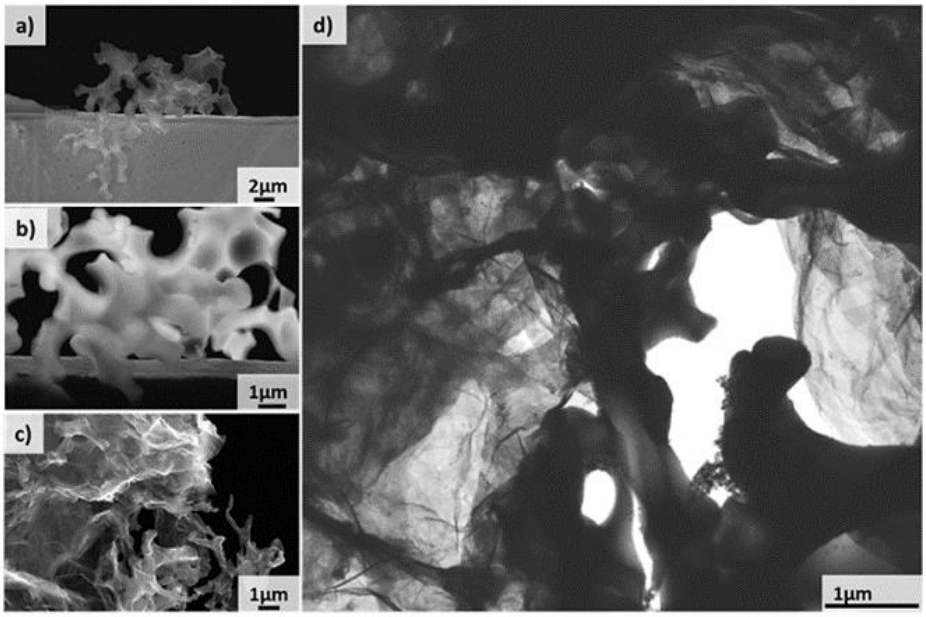

Fig. 2. STEM-SEM micrographs of the synthesized activated carbon recorded from the inner part of the fig confirming the foam-like structure of the sample.

The microstructure of the sample after thermal treatment at 900 °C was also investigated by STEM-SEM mode and the results are shown in **Fig. 2**, and it reveals the highly porous and open cell foam-like structures. The TEM micrographs of the samples annealed at 900 °C with highest specific surface area are presented in **Fig. 3**. The TEM analysis confirms the porous and hierarchical structure of the sample (Fig. 3a-b) in good agreement with the SEM results. Medium resolution TEM micrograph (Fig. 3c-d) indicates the presence of thin and large carbon-sheet structure decorated with random pores with high accessibility. The observed results are similar to those reported by Shi et al. using KOH pyrolysis of carbon raw materials issued from biomass waste [38]. High resolution TEM (HR-TEM) micrographs (Fig. 3d) confirm the thin

morphology of the sample leading to the high accessibility of the surface towards ion diffusion, especially at high charging rate. And it also evidences the presence of large amount of small meso- and micropores, with an average diameter of ca. 3 to 8 nm, inside the graphene sheet. It is expected that the combination of sheet-like structure and hierarchical connected porosity will play a central role on the performance of the electrode for energy storage. Such structure is close to those of the transition metal carbides and nitrides reported by other research groups [23, 24].

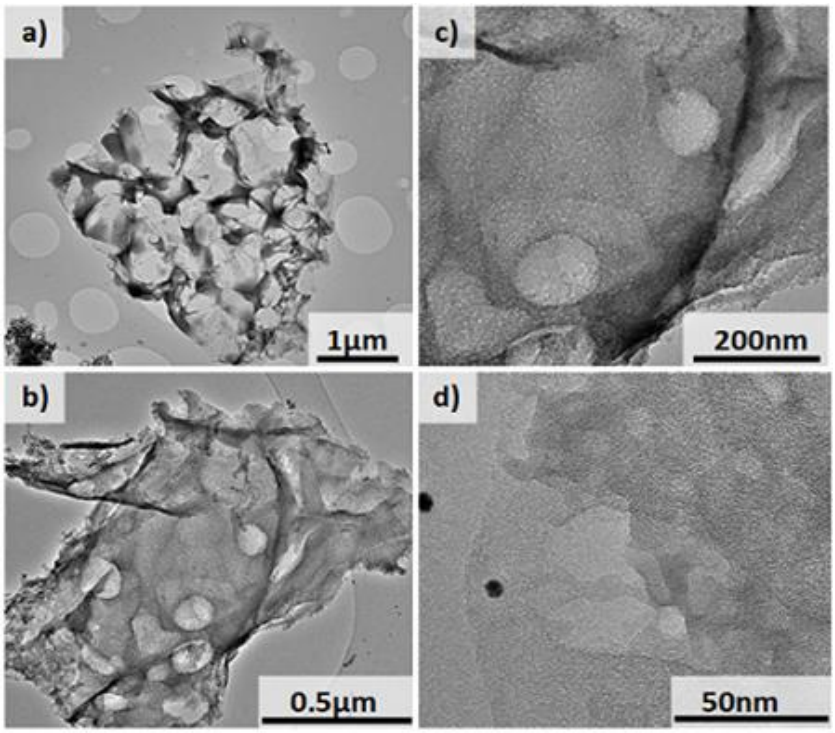

Fig. 3. (a, b) TEM micrographs of the $^{3Act.}$C-Fig$_{IN}$ 900 °C showing the interconnected carbon sheet morphology arranged in the foam structure. (c, d) HR-TEM micrographs showing the carbon sheet structure decorated with micro- and meso-pores.

For a better visualization of the porosity TEM tomography was performed and the results are presented in **Fig. 4** [45, 46]. In Fig. 4a-c the TEM tomography bright-field micrographs with various perspective, obtained by tilting $^{3Act.}$C-Fig$_{IN}$ 900 °C sample with different angles, *i.e.* -64°, 0° and +72°. The TEM-3D slices along the Z axis displayed in Fig. 4. d1-d6 clearly evidence the 3D structure of the sample with a highly-connected between the different porosity. Such connected porosity is expected to play a crucial role in ions diffusion process to the whole surface of the material leading to a high supercapacitance. Various types of porosity can be distinguished, namely micro-,

meso- and macro-pores, with a predominance of micropores structures, highlighted on the image slices recorded from the tilted sample. These physical characteristics are perfectly in agreement with the results obtained from the following analysis and those collected from HR-TEM micrographs (Fig. 3).

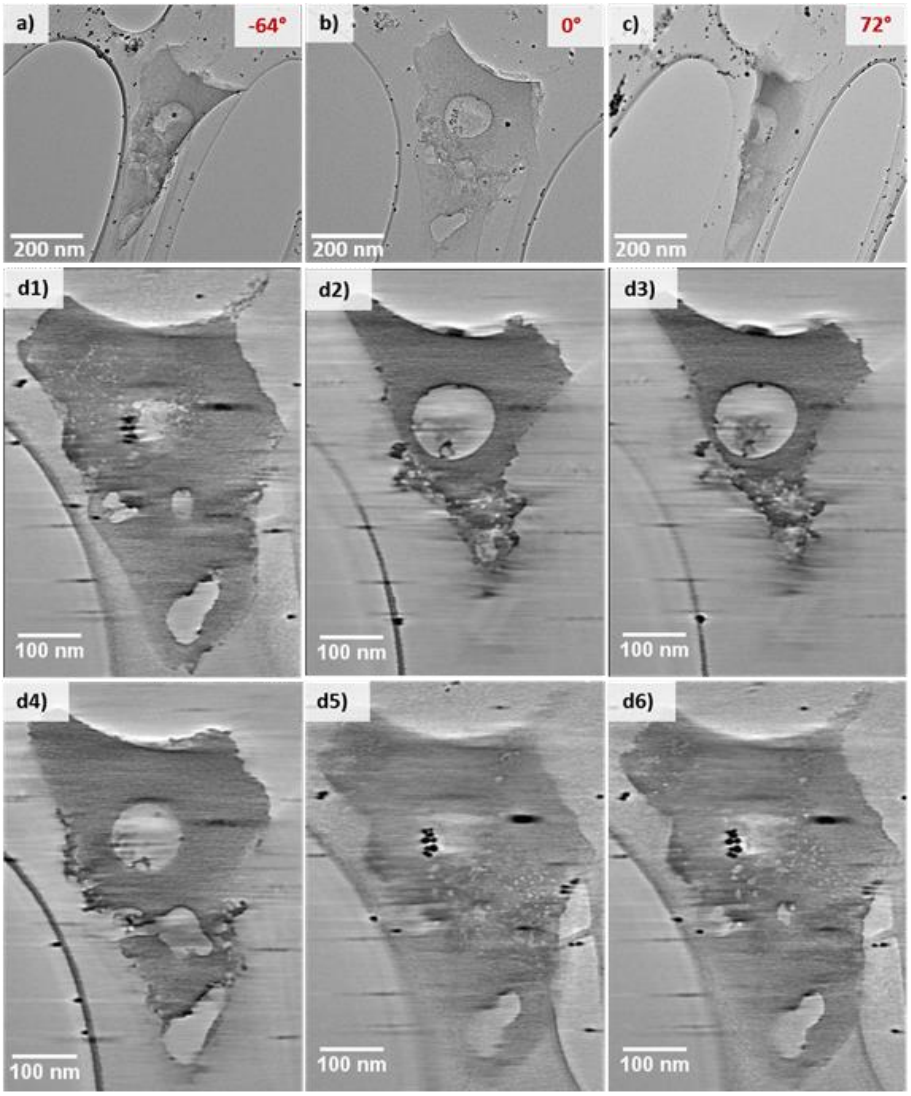

Fig. 4. TEM tomography images (a-c) 3D projection images at various tilting angles, and (d1-d6) slice images reconstructed along the Z axis of the sample annealed at 900 °C. The presence of the different types of porosity is clearly evidenced in d1 to d3 while the interconnected porous structure with different sizes is evidenced in d4 to d6.

The graphitization characteristic and structural behavior of the $^{3Act.}$C-Fig$_{IN}$ carbonized at different temperature were efficiently monitored by Raman spectroscopy, and the corresponding spectra are presented in **Fig. 5a**. The Raman spectrum shows a

typical D-band at 1340 cm^{-1}(sp^3 defects) and G-band at 1580 cm^{-1} (tangential vibration of sp^2 carbon atoms) corresponding respectively to disordered and graphite carbon [47]. A comparison of the intensity ratio of D and G band (I_D/I_G) for all samples allows one to evaluate the graphitization degree as a function of the carbonization temperatures [48]. Increasing the annealing temperature, from 700 to 900 °C, obviously decrease the I_D/I_G ratio from 1.04 to 0.67, which means a significant improvement of the graphitization degree of the sample, and in turn, its electrical conductivity [49, 50].

The XRD patterns of the carbon materials are presented in **Fig. 5b**. The XRD patterns showed a main broad peak centered at 2θ of 21.4° corresponding to the C (002) diffraction of hexagonal graphite [51], while a second peak centered at 2θ of 26.3° was observed on the $^{3Act.}$C-Fig$_{IN}$ pyrolyzed at 900 °C. It means that the crystallinity of the $^{3Act.}$C-Fig$_{IN}$ material increased as a function of thermal treatment, and when the temperature reached 900 °C we may have large graphite-like structure in the products, it is consistence with the Raman measurement [49].

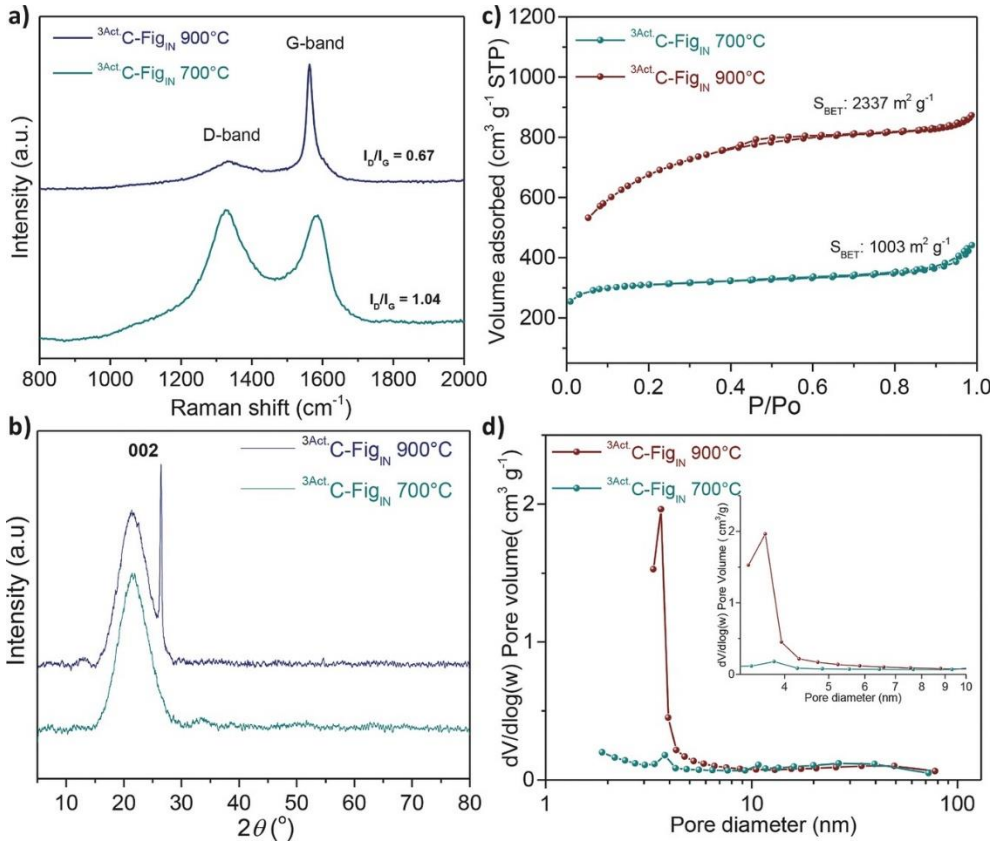

Fig. 5. (a) Raman and (b) XRD results of the hierarchical carbon materials. (c) Adsorption-desorption isotherms and SSA and (d) pore size distribution of the fig-fruit derived carbon materials after pyrolysis in the presence of KOH at various temperatures.

The SSA and pore size distribution of the samples, measured by N_2 adsorption at liquid N_2 temperature, are presented in **Fig. 5c-d**. The N_2 adsorption-desorption isotherms on both samples belong to the type IV isotherm with a plateau running parallel to the P/P_0 axis which are typically for microporous solid. The SSA is significantly modified as a function of the annealing temperature, *i.e.* 1003 $m^2 \cdot g^{-1}$ at 700 °C to 2337 $m^2 \cdot g^{-1}$ at 900 °C. High temperature annealing should allow one to burn out unstable carbon phase with low porosity leading to a significant increase of the sample SSA. The high annealing temperature seems also to improve the reaction between the KOH and the solid to generate a large number of microspores which contribute to the high SSA for the final sample. It is worthy to note that the SSA obtained in this work is ranked among the highest ones, close to the theoretical SSA of graphene [52]. The high SSA of the graphene-KOH sample reported by Ruoff and co-workers could be attributed to the sheet-like structure of the sample which is close to that obtained in the present work [37].

The influence of the precursor (different fig part) on the SSA and pore size distribution of the samples is also presented in **Fig. S4**. According to the results the part of the fruit which yield the highest SSA is the inner part while the peel only yields relatively low SSA (Fig. S4). The annealed material from the entire fruit leads to an intermediate SSA, *i.e.* 1129 $m^2 \cdot g^{-1}$, which confirms the interest of using specific part of the fruit and not a whole raw material. The different physical characteristics of the samples are summarized in **Table 1**. The micropores contribution of the samples is also presented for comparison. According to the results the large increase of the SSA is directly linked with the formation of a higher amount of micro- and small mesopores inside the sample. It is expected that the formation of large pores (2 to 10 µm in diameter) in the sample annealed at 900 °C only hardly impacting the overall SSA of the sample. However, such large pores could play an important role in the diffusion of the liquid electrolyte inside the whole sample matrix and to micropores which is of great interest for rapid charging and discharging cycle for SCs [44]. The two main important parameters are: (i) the small meso- and micropores, *i.e.* ≤ 3 nm, which could be rapidly wetted by the electrolyte ions during charge/discharge process, and (ii) the absence of long micropore channels according to the TEM analysis which are disadvantage for ion diffusion, especially at high charging rate. Thus, hierarchical porous carbon composite with thin sheet-like along with hierarchical structure is of great interest for SCs with simultaneous high energy and power densities for energy storage applications.

Table 1 - Textural properties of carbon derived from pyrolysis fig fruit.

Samples	SSA[a] ($m^2 \cdot g^{-1}$)	$SSA_{\mu\text{-pore}}$ ($m^2 \cdot g^{-1}$)	PV[b] ($cm^3 \cdot g^{-1}$)	$PV_{\mu\text{-pore}}$ ($cm^3 \cdot g^{-1}$)	PD[c] (nm)
$^{3Act.}$ C-Fig_{Peel} 900 °C	358	241	0.394	0.120	6.8
$^{3Act.}$ C-Fig_{All} 900 °C	1129	103	0.744	0.039	3.9
$^{3Act.}$ C-Fig_{IN} 900 °C	2338	2182	1.005	1.114	2.6
C-Fig_{IN} 900 °C	438	365	0.033	0.179	3.1
$^{3Act.}$ C-Fig_{IN} 700 °C	1003	765	0.270	0.374	6.8

[a)] Estimated by the BET equation; [b)] BJH adsorption pore volume (PV) between 1.7nm to 300 nm; [c)] BJH adsorption average pore diameter (PD).

The cyclic voltammetry (CV) curves of the carbon samples reveal typical capacitive behaviors without contribution of bulk redox reactions with the rectangular-like shapes (as shown in **Fig. 6a**). Specific capacitance calculated from initial CV curves (10 cycles) is presented in **Fig. 6b**. The carbon materials derived from the inner part of the fig fruit displays the highest specific capacitance. Such high capacitance could be attributed to the high SSA as well as to the foam-like porosity of the samples which improve the ion diffusion during the charge/discharge process. CV curves measured after 10,000 cycles on the $^{3Act.}$C-Fig_{IN} 700°C and the $^{3Act.}$C-Fig_{IN} 900°C are also presented in **Fig. 6c** and the results confirm a significant increase of the capacitance after cycling tests on both samples. The results also confirm the higher specific capacitance of the $^{3Act.}$C-Fig_{IN} 900°C versus the $^{3Act.}$C-Fig_{IN} 700°C sample. The lower capacitance recorded on the $^{3Act.}$C-Fig_{IN} 700°C can be attributed to the narrow pores which are less accessible for an electrolyte and broader distribution of pore diameters. It agrees with the observations of electron microscopy which indicate a higher open porosity for the sample after pyrolysis at higher temperature (Fig. 3 and 4). After 10,000 galvanostatic cycles Nyquist plots of $^{3Act.}$C-Fig_{IN} 700 °C resemble more that of the sample $^{3Act.}$C-Fig_{IN} 900 °C, allowing one to suggest similar changes of porous structure upon cycling in both samples. The specific capacitance C_m measured by CV curve on the $^{3Act.}$C-Fig_{IN} 900 °C is ca. 234 $F \cdot g^{-1}$ at a scan rate of 20 $mV \cdot s^{-1}$ after 10,000cycles. The shape of CV remains rectangular with detectable weak reversible redox peaks at

ca. 0.55-0.60 V RHE. Appearance of these peaks can be attributed to quinone/hydroquinone surface redox transition and indicates changes in the chemical composition of carbon surface upon cycling [45]. Since surface chemical groups play important role in the wetting of the micropores, these changes may be responsible for improved wetting and opening of micropores observed during galvanostatic cycling.

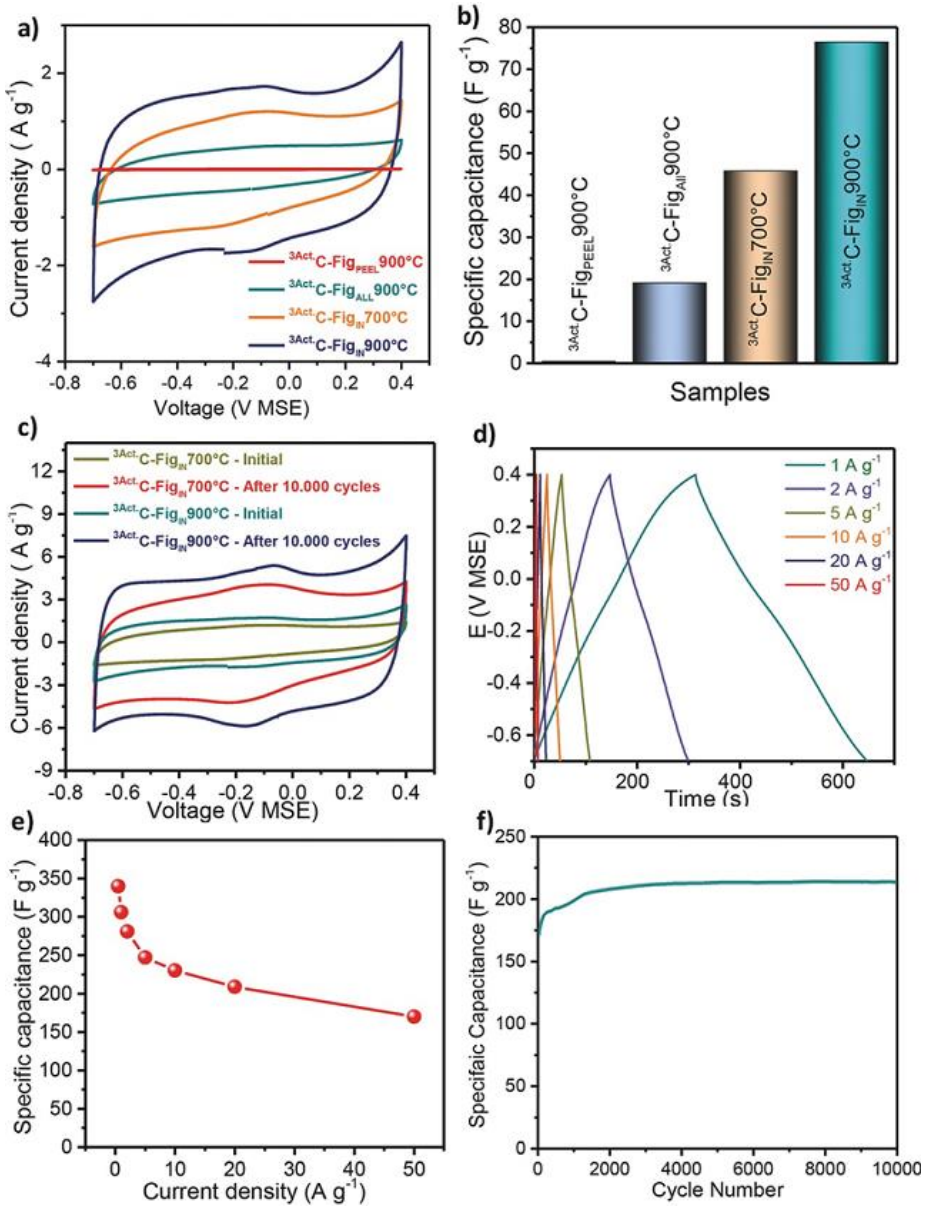

Fig. 6. (a) Typical CV curves (10 cycles) of the carbon samples in 0.5 M H_2SO_4 at a charging rate of 20 $mV \cdot s^{-1}$. (b) Specific capacitance determined from the CV curves. (c) CV curves of the $^{3Act.}C\text{-}Fig_{IN}$ 700 °C and $^{3Act.}C\text{-}Fig_{IN}$ 900 °C recorded initially and after 10,000 cycles. (d) Charge-discharge curves of the $^{3Act.}C\text{-}Fig_{IN}$ 900 °C at different current densities at 25 °C. (e) Specific capacitance of the $^{3Act.}C\text{-}Fig_{IN}$ 900° C at various current densities. (f) Cycling stability at a current density of 20 $A \cdot g^{-1}$.

The charge-discharge curves at varied current density were presented in **Fig. 6d**, and all the collected curves shows nearly linear and symmetrical shape, which demonstrate the capacitor-like behavior and the excellent electrochemical reversibility. The specific capacitance (C_m) measurement as a function of the current density is calculated based on discharge curves and highlighted in **Fig. 6e** and **Table S1**. The collected Cm from the $^{3Act.}$C-Fig$_{IN}$ 900 ºC sample was 340, 306, 281, 247, 230, 217, 170 $F \cdot g^{-1}$ at discharge current densities of 0.5, 1, 2, 5, 10, 20 and 50 $A \cdot g^{-1}$, respectively. Such high capacitance could be attributed to different facts: (i) the combination of a high specific surface area, > 2000 $m^2 \cdot g^{-1}$, and graphene-like nanoplatelet microstructure which provide a high ion diffusion and large effective surface during charge/discharge process, (ii) the hierarchical porosity of the $^{3Act.}$C-Fig$_{IN}$ 900 °C sample consisting with interconnected micro- and mesopores also provide high capacitance and rate performance, and (iii) the high electrical conductivity of the sample. Those obtained results are higher than on different pure or assembled nanostructured carbon-based materials, *i.e.* graphene and carbon nanotubes [53, 54], and also to that reviewed active carbon such as coconut shell, sugar cane bagasse, potato starch, cellulose, rubber wood sawdust, Cherry stone, carbon aerogel, corn grains, and more [19, 55].

In order to evaluate the long-term cycling stability, the samples were then subjected to galvanostatic charging/discharging cycles measurement within the potential limits used for CV measurements with charging current 20 $A \cdot g^{-1}$ up to 10,000 cycles. The evolution of the capacitance with cycle number is shown in **Fig. 6f**. Significant increase in specific capacitance was systematically observed for $^{3Act.}$C-Fig$_{IN}$ 900 °C sample during first few thousands of cycles with plateau after ca. 4,000-5,000 cycles. It is important to highlight that after such induction period the capacitance was stabilized and no degradation of performance was detected during at least 10,000 of charging cycles. The gradual capacitance increases could be attributed to the slow wetting of the electrode micro-porosity by the electrolyte and/or opening of small micropores which were extensively present in the foam-like structure and have been clearly evidenced by TEM (Fig. 3 and 4). Such phenomenon could also be attributed to the slow replacement of micropores filled with gas by the liquid electrolyte as a function of cycling. It is expected that for small pores the gas-liquid exchange becomes slow and longer time is needed for completing the exchange.

Impedance measurements allow deeper insight on the processes of energy storage and structural changes in the carbon electrode during charging. In the absence of bulk

redox reaction, the total impedance of an electrode consists of electrolyte resistance and interfacial capacitance. In Nyquist plots the impedance of an ideal capacitor is represented by straight vertical line indicating phase angle 90º, or constant phase element (CPE) constant a = 1. The impedance of electrochemical capacitors deviates from this shape due to:

(i) Inhomogeneity of electrode surface, resulted in CPE constant slightly lower than 1 [56, 57]. Nyquist plots in this case show a slightly tilted straight line.

(ii) Electrode porosity, resulted in dependence of CPE constant a changing with frequency from 0.5 at low frequencies and approaching 1 at high frequencies [58]. Nyquist plots in this case may show change in the slope in a certain frequency range.

Exact correlation between the impedance of porous electrode and its porosity parameters is yet to be established. However, certain qualitative conclusions can be made by analysis of impedance spectra.

Typical Nyquist plots measured under open circuit conditions are present in **Fig. 7**a. Details of the fitting procedure are explained in **Fig. S5**. Impedance spectra for $^{3Act.}$C-Fig$_{IN}$ 900 °C sample shown gradual change in CPE constant between high and low frequency domains, and constant slope at low frequencies corresponding to a = 0.70. It can be interpreted as an effect of micro-porosity of electrode with relatively narrow pore diameter and shape distribution [59]. After 10,000 galvanostatic cycles the impedance spectrum of $^{3Act.}$C-Fig$_{IN}$ 900 °C changes (Fig. 7a): CPE at low frequencies (below 1 Hz) a = 0.88 and close to 1, while effect of micro-porosity is observed only at high frequencies. This effect observed simultaneously with significant (more than 4-fold) increase in capacitance, as discussed above. This observation supports the assumption made above of porous structure of electrode which becomes more open upon cycling, and more accessible for an electrolyte through gas-liquid exchange.

The energy and power of the carbon sample electrodes were calculated according to the Eq. (18) and Eq. (19). By varying I the energy dependence on the power (*i.e.* Ragone plots) were obtained at different temperature in the range 25-55 ºC, as shown in **Fig. 7b**. We have observed a considerable increase in energy density for the same power as temperature increases up to 55 ºC, which can be related to higher ionic mobility and lower electrolyte resistance. For the sample after pyrolysis at 900 °C an energy density of ca. 26 Wh·kg^{-1} was obtained at a power density of 700 W·kg^{-1} and an energy density of 18 Wh·kg^{-1} was still measured at a power density of 10,000 W·kg^{-1} in an aqueous electrolyte medium. According to the results one can stated that the

hierarchical porous carbon electrode displays an extremely high energy density and power density compared to other carbons reported in the literature (**Fig. 7c**) [60]. We would also like to highlight excellent stability of the carbon samples under study despite relatively wide potential range (1.1 V) applied.

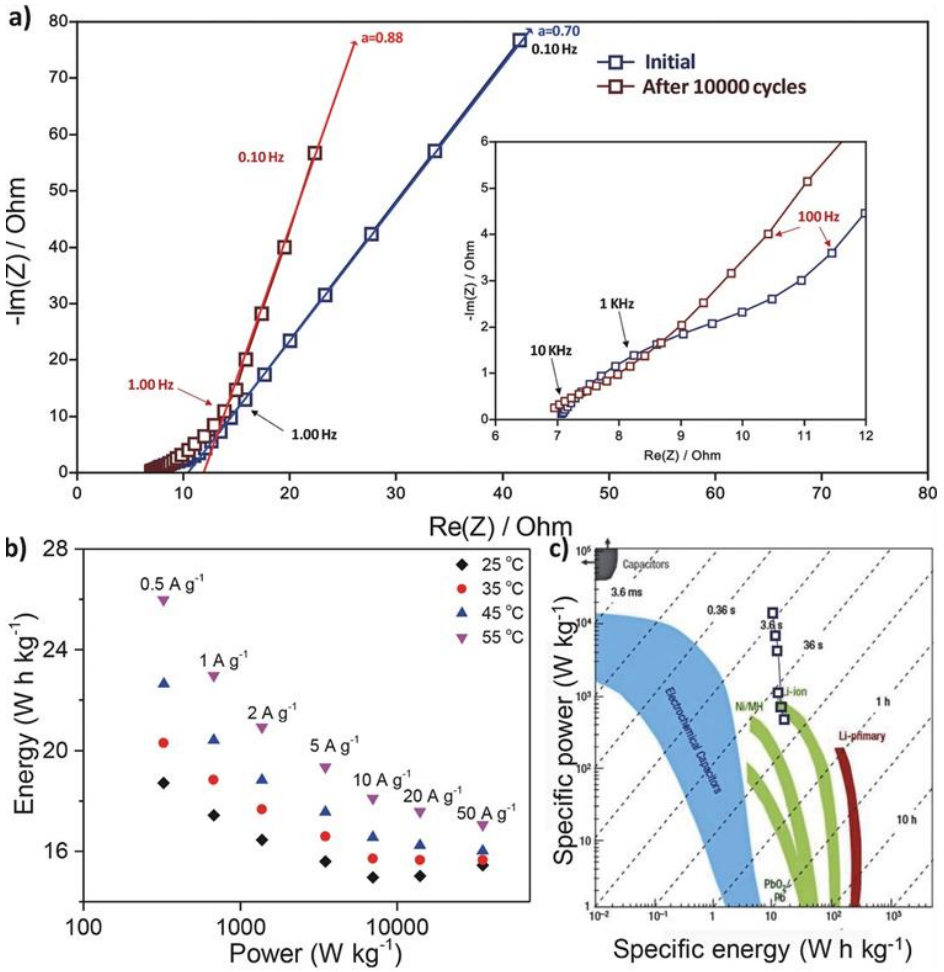

Fig. 7. (a) Impedance spectra of carbon sample measured in 0.5 M H_2SO_4: initial (blue) and after 10,000 galvanostatic charging cycles (red) and an equivalent circuit model. (b) Ragone plots of carbon sample measured at different temperatures and current density. (c) Comparison of the results obtained in the present work with various electrical energy storage devices.

3.1.3 Conclusion

In summary, micro- and mesoporous carbon materials connected through macropores with extremely high specific surface area and hierarchical structure have been synthesized from chemical activation of bio-sourced precursor. The high specific surface area and the 3D-like structure of these carbon-based materials significantly

improve the ions diffusion during the charge and discharge steps leading to promising supercapacitor devices with high energy and power density. The high performance of the material allows one to envision the replacement of batteries by supercapacitors in the field of energy storage with high charge and discharge rates, not limited by electrochemical charge transfer kinetic, and long-life time operating. The bio-sourced raw material, fig fruit and specifically waste ones, is abundant at ton quantities and the synthesis can be done at industrial scale without any modification of the carbonization process and thus, it is expected that the laboratory to market time should be reached within a relatively short period. Work is ongoing to evaluate such material as supercapacitor using organic or ionic liquids electrolytes with higher operating voltage range. The combination of the double-layer capacitors and pseudo-capacitors by doping the sample with oxygenated functional groups or with other oxide-based materials will be also investigated. Finally, such materials with high specific surface area and connected porosity could also be useful as catalyst support with high accessible surface along with defects for anchoring metal nanoparticles.

3.1.4 Experimental section

Carbon materials preparation from waste fig fruit and their characterization please refer to **Chapter 2.1.1** and **Chapter 2.2**. TEM tomography was done on a JEOL 2100 F (FEG) electron microscope operating at a beam voltage of 200 kV, using a 2048 × 2048 pixels Ultrascan cooled CCD array detector, and a high tilt sample holder. The process was controlled by the tomography plug-in of Digital Micrograph, which allows varying systematically the tilt angle step by step, to correct for defocusing, to maintain the object under study within the field of view and to record and store the object projections. In our work the acquisition of the projection series was acquired by tilting the object between -64° and +72° with a tilt increment of 2° in saxton mode, resulting in a total of 85 projections. No apparent irradiation damage was observed on the specimen at the end of the acquisition process (about 40 min). The treatment of tilt series for image processing and reconstruction procedure was performed using the IMOD software from the University of Colorado which uses a weighted-back projection method to compute the volume of the specimen.

Preparation of the working carbon electrode and its electrochemical characterizations: Please refer to **Chapter 2.3.1**.

Reference

[1] R. Wüstenhagen, M. Wolsink, M. J. Bürer. *Energy Policy*, 2007, 35: 2683-2691.

[2] S. Bilgen, K. Kaygusuz, A. Sari. *Energy Sources*, 2004, 26: 1119-1129.

[3] J. A. Turner. *Science*, 1999, 285(5428): 687-689.

[4] I. Dincer. *Renew. Sust. Energy Rev.*, 2000, 4: 157-175.

[5] T. B. Johansson, H. Kelly, A. K. N. Reddy, L. Burnham, R. H. Williams. *Island Press, 2nd Ed.*, 1992, ISBN: 978-155-963138-9.

[6] W. Kempton, J. Tomić. *J. Power Sources*, 2005, 144(1): 280-294.

[7] H. D. Yoo, E. Markevich, G. Salitra, D. Sharon, D. Aurbach. *Mater. Today*, 2014, 17(3), 110-121.

[8] Y. Huang, M. Zhu, Y. Huang, Z. Pei, H. Li, Z. Wang, Q. Xue, C. Zhi. *Adv. Mater.*, 2016, 28(38): 8344-8364.

[9] H. Wei, D. Cui, J. Ma, L. Chu, X. Zhao, H. Song, H. Liu, T. Liu, N. Wang, Z. Guo, *J. Mater. Chem. A*., 2017, 5(5): 1873-1894.

[10] P. Simon, Y. Gogotsi. *Nat. Mater.*, 2008, 7: 320-329.

[11] K. Chen, S. Song, F. Liu, D. Xue. *Chem. Soc. Rev.*, 2015, 44(17): 6230-6257.

[12] A. González, E. Goikolea, J. A. Barrena, R. Mysyk. *Renew. Sust. Energy Rev.*, 2016, 58: 1189-1206.

[13] G. Wang, L. Zhang, J. Zhang. *Chem. Soc. Rev.*, 2012, 41(2): 797-828.

[14] L. L. Zhang, R. Zhou, X. S. Zhao. *J. Mater. Chem.*, 2010, 20(29): 5983-5922.

[15] Y. Zhang, H. Feng, X. Wu, L. Wang, A. Zhang, T. Xia, H. Dong, X. Li, L. Zhang. *Int. J. Hydrogen Energy*, 2009, 34(11): 4889-4899.

[16] A. Burke. *Electrochim. Acta*, 2007, 53(3): 1083-1091.

[17] J. A. Fernández, T. Morishita, M. Toyoda, M. Inagaki, F. Stoeckli, T. A. Centeno. *J. Power Sources*, 2008, 175(1): 675-679.

[18] J. Li, X. Cheng, A. Shashurin, M. Keidar. *Graphene*, 2012, 1: 1-13.

[19] M. Sevilla, R. Mokaya. *Energy Environ. Sci.*, 2014, 7(4): 1250-1280.

[20] X. Wang, H. Zhou, E. Sheridan, J. C. Walmsley, D. Ren, D. Chen. *Energy Environ. Sci.*, 2016, 9: 232-239.

[21] B. Gao, H. Zhou, J. Yang. *J. Mater. Chem. A*, 2017, 5(2): 524-528.

[22] X. Zhang, J. Luo, P. Tang, X. Ye, X. Peng, H. Tang, S.-G. Sun, J. Fransaer. *Nano Energy*, 2017, 31: 311-321.

[23] K. Krishnamoorthy, P. Pazhamalai, S. Sahoo, S.-J. Kim. *J. Mater. Chem. A*, 2017,

5(12): 5726-5736.

[24] C. (John) Zhang, B. Anasori, A. Seral-Ascaso, S.-H. Park, N. McEvoy, A. Shmeliov, G. S. Duesberg, J. N. Coleman, Y. Gogotsi, V. Nicolosi. *Adv. Mater.*, 2017, 29(36): 1702678.

[25] G. K. Veerasubramani, A. Chandrasekhar, S. M. S. P., Y. S. Mok, S. J. Kim. *J. Mater. Chem. A*, 2017, 5(22): 11100-11113.

[26] J. Wang, S. Kaskel. *J. Mater. Chem.*, 2012, 22(45): 23710-23725.

[27] Y. Zhang, Z. Gao, N. Song, X. Li. *Electrochim. Acta*, 2016, 222, 1257-1266.

[28] Z. Gao, C. Bumgardner, N. Song, Y. Zhang, J. Li, X. Li. *Nat. Commun.*, 2016, 7: 11586.

[29] J. Xu, K. Zhou, F. Chen, W. Chen, X. Wei, X.-W. Liu, J. Liu. *ACS Sust. Chem. Eng.*, 2016, 4(3): 666-670.

[30] F. Chen, J. Yang, T. Bai, B. Long, X. Zhou. *Electrochim. Acta*, 2016, 192: 99-109.

[31] Z. Gao, N. Song, Y. Zhang, X. Li. *RSC Adv.*, 2015, 5(20): 15438-15447.

[32] H. Chen, D. Liu, Z. Shen, B. Bao, S. Zhao, L. Wu. *Electrochim. Acta*, 2015, 180: 241-251.

[33] W. Tian, Q. Gao, Y. Tan, K. Yang, L. Zhu, C. Yang, H. Zhang. *J. Mater. Chem. A*, 2015, 3(10): 5656-5664.

[34] J. Li, F. Qin, L. Zhang, K. Zhang, Q. Li, Y. Lai, Z. Zhang, J. Fang. *J. Mater. Chem. A*, 2014, 2(34): 13916-13922.

[35] Y. Deng, Y. Xie, K. Zou, X. Ji. *J. Mater. Chem. A*, 2016, 4(4): 1144-1173.

[36] K. Y. Foo, B. H. Hameed. *Bioresour. Technol.*, 2011, 102(20): 9814-9817.

[37] Y. Zhu, S. Murali, M. D. Stoller, K. J. Ganesh, W. Cai, P. J. Ferreira, A. Pirkle, R. M. Wallace, K. A. Cychosz, M. Thommes, D. Su, E. A. Stach, R.S. Ruoff. *Science*, 2011, 332(6037): 1537-1541.

[38] C. Shi, L. Hu, K. Guo, H. Li, T. Zhai. *Adv. Sust. Syst.*, 2017, 1(1-2): 1600011.

[39] X. Wei, S. Wan, S. Gao. *Nano Energy*, 2016, 28: 206-215.

[40] L. T. Song, Z. Y. Wu, H. W. Liang, F. Zhou, Z. Y. Yu, L. Xu, Z. Pan, S. H. Yu. *Nano Energy*, 2016, 19: 117-127.

[41] M. Kim, I. Oh, J. Kim. *J. Mater. Chem. A*, 2015, 3(7): 3944-3951.

[42] M. Kim, H. Ju, J. Kim. *Phys. Chem. Chem. Phys.*, 2016, 18(4): 3331-3338.

[43] A. González, E. Goikolea, J. A. Barrena, R. Mysyk. *Renew. Sust. Energy Rev.*, 2016, 58: 1189-1206.

[44] L. Wei, G. Yushin. *Nano Energy*, 2012, 1(4): 552-565.

[45] O. Ersen, I. Florea, C. Hirlimann, C. Pham-Huu. *Mater. Today*, 2015, 18(7): 395-408.

[46] I. Florea, O. Ersen, R. Arenal, D. Ihiawakrim, C. Messaoudi, K. Chizari, I. Janowska, C. Pham-Huu. *J. Am. Chem. Soc.*, 2012, 134(23): 9672-9680.

[47] M. S. Dresselhaus, A. Jorio, A. G. S. Filho, R. Saito. *Phil. Trans. R. Soc. A*, 2010, 368: 5355-5377.

[48] A. Cuesta, P. Dhamelincourt, J. Laureyns, A. Martínez-Alonso, J. M. D. Tascón. *Carbon*, 1994, 32(8): 1523-1532.

[49] H. Zhao, Q. Wang, Y. Deng, Q. Shi, Y. Qian, B. Wang, L. Lü, X. Qiu. *RSC Adv.*, 2016, 6(81): 77143-77150.

[50] T. Gruber, T. W. Zerda, M. Gerspacher. *Carbon*, 1994, 32(7): 1377-1382.

[51] A. Lazzarini, A. Piovano, R. Pellegrini, G. Agostini, S. Rudić, C. Lamberti, E. Groppo. *Phys. Procedia*, 2016, 85: 20-26.

[52] T. Kim, G. Jung, S. Yoo, K. S. Suh, R. S. Ruoff. *ACS Nano*, 2013, 7: 6899-6905.

[53] C. X. Guo, C. M. Li. *Energy Environ. Sci.*, 2011, 4(11): 4504-4507.

[54] A. J. Roberts, R. C. T. Slade. *Energy Environ. Sci.*, 2011, 4: 2813-2817.

[55] J. Yan, Q. Wang, T. Wei, Z. Fan. *Adv. Energy Mater.*, 2014, 4(4): 1300816

[56] Z. Kerner, T. Pajkossy. *Electrochim. Acta*, 2000, 46(2-3): 207-2011.

[57] T. Pajkossy. *J. Electroanal. Chem.*, 1994, 364(1-2): 111-125.

[58] Y. M. Vol'fkovich, T. M. Serdyuk. *Russ. J. Electrochem.*, 2002, 38(9): 935-959.

[59] H. K. Song, Y. H. Jung, K. H. Lee, L. H. Dao. *Electrochim. Acta*, 1999, 44(20): 3513-3519.

[60] J. R. Miller, P. Simon. *Science*, 2008, 321(5889): 651-652.

Supporting Information

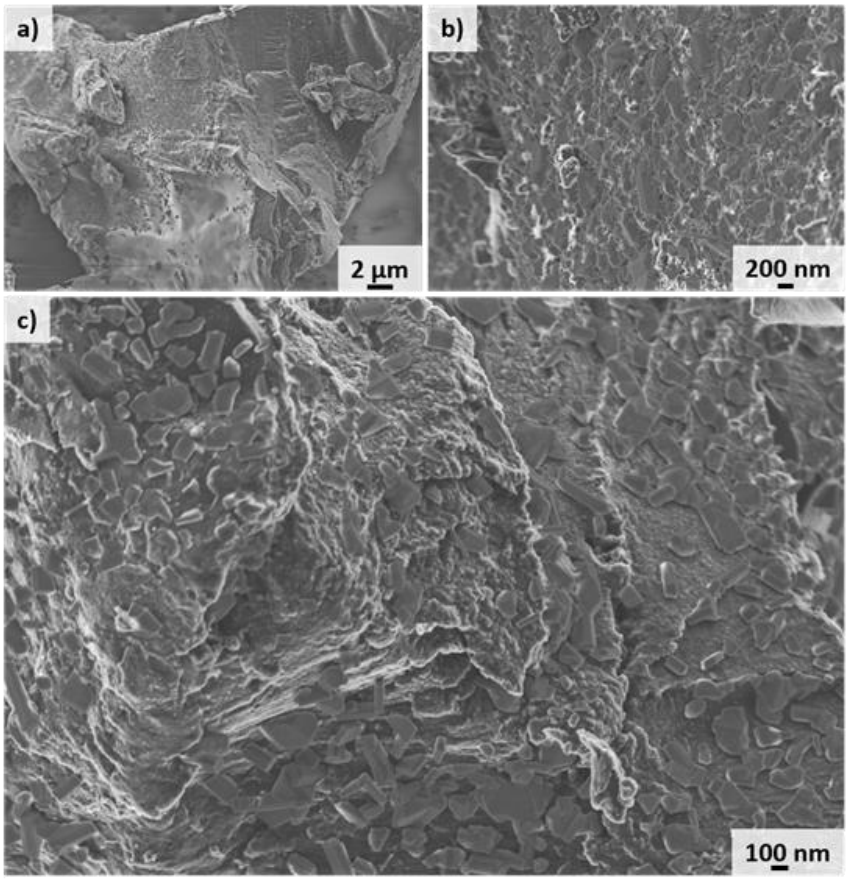

Fig. S1. SEM micrographs of the carbon materials derived from the pyrolysis of the inner part of the fig fruit (IN) without KOH after calcination at 900 °C.

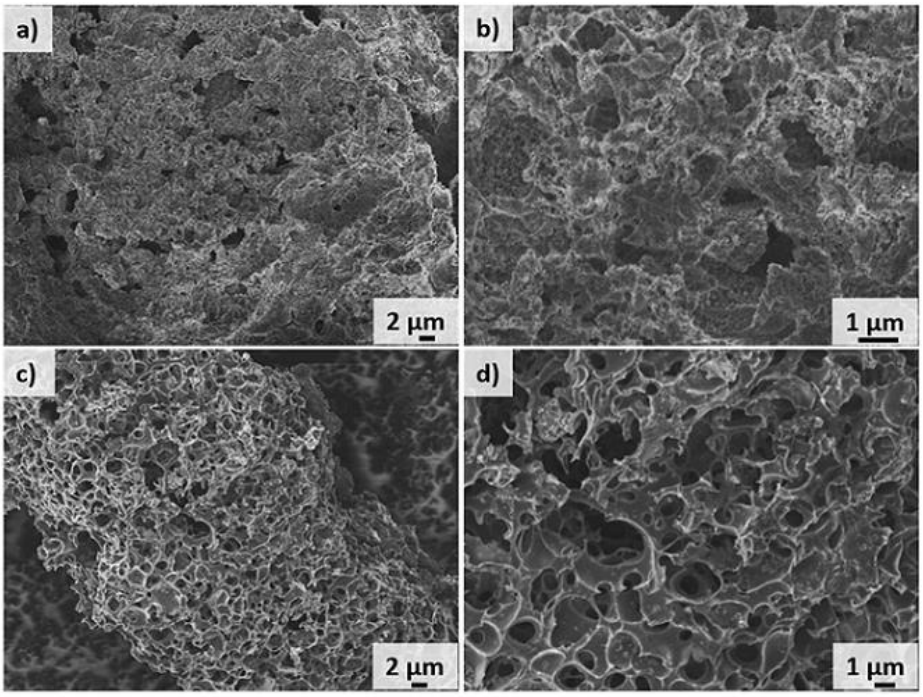

Fig. S2. SEM micrographs of the as-synthesized activated carbon in the presence of KOH (KOH/Carbon ratio of 3) from different parts of the fig fruit. (a, b) Peel and (c, d) All the fig fruit.

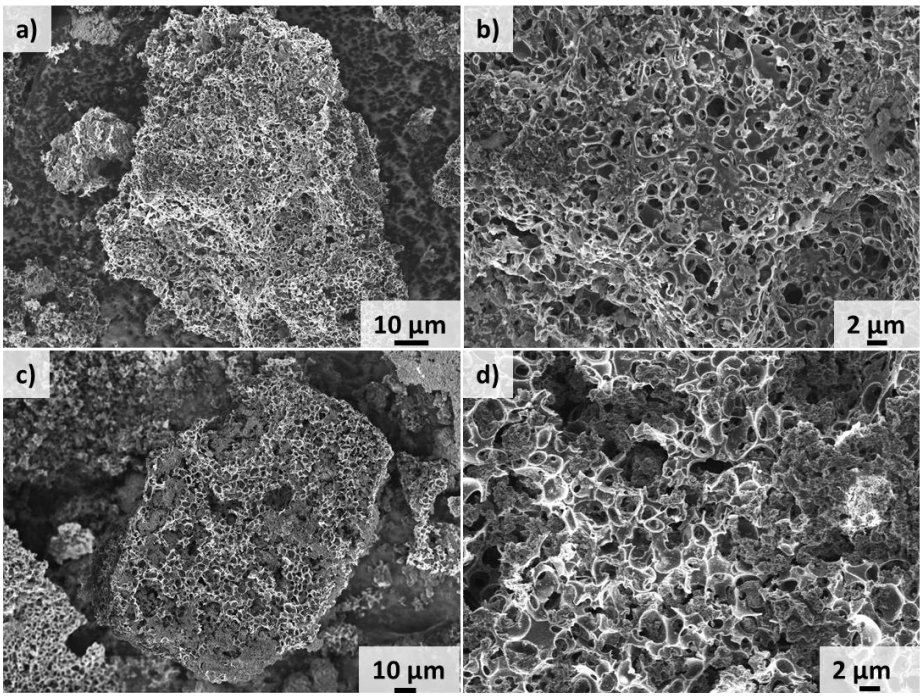

Fig. S3. SEM micrographs of the as-synthesized activated carbon from the inner part of the fig fruit with different KOH activation. (a, b) KOH/Carbon ratio 1/1 (c, d) KOH/Carbon ratio 2/1.

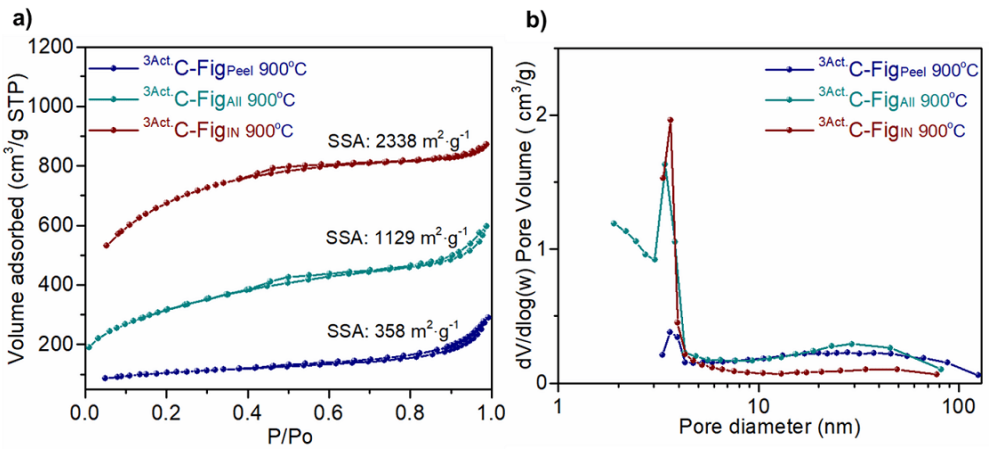

Fig. S4. (a) Adsorption-desorption isotherms and specific surface area (SSA) and (b) pore size distribution of the different parts of the fruit on the SSA and pore size distribution after pyrolysis at 900 °C. Legend: Peel: peel, All: the entire fruit, IN: inner part of the fruit.

Table S1 Specific capacitances of the $^{3Act.}$C-Fig$_{IN}$ 900 °C sample.

Current Density ($A \cdot g^{-1}$)	0.5	1	2	5	10	20	50
Capacitance ($F \cdot g^{-1}$)	340	306	281	247	230	209	170

* The specific capacitances are calculated from the galvanostatic charge-discharge curves based on Eq. (17).

Equivalent circuit contains 2 elements: serial resistance R, related to the resistance of an electrolyte and electrode layer, and constant phase element (CPE). The latter is interpreted as the capacitance of carbon/electrolyte interface, complicated by the inhomogeneity of carbon surface.

Nyquist diagram of porous electrode was fitted by simple equivalent circuit, containing serial resistance R and constant phase element CPE. The latter correspond to the capacity of electrode/electrolyte interface with certain inhomogeneity [1]. At higher frequencies impedance diagram deviates from this simple behavior, phase angle decreasing (see also Bode plots Fig. S5) eventually to 0, as expected for pure resistance. This behavior is in agreement with the models of impedance of porous electrodes with finite pores with non-uniform distribution of their morphology.

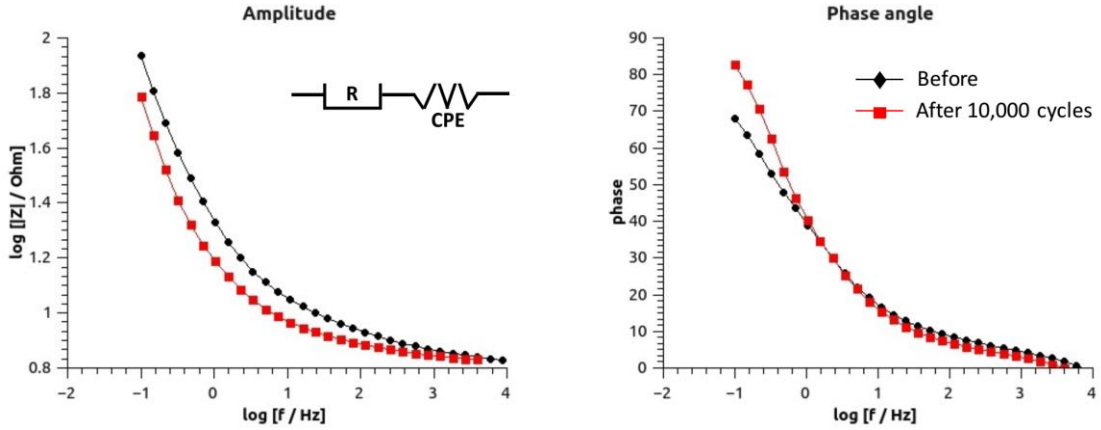

Fig. S5. Equivalent circuit model and Bode plots of the $^{3Act.}$C-Fig$_{IN}$ 900 °C sample before and after 10,000 cycles.

Reference:

[1] G. J. Brug, A. L. G. van den Eeden, M. Sluyters-Rehbach, J. H. Sluyters. *J. Electroanal. Chem. Interfacial Electrochem.*, 1984, 176(1-2): 275-295.

Chapter 3.2

Tridimensional few-layer graphene-like structures from sugar salt mixtures as high-performance supercapacitor electrode

Abstract

This work describes a straightforward approach to the production of highly-performing and cost-effective C-based materials for energy storage application while proposing an original and effective method to the control of the final material morphology. Indeed, robust few-layer graphene-like and highly open-cell structures have been prepared by a modified chemical activation procedure starting from costless sugar/salt mixtures. The as-prepared C-samples ensure high ion-accessible surface area and low ion transport resistance, two key features for the fabrication of effective electrochemical double layer supercapacitors. A selected sample from this series exhibits high specific capacitance (C_g) (312 and 234 $F \cdot g^{-1}$ at 0.5 and 50 $A \cdot g^{-1}$, respectively, in 0.5 M H_2SO_4), particularly at high current density values, along with excellent cycling stability and C_g retention for increasing charge-discharge rates.

Keywords

3D graphene-like materials; Salt templating method; Chemical activation; Natural C-sources; Supercapacitors.

This chapter is based on the following publication:

H. Ba, W. Wang, G. Tuci, S. Pronkin, C. Weinberg, L. Nguyen-Dinh, G. Giambastiani, C. Pham-Huu. *Mater. Today Energy*, 2018, 10: 118-125.

3.2.1 Introduction

The ever-growing need of reducing fossil fuels consumption and greenhouse gas emissions are commonly recognized as priorities to fight against global warming and related climate change phenomena while addressing the objectives of a modern circular energy economy [1]. The production of electricity from renewable resources along with the development of highly-performing and cost-effective energy storage devices are among the most promising solutions to rapidly accomplish these challenging goals. To this end, batteries and supercapacitors have rapidly emerged as the main actors of a world economy based on the large-scale renewable energy management and storage [2-5]. In recent years, supercapacitors based on electrical double layer (EDL) charge storage mechanism have attracted the interest of chemists, physics and engineers as high power density and long-lifecycle devices, suitable for bridging the power/energy gap between batteries (featured by high energy but low power) and conventional capacitors (featured by high power but low energy). As far as energy density is concerned, research in design and synthesis of new electrodes and electrolytes has boosted progresses in EDL technology, thus providing devices with steadily increasing performance (high power density and long-term life under operating conditions) [6-10]. Microporous carbons (pure or doped) are prominent electrode materials in EDL capacitors because of their high electrical conductivity, essential for power applications, and large specific surface area (SSA), necessary for enhancing capacitance. They can be derived from natural and abundant sources and prepared in a wide variety of textures (*i.e.* powders, fibers, nanotubes, sheets, monoliths and nanospheres just to mention a few). In addition to their structural diversity, the rich surface chemistry of C-based structures allows tuning their performance as EDL supercapacitors or adapting them to various electrochemical configurations [4-5, 11-13]. Among sp^2 carbon structures, graphene is emerged as one of the most promising electrode materials due to its high theoretical SSA, electrical conductivity and specific capacitance [14-19]. As a matter of fact, several graphene-based systems have been successfully exploited so far as supercapacitors [20-24]. However, the tendency of graphene sheets to π-π restack into larger aggregates, limits the electrolyte transfer and reduces the material ion-accessible surface area thus hampering an ideal exploitation of its capacitive potential [25]. To overcome these drawbacks, graphene-based composites, comprising nano-spacers (*i.e.* carbon nanotubes [26-29] or nano-spheres [30]) to separate graphene sheets, have been

proposed for the generation of hierarchical, tridimensional (3D) assemblies with enhanced specific capacitance.

In this contribution we describe a straightforward, environmentally friendly and easy-to-scale up approach to the fabrication of open-cell, few layer graphene-like structures starting from cheap foodstuff components. Sucrose and NaCl in variable ratio (wt./wt.) are employed as renewable carbon source and sacrificial templating agent, respectively [31-36]. Robust and durable graphene-like carbon nanosheets are prepared from those mixtures through KOH chemical activation at 800 °C [37-38]. The as-prepared samples display SSA as high as 896 $m^2 \cdot g^{-1}$ along with superior specific capacitances and capacitance retentions compared to many related C-based systems of the state-of-the-art.

3.2.2 Experimental section

Materials and characterization: please refer to **Chapter 2.1-2.2**.
Electrode preparation and performance evaluation: please refer to **Chapter 2.3.1**.

3.2.3 Results and discussion

Material synthesis and characterization

The synthetic procedure to the fabrication of 3D few layer graphene-based structures from mixtures of sucrose/NaCl [Sugar-to-Saltx/y(wt./wt.), *St*Sx/y(wt./wt.)] is outlined in **Scheme 1**. Physical mixtures of the two raw components (at variable x/y composition = 1/1, 1/0, 1/2, 1/5 and 2/1 wt./wt.) are finely grinded together in a pestle and mortar before undergoing a first thermal heating in air at 150 °C where sugar polycondensation starts. Afterwards, the reddish-brown composite is milled in a fine powder and impregnated with a concentrated KOH water solution obtained by dissolving an amount of the inorganic base equal to that of the starting salt/sugar mixture (wt./wt.). At odds with the classical chemical activation from physical mixtures of C-sources and KOH, the impregnation of the sucrose/NaCl calcinated mixture with an aqueous KOH solution allows a capillary distribution of the activator in the material that controls the ultimate material morphology. Indeed, $KOH_{(sol)}$ penetrates the sugar/salt matrix through a partial dissolution of the organic network or a NaCl/KOH salt scrambling and fosters the formation of thin C-layers (like onion veils) around the inorganic cores. The impregnated samples are then gently heated at 150 °C on air to

remove water till dryness and then pyrolyzed in a tubular furnace under an Ar flow (100 $mL \cdot min^{-1}$) at 800 °C for 1 h, where the chemical activation takes place and the definitive 3D carbon network is formed. The as-obtained composites are thoroughly washed with deionized water till neutrality of the discharged aqueous phases. During the washing treatment, NaCl is leached out from the composite thus leaving behind highly accessible and non-stackable few layer graphene-like carbon materials. The carbon products are dried at 110 °C under vacuum overnight before use.

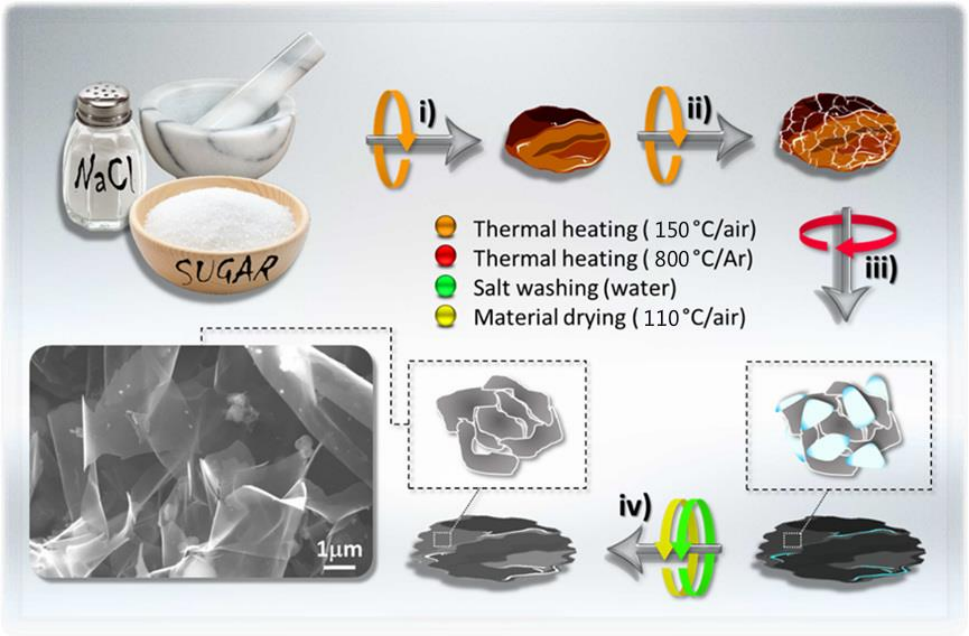

Scheme 1. Sequential steps (**i** → **iv**) for the preparation of $StS_{x/y}$ materials from physical mixtures (wt/wt) of finely grinded sucrose and table salt (NaCl). (**i**) sugar/salt melting at 150 °C in air; (**ii**) $KOH_{(sol)}$ impregnation of the finally milled composite and drying at 130 °C in air; (**iii**) Thermal annealing and "chemical activation" step at 800 °C for 1h under inert atmosphere (Ar); (**iv**) salt(s) washing treatment. The image refers to a SEM magnification of $StS_{1/1}$ sample.

Thermal gravimetric analysis (TGA) was carried out under oxidative flow on all washed samples in order to estimate the residual amount of inorganic components. Although the presence of salt traces cannot be definitively ruled out (particularly for samples prepared at low sugar/salt ratios), all materials showed ash-contents (T > 650 °C) ranging from ~ 2 wt.% ($StS_{1/1}$) (**Fig. S1**) to nearly 6 wt.% for $StS_{1/5}$. SEM and TEM characterizations have been used to demonstrate the role of NaCl and $KOH_{(sol)}$ treatment on the microstructure of the carbon samples prepared as described above. **Fig.**

1A-C and **1D-F** refer to samples $StS_{1/0}$ and $StS_{1/1}$, respectively. At a first glance, the two materials present radically different morphologies with a foamy structure for $StS_{1/0}$ and a wrinkled graphene-like surface in the sample prepared with a one-to-one (wt./wt.) sugar/salt ratio ($StS_{1/1}$) (Fig. 1A vs. 1D). Images at higher magnifications confirm the morphological differences between the two materials. The wrinkled surface and curved few layer graphene-like carbon nanosheets observed in the domain of $StS_{1/1}$ sample (Fig. 1E and F) are replaced by a thicker and foamier phase in $StS_{1/0}$ obtained without NaCl (Fig. 1B and C). Remarkably, the open microstructure in $StS_{1/1}$ is maintained throughout the whole material work-up without any re-stacking of graphene sheets. TEM and HRTEM images (**Fig. 1G-I**) clearly reveal the thin, flat and transparent nature of graphene sheets (few layers) in $StS_{1/1}$. Overall, it can be inferred that the joint action of NaCl as sacrificial templating agent and chemical activation by material impregnation with $KOH_{(sol)}$ generate robust C-networks formed by stable graphene-like domains featuring with an ideal contact area for electrolytes (vide infra). As a proof of concept, $StS_{1/1}$ has also been prepared from a classical physical mixture of the three components (sucrose, NaCl and KOH), following the sequential procedure outlined in Scheme 1, except for the impregnation phase. Under these conditions, SEM micrographs (**Fig. S2**) of the salt-leached carbon material reveal that only thick, shell-like structures are formed with no evidence for the generation of thinner graphene-like domains.

To get further details on the role of sugar/salt mass ratio on the materials morphology, two representative samples ($StS_{1/5}$ and $StS_{2/1}$) have been prepared and characterized by SEM analysis. As **Fig. S3** shows, at low sugar/salt ratio, activated samples present a rather homogeneous morphology made almost exclusively of layered and thin graphene sheets ($StS_{1/5}$, Fig. S3a-c). On the contrary, samples prepared from mixtures at low salt contents ($StS_{2/1}$) present a prevalent thick and foamy phase together with few layered graphene domains (Fig. S3d-f). Finally, no graphene-like phases are detected in the activated samples obtained from the plain sucrose ($StS_{1/0}$, Fig. 1A-C).

For the representative $StS_{1/1}$ sample, the presence of graphene-like domains is corroborated by Raman spectroscopy and XRD analyses (**Fig. 2**). The Raman spectrum (**Fig. 2A**) exhibits two prominent peaks at 1340 and 1585 cm^{-1} assigned to disorder (D) and graphitic C-sp^2 (G) vibrational modes, respectively, along with their overtone and combination bands between 2400 and 3400 cm^{-1} (G0 = 2D) [39]. The I_D/I_G and I_{2D}/I_G peaks ratio measured on $StS_{1/1}$ are ~ 1.2 and ~ 0.19, respectively, and they fall in the typical range of values measured for defective graphene nanoplatelets [40-41].

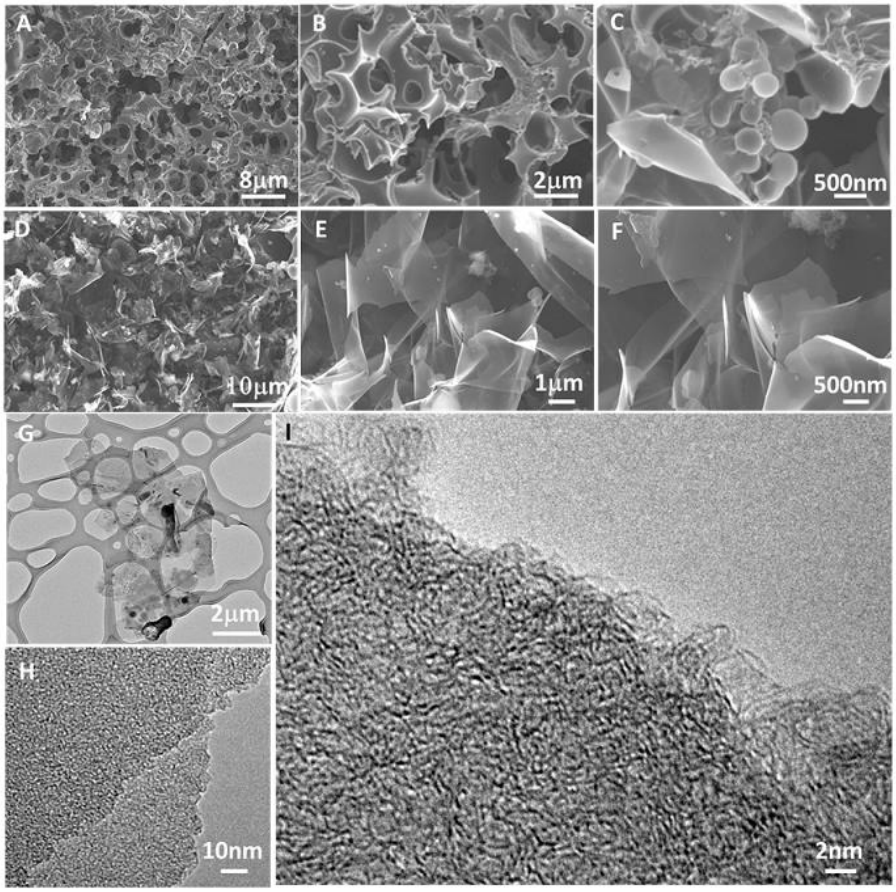

Fig. 1. SEM micrographs at various magnifications of $StS_{1/0}$ (A-C) and $StS_{1/1}$ (D-F). TEM (G) and HRTM (H, I) images of $StS_{1/1}$.

XRD measurement (**Fig. 2B**) shows one main peak located at 2θ around 24° and assigned to (002) diffraction of hexagonal graphite. The broad shape of this peak is indicative of long-range disordered C-structures [42]. Despite different morphologies of *StS* materials prepared at variable sucrose/NaCl ratio, their relatively high SSA and pore size distributions are largely controlled by the common chemical activation treatment [$KOH_{(sol)}$] (**Table S1**, entries 2 vs. 6).

Indeed, the impregnation phase with $KOH_{(sol)}$ increases the micropore content in the activated samples and, in turn, their ultimate SSA. All samples present Type IV adsorption-desorption isotherms (BET) with distinctive H_4 hysteresis loops (**Fig. 2C** and **S4**A, C, E, G), typical of many other activated carbons and nano-porous adsorbents [43-45]. SSA measured on $StS_{1/0}$, $StS_{1/1}$ and $StS_{1/2}$ are rather close to each other and fall in the 750-800 $m^2 \cdot g^{-1}$ range (Table S1, entries 1-3).

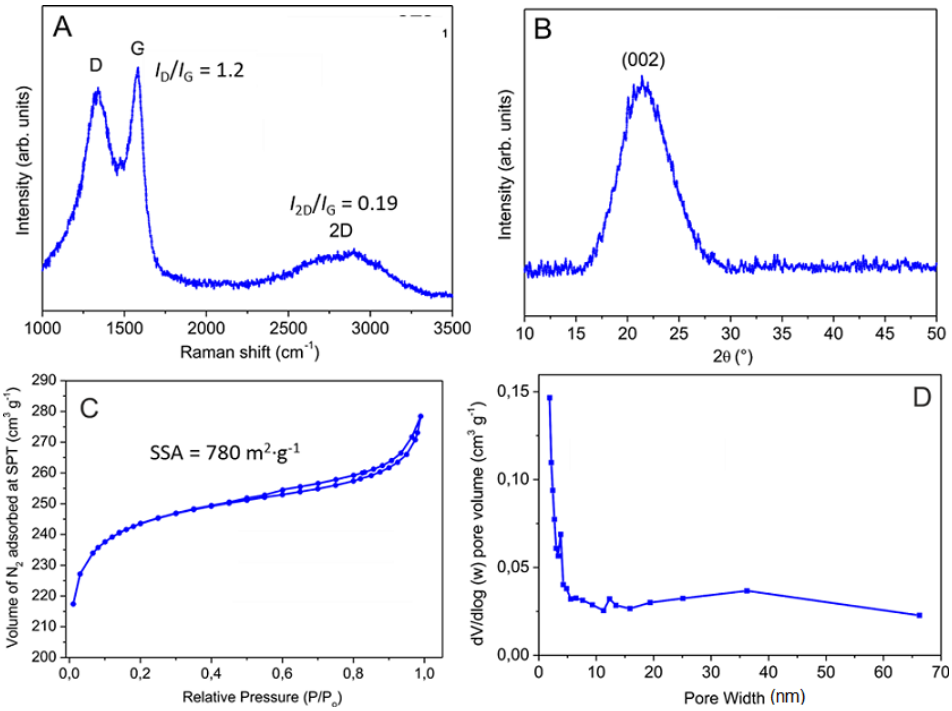

Fig. 2. (A) Raman spectrum and (B) XRD analysis (C) Nitrogen adsorption-desorption isotherm line and (D) pore size distribution as measured with the BJH method of *StS*$_{1/1}$ as representative sample.

Higher NaCl contents (*StS*$_{1/5}$) or sucrose/NaCl ratios > 1 (*StS*$_{2/1}$) translate into activated C-samples with lower (631 m^2·g^{-1}) and higher (896 m^2·g^{-1}) SSA values, respectively (Table S1, entries 4 and 5). This trend is ascribable to the variable salt concentration in the starting mixtures that may alter: i) the effectiveness of KOH impregnation phase ii) the total macropore contribution in the final samples [31-32]. Similarly, all pore-size distributions (BJH method) measured on the activated materials account for mesoporous materials with a major micropore contribution (t-Plot) to the total pore volume (Table S1 and Fig. S4B, D, F, H). For the sake of completeness, SSA and pore size distribution have also been determined for the *StS*$_{1/1}$phys sample prepared from a homogeneous physical mixture of sugar/NaCl/KOH, avoiding the impregnation step. As BET isotherm profiles of *StS*$_{1/1}$ and *StS*$_{1/1}^{phys}$ show (Fig. 2C vs. Fig. S4I) the higher the homogeneous distribution of the chemical activator in the mixture, the higher the SSA of the final sample (Table S1, entries 2 vs. 7). Although high SSA values in carbon-based EDL electrodes typically translate into materials with enhanced capacitance values, other morphological features can be responsible for their performance, particularly at high current density values. As discussed above, the material morphology of *StS* samples is deeply influenced by the chemical activation

method with the impregnation procedure offering a unique control on the generation of graphene-like domains. Therefore, the two morphologically different samples $StS_{1/1}$ and $StS_{1/1}^{phys}$ have been electrochemically compared and their final performance as double layer supercapacitors have been discussed at various current rates (vide infra).

To establish the electrochemical performance of *StS* samples as supercapacitors, all materials were fabricated into electrodes and characterized in a conventional three-electrode glass cell using 0.5 M H_2SO_4 as electrolyte. Cyclic voltammetry (CV) tests in the potential range from 0 to 1.1 V (RHE) recorded at a scan rate of 20 $mV \cdot s^{-1}$ exhibit different quasi-rectangular shape (mainly in the case of samples featured by graphene-like structures) along with evident and reversible humps which reflect the existence of minor pseudocapacitance contributions (**Fig. 3A**). The latter are more likely to occur in the presence of acidic electrolytes and typically originate from redox processes involving oxygen-containing surface functionalities [40, 46].

Among different samples, those prepared from a sugar/salt ratio ≤ 1 show the most relevant specific capacitance values (C_{cv} from 173 to 208 $F \cdot g^{-1}$; **Table S2**, entries 2-4). On the other hand, samples prepared from the pure sugar ($StS_{1/0}$) or a sugar/salt ratio > 1 display moderate C_{cv} values ($StS_{1/0} \approx 72$ F·g-1 and $StS_{2/1} \approx 63$ $F \cdot g^{-1}$; Table S2, entries 1 and 5) in line with their thicker and foamy morphologies where graphene-like domains are virtually absent. $StS_{1/1}$ is the sample from this series obtained with high carbon-yield that additionally offers high C_{cv} (Table S2, entry 2) as EDL for energy storage. Therefore, it has been selected as model compound for further electrochemical investigations.

As **Fig. 3B** shows, $StS_{1/1}$ retains a quasi-rectangular shape even at potential scan rates as high as 500 $mV \cdot s^{-1}$ which indicates a good material ion response in the acid electrolyte. Galvanostatic charge-discharge curves (**Fig. 3C**) recorded on $StS_{1/1}$ at different current densities (0.5, 1, 2, 5, 10 and 20 $A \cdot g^{-1}$) are highly linear and symmetrical, which indicate an ideal supercapacitor behavior of the C-sample. Specific capacitance (C_g) values of $StS_{1/1}$ as obtained from the galvanostatic charge-discharge measurements are outlined in **Table 1** and graphically represented in **Fig. S5**. It should be noticed that capacitance gradually increases from 208 $F \cdot g^{-1}$ to 271 $F \cdot g^{-1}$ and it stabilizes to the latter value after cycling the material for a relatively long time (15K cycles, **Fig. S6**A).

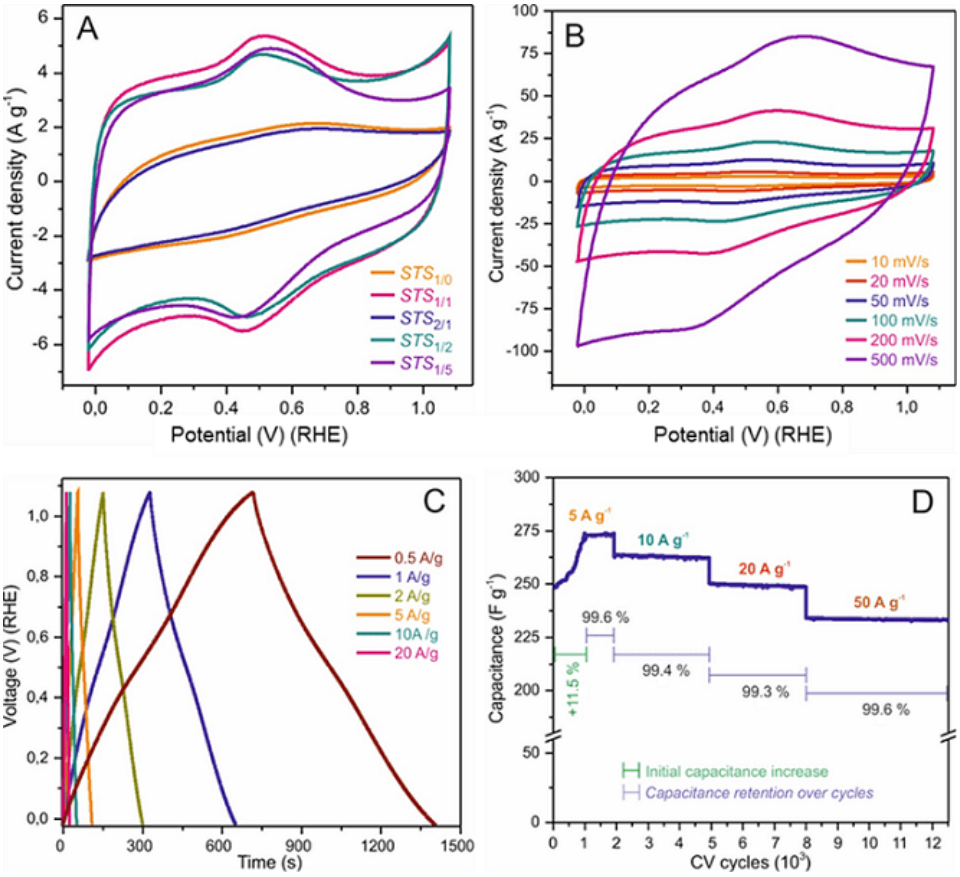

Fig. 3. (A) CV curves (initial 60 cycles) recorded on all $StS_{x/y}$ at a 20 mV·s^{-1} scan rate using a three-electrode glass cell operating in 0.5 M H_2SO_4. (B) CV curves of $StS_{1/1}$ in 0.5 M H_2SO_4 electrolyte at various scan rates. (C) Charge-discharge curves recorded for $StS_{1/1}$ at different current densities (A·g^{-1}). (D) Stability evaluation of $StS_{1/1}$.

Table 1. Specific capacitance (C_g, F·g^{-1}) of $StS_{1/1}$ calculated from galvanostatic charge-discharge curves.

Entry	Current density [A·g^{-1}]	Capacitance [F·g^{-1}]
1	0.5	312
2	1	293
3	2	281
4	5	273
5	10	262
6	20	249
7	50	234

Long-term cycling tests conducted at various current densities have been used to highlight the remarkable performance of $StS_{1/1}$ as EDL for energy storage. As Fig. 3D shows, C_g of $StS_{1/1}$ gradually increases, upon cycling the sample, from 248 $F \cdot g^{-1}$ to 273 $F \cdot g^{-1}$ (at 5 $A \cdot g^{-1}$) and it stabilizes to the latter value after about thousand cycles [47]. Notably, $StS_{1/1}$ presents an almost complete capacitance retention (> 99%) at fixed current densities upon thousands cycles along with markedly high C_g values, particularly for high current densities. As a result, $StS_{1/1}$ retains over 86% of its specific capacitance when the charge-discharge rate is increased from 5 $A \cdot g^{-1}$ (273 $F \cdot g^{-1}$) to 50 $A \cdot g^{-1}$ (234 $F \cdot g^{-1}$), within over 12,000 cycles (Fig. 3D). Remarkably, it also holds over 98% of the specific capacitance measured at 5 $A \cdot g^{-1}$ after long-term cycling tests conducted under variable charge-discharge rates (**Fig. S7**).

Although any comparative analysis of $StS_{1/1}$ with other EDL systems of the state-of-the-art is hard to be fully accomplished because of different electrochemical conditions and configurations used, it can be inferred that capacitance (C_g) values measured for $StS_{1/1}$ rank among the highest reported so far for EDL samples obtained from biomass wastes [48-53], feedstock [54-55] or other C-abundant resources endowed by nature (**Table S3**) [40, 56-67]. With values as high as 312 and 234 $F \cdot g^{-1}$ at low (0.5 A g^{-1}) and high (50 $A \cdot g^{-1}$) current densities, respectively, $StS_{1/1}$ capacitances are comparable to those claimed for other activated carbons [40, 50, 56, 60] although $StS_{1/1}$ maintains markedly higher BET area-normalized capacitances (Table S3, entries 1 vs. 3, 7, 16 and 17). Finally, C_g retention of $StS_{1/1}$ outperforms that measured for benchmark EDL samples derived from natural feedstock or biomass wastes. Notably, at the steady-state conditions, $StS_{1/1}$ retains 75, 80 and 84% of its specific capacitance while increasing current density in the 0.5-50, 1-50 and 0.5-10 $A \cdot g^{-1}$ range, respectively. These percentages are higher compared with those measured for hair-derived carbon flakes [51] (38% retention in the 0.5-50 $A \cdot g^{-1}$ range; Table S3, entry 1 vs. 4), microporous C-nanoplates [41] (46% retention in the 0.1-52.5 $A \cdot g^{-1}$ range; entry 1 vs. 22), C-derived plant leaves [68] (64% retention in the 0.5-10 $A \cdot g^{-1}$ range; entry 1 vs. 23), bean dregs-derived carbons [56] (65% retention in the 1-50 $A \cdot g^{-1}$ range; entry 1 vs. 16), rice bran-derived carbons [69] (68% retention in the 0.1-50 $A \cdot g^{-1}$ range; entry 1 vs. 25) or other carbon nanosheets [66] from biomasses (74% retention in the 1-30 $A \cdot g^{-1}$ range; entry 1 vs. 15) within comparable current density ranges.

Electrochemical impedance spectroscopy (EIS) measurement has finally been performed on $StS_{1/1}$ to get additional insights on ion transport kinetics and charge

transfer at the graphene-like electrode. Fig. S6B shows the impedance plot for $StS_{1/1}$ electrode in the 10 kHz - 0.1 Hz frequency range along with a magnified view of the high frequency region. In this frequencies range one observed inclined Nyquist plots with phase angle gradually changing from 0° (pure resistive behavior) at f >1 kHz to nearly ideal capacitive behavior (phase angle > 86°) at low frequencies. This behavior can be rationalized in terms of de Levie model of an impedance of porous electrodes as an indication of open and easily ion-accessible pores with certain irregularity in size and shapes [70-72].

As an additional trial, $StS_{1/1}$ and $StS_{1/1}^{phys}$ have been put at comparison as EDL electrodes at variable current rates (in the 0.5-50 $A \cdot g^{-1}$). These experiments have been used to stress the relevance of the morphological control on carbon samples prepared using different activation paths, with respect to their final electrochemical performance as EDL supercapacitors (Table S3, entries 1 vs. 26). Although none of BET area-normalized capacitance values for $StS_{1/1}^{phys}$ outperform those of $StS_{1/1}$, the higher SSA of the former gives rise to increased C_g values, particularly at low current densities. On the other hand, the stable few layer graphene-like domains in $StS_{1/1}$ ensures better C_g at higher current density rates along with markedly high capacitance retention measured at increased charge-discharge rates (75% and 52% C_g retention in the 0.1-50 $A \cdot g^{-1}$ range for $StS_{1/1}$ and $StS_{1/1}^{phys}$, respectively. See Table S3 and Fig. S5, blue curve vs. red curve).

3.2.4 Conclusion

Robust and durable graphene-like networks featured by open-cell structures and relatively high specific surface areas are straightforwardly prepared by the thermal treatment of physical mixtures of sucrose and table salt, upon KOH chemical activation. At odds with more conventional chemical activation of C-sources in physical mixtures with KOH, the impregnation of carbon source with a KOH solution deeply influences both the material specific surface area and morphology. Indeed, the joint action of NaCl as sacrificial templating agent and chemical activation by material impregnation with $KOH_{(sol)}$ foster the formation of "onion veils"-like C-coatings around the inorganic core. Thermal annealing, chemical activation and salts washing steps, leave behind carbon samples featured by highly accessible and non-stackable few-layer graphene-like structure. This simple approach enables sub-nanometer scale integration of graphene sheets with electrolytes to form highly effective C-based electrodes with a continuous

ion transport network. Supercapacitor electrode based on the as-prepared materials have shown markedly high specific capacitance values, particularly at high current densities, along with excellent capacitance retentions upon thousands of cycles and increasing charge-discharge rates. Notably, the impregnation strategy with a KOH solution, markedly impacts on the final material morphology. Indeed, this approach ensures a unique control on the formation of stable few-layer graphene-like domains, a key feature to generate EDL supercapacitors with markedly high C_g at high current density rates. Overall, the outlined material technology sets the way to the easy and cheap scale-up of non-stackable graphene-like carbon samples to be employed as supercapacitors for charge storage with better performance respect to many related samples from the state-of-the-art (high specific capacitance and retention along with long-term life under operating conditions).

Reference

[1] http://ec.europa.eu/environment/circular-economy/implementation_report.pdf.

[2] P. Simon, Y. Gogotsi. *Acc. Chem. Res.*, 2013, 46(5): 1094-1103.

[3] G. Wang, L. Zhang, J. Zhang. *Chem. Soc. Rev.*, 2012, 41(2): 797-828.

[4] J. Yan, Q. Wang, T. Wei, Z. Fan. *Adv. Energy Mater.*, 2014, 4(4): 1300816.

[5] F. Béguin, V. Presser, A. Balducci, E. Frackowiak. *Adv. Mater.*, 2014, 26(4): 2219-2251.

[6] J. R. Miller, P. Simon. *Science*, 2008, 321(5889): 651-652.

[7] J. Wang, S. Kaskel. *J. Mater. Chem.*, 2012, 22(45): 23710-23725.

[8] L. Wei, G. Yushin. *Nano Energy*, 2012, 1(4): 552-565.

[9] Q. Wang, J. Yan, Z. Fan. *Energy Environ. Sci.*, 2016, 9(3): 729-762.

[10] A. Borenstein, O. Hanna, R. Attias, S. Luski, T. Brousse, D. Aurbach. *J. Mater. Chem. A*, 2017, 5(25): 12653-12672.

[11] X. Zheng, J. Luo, W. Lv, D. W. Wang, Q. H. Yang. *Adv. Mater.*, 2015, 27(36): 5388-5395.

[12] Y. Zhai, Y. Dou, D. Zhao, P. F. Fulvio, R. T. Mayes, S. Dai. *Adv. Mater.*, 2011, 23(42): 4828-4850.

[13] L. Hao, X. Li, L. Zhi. *Adv. Mater.*, 2013, 25(28): 3899-3904.

[14] X. Yang, C. Cheng, Y. Wang, L. Qiu, D. Li. *Science*, 2013, 341(6145): 534-537.

[15] K. Chen, S. Song, F. Liu, D. Xue. *Chem. Soc. Rev.*, 2015, 44(17): 6230-6257.

[16] Y. Xu, G. Shi, X. Duan. *Acc. Chem. Res.*, 2015, 48(6): 1666-1675.

[17] J. Ji, Y. Li, W. Peng, G. Zhang, F. Zhang, X. Fan. *Adv. Mater.*, 2015, 27(36): 5264-5279.

[18] Y. Zhu, S. Murali, W. Cai, X. Li, J. W. Suk, J. R. Potts, R. S. Ruoff. *Adv. Mater.*, 2010, 22(35): 3906-3924.

[19] Y. Wang, Z. Shi, Y. Huang, Y. Ma, C. Wang, M. Chen, Y. Chen. *J. Phys. Chem. C*, 2009, 113(30): 13103-13107.

[20] Y. Zhu, S. Murali, M. D. Stoller, K. J. Ganesh, W. Cai, P. J. Ferreira, A. Pirkle, R. M. Wallace, K. A. Cychosz, M. Thommes, D. Su, E. A. Stach, R. S. Ruoff. *Science*, 2011, 332: 1537-1541.

[21] K. Sheng, Y. Sun, C. Li, W. Yuan, G. Shi. *Sci. Rep.*, 2012, 2: 247-253.

[22] L. T. Le, M. H. Ervin, H. Qiu, B. E. Fuchs, W. Y. Lee. *Electrochem. Commun.*, 2011, 13(4): 355-358.

[23] C. Liu, Z. Yu, D. Neff, A. Zhamu, B. Z. Jang. *Nano Lett.*, 2010, 10(12): 4863-4868.

[24] T. Kim, G. Jung, S. Yoo, K. S. Suh, R. S. Ruoff. *ACS Nano*, 2013, 7(8): 6899-6905.

[25] M. Q. Zhao, Q. Zhang, J. Q. Huang, G. L. Tian, J. Q. Nie, H. J. Peng, F. Wei. *Nat. Commun.*, 2014, 5: 3410-3417.

[26] Y. Wang, Y. Wu, Y. Huang, F. Zhang, X. Yang, Y. Ma, Y. Chen. *J. Phys. Chem. C*, 2011, 115(46): 23192-23197.

[27] Z. Fan, J. Yan, L. Zhi, Q. Zhang, T. Wei, J. Feng, M. Zhang, W. Qian, F. Wei. *Adv. Mater.*, 2010, 22: 3723-3728.

[28] Q. Cheng, J. Tang, J. Ma, H. Zhang, N. Shinya, L. C. Qin. *Phys. Chem. Chem. Phys.*, 2011, 13(39): 17615-17624.

[29] H. Wang, Z. Liu, X. Chen, P. Han, S. Dong, G. Cui. *J. Solid State Electrochem.*, 2011, 15(6): 1179-1184.

[30] C. X. Guo, C. M. Li. *Energy Environ. Sci.*, 2011, 4(11): 4504-4507.

[31] A. H. Lu, W. C. Li, W. Schmidt, F. Schuth. *Micropor. Mesopor. Mat.*, 2006, 95(1-3): 187-192.

[32] C. J. Liao, C. F. Chen, J. H. Chen, S. F. Chiang, Y. J. Lin, K.-Y. Chang. *J. Biomed. Mater. Res.*, 2002, 59(4): 676-681.

[33] The “salt templating” method described hereafter should not mixed up with the more recent “salt melting” technique where eutectic mixtures of inorganic salts are employed to maximize formation of micro- and small meso-pores in carbons. For recent papers on this topic see: refs 34-36.

[34] N. Fechler, T. P. Fellinger, M. Antonietti. *Adv. Mater.*, 2013, 25(1): 75-79.

[35] S. Porada, F. Schipper, M. Aslan, M. Antonietti, V. Presser, T. P. Fellinger. *ChemSusChem*, 2015, 8(11): 1867-1874.

[36] R. Yan, T. Heil, V. Presser, R. Walczak, M. Antonietti, M. Oschatz. *Adv. Sustainable Syst.*, 2017, 2(2): 1700128.

[37] S. Ghosh, A. R. Barron. *Sustain. Energy Fuels*, 2017, 1(4): 806-813.

[38] K. C. Bedin, A. C. Martins, A. L. Cazetta, O. Pezoti, V. C. Almeida. *Chem. Eng. J.*, 2016, 286: 476-484.

[39] J. Robertson. *Mater. Sci. Eng. R.*, 2002, 37(4-6): 129-281.

[40] C. Shi, L. Hu, K. Guo, H. Li, T. Zhai. *Adv. Sustainable Syst.*, 2017, 1: 1600011.

[41] Y. S. Yun, S. Y. Cho, J. Shim, B. H. Kim, S. J. Chang, S. J. Baek, Y. S. Huh, Y.

Tak, Y. W. Park, S. Park, H. J. Jin. *Adv. Mater.*, 2013, 25(14): 1993-1998.

[42] H. Zhao, Q. Wang, Y. Deng, Q. Shi, Y. Qian, B. Wang, L. Lü, X. Qiu. *RSC Adv.*, 2016, 6(81): 77143-77150.

[43] S. J. Gregg, K. S. W. Sing. Adsorption, surface area and porosity, 2nd Ed., *Academic Press, London*, 1982, ISBN: 978-012-300956-2.

[44] K. S. W. Sing, R. T. Williams. *Adsorpt. Sci. Technol.*, 2004, 22: 773-782.

[45] In a model experiment, $STS_{1/1}$* sample has been prepared following the proposed synthetic protocol except for the treatment with KOH as activation agent. The SSA measured for this sample is over one order of magnitude lower than that of $STS_{1/1}$ (Table S1, entry 6).

[46] M. Noked, A. Soffer, D. Arubach. *J. Solid State Electrochem.*, 2011, 15(7): 1563-1578.

[47] L. Lai, H. Yang, L. Wang, B. K. Teh, J. Zhong, H. Chou, L. Chen, W. Chen, Z. Shen, R. S. Ruoff, J. Lin. *ACS Nano*, 2012, 6(7): 5941-5951.

[48] C. Falco, J. M. Sieben, N. Brun, M. Sevilla, T. van der Mauelen, E. Morallon, D. Cazorla-Amoros, M. M. Titirici. *ChemSusChem*, 2013, 6(2): 374-382.

[49] C. Huang, T. Sun, D. Hulicova-Jurcakova. *ChemSusChem*, 2013, 6: 2330-2339.

[50] Q. Liang, L. Ye, Z. H. Huang, Q. Xu, Y. Bai, F. Kang, Q. H. Yang. *Nanoscale*, 2014, 6(22): 13831-13837.

[51] W. Qian, F. Sun, Y. Xu, L. Qiu, C. Liu, S. Wang, F. Yan. *Energy Environ. Sci.*, 2014, 7(1): 379-386.

[52] W. Si, J. Zhou, S. Zhang, S. Li, W. Xing, S. Zhuo. *Electrochim. Acta*, 2013, 107: 397-405.

[53] Z. Li, L. Zhang, B. S. Amirkhiz, X. Tan, Z. Xu, H. Wang, B. C. Olsen, C. M. B. Holt, D. Mitlin. *Adv. Energy Mater.*, 2012, 2(4): 431-437.

[54] X. Zheng, W. Lv, Y. Tao, J. Shao, C. Zhang, D. Liu, J. Luo, D. W. Wang, Q.-H. Yang. *Chem. Mater.*, 2014, 26(23): 6896-6903.

[55] Z. Ling, C. Yu, X. Fan, S. Liu, J. Yang, M. Zhang, G. Wang, N. Xiao, J. Qiu. *Nanotechnology*, 2015, 26: 374003.

[56] C. Ruan, K. Ai, L. Lu. *RSC Adv.*, 2014, 4(58): 30887-30895.

[57] G. Xu, J. Han, B. Ding, P. Nie, J. Pan, H. Dou, H. Li, X. Zhang. *Green Chem.*, 2015, 17(3): 1668-1674.

[58] H. Li, D. Yuan, C. Tang, S. Wang, J. Sun, Z. Li, T. Tang, F. Wang, H. Gong, C. He. *Carbon*, 2016, 100: 151-157.

[59] L. Sun, C. Tian, M. Li, X. Meng, L. Wang, R. Wang, J. Yin, H. Fu. *J. Mater. Chem. A*, 2013, 1(21): 6462-6470.

[60] R. Wang, P. Wang, X. Yan, J. Lang, C. Peng, Q. Xue. *ACS Appl. Mater. Interfaces*, 2012, 4(11): 5800-5806.

[61] S. Song, F. Ma, G. Wu, D. Ma, W. Geng, J. Wan. *J. Mater. Chem. A*, 2015, 3(35): 18154-18162.

[62] X. Xu, J. Zhou, D. H. Nagaraju, L. Jiang, V. R. Marinov, G. Lubineau, H. N. Alshareef, M. Oh. *Adv. Funct. Mater.*, 2015, 25(21): 3193-3202.

[63] Y. Wang, R. Yang, M. Li, Z. Zhao. *Ind. Crops Prod.*, 2015, 65: 216-226.

[64] Y. Q. Zhao, M. Lu, P. Y. Tao, Y. J. Zhang, X. T. Gong, Z. Yang, G. Q. Zhang, H. L. Li. *J. Power Sources*, 2016, 307: 391-400.

[65] Z. Jin, X. Yan, Y. Yu, G. Zhao. *J. Mater. Chem. A*, 2014, 2: 11706-11715.

[66] Z. Ling, Z. Wang, M. Zhang, C. Yu, G. Wang, Y. Dong, S. Liu, Y. Wang, J. Qiu. *Adv. Funct. Mater.*, 2016, 26(1): 111-119.

[67] For a recent and comprehensive review article on biomass-derived carbon electrodes for supercapacitors see: H. Lu, X. S. Zhao. *Sustain. Energy Fuels*, 2017, 1(6): 1265-1281.

[68] M. Biswal, A. Banerjee, M. Deo, S. Ogale. *Energy Environ. Sci.*, 2013, 6(4): 1249-1259.

[69] J. Hou, C. Cao, X. Ma, F. Idrees, B. Xu, X. Hao, W. Lin. *Sci. Rep.*, 2014, 4: 7260.

[70] Y. M. Vol'fkovich, T. M. Serdyuk. *Russ. J. Electrochem*, 2002, 38(9): 935-959.

[71] D. Cericola, M. E. Spahr. *Electrochim. Acta*, 2016, 191: 558-566.

[72] O. E. Barcia, E. D'Elia, I. Frateur, O. R. Mattos, N. Pébère, B. Tribollet. *Electrochim. Acta*, 2002, 47(13-14): 2109-2116.

Supporting information

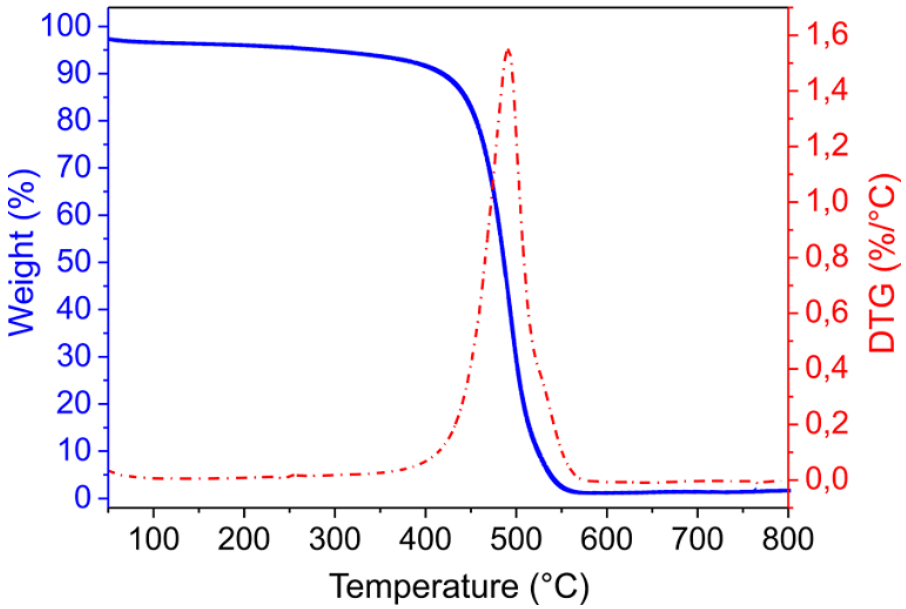

Fig. S1. TGA/DTG profiles of $StS_{1/1}$ recorded under oxidative O_2-He flow (20/80 v./v.%, 30 mL·min^{-1}) in the 50-800 °C temperature range; heating rate 10 °C·min^{-1}.

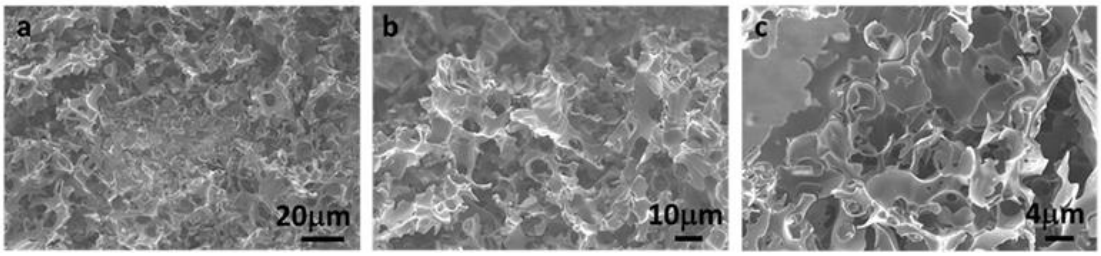

Fig. S2. SEM micrograph of $StS_{1/1}^{phys}$ at different magnifications. Sample prepared starting from a physical mixture of sucrose/NaCl/KOH without the impregnation phase.

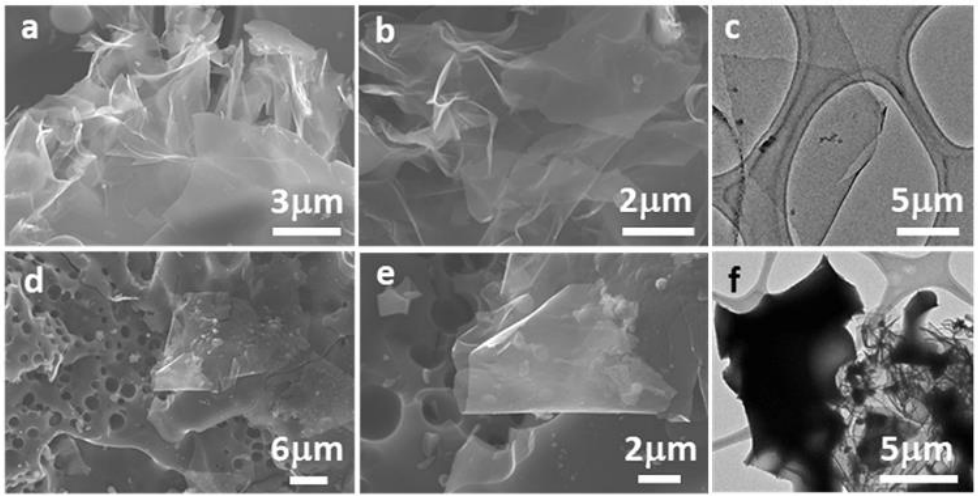

Fig. S3. SEM micrograph of $StS_{1/5}$ (a, b and c) and $StS_{2/1}$ (d, e and f) at comparison.

Table S1. Specific surface area (SSA), total and micropore volume of $StS_{x/y}$ samples.

Entry	Sample	SSA[a] [$m^2 \cdot g^{-1}$]	$V_{p(total)}$[b] [$cm^3 \cdot g^{-1}$]	$V_{p(micro)}$[c] [$cm^3 \cdot g^{-1}$]
1	$StS_{1/0}$	747	0.38	0.31
2	$StS_{1/1}$	780	0.42	0.32
3	$StS_{1/2}$	797	0.42	0.33
4	$StS_{1/5}$	631	0.33	0.25
5	$StS_{2/1}$	896	0.46	0.34
6	$StS_{1/1}$*	68	0.28	0.13
7	$StS_{1/1}^{phys}$	1279	0.66	0.38

[a] Brunauer-Emmett-Teller (BET) specific surface area (SSA) measured at T = 77 K. [b]Total pore volume determined by using the adsorption branch of N_2 isotherm at p/p_0 = 0.98. [c] Micropore volume by t-Plot model. $StS_{1/1}$* has been prepared following the proposed synthetic protocol except for the chemical activation (KOH impregnation) step. $StS_{1/1}^{phys}$ prepared from a physical mixture of sugar/salt/KOH.

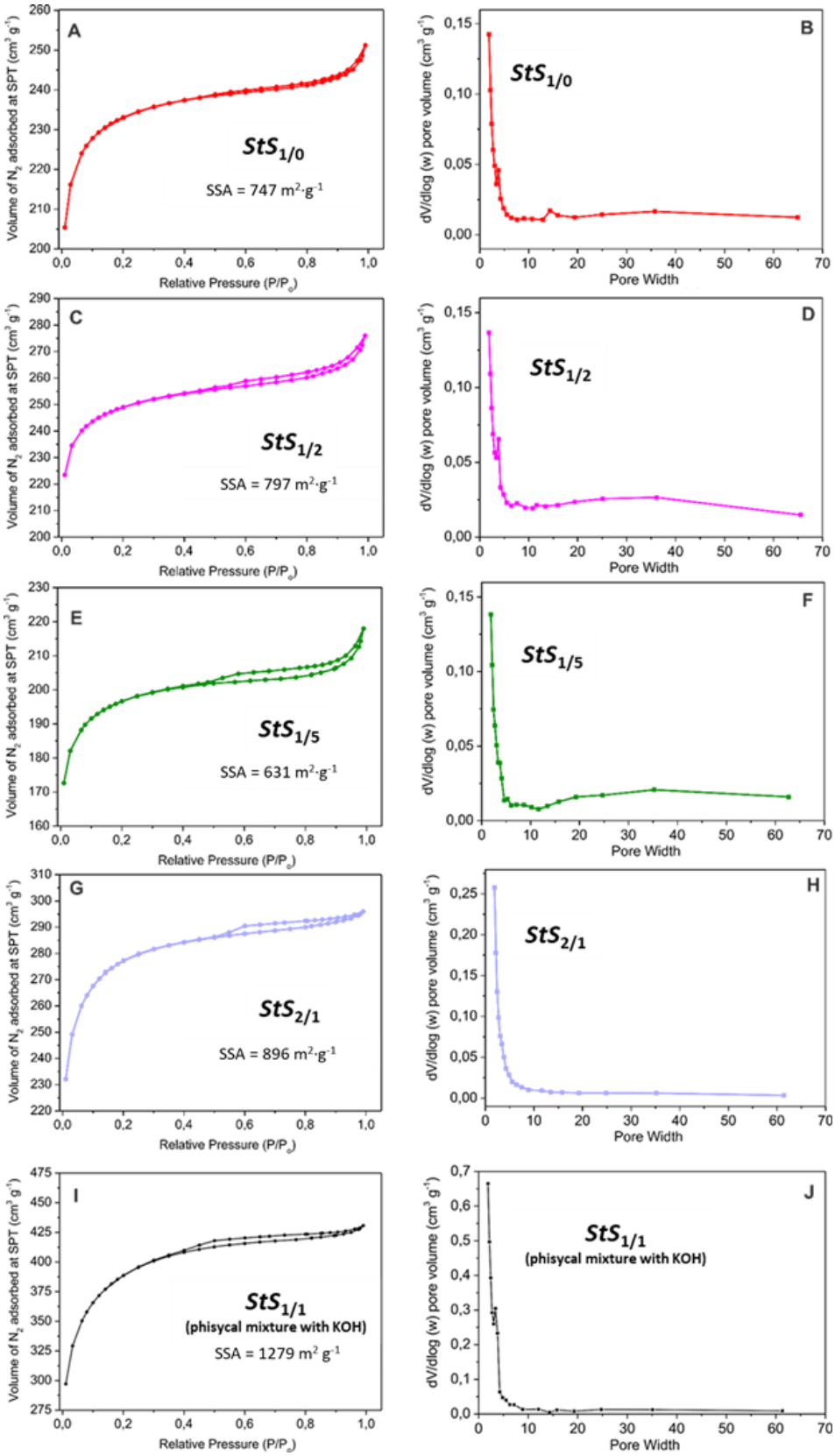

Fig. S4. Nitrogen adsorption-desorption isotherm line (A, C, E, G) and pore size distribution (X axis unit: nm, B, D, F, H) of *StS*$_{x/y}$. (I) and (J) refer to *StS*$_{1/1}$ sample prepared from a physical mixture of sugar/NaCl/KOH without the impregnation step.

Table S2. Specific capacitance (C_{cv}) of $StS_{x/y}$ samples from cyclic voltammetry (CV) tests.

Entry	Sample	Capacitance* [F g^{-1}]
1	$StS_{1/0}$	72
2	$StS_{1/1}$	208
3	$StS_{1/2}$	190
4	$StS_{1/5}$	173
5	$StS_{2/1}$	63

* Specific capacitance value calculated on the basis of the initial CV scans (60 cycles) at scan rate of 20 mV·s^{-1} in 0.5 M H_2SO_4.

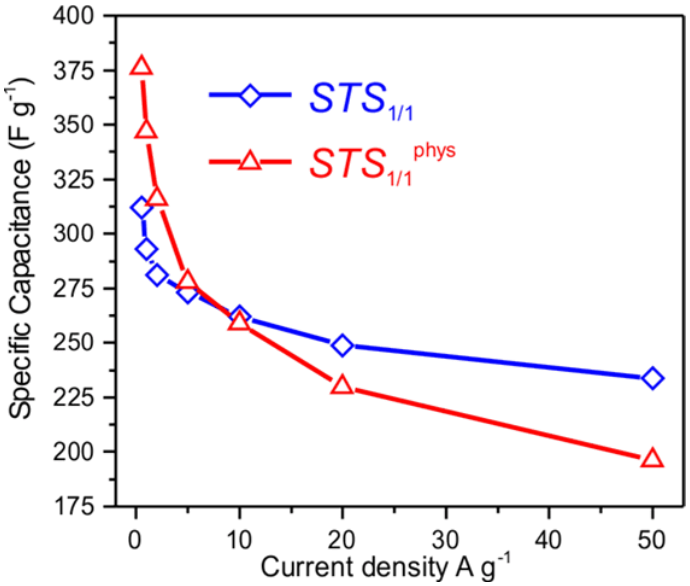

Fig. S5. Specific capacitance values (C_g) as a function of current densities for $StS_{1/1}$ (blue curve) and $StS_{1/1}^{phys}$ (red curve)

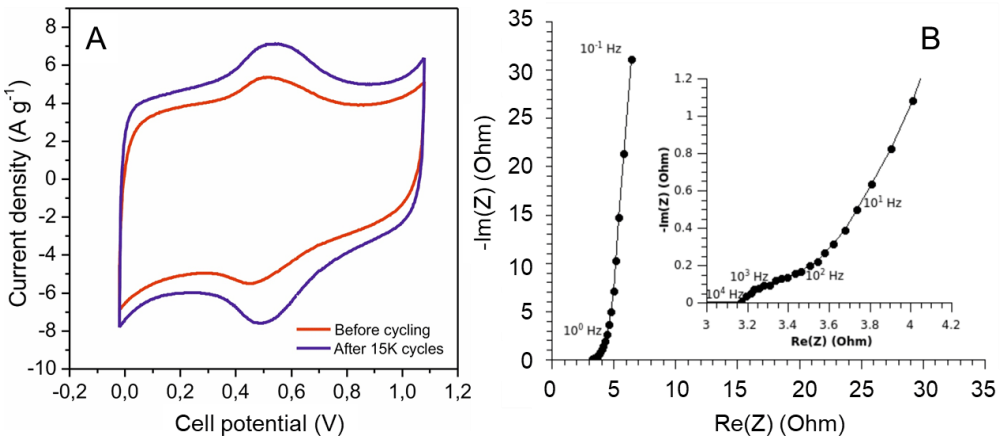

Fig. S6. (A) CV curves of *StS*$_{1/1}$ (red) after few cycles (~ 60) and after long-term tests (blue) in 0.5 M H_2SO_4 electrolyte at a scan rate of 20 mV/s. (B) Nyquist plot of *StS*$_{1/1}$ in 0.5 M H_2SO_4; inset refers to the same data in the high frequency region.

Table S3. Specific capacitances (C_g) and BET area-normalized capacitance of various C-based samples derived from biomass wastes, feedstock or other abundant natural resources. [a]

Entry	Sample	SSA (m^2g^{-1})	C_g/SSA ($\mu F \cdot cm^{-2}$)	Capacitance ($F \cdot g^{-1}$)	Current ($A \cdot g^{-1}$)	Electrolyte	Ref.
1	***StS*$_{1/1}$**	780	400	312	0.5	0.5 M H_2SO_4	**This work**
			376	293	1		
			350	273	5		
			336	262	10		
			319	249	20		
			300	234	50		
2	G-CS-8	1025	236	242	0.1	1 M H_2SO_4	[1]
			157	161	10		
3	HPC-K750	3047	102	311	1	1 M H_2SO_4	[2]
			68	208	50		
4	HMC-800	1306	341	445[b]	0.5	6M KOH	[3]
			130	170[b]	50		
5	C-nanosheets	2633	98	257	0.5	6 M KOH	[4]
			72	190[b]	50		
6	AHC-4	849	311	264	0.25	6 M KOH	[5]
			183	155[b]	5		

7	HLPC	2725	126 78	342 212	0.2 20	6 M KOH	[6]
8	ACFs180	3223	87 71	280 229	0.5 10	1 M H_2SO_4	[7]
9	TC-1	2115	134 103	283 218[b]	0.5 30	6M KOH	[8]
10	CHHPC-7	867	411 346	356 300	1 20	6M KOH	[9]
11	SLC	803	259 125	208 100	0.1 10	6M KOH	[10]
12	BC–LRF16	199	623 538	124 107	0.5 1	6M KOH	[11]
13	HACS-5	3062	104 63	318 193	0.1 50	6M KOH	[12]
14	CESM-300	221	1344 887	297 196	0.2 20	1M KOH	[13]
15	B/N-CS	416	861 642	358 267	0.1 30	1 M H_2SO_4	[14]
16	BD-700-A3	2876	168 108	482 312	1 50	1M H_2SO_4	[15]
17	a-CL	3404	124 76	421 260[b]	0.5 10	2M KOH	[16]
18	ACSB	655	308 192	202 126	0.5 10	6M KOH	[17]
19	PGNS-3-900	1874	147 98	276 184	1 30	6M KOH	[18]
20	PC-2	742	243 212	180 157	0.05 1	1M H_2SO_4	[19]
21	E2	2300	130 78	300 180[b]	0.25 1	0.5 M H_2SO_4	[20]
22[c]	H-CMNs	2557	103 63 47	264 162 120	0.1 6.2 52.5	1 M H_2SO_4	[21]

23[c]	CDDPL	1230	326 246 210	401 302 258	0.5 1 10	1 M H_2SO_4	[22]
24[c]	KS-2.5	2823	112 77 64	316 218 182	0.2 1 20	6 M KOH	[23]
25[c]	RBC-4	2475	131 107 89	323 265 220[b]	0.1 10 50	6M KOH	[24]
26	***StS*$_{1/1}^{phys}$**	1279	294 271 217 203 180 153	376 347 278 259 230 196	0.5 1 5 10 20 50	0.5 M H_2SO_4	**This work**

[a] Electrochemical performance of activated carbons in various electrolytes measured by a three-electrode system. [b] Estimated values from the original paper.

[c] Electrochemical performance measured by a two-electrode system.

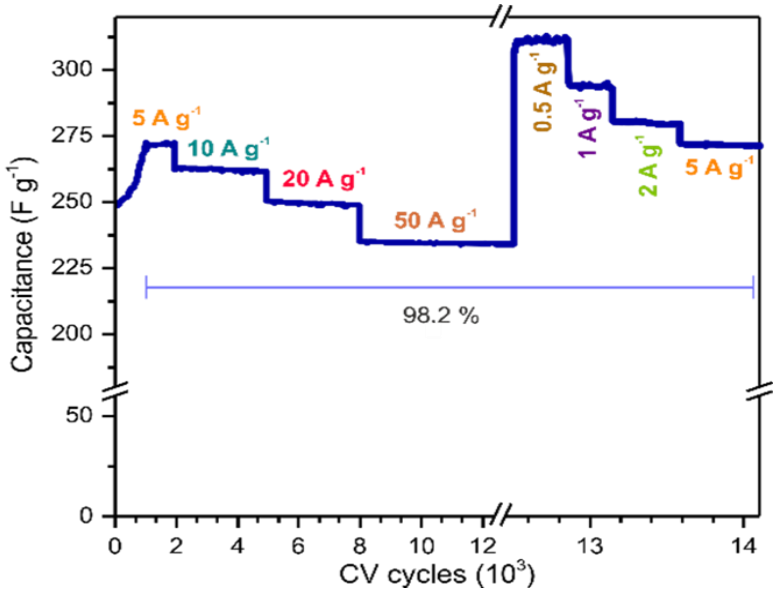

Fig. S7. Stability of *StS*$_{1/1}$ over thousands of cycles and its retention of capacitance at 5 A·g^{-1} after long-term cycling test at variable current densities.

Reference:

[1] Z. Ling, C. Yu, X. Fan, S. Liu, J. Yang, M. Zhang, G. Wang, N. Xiao, J. Qiu. *Nanotechnology*, 2015, 26(37): 374003.

[2] C. Shi, L. Hu, K. Guo, H. Li, T. Zhai. *Adv. Sustainable Syst.*, 2017, 1: 1600011.

[3] W. Qian, F. Sun, Y. Xu, L. Qiu, C. Liu, S. Wang, F. Yan. *Energy Environ. Sci.*, 2014, 7(1): 379-386.

[4] X. Zheng, W. Lv, Y. Tao, J. Shao, C. Zhang, D. Liu, J. Luo, D. W. Wang, Q. H. Yang. *Chem. Mater.*, 2014, 26(23): 6896-6903.

[5] W. Si, J. Zhou, S. Zhang, S. Li, W. Xing, S. Zhuo. *Electrochim. Acta*, 2013, 107: 397-405.

[6] Q. Liang, L. Ye, Z. H. Huang, Q. Xu, Y. Bai, F. Kang, Q. H. Yang. *Nanoscale*, 2014, 6(22): 13831-13837.

[7] Z. Jin, X. Yan, Y. Yu, G. Zhao. *J. Mater. Chem. A*, 2014, 2(30): 11706-11715.

[8] Y. Q. Zhao, M. Lu, P. Y. Tao, Y. J. Zhang, X. T. Gong, Z. Yang, G. Q. Zhang, H. L. Li. *J. Power Sources*, 2016, 307: 391-400.

[9] S. Song, F. Ma, G. Wu, D. Ma, W. Geng, J. Wan. *J. Mater. Chem. A*, 2015, 3(35): 18154-18162.

[10] H. Li, D. Yuan, C. Tang, S. Wang, J. Sun, Z. Li, T. Tang, F. Wang, H. Gong, C. He, *Carbon*, 2016, 100: 151-157.

[11] X. Xu, J. Zhou, D. H. Nagaraju, L. Jiang, V. R. Marinov, G. Lubineau, H. N. Alshareef, M. Oh. *Adv. Funct. Mater.*, 2015, 25(21): 3193-3202.

[12] Y. Wang, R. Yang, M. Li, Z. Zhao. *Ind. Crops Prod.*, 2015, 65: 216-226.

[13] Z. Li, L. Zhang, B. S. Amirkhiz, X. Tan, Z. Xu, H. Wang, B. C. Olsen, C. M. B. Holt, D. Mitlin. *Adv. Energy Mater.*, 2012, 2(4): 431-437.

[14] Z. Ling, Z. Wang, M. Zhang, C. Yu, G. Wang, Y. Dong, S. Liu, Y. Wang, J. Qiu. *Adv. Funct. Mater.*, 2016, 26(1): 111-119.

[15] C. Ruan, K. Ai, L. Lu. *RSC Adv.*, 2014, 4(58): 30887-30895.

[16] R. Wang, P. Wang, X. Yan, J. Lang, C. Peng, Q. Xue. *ACS Appl. Mater. Interfaces*, 2012, 4(11): 5800-5806.

[17] G. Xu, J. Han, B. Ding, P. Nie, J. Pan, H. Dou, H. Li, X. Zhang. *Green Chem.*, 2015, 17(3): 1668-1674.

[18] L. Sun, C. Tian, M. Li, X. Meng, L. Wang, R. Wang, J. Yin, H. Fu. *J. Mater. Chem. A*, 2013, 1(21): 6462.

[19] C. Huang, T. Sun, D. Hulicova-Jurcakova. *ChemSusChem*, 2013, 6: 2330-2339.

[20] C. Falco, J. M. Sieben, N. Brun, M. Sevilla, T. van der Mauelen, E. Morallon, D. Cazorla-Amoros, M. M. Titirici. *ChemSusChem*, 2013, 6(2): 374-382.

[21] Y. S. Yun, S. Y. Cho, J. Shim, B. H. Kim, S. J. Chang, S. J. Baek, Y. S. Huh, Y. Tak, Y. W. Park, S. Park, H. J. Jin. *Adv. Mater.*, 2013, 25(14): 1993-1998.

[22] M. Biswal, A. Banerjee, M. Deo, S. Ogale. *Energy Environ. Sci.*, 2013, 6(4): 1249-1259.

[23] L. Mao, Y. Zhang, Y. Hu, K. H. Ho, Q. Ke, H. Liu, Z. Hu, D. Zhao, J. Wang, *RSC Adv.*, 2015, 5(12): 9307-9313.

[24] J. Hou, C. Cao, X. Ma, F. Idrees, B. Xu, X. Hao, W. Lin. *Sci. Rep.*, 2014, 4: 7260.

Chapter 4

Chemical energy storage: catalytic CO_2 methanation

Chapter 4.1

CO_2 methanation under dynamic operational mode using nickel nanoparticles decorated carbon felt (Ni/OCF) combined with inductive heating

Abstract

Carbon dioxide (CO_2) hydrogenation to methane (CH_4) (Sabatier reaction) is a fundamental process that meets with several key challenges of our modern society. Besides representing a convenient way to the metal-mediated conversion of a natural and abundant "waste" into a fuel of added value, its combination with H_2 from renewable resources (RES) represents a challenging technology for the RE storage. In addition, its practical exploitation can give a concrete answer to many critical societal and environmental issues largely related to the steadily increase of CO_2 concentration in atmosphere caused by the main anthropic activities. Although many fundamental achievements have been reached since its discovery at the beginning of the twentieth century, alternative and conceptually new protocols for the process can provide valuable solutions to the optimization of the catalyst performance, process energetics and catalyst life-time on stream.

This contribution describes the synthesis of an efficient and robust catalyst for CO_2 methanation, based on Nickel nanoparticles (Ni-NPs) decorated on electrically conductive and macroscopically shaped oxidized carbon-felt disks (OCF), heated at the target reaction temperature by electromagnetic induction. At odds with the more classical external heat sources (based on contact heat conduction), induction heating allows the electromagnetic energy to be directly absorbed by the susceptor (OCF) who converts it into heat to be transferred to the catalyst active sites (Ni NPs). Inductive heating (IH) of Ni/OCF gives CO_2 conversion (X_{CO2}) up to 74% and CH_4 selectivity (S_{CH4}) close to 97% already at 320 °C, showing an excellent control of the catalyst stability under forced dynamic operational conditions.

Keywords

CO_2 methanation; Inductive heating; Oxidized carbon felt; Nickel nanoparticles; Synthetic natural gas.

This chapter is based on the following publication:

W. Wang, C. Duong-Viet, Z. Xu, H. Ba, G. Tuci, G. Giambastiani, Y. Liu, T. Truong-Huu, J. M. Nhut, C. Pham-Huu. *Catal. Today*, 2019, in press, Doi: 10.1016/j.cattod.2019.02.050

4.1.1 Introduction

The restless development of renewable energy sources (RES), *i.e.* solar and wind, calls for the development of more efficient energy storage systems capable to cope with problems related to the extra and intermittent renewable energy supply. Indeed, the fluctuating nature of RES has to be taken into account while managing electricity grids in order to reduce problems linked to security and stability of power networks and ensure a constant supply of electricity on demand [1-3]. Apart from electrochemical storage devices, *i.e.* supercapacitors and batteries, chemical energy storage is a fast growing technology that allows the conversion of exceeding electricity from RES into H_2 (by water electrolysis) [4-6]. The latter is supposed to be used in turn as an energy vector or an intermediate for the production of chemicals and commodities. On this regard, CO_2 hydrogenation [7-10] (Sabatier reaction) using H_2 from RES [11, 12] is a highly promising approach that meets with several key challenges of our modern society. Besides representing a sustainable method towards the production of chemicals and fuels [13-20] from RES it also copes with the main environmental and climate urgencies directly linked to steadily state increase of CO_2 concentration in the atmosphere. Catalytic hydrogenation of CO_2 with H_2 is nowadays at the forefront of many chemical technologies devoted to the production of low molecular weight olefins [21], hydrocarbons [22], formic acid [23], and alcohols [24-26]. It also represents the core business of the PtG technology [5, 6, 27-29]. Indeed, it provides a powerful approach to the production of SNG as fuel (CO_2 methanation) that can be injected in the existing natural gas pipelines, thus creating a virtuous link between existing power networks and natural gas grids [30]. CO_2 methanation is a well-established transformation promoted by a relatively large number of metal active phases [*i.e.* Ni, Ru, Rh, Co, Pd nanoparticles (NPs)] deposited on various oxide supports (*i.e.* TiO_2, SiO_2, Al_2O_3, CeO_2, MgO and ZrO_2) [31-40]. It is a highly exothermic process (ΔH = -165 $kJ \cdot mol^{-1}$) and thus, thermal conductive supports (carbon nanotubes, graphene, and silicon carbide just to mention a few) [41-45] are generally recommended in order to prevent as much as possible the generation of local temperature gradients (hot spots) inside the catalyst bed during the process. Indeed, the generation of "hot spot" inside the catalyst can be largely detrimental both in terms of catalyst life-time and performance of the methanation process.

PtG technical chain urgently needs of novel concepts and breakthroughs to

optimize performance of existing plants and to cope as much as possible with dynamic operational conditions that often occur within the reactor. One main dynamic parameter to be controlled is represented by the intermittent nature of reactants supply from RES. Such dynamic conditions can be responsible for the occurrence of severe temperature fluctuations within the reactor, not easy to be controlled even in apparatus equipped with external cooling systems [46].

Induction heating (IH) represents a valid alternative to the more traditional Joule heating (JH) approach, with the former listing a series of key advantages compared to the latter in the heating of electrically conductive materials. Induction heating is likely a cleaner, efficient, cost-effective, precise and repeatable method for providing heat necessary for chemical processes to occur. Heating takes place on electrically conductive objects when they are placed in a varying magnetic field and it occurs precisely where heat is needed and not to the whole volume of the medium and the gaseous reactants; it is also defined as a noncontact heating method. Such a heating scheme allows for rapid up/down temperature ramps (*i.e.* hundred degrees per minute), with great potentials for large scale and rapid manufacturing processes and improved energy efficiencies [47].

IH is expected to be a technique of choice for operating heterogeneous catalysis and in particular for those processes where high heat targeting along with fast heating/cooling rate provide key control on the reaction course and catalyst stability on stream, *i.e.* rapid temperature gradient control during exothermic or endothermic processes also caused by variable reagents loads. Most importantly, the temperature control at the catalyst sites can be directly monitored by a laser pyrometer that maps the catalyst temperature in real time (and not that of the reactor) thus allowing an extremely fast response to any temperature deviation occurring at the catalyst bed. By this way, the catalyst operates under almost isothermal conditions.

IH has already been used with success for running liquid-phase catalytic reactions [48, 49] and recently for the gas-phase CO_2 methanation reaction. On the latter process, Bordet et al. [50] have elegantly demonstrated the use of the induction heating with Ni-coated iron-carbide NPs (ICNPs@Ni) or ICNPs supported on Ru-doped Silica-alumina hydrate oxides (SIRALox) as catalysts for continuous-flow reactors working under atmospheric pressure. For both their systems, the authors idea was to take advantage of ICNPs heating capacities and transfer the heat released from that NPs to activate either their Ni-coating or the neighboring Ru NPs, thus catalyzing the Sabatier process.

In this work we describe the straightforward synthesis of Ni NPs decorated on a highly defective carbon felt (Ni/OCF) support and the use of the composite as a stable and effective heterogeneous catalyst for CO_2 methanation powered by an IH setup. We took advantage from the high and rapid heat response (heating/cooling) of OCF to magnetic stimuli of the inductive heater for a rapid temperature control at the heart of the catalytic system. Such a configuration provides an effective way to control the catalyst temperature from sudden deviations especially occurring during the start/stop of the catalytic runs where gradients of reactants loads can be formed.

4.1.2 Experimental section

Materials, catalyst preparation and characterization: please refer to **Chapter 2.1.2** and **Chapter 2.2**. Nickel loading was fixed by Inductively Coupled Plasma Atomic Emission spectrophotometry (ICP-AES) after complete acidic mineralization of NiO_x/OCF sample, using an Optima 2000 Perkin Elmer Inductively Coupled Plasma Dual Vision instrument; And the effective nickel charge was then fixed to 8.4 wt.%.

The CO_2 methanation reaction was carried out under atmospheric pressure in a fixed-bed quartz tubular reactor [Ø(ID) 20 mm, length of 600 mm] charged with the disk catalyst and equipped with an advanced EASYHEAT IH system for the precise control of the reaction temperature. Prior of each experiment, the catalyst was reduced at 350 °C for 1 h under a stream of H_2 (100 $mL \cdot min^{-1}$). CO_2 and H_2 were fed into the reactor with a well-defined molar ratio by a series of calibrated Mass Flow Controllers (Brookhorst®). For comparative CO_2 methanation trials carried out using a classical external heater, the quartz tube reactor containing Ni/OCF was housed inside an electric furnace controlled by a thermocouple for the monitoring of the temperature ramp. In a typical run, gas mixture with H_2-to-CO_2 ratio of 4/1 (v/v) was admitted at the top of the reactor and passed downward through the catalytic disk. Reactants and products were analyzed on-line. The CO_2 conversion and CH_4 selectivity are calculated by Eq. (20) and Eq. (21), please refer to **Chapter 2.3.2**.

For the present CO_2 methanation study, catalyst underwent a series of successive start and shut-down steps as to simulate the dynamic operation conditions of a CO_2 methanation plant as a consequence of the intermittent nature in reactants supply. To this aim, the start/stop process was operated as follows: at the steady-state (320 °C) the reaction temperature was decreased to 260 °C and the reactants flow was replaced by

helium for 15 minutes before raising rapidly again the reaction temperature to 320 °C (or 340 °C) and re-start the reactants flow supply. Such start/stop sequences are repeated several times in order to evaluate all possible deactivation/alteration effects occurring on Ni/OCF.

The induction heating setup (EasyHeat LI) was purchased from Ambrell Ltd. (Netherlands). It consists in a spiral 6-turn induction coil internally cooled with recirculated water (10% glycerol) provided by an external chiller. The quartz reactor containing the catalyst is placed inside induction heater coils as shown in Fig. 1. Temperature regulation was ensured by a PID system (Eurotherm model 3504) connected to a laser pyrometer (Optris®, Germany, **Fig. 1**) working in the 150 - 1000 °C temperature range (accuracy at ambient temperature 23 ± 5°C), for the real-time control of the temperature inside the catalyst bed. The heating/cooling rate allowed for the system is in the order of c.a. 200 $^{o}C \cdot min^{-1}$.

Fig. 1. Digital photos of the Ni/OCF catalyst in the quartz tubular reactor placed inside the coils of the inductive heater along with the laser pyrometer for the control of the temperature inside the catalyst bed.

4.1.3 Results and discussion

The acid treatment of CF is used to confer a hydrophilic character to the pristine hydrophobic material as to get a more wettable surface for the impregnation step with an aqueous solution of $[Ni(NO_3)_2 \cdot 6H_2O]$. Although such an acid treatment deeply contributes to the modulation of the chemico-physical properties (vide infra) of the CF surface (**Fig. S1** and **Table S1**), it negligibly affects the sample's macroscopic shape. Accordingly, the catalyst shape can be fixed at priori on the pristine CF as a function of its final downstream application (**Fig. 2A**). SEM and TEM micrographs of OCF at

different magnifications show a composition made of carbon microfilaments with an average diameter of 10 ± 1 µm, featured by a highly defective and low structured C-surface morphology (**Fig. 2B-E**). Indeed, the initial oxidation treatment with HNO_3 vapors is supposed to deeply modify the CF surface properties in terms of chemical composition (*i.e.* formation of oxygenated functional groups on highly defective C-atoms), specific surface area (SSA) and pore-size distribution (vide infra) [51].

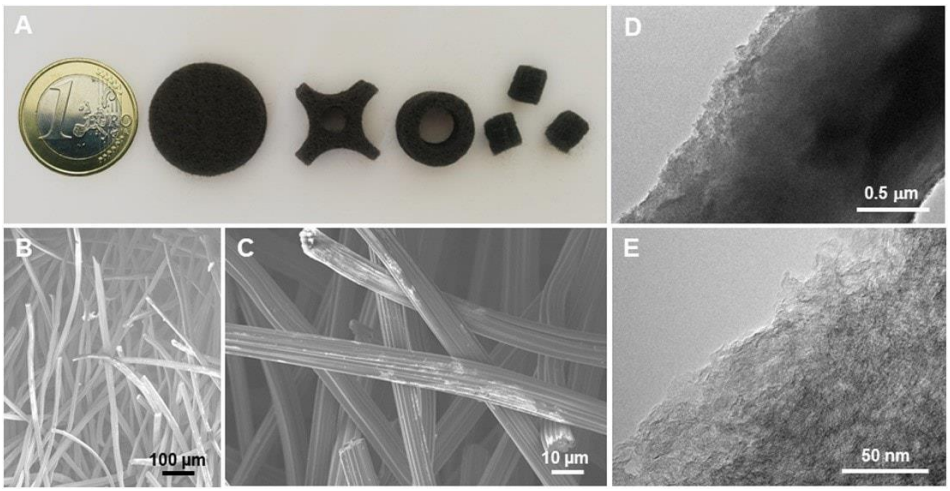

Fig. 2. (A) Examples of macroscopic shapes available for potential applications. (B) SEM micrograph of CF. (C to E) Representative SEM and TEM micrographs of the OCF sample after acid treatment showing the formation of disordered carbon structure at the outer material surface.

TGA/DTG profiles of the CF samples before and after acid treatment are outlined in **Fig. 3A**. OCF displays a significant decrease of the oxidation temperature compared to its pristine counterpart. This trend is in line with the presence on OCF of a reduced degree of structured carbons [51, 52]. Most importantly, the oxidative treatment translates in a significant change of the material SSA that increases from about 2 (CF) to 689 $m^2 \cdot g^{-1}$ (OCF) (**Fig. 3B** and **Table 1**). After OCF impregnation with a solution of catalyst precursor and calcination, the SSA of the composite is reduced down to 463 $m^2 \cdot g^{-1}$ in line with a modification of the material morphology as a consequence of the calcination treatment and the partial pore clogging caused by the NiO NPs deposition (Fig. 3B and Table 1).

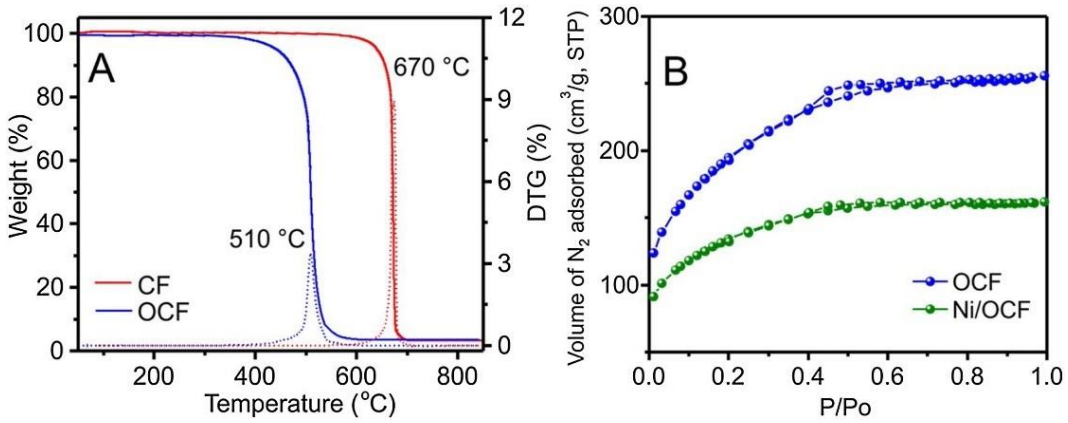

Fig. 3. (A) TGA/DTG profiles of the CF and OCF recorded under an oxidative flow (O_2/He: 20/80 v/v%, 30 mL·min^{-1}) in the 50 - 850 °C temperature range. (B) N_2 adsorption-desorption isotherms of the support and catalyst.

Table 1. Specific surface area (SSA), total and micropore volume of the samples.

Sample	SSA[a] [$m^2 \cdot g^{-1}$]	$V_{p(total)}$[b] [$cm^3 \cdot g^{-1}$]	$V_{p(micro)}$[c] [$cm^3 \cdot g^{-1}$] (%)[d]
CF	≈ 2	0.004	n.d.
OCF	689	0.26	0.038 (14.6%)
NiO_x/OCF	463	0.45	0.037 (8.2%)

[a] Brunauer-Emmett-Teller (BET) specific surface area (SSA); [b] Total pore volume determined by using the adsorption branch of N_2 isotherm at p/p_0 = 0.98; [c] Micropore volume calculated by t-Plot method; [d] % of micropore volume over $V_{p(total)}$.

Both samples exhibit a Type IV isotherm with a moderate but distinctive (for OCF in particular) H_4 hysteresis loop in the range of 0.4-1.0 p/p_0, typical of mesoporous structures featured by complex pore networks of ill-defined shape [53]. Under the reduction condition, NiO could be effectively reduced to Ni (**Fig. S2**). The NPs distribution on the Ni/OCF catalyst, after calcination/reduction, was analyzed by TEM and the representative images of the sample at different magnifications are given in **Fig. 4 (A, B)**. TEM micrographs reveal a roughly monodisperse and dense distribution of Ni NPs all over the sample with an average particle size of about 4 ± 1 nm (refers to the particle size distribution as measured over 200 NPs). The relatively narrow Ni NPs dispersion on OCF can be ascribed to a non-innocent role played by the oxidized nanocarrier. Indeed, relatively strong interactions between the Ni salt precursor and the

highly defective and hydrophilic OCF surface are thought to be crucial for limiting NPs agglomeration phenomena throughout all thermal phases the composite undergoes.

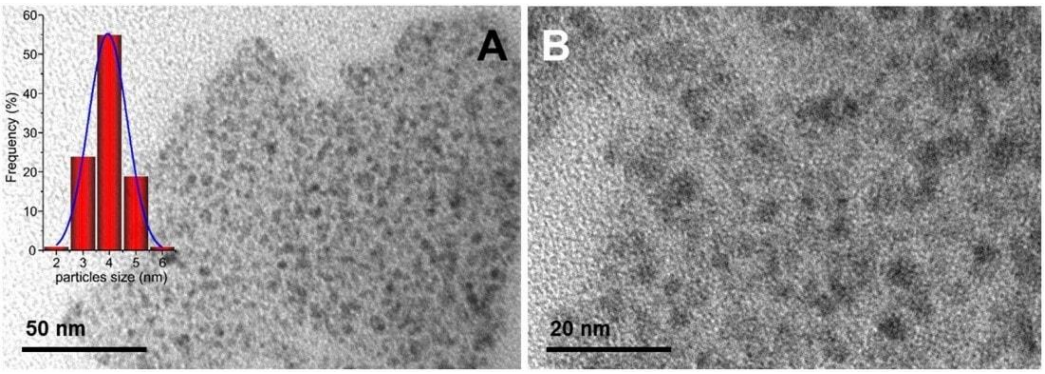

Fig. 4. (A, B) Low and medium magnification TEM micrographs of Ni/OCF.

The influence of the reaction temperature: In a typical methanation run, the catalyst is fixed in a quartz tubular reactor, housed inside the inductor heating coils and pre-treated for 1 h at 350 °C under a stream of pure H_2. Afterwards, the temperature of the reduced Ni/OCF catalyst is fixed at the desired target value and a H_2/CO_2 mixture (4 v/v ratio) is introduced downward through the catalyst bed at ambient pressure and at a GHSV of 30,000 $mL \cdot g_{cat}^{-1} \cdot h^{-1}$. CO_2 conversion (X_{CO2}) and methane selectivity (S_{CH4}) measured in the 160 - 380 °C temperature range are outlined in **Fig. 5**. According to literature precedents, X_{CO2} steadily increases while increasing the reactor temperature and it rapidly approaches conversion values close to those at the thermodynamic equilibrium (**Fig. S3**) [54-56]. Noteworthy, Ni/OCF offers excellent performance already at moderately high temperature values. Indeed, it reaches a X_{CO2} up to 74% with a S_{CH4} close to 97% at 320 °C under the same experimental conditions mentioned above (H_2/CO_2 = 4 v/v ratio; GHSV = 30,000 $mL \cdot g_{cat}^{-1} \cdot h^{-1}$). This result is even more relevant if we consider that Ni/OCF operates under more severe reaction conditions compared to many other systems reported so far, using pure reactants flows with no need of their dilution by any inert carrier. CO represents the unique reduction intermediate for the process detected along with CH_4 at the reactor outlet. For methanation trials at temperatures < 300 °C, S_{CH4} is rather moderate because of the kinetic stability of CO that makes its conversion into CH_4 hard to be accomplished under these conditions. At higher temperatures, (*i.e.* > 320 °C) both X_{CO2} and S_{CH4} decrease mainly as a consequence of side processes at work *i.e.* steam reforming (< S_{CH4}), water-gas shift (< X_{CO2}) or reverse water-gas shift reactions (< S_{CH4}) [57].

For the sake of comparison with a more traditional external heating system (JH), the methanation process was repeated on a new batch of Ni/OCF under the same catalytic conditions operated above except for the use of an electrical furnace for the set-up of the target reaction temperature. Accordingly, the reactor containing the reduced Ni/OCF catalyst was housed inside the electric furnace equipped with a thermocouple for the monitoring the temperature ramp and with a second temperature controller placed in contact with the catalyst bed. Under these conditions, Ni/OCF performance changes significantly with a X_{CO2} that is reduced down by a factor of 57% (at 320 °C) respect to the value measured under IH at the same temperature (X_{CO2}^{IH} and X_{CO2}^{JH} at 320 °C are 74% and 32%, respectively; **Fig. 5**).

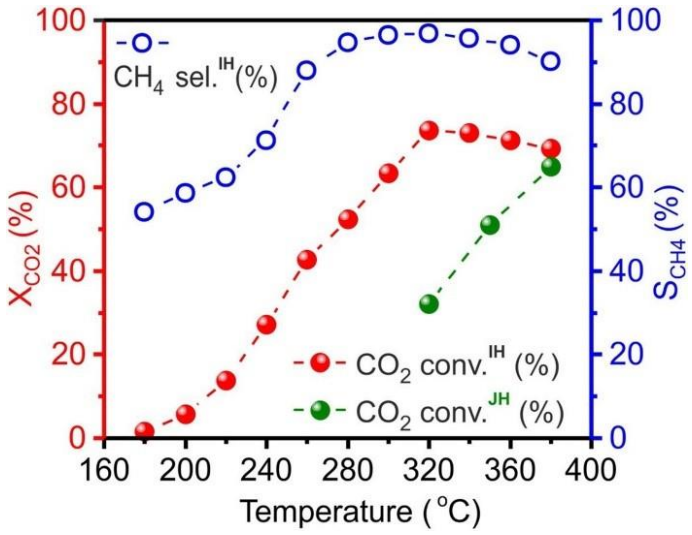

Fig. 5. CO_2 methanation runs with Ni/OCF catalyst operated by induction heating (IH) and classical Joule heating (JH). Reaction conditions: m (catalyst) = 0.23 g, GHSV (STP) = 30,000 mL·g_{cat}^{-1}·h^{-1}), [CO_2] = 20%, [H_2] = 80%, H_2-to-CO_2 v/v ratio = 4.

Noteworthy, under JH conditions, Ni/OCF catalyst reaches a X_{CO2} value of 65% (S_{CH4} = 92.5%, **Fig. S4**) only after increasing the reactor temperature over 380 °C. Such a result can be ascribed to the effectiveness of the induction heating approach that supplies the heat necessary for the process directly to the catalyst. Besides providing a precise and easily tuning temperature control at the catalyst bed throughout the reaction process, IH largely prevents heat losses mainly due to conduction and convection phenomena typical of contact heating modes (*i.e.* JH). This aspect is crucial for many industrial processes where limited catalyst performance is often due to physical constraints related to an effective heat transfer to the catalyst rather than to the inherent

catalyst activity. Rostrup-Nielsen and co-workers [58] have calculated that only 10% (or even less) of the external heating provided to reformer tubes is employed in the catalytic process, while the (large) remaining part is dissipated by heat transfer restrictions encountered in contact heating modes from the heat source to the catalyst. Recently, Vinum et al. [59] have described the use of dual-function Co-Ni NPs in combination with the induction heating as unique energy source for operating steam methane reforming (SMR). At odds with more classical heating supply systems, the authors have concluded that under IH the catalyst operates at its kinetic limit; *i.e.* the catalyst performance is limited by the reaction kinetic and not by the heat transfer.

Influence of dynamic operational modes on Ni/OCF. As a model trial for testing Ni/OCF under dynamic conditions, successive start/stop process cycles have been investigated while keeping the catalyst under variable reaction temperatures, GHSVs and using pure reactants as reaction feed. These trials are made possible due to the fine and almost instantaneous catalyst temperature control within the processes operated under induction heating. Indeed, heating and cooling rates with IH are extremely fast (*i.e.* $\geq 200°C \cdot min^{-1}$) and they can be easily controlled avoiding sudden and detrimental temperature deviations on the catalyst at work. A complete overview of several start/stop CO_2 methanation cycles carried out with Ni/OCF under variable conditions (temperature and GHSV) is presented on **Fig. 6**.

According to the catalytic outcomes (X_{CO2} and S_{CH4}), successive start/stop cycles consisting in a rapid catalyst cooling/heating in the 260 - 320 °C temperature range and simultaneous replacement of the H_2/CO_2 feed with Helium, do not show any appreciable modification of the catalyst performance even after several cycles. Noteworthy, such start/stop tests cannot be run under conventional heating mode (*i.e.* JH) because of longer time required for the cooling and heating phases. Moreover, fast heating/cooling rates along with a fine control of the target temperature at the catalyst bed provide the reactor with a powerful tool for the control (almost in real time) of the phenomena related to the discontinuous supply of reagents into the reactor.

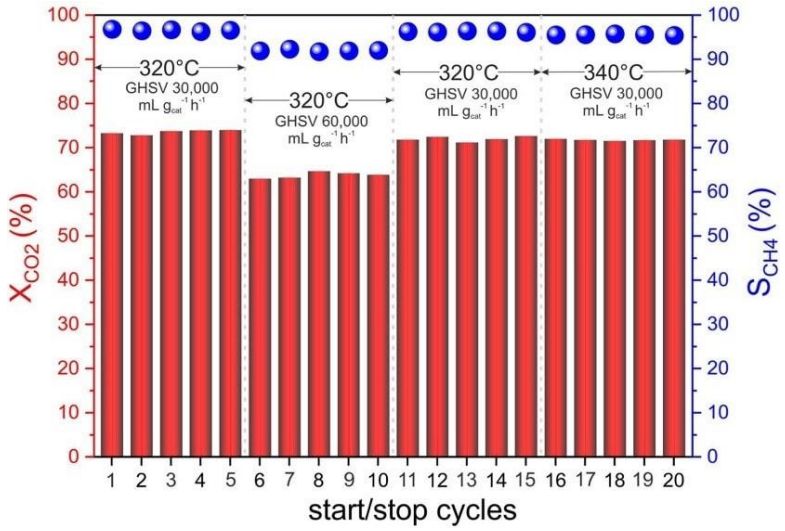

Fig. 6. Ni/OCF catalytic performance miming dynamic operational conditions in the form of successive start/stop cycles under different temperature and GHSV. Reaction conditions: m (catalyst) = 0.23 g, GHSV (STP) = 30,000 or 60,000 mL·$g_{cat.}^{-1}$·h^{-1}; H_2-to-CO_2 = 4 v/v ratio; reaction temperatures and time: 320 °C or 340 °C for 1 h; hold-on temperature value for the shut-down period: 260 °C for 0.25 h.

Indeed, a fine and fast temperature control is crucial to avoid sudden temperature raises at the catalyst bed, thus limiting detrimental effects for the catalyst (*i.e.* decomposition and/or NPs sintering) and the catalytic process. Besides the role played by the support thermal conductivity, the generation of local temperature gradients ("hot spots") inside the catalyst can be conveniently balanced by the high heating/cooling rates operated with the IH system. It is known that local temperature gradients at the catalyst bed can be generated in the CO_2 methanation even within reactors operating at low GHSVs and using reagent feeds diluted with inert carriers [45]. Accordingly, their generation can have even more drastic effects in reactors working at higher GHSV and fed with pure reactants flows. In the CO_2 methanation with Ni/OCF operated by IH, the combination of the temperature control inside the catalyst (ensured by IH mode) together with the medium thermal conductivity of the OCF support, provide a robust and effective system for the process where the generation of local "hot spots" is largely prevented if not totally suppressed. This key feature well matches with the high catalyst stability under the discontinuous (start/stop) and dynamic (temperature and GHSVs) operational modes described above for the Sabatier reaction. As an additional proof of the Ni/OCF stability on stream, long-term evaluation tests have been properly addressed under constant reaction conditions.

Long-term stability evaluation tests. The stability of Ni/OCF to perform CO_2 methanation efficiently has also been investigated as a function of the catalyst time on stream and results are presented on **Fig. 7**. Ni/OCF displays a high and stable CO_2 conversion for more than 80 h on stream thus indicating that deactivation phenomena (*i.e.* active phase sintering, metal-nanoparticles passivation by coke deposits or metal leaching) are unlikely to occur under these conditions. Wang and co-workers [60] have recently shown how unpromoted Ni NPs decorated carbon nanotubes (Ni/CNTs) as a catalyst for the CO_2 methanation, gradually deactivates over time on stream, mainly due to the generation of coke deposits.

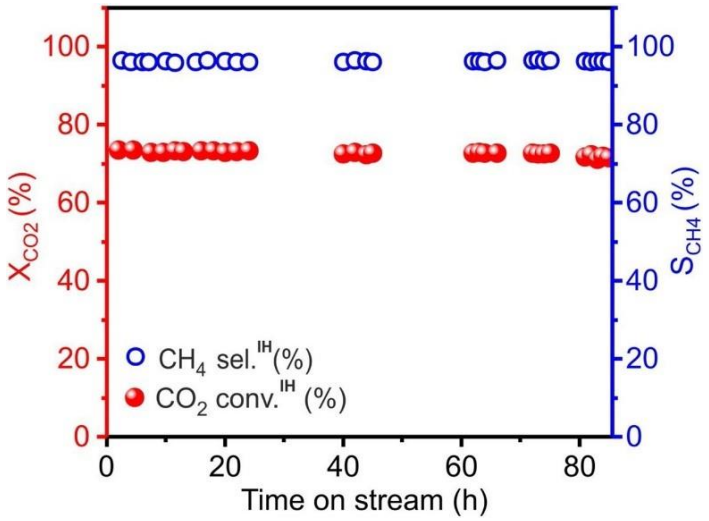

Fig. 7. Long-term evaluation tests with Ni/OCF catalyst. Reaction conditions: m (catalyst) = 0.23 g, GHSV (STP) = 30,000 $mL \cdot g_{cat}^{-1} \cdot h^{-1}$; H_2/CO_2 (v/v) = 4; reaction temperature = 320 ºC, 1 atm.

Feng [43], Centi [61] and Stangeland [54] have also described Ni-based catalysts for the process, using different alumina or promoted supports. Examples from this series show that catalyst deactivation can also take place through Ni NPs sintering induced by the local generation of temperature gradients that progressively reduce the number of available active sites. TEM analysis of the exhaust Ni/OCF catalyst (**Fig. 8A-B**) is used to unveil the stability of the composite on stream. A comparative analysis of Ni NPs on the exhaust catalyst (after more than 80 h on stream) with those of its freshly prepared counterpart (see Fig. 4A-B) shows only a moderate NPs sintering.

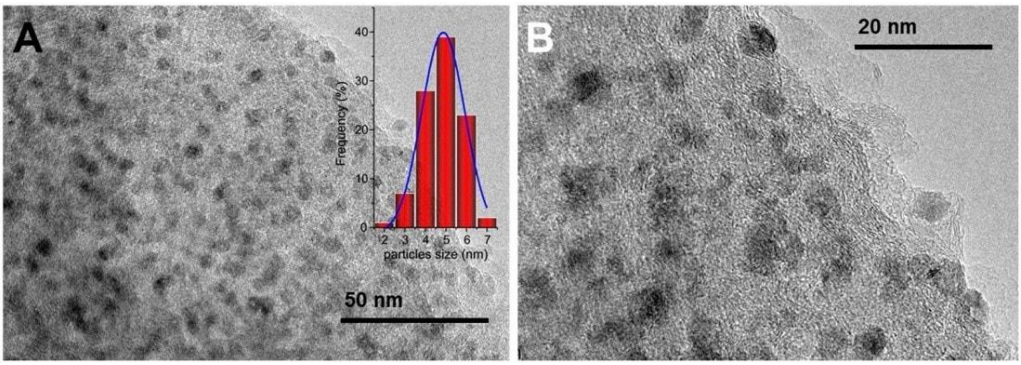

Fig. 8. (A, B) Low and medium magnification TEM micrographs of the exhaust Ni/OCF catalyst after long-term evaluation test (> 80 h).

TEM micrographs show that exhaust catalyst maintains a similar dispersion and distribution of Ni NPs than its pristine counterpart with an average particle size distribution of about 5 ± 1 nm and the absence of any macro-aggregate all over the scanned area. Such a high thermal resistance of Ni NPs throughout the whole catalytic run is also ascribed to the existence of relatively strong interactions engaged between NPs and the highly defective OCF support. These evidences indirectly confirm the excellent thermal control at the catalyst active phase ensured by IH and the OCF thermal conductivity. Both of features have largely beneficial effects on the catalyst stability, in particular with respect to the control on the generation of local temperature gradients that can easily start NPs sintering phenomena.

4.1.4 Conclusion

In summary, an efficient and robust catalyst for the CO_2 methanation, based on nickel nanoparticles (Ni NPs) decorated on electrically conductive and macroscopically shaped oxidized carbon-felt disks (OCF), has been prepared and heated at the target reaction temperature by electromagnetic induction heating (IH) approach. IH is proved to have largely beneficial effects on the catalyst performance compared to the more classical Joule heating methods. Indeed, the electromagnetic energy provided by the induction heater can be directly absorbed by the electrically conductive susceptor (OCF) who converts it into heat to be transferred to Ni NPs [62]. By this way, an almost real-time control of the target temperature at the catalyst active sites can be set-up with valuable advantages in terms of process energetics, catalyst efficiency and catalyst stability on stream. Indeed, the fast temperature regulation rate (hundreds of °C per min)

ensured by IH, can control and balance undesired and sudden temperature changes at the catalyst bed. As a matter of fact, temperature fluctuation at the catalyst bed, frequently encountered in real systems (as the consequence of a discontinuous supply of reagents loads), can be finely controlled thus allowing the reactor to operate under virtually isothermal conditions. IH of Ni/OCF gives CO_2 conversion up to 74% and CH_4 selectivity close to 97% already at 320 °C using pure reactants flows with no need of their dilution by any inert carrier. Noteworthy, the same catalyst under a more conventional JH control, reaches X_{CO2} value of 65% and S_{CH4} of 92.5% for a reactor temperature set-up to 380 °C.

Ni/OCF has also shown an excellent stability upon IH when forced dynamic operational conditions are applied. In a model trial, dynamic operational modes have been expressly forced in the system as to mimic the process discontinuity under conditions close to those operated in real plant. Accordingly, several and sequential start/stop cycles have been run, including changes in the target reaction temperature and GHSV, thus unveiling the extremely high stability of Ni/OCF under harsh experimental conditions. Finally, a long-term experiment (> 80 h) has been used to confirm the stability of the catalyst after several hours on stream. TEM analyses of the exhaust Ni/OCF have been finally used to rule out the occurrence of any appreciable NPs sintering throughout the process. Moreover, NPs passivation by the generation of coke deposits seems to be unlikely to occur due to the efficient heat management within the process ensured by IH. Studies on Ni/OCF in CO_2 methanation under more severe reaction conditions are currently ongoing in our labs and will be reported.

Reference

[1] R. Schlögl (Ed.). *Chemical Energy Storage*. Berlin: De Gruyter, 2013.

[2] T. M. Gür. *Energy Environ. Sci.*, 2018, 11(10): 2696-2767

[3] F. Mohamad, J. Teh, C. M. Lai, L. R. Chen. *Energies*, 2018, 11(9): 2278.

[4] www.powertogas.info/power-to-gas/pilotprojekte-im-ueberblick/audi-e-gas-projekt/.

[5] M. Jentsch, T. Trost, M. Sterner. *Energy Procedia*, 2014, 46: 254-261.

[6] K. Hashimoto, N. Kumagai, K. Izumiya, H. Takano, Z. Kato. *Energy Sustain. Soc.*, 2014, 4: 17.

[7] J. Ma, N. Sun, X. Zhang, N. Zhao, F. Xiao, W. Wei, Y. Sun. *Catal. Today*, 2009, 148(1-3): 221-231.

[8] P. G. Jessop, F. Joo, C. C. Tai. *Coord. Chem. Rev.*, 2004, 248(21-24): 2425-2442.

[9] W. Wang, S. Wang, X. Ma, J. Gong. *Chem. Soc. Rev.*, 2011, 40(7): 3703-3727.

[10] S. Saeidi, N. A. S. Amin, M. R. Rahimpour. *J. CO_2 Util.*, 2014, 5: 66-81.

[11] G. Centi, S. Perathoner. *Catal. Today*, 2009, 148(3-4): 191-205.

[12] G. Centi, S. Perathoner. *Greenhouse Gases: Sci. Technol.*, 2011, 1(1): 21-35.

[13] L. Zhou, Q. Wang, L. Ma, J. Chen, J. Ma, Z. Zi. *Catal. Lett.*, 2015, 145(2): 612-619.

[14] A. Westermann, B. Azambre, M. C. Bacariza, I. Graca, M. F. Ribeiro, J. M. Lopes, C. Henriques. *Appl. Catal., B*, 2015, 174: 120-125.

[15] D. C. Upham, A. R. Derk, S. Sharma, H. Metiu, E. W. McFarland. *Catal. Sci. Technol.*, 2015, 5(3): 1783-1791.

[16] N. Shimoda, D. Shoji, K. Tani, M. Fujiwara, K. Urasaki, R. Kikuchi, S. Satokawa. *Appl. Catal., B*, 2015, 174: 486-495.

[17] R. Razzaq, C. Li, M. Usman, K. Suzuki, S. Zhang. *Chem. Eng. J.*, 2015, 262: 1090-1098.

[18] S. K. Beaumont, S. Alayoglu, C. Specht, W. D. Michalak, V. V. Pushkarev, J. Guo, N. Kruse, G. A. Somorjai. *J. Am. Chem. Soc.*, 2014, 136(28): 9898-9901.

[19] F. Wang, C. Li, X. Zhang, M. Wei, D. G. Evans, X. Duan. *J. Catal.*, 2015, 329: 177-186.

[20] M. D. Porosoff, B. Yan, J. G. Chen. *Energy Environ. Sci.*, 2016, 9(1): 62-73.

[21] C. G. Visconti, M. Martinelli, L. Falbo, A. Infantes-Molina, L. Lietti, P. Forzatti, G. Iaquaniello, E. Palo, B. Picutti, F. Brignoli. *Appl. Catal., B*, 2017, 200: 530-

542.

[22] P. Gao, S. Li, X. Bu, S. Dang, Z. Liu, H. Wang, L. Zhong, M. Qiu, C. Yang, J. Cai, W. Wei, Y. Sun. *Nat. Chem.*, 2017, 9(10): 1019-1024.

[23] H. Song, N. Zhang, C. Zhong, Z. Liu, M. Xiao, H. Gai. *New J. Chem*., 2017, 41(17): 9170-9177.

[24] K. Larmier, W. C. Liao, S. Tada, E. Lam, R. Verel, A. Bansode, A. Urakawa, A. Comas-Vives, C. Coperet. *Angew. Chem. Int. Ed.*, 2017, 56(9): 2318-2323.

[25] X. Jiang, N. Koizumi, X. Guo, C. Song. *Appl. Catal., B*, 2015, 170: 173-185.

[26] S. Bai, Q. Shao, P. Wang, Q. Dai, X. Wang, X. Huang. *J. Am. Chem. Soc.*, 2017, 139(20): 6827-6830.

[27] G. Gahleitner. *Int. J. Hydrogen Energy*, 2013, 38(5): 2039-2061.

[28] C. Graves, S. D. Ebbesen, M. Mogensen, K. S. Lackner. *Renew. Sust. Energy Rev.*, 2011, 15(1): 1-23.

[29] M. Götz, J. Lefebvre, F. Mörs, A. M. Koch, F. Graf, S. Bajohr, R. Reimert, T. Kolb. *Renew. Energy*, 2016, 85: 1371-1390.

[30] W. Li, H. Wang, X. Jiang, J. Zhu, Z. Liu, X. Guo, C. Song. *RSC Adv.*, 2018, 8: 7651-7669.

[31] J. Martins, N. Batail, S. Silva, S. Rafik-Clement, A. Karelovic, D. P. Debecker, A. Chaumonnot, D. Uzio. *Catal. Commun.*, 2015, 58: 11-15.

[32] J. Zheng, C. Wang, W. Chu, Y. Zhou, K. Köhler. *ChemistrySelect*, 2016, 1(12): 3197-3203.

[33] S. Abate, C. Mebrahtu, E. Giglio, F. Deorsola, S. Bensaid, S. Perathoner, R. Pirone, G. Centi. *Ind. Eng. Chem. Res.*, 2016, 55(16): 4451-4460.

[34] N. Bette, J. Thielemann, M. Schreiner, F. Mertens. *ChemCatChem*, 2016, 8(18): 2903-2906.

[35] Y. Traa, J. Weitkamp. *Chem. Eng. Technol.*, 1999, 22(4): 291-293.

[36] R. E. Owen, J. P. O'Byrne, D. Mattia, P. Plucinski, S. I. Pascua, M. D. Jones. *Chem. Commun.*, 2013, 49(99): 11683-11685.

[37] R. Büchel, A. Baiker, S. E. Pratsinis. *Appl. Catal., A*, 2014, 477: 93-101.

[38] J. H. Kwak, L. Kovarik, J. Szanyi. *ACS Catal.*, 2013, 3(9): 2449-2455.

[39] S. Sharma, Z. Hu, P. Zhang, E. W. McFarland, H. Metiu. *J. Catal.*, 2011, 278(2): 297-309.

[40] J. N. Park, E.W. McFarland. *J. Catal.*, 2009, 266(1): 92-97.

[41] L. Li, J. Zheng, Y. Liu, W. Wang, Q. Huang, W. Chu. *ChemistrySelect*, 2017,

2(13): 3750-3757.

[42] L. Roldàn, Y. Marco, E. Garcìa-Bordejé. *ChemSusChem*, 2017, 10: 1139-1144.

[43] Y. Feng, W. Yang, S. Chen, W. Chu. *Integr. Ferroelectr.*, 2014, 151: 116-125.

[44] J. P. O'Byrne, R. E. Owen, D. R. Minett, S. I. Pascu, P. K. Plucinski, M. D. Jones, D. Mattia. *Catal. Sci. Technol.*, 2013, 3(5): 1202-1207.

[45] M. Frey, T. Romero, A.-C. Roger, D. Edouard. *Catal. Today*, 2016, 273: 83-90.

[46] J. Kopyscinski, T. J. Schildhauer, S. M. A. Biollar. *Fuel*, 2010, 89: 1763-1783.

[47] R. Piner, H. Li, X. Kong, L. Tao, I. N. Kholmanov, H. Ji, W. H. Lee, J. W. Suk, J. Ye, Y. Hao, S. Chen, C. W. Magnuson, A. F. Ismach, D. Akinwande, R. S. Ruoff. *ACS Nano*, 2013, 7(9): 7495-7499.

[48] S. Ceylan, C. Friese, C. Lammel, K. Mazac, A. Kirschning. *Angew. Chem. Int. Ed.*, 2008, 47(46): 8950-8953.

[49] S. Ceylan, L. Coutable, J. Wegner, A. Kirschning. *Chem. Eur. J.*, 2011, 17(6): 1884-1893.

[50] A. Bordet, L. M. Lacroix, P. F. Fazzini, J. Carrey, K. Soulantica, B. Chaudret. *Angew. Chem. Int. Ed.*, 2016, 55(51): 15894-15898.

[51] Z. Xu, C. Duong-Viet, H. Ba, B. Li, T. Truong-Huu, L. Nguyen-Dinh, C. Pham-Huu. *Catalysts*, 2018, 8(4): 145.

[52] J. Luo, H. Wei, Y. Liu, D. Zhang, B. Zhang, W. Chu, C. Pham-Huu, D. S. Su. *Chem. Commun.*, 2017, 53(95): 12750-12753.

[53] K. S. W. Sing, D. H. Everett, R. A. W. Haul, L. Moscou, R. A. Pierotti, J. Rouquérol. *Pure Appl. Chem.*, 1985, 57(4): 603-619.

[54] K. Stangeland, D. Y. Kalai, H. Li, Z. Yu. *Appl. Energy*, 2018, 227: 206-212.

[55] J. Gao, Y. Wang, Y. Ping, D. Hu, G. Xu, F. Gu, F. Su. *RSC Adv.*, 2012, 2(6): 2358-2368.

[56] F. Koschany, D. Schlereth, O. Hinrichsen. *Appl. Catal., B*, 2016, 181: 504-516.

[57] A. Yamaguchi, E. Iglesia. *J. Catal.*, 2010, 274(1): 52-63.

[58] K. Aasberg-Petersen, J.-H. Bak Hansen, T. S. Christensen, I. Dybkjaer, P. Seier Christensen, C. Stub Nielsen, S. E. L. Winter Madsen, J. R. Rostrup-Nielsen. *Appl. Catal., A*, 2001, 221(1-2): 379-387.

[59] M. G. Vinum, M. R. Almind, J. S. Engbæk, S. B. Vendelbo, M. F. Hansen, C. Frandsen, J. Bendix, P. M. Mortensen. *Angew. Chem. Int. Ed.*, 2018, 57(33): 10569-10573.

[60] W. Wang, W. Chu, N. Wang, W. Wang, C. Jiang. *Int. J. Hydrogen Energy*, 2016,

41: 967-975.

[61] C. Mebrahtua, S. Abate, S. Perathoner, S. Chen, G. Centi. *Catal. Today*, 2018, 304: 181-189.

[62] A susceptor is defined any material that can be easily heated by IH and which passes its heat to another material by radiation, convection or conduction.

Supporting Information

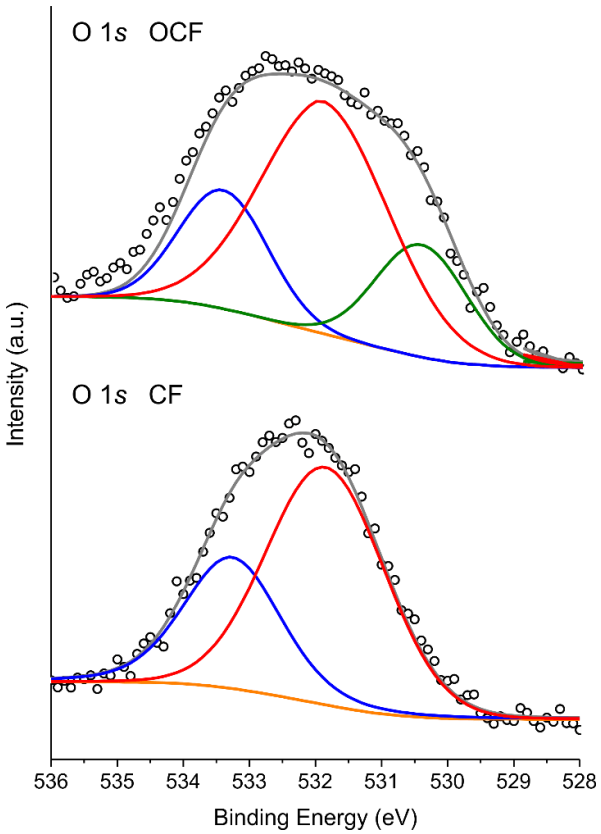

Fig. S1. X-ray photoelectron spectroscopy (XPS), O 1s core region of CF and OCF and their respective peaks deconvolution at comparison.

Table S1. O % as measured by XPS analysis on CF before and after the oxidation treatment.

		O-containing functionalities[a]		
	O %[a]	C-O 533.3±0.1 eV	O-C=O 531.9±0.1 eV	C=O 530.4 eV
CF	0.65	0.21	0.44	-
OCF	0.86	0.17	0.52	0.17

[a] Determined by XPS analyses.

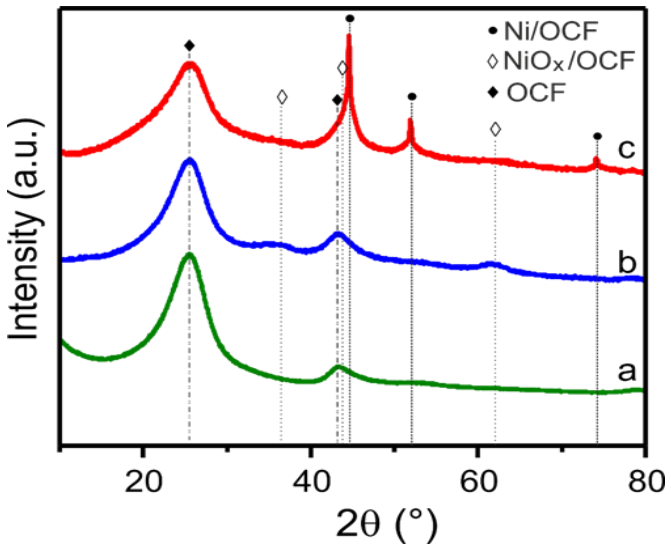

Fig. S2. XRD profiles of (a) OCF, (b) NiO_x/OCF and (c) Ni/OCF. Diffraction peaks at 2θ = 44.5° and 51.8° are attributed to the (111), and (200) planes of Ni^0 NPs whereas diffraction peaks at 2θ = 37.09°, 43.10° and 62.58° are ascribed to the NiO [1-3].

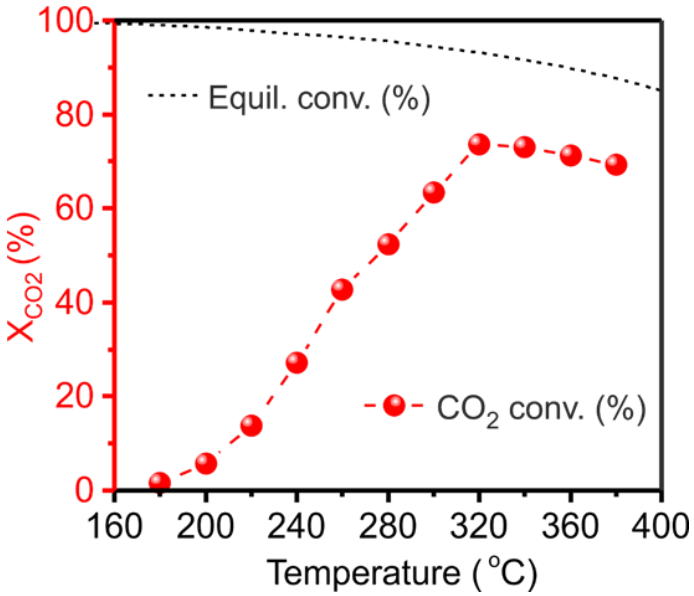

Fig. S3. CO_2 methanation runs with Ni/OCF as catalyst [CO_2 conversion (X_{CO2}: ●) operated by IH setup. Dashed black line refers to the equilibrium conversion. Reaction conditions: m (catalyst) = 0.23 g (8.4 wt.% of Ni), GHSV (STP) = 30,000 mL g_{cat}^{-1} h^{-1}), [CO_2] = 20%, [H_2] = 80%, H_2-to-CO_2 v/v ratio = 4.

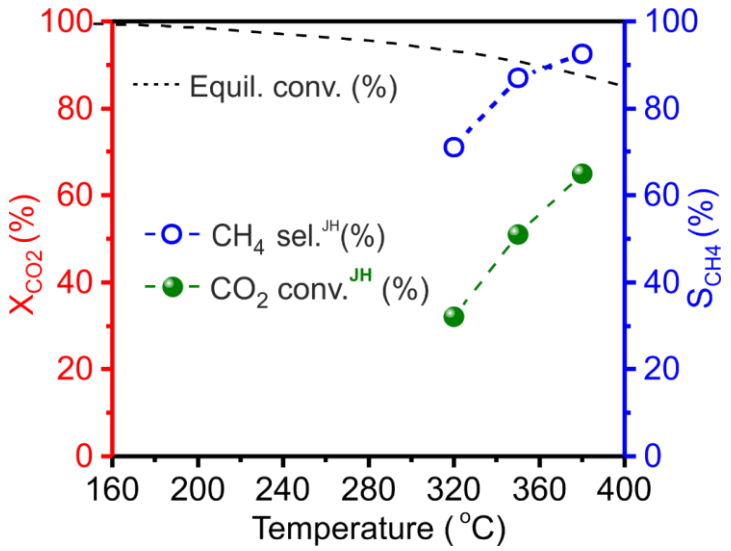

Fig. S4. CO_2 methanation runs with Ni/OCF as catalyst [CO_2 conversion (-●-) and CH_4 selectivity (-O-)], operated with a classical Joule heating system. Reaction conditions: m (catalyst) = 0.23 g (8.4 wt.% of Ni), GHSV (STP) = 30,000 mL $g_{cat}^{-1}h^{-1}$), [CO_2] = 20%, [H_2] = 80%, H_2-to-CO_2 v/v ratio = 4.

Reference

[1] W. Chu, M. Ran, X. Zhang, N. Wang, Y. Wang, H. Xie, X. Zhao. *J. Energy Chem.*, 2013, 22: 136-144.

[2] D.-W. Wang, F. Li, H.-M. Cheng. *J. Power Sources*, 2008, 185: 1563-1568.

[3] W. Xing, F. Li, Z.-F. Yan, G.Q. Lu. *J. Power Sources*, 2004, 134: 324-330.

Chapter 4.2

Decoupling active phase and support heating for low temperature CO_2 methanation on Ni/Al_2O_3 by inductive heating

Abstract

CO_2 methanation is receiving a steadily increase interest from the scientific community because it represents an ideal process for the long-term chemical energy storage of renewable energy (RE). However, the design of effective heat management to operate CO_2 methanation with high performance and low temperatures still remains a big challenge. This work describes the use of nickel decorated alumina catalysts in combination with induction heating (IH) for operating a highly efficient CO_2 methanation reaction already at low temperatures. Results indicates that the optimized catalyst exhibits significantly enhanced low-temperature catalytic performance in the process (*i.e.* 82% CO_2 conversion and 100% CH_4 selectivity) already at 210 ºC, using IH mode under relatively high gas hourly space velocity (GHSV: 20 $L \cdot g_{cat.}^{-1} \cdot h^{-1}$). IH mode allows to carry on the reaction "virtually" under isothermal conditions with only minor temperature runaway from the targeted operative value (less than 5 ºC). On the other hand, a serious temperature runaway has been measured at the catalyst bed when catalysis is run under traditional Joule heating (JH) mode with a temperature increase of about 60 ºC at the rate of 9 $ºC \cdot min^{-1}$ under test conditions. These two operative protocols at comparison have unveiled the overwhelming potentialities of IH over JH mode. IH allows the decoupling of the reaction temperature between the active phase (Ni, NPs suitable for converting the electromagnetic energy generated by an external AC magnetic field into heat) and the whole catalyst thus providing high methanation efficiency already at low catalyst bed temperature. The results described hereafter contribute to make a decisive step-forward towards the development of catalysts and catalytic protocols for operating CO_2 methanation efficiently already under mild reaction conditions.

Keywords

Induction heating; Low-temperature methanation; Nickel catalysts; Power-to-Gas; Synthetic natural gas.

4.2.1. Introduction

The rapid development of modern society along with a steadily increase of the world population call for an ever-growing energy demand associated to the production of goods, foods and commodities. The world total primary energy supply (TPES) increased by almost 2.5 times (from 5,519 Mtoe to 13,972 Mtoe) between 1971 and 2017. Up to now, fossil fuels, such as coal and oil, still dominate the overall energy supply around the world, accounting about 81% of the total energy production in 2017 [1]. However, burning of fossil fuels invariably translates into a large amount of greenhouse gas (GHG) emissions, which are listed among the main players of the current global warming [2-4]. In order to reduce the dependency on fossil fuels, decrease GHG emissions and alleviate the global warming trend, integration of renewable energy (RE) into the energy mix is becoming a primary urgency worldwide. Thus, renewable energy sources (RES), such as solar, wind or hydro power, which are considered as the most attractive substitutes of fossil fuels, have been deeply investigated as electricity production sources [5-7]. In 2017, RES accounted for about 17.5% of the gross final energy consumption in the European Union (EU) and this value is expected to increase up to 20% by 2020 [8]. However, the spatial and temporal mismatch between the generation of electricity from RES and its consumption limits the implementation of RES to a large extent [9, 10]. Indeed, RE electricity generation and its consumption can be often far from each other, and face this matter need large money investments for the reinforcement of electricity network capacity and for the long-distance electricity transportation [11]. Moreover, for a massive integration of RES, their fluctuating and intermittent nature has to be properly taken into account. Indeed, the use of RES can meet with serious technical limits when a reliable load power has to be guaranteed (*i.e.* during electricity peak consumption). This aspect can create large discrepancies between power supply and power demand that need to be properly balanced for electric grid stability purposes. Electricity cannot be stored easily with large scale, hence when the electricity supply exceeds its demand, the electricity surplus has to be converted into other storable forms to avoid energy waste and prevent grid troubles. All these aspects call for the development of long-term, large electricity storage capacity systems with sufficient transmission capacity to provide an ideal balance for the energy grid and facilitate the future development of RES [12, 13].

Among different energy storage technologies, PtG processes, especially, the PtG

technical chains for the production of SNG through the Sabatier reaction, have been considered as promising strategies for the development of energy systems fostering a large-scale integration of RE deriving from different RES [14-16]. This strategy for the chemical energy storage can be effectively used to transform and store the surplus of electrical energy obtained from intermittent RES into long-term and large-scale storable and transportable chemical energy carriers, *i.e.* synthetic methane. Indeed, the latter can be used as fuel for vehicles, energy vector for domestic and industrial heating systems, employed as raw material for the production of commodities in chemical industries or (whenever required) it can be converted back to generate low-carbon electricity. Hence, this technical chain can effectively balance the energy supply and demand with time and facilitate the energy distribution among different energy supply systems by connecting the electricity network with the existing gas distribution grids [10-13]. In addition, the use of renewable H_2 (produced by primary water electrolysis with electricity from RES) with CO_2 for the conversion of the latter into CH_4 can greatly improve the compatibility of the energy storage system with the existing gas grid [13, 17, 18]. At the same time, this technology can effectively reduce the emission of CO_2 thus fulfilling with the urgent needs of a clean energy development [16, 19].

CO_2 hydrogenation to CH_4, also known as CO_2 methanation or Sabatier reaction (Eq. (13)), can be catalyzed by different metals, including Ru, Rh, Pd, Co and Ni, deposited on various supports, such as Al_2O_3, CeO_2, ZrO_2 and SiC, with or without promoters [20-22]. Among them, nickel-based catalysts are the most preferred ones due to the low metal price, its large availability on the market as well as its high activity, selectivity and stability in the process [12, 23]. This reaction is a highly exothermic, therefore, high temperature will greatly limit the CO_2 conversion as well as the CH_4 selectivity. Moreover, during the reaction process, large amount of heat will be released by the reaction itself thus forming “local hot spots”. The latter phenomenon is at the origin of serious drawbacks that typically give rise to the formation of reaction by-products (*i.e.* CO), deactivation of the catalyst active phase (sintering phenomena) up to security issues related to the exploitation of this technology on industrial plants [24-26]. Recent reports have pointed out the efficient use of structured catalysts featured by thermally conductive supports selected for mitigate the generation of local hot spots and avoid temperature runaway phenomena at the catalyst bed [26, 27]. With the same purposes, different types of reactors have also been designed, such as fluidized-bed reactors and three-phase reactors [12, 28]. Despite these seminal achievements for the

temperature control at the catalyst bed, the CO_2 methanation activity remains generally modest when the process is carried out under medium reaction temperatures with limited mass processing ability. Furthermore, most of these designs are relatively complex and expensive, and some of them are still in the development stage.

Electromagnetic induction heating (IH), also known as radiofrequency (RF) heating, has gained extensive attention from the scientific community, recently from catalysis community as well [29-31]. IH allows heat to be generated directly where it is required for running a specific transformation. As far as catalysis is concerned, IH allows heat to be generated directly inside the catalyst bed by converting the electromagnetic energy generated by an external alternating magnetic field into heat. At odds with traditional Joule heating (JH) schemes, such a heat management ensures high thermal efficiency and fast heating rates (up to several hundred degree per minute) with almost no thermal inertia [31-33]. The temperature control at the object can be monitored by a laser pyrometer or optical devices in almost real time thus ensuring an extremely fast response to any temperature deviation [33, 34]. As a matter of fact, temperature fluctuations, frequently encountered in real CO_2 methanation systems (as the consequence of a discontinuous supply of reagents loads), can be finely controlled hence allowing the process to operate under virtually isothermal conditions. In a recent work from our group, we described enhanced catalytic performance and superior advantages for start/stop dynamic operation when IH mode was used in combination with macroscopic Ni/OCF as catalyst (OCF = oxidized carbon-felt) for the CO_2 methanation reaction [34].

The aim of the present work is to demonstrate the use of IH for the selective heating and temperature control at the active phase (Ni NPs) of Ni/Al_2O_3 composites suitable to perform the methanation reaction already at relatively low catalyst bed temperatures and in a continuous-flow process. Ni NPs decorating the surface of an alumina support act as both susceptors for the fast heat generation driven by IH and as active phase for the reaction, and their ultimate temperature is related to the concurrent contribution of the followings: 1) the heat generated by the conversion of the electromagnetic energy produced by the applied external AC magnetic field; 2) the heat generated by the exothermic nature of the catalytic process at work; 3) the heat loss (dissipation phenomena) through the active phase to the support and finally to the surroundings as well as temperature gradients generated by flowing reagents and products in the reactor. The moderate thermal conductivity of alumina in the composite

mitigate the heat dissipation and allows Ni NPs to harvest and store heat also from the process exothermicity, to be spent in turn for running the methanation reaction. By this way "functional hot-spots" can be generated and exploited for catalysis purposes. At the same time the local and fast control exerted by IH on the catalyst target temperature, prevents any undesired temperature runaway and allows the whole process to occur under "virtually" isothermal conditions. By this way, classical drawbacks occurring in reactors operating under JH mode (sintering/deactivation of the catalyst active phase and reduction of the catalyst performance-activity and selectivity) are largely circumvented and a more favorable energy balance for the process is granted.

Catalytic performance of the system was comprehensively investigated using both IH and JH modes. The effect of the nickel loading and nickel particle size in combination with the excellent control on the temperature ramps (up and down) exerted by IH, have been carefully investigated under either static or dynamic reagents supplies. Results from this study have also unveiled the Ni/Al_2O_3 in combination with IH set-up allow the methanation process to take place at high conversion per pass and almost quantitative selectivity already at operative temperatures significantly lower to those classically claimed for related catalytic systems of the state-of-the-art operating under JH mode.

4.2.2 Experimental section

Catalyst preparation and characterization please refer to **Chapter 2.1.2** and **Chapter 2.2**. In this section, transmission electron microscopy (TEM) was performed on a Themis ETEM G3 (Thermo Scientific) microscope equipped with high angle annular dark field (HAADF) and energy dispersive X-ray analysis (EDX) detectors operating at 300 keV. For these measurements, the reduced samples were dispersed in ethanol using ultrasounds for few minutes and a drop of the suspension was casted over a copper grid covered with a holey carbon membrane.

A fixed-bed quartz reactor (ID = 12 mm, length = 400 mm) equipped with a continuous flow system for the reagents supply was used to evaluate the catalyst CO_2 methanation performance at ambient pressure. Prior running the reaction, the catalyst was reduced at 350 °C for 3 h under a stream of H_2 (100 $mL \cdot min^{-1}$) using an external electric furnace. 0.4 g of the reduced catalyst was packed in the middle of the reactor with quartz wool. The catalytic performance was detected under both traditional

thermal heating and IH models. Please refer to **Chapter 2.3.2**. For IH catalytic processes, no external susceptor was used (**Fig. S1**).

4.2.3 Results and discussion

The textural properties of the as-synthesized and the reduced catalysts were determined by liquid N_2 adsorption and desorption analysis. The adsorption-desorption isotherms and pore size distribution (PSD) of the reduced catalysts are collected in **Fig. 1A** and **1B**. Detailed textural characteristics, including specific surface area (SSA), total pore volume (PV) and average pore diameter (PD), are finally summarized in **Table 1**. Structural properties of all pre-catalysts (before the reduction step) are displayed in **Fig. S2** and **Table S1**. All these samples exhibit similar type-IV isotherm profiles which are considered typical of mesoporous samples [35, 36]. By increasing the nickel loading, the hysteresis loop gradually shifts from type-H_3 (classical for A_2O_3 samples) to type-H_4 (*e.g.* in $40Ni/Al_2O_3$) that reflects a gradual narrowing of the catalyst pore structure (see Fig. 1B), likely due to a partial clogging of Al_2O_3 pore channels by Ni NPs.

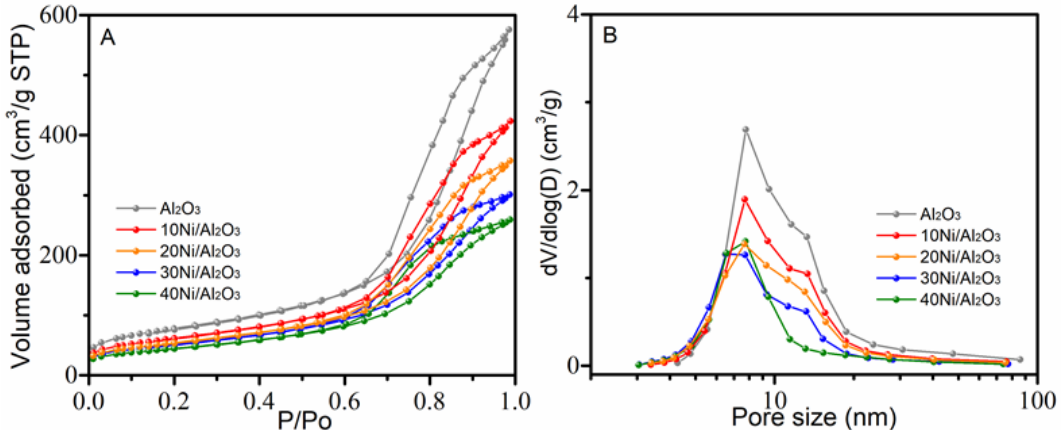

Fig. 1. N_2 adsorption-desorption isotherms (A) and pore size distributions (B) of the Al_2O_3 support and catalysts.

From Table 1 it can be argued that the increase of Ni loading decreases both SSA and PV of the composites. Despite a significant decrease of SSA and PV in the sample at higher Ni loading ($40Ni/Al_2O_3$), pore distribution in this sample does not change significantly. This aspect can be due to the large SSA of the Al_2O_3 support and the relatively high dispersion of Ni NPs at its surface (also according to the following analysis results).

Table 1 - Textural properties of the samples.

Samples	Ni loading Wt.%	SSA[a] $m^2 \cdot g^{-1}$	PV[b] $cm^3 \cdot g^{-1}$ STP	PD[c] nm
Al_2O_3	0	279	0.951	9.96
10Ni/Al_2O_3	10	221	0.693	9.50
20Ni/Al_2O_3	20	195	0.584	9.18
30Ni/Al_2O_3	30	183	0.491	8.33
40Ni/Al_2O_3	40	160	0.426	8.04

[a] Calculated by the BET equation.

[b] BJH desorption pore volume between 1.7 nm and 300 nm.

[c] BJH desorption average pore diameter.

H_2-TPR analyses on the catalyst precursors were carried out to investigate the reducibility and the interaction between nickel oxide and the support (**Fig. 2A**). All the samples displayed three main H_2 consumption peaks with different peak areas, indicating the sequential reduction of different metal oxide species in the samples. The first peak with reduction temperature < 300 ºC can be attributed to the reduction of small NiO NPs prevalently located at the outermost layer of the support and featuring with a relatively weak interaction with the alumina support [37, 38]. The broader reduction peaks comprise between 300 ºC and 480 ºC and showing a small shoulder in the lower temperature range, should be originated from the reduction of bulk NiO within larger particles featuring a medium interaction with the support [39, 40]. The final reduction shoulder centered around 520 ºC can be ascribed to the reduction of highly-dispersed NiO species with small particle sizes, prevalently located in the alumina channels and hence displaying strong interactions with the support [38, 41]. These attributions found confirmation from other reports in the literature on related Ni-Al_2O_3 systems [42]. The increase of the nickel loading can lead to the generation of NiO particles with both small and larger sizes, hence shifting the low reduction peak to lower temperatures and the second reduction peak towards higher temperatures, respectively. Similar results have also been reported by Guo [43] and Lin [44]. It should be pointed out that the increase of Ni loading translates into an increase of Ni particle size. This aspect is supposed to have an important effect on the ultimate ability of Ni NPs to convert electromagnetic energy into heat as well as on their inherent ability to perform the methanation process efficiently.

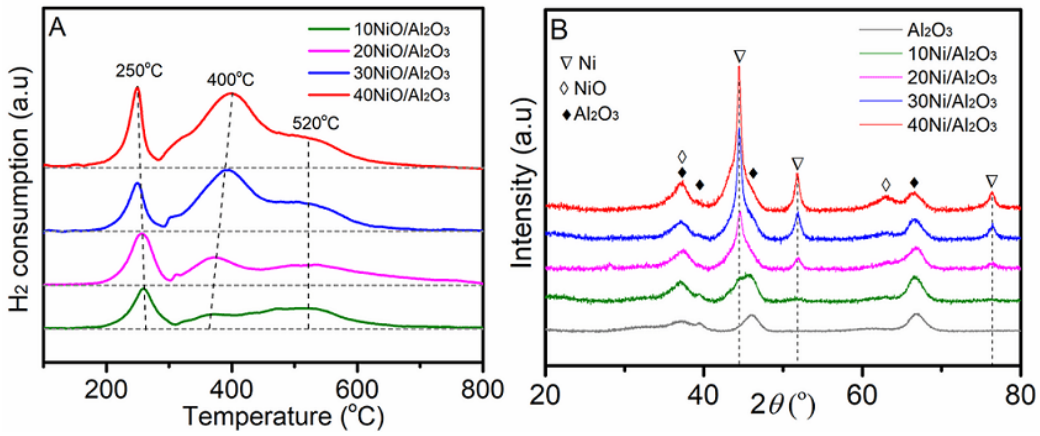

Fig. 2. (A) H_2-TPR profiles of the pre-synthesized catalysts; (B) XRD patterns of the reduced catalysts.

Fig. 2B shows the XRD patterns of the reduced catalysts prepared at different nickel loadings. The well crystallized, sharp and symmetric diffraction peaks located at $2\theta = 44.5^o$, 51.8^o and 76.4^o are attributed to (111), (200) and (220) reflection planes of metallic nickel species (ICDD PDF#65-2865), respectively, while the broad weak diffraction peaks centered around $2\theta = 37.6^o$, 39.5^o, 45.8^o and 66.8^o are assigned to the (311), (222), (400) and (440) crystal planes of alumina oxide [ICDD PDF#10-0425]. An increase of the nickel loading translates into an increase of the nickel particle size; hence the intensity of the corresponding diffraction peaks increases [37, 45]. The XRD patterns of samples after NiO NPs reduction in a stream of pure H2 indicate that all oxides (**Fig. S3**) are well reduced under the applied conditions. Such an evidence well fits with the H_2-TPR profiles acquired for all these samples. The appearance of minor components ascribable to residual nickel oxide species (located at $2\theta = 37.2^o$ and 62.9^o, respectively) are likely originated from a superficial and spontaneous oxidation of reduced Ni NPs upon their exposure to air before analysis [ICDD PDF#65-5745].

In general, nickel NPs tend to be highly dispersed across the Al_2O_3 support for low samples prepared at metal loadings. On the other hand, once high metal loadings are used, Ni NPs tend to aggregate thus forming larger metal islands. This has been evidenced by STEM analyses (**Fig. 3** and **Fig. S4**) as well as EDX-elemental mapping (**Fig. S5**). These analyses confirm that for Ni loadings lower than 30 wt.%, NPs are well dispersed on the relatively large surface area of the alumina support (Fig. S4-S5); this datum is in accord with the XRD results (Fig. 2B). At higher nickel loadings, Ni NPs become larger and form aggregates (Fig. 3).

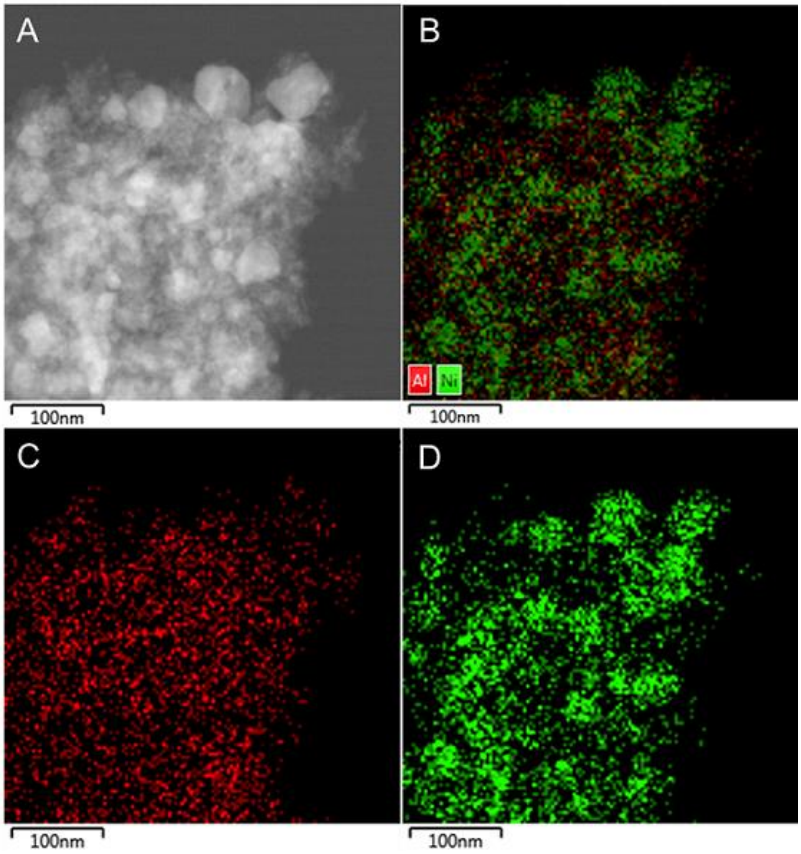

Fig. 3. STEM images of the Ni species on the surface of 40Ni/Al_2O_3 catalyst (A), and the EDX-elemental mapping results (B-D).

The CO_2 methanation performance of nickel-based catalysts featured by different metal loadings were firstly evaluated in combination with IH and the initial reaction temperature was fixed at 230 °C. The catalysts with Ni loadings lower than 30 wt.% were hardly heated up to the desired temperature (230 °C), under the test conditions. The CO_2 methanation performance of the 30Ni/Al_2O_3 and 40Ni/Al_2O_3 catalyst was evaluated under different GHSV (**Fig. 4A**). Indeed, for low metal loadings and moderate reagents GHSV (below 20 $L \cdot g_{cat.}^{-1} \cdot h^{-1}$) the target temperature for operating the process was very difficult to be reached and maintained. This is basically due to the scarce heatability of Ni NPs of moderate size under IH mode. However, when GHSV higher than 20 $L \cdot g_{cat.}^{-1} \cdot h^{-1}$ were supplied, additional heat can be provided to the catalyst bed directly from the exothermicity of the methanation process.

In order to keep the catalyst at the desired reaction temperature, *i.e.* 230 °C, the input current was varied as to balance the additional heat input coming from the reaction exothermicity (**Fig. 4B**). It is worthy to note that for the same reaction temperature, the catalyst with 40 wt.% as nickel loading needed much less energy input compared to its

counterpart at 30 wt.% nickel loading (Fig. 4B). The observed difference is basically ascribed to the most important contribution of eddy currents dissipation phenomena on Ni NPs of larger sizes (40 wt.% vs. 30 wt.%). Similarly, input currents are progressively decreased while increasing GHSV. Indeed, the additional heat provided to the systems from the reaction exothermicity when high GHSV are operated, is compensated by reduced input currents. By this way, the system is continuously maintained at the target temperature and the process is operated virtually under "isothermal" conditions. Noteworthy, IH ensures the process to occur efficiently already under moderate reaction temperatures. Indeed, the inductively heated Ni/Al_2O_3 catalysts (30 wt.% and 40 wt.% of Ni) show remarkable CO_2 methanation activity at a relatively low temperature of the catalyst bed, *i.e.* 85% of CO_2 conversion with 100% of CH_4 selectivity at 230 °C under the GHSV of 20 $L \cdot g_{cat.}^{-1} \cdot h^{-1}$. This result is superior to many related Ni-base systems of the state-of-the-art [46, 47], including catalysts based on noble metals [48-50]. Overall, these preliminary results (compared with the literature) indicate a radical difference in the catalysts behavior depending on the heating mode (IH vs. JH) applied to the system (vide infra). Compared to $30Ni/Al_2O_3$, the enhanced catalytic performance of $40Ni/Al_2O_3$ is ascribable to the followings: (1) the increase of the nickel loading could in part contributed to the increase of the amount of active sites after reduction, hence a higher Ni loading translates into higher CO_2 conversions [21]; (2) the higher Ni loading give rise to catalysts based on larger nickel aggregates and particle size which display higher interaction with the IH current enabling the effective local heat up of the nickel phase and as a consequence, increase the catalytic performance.

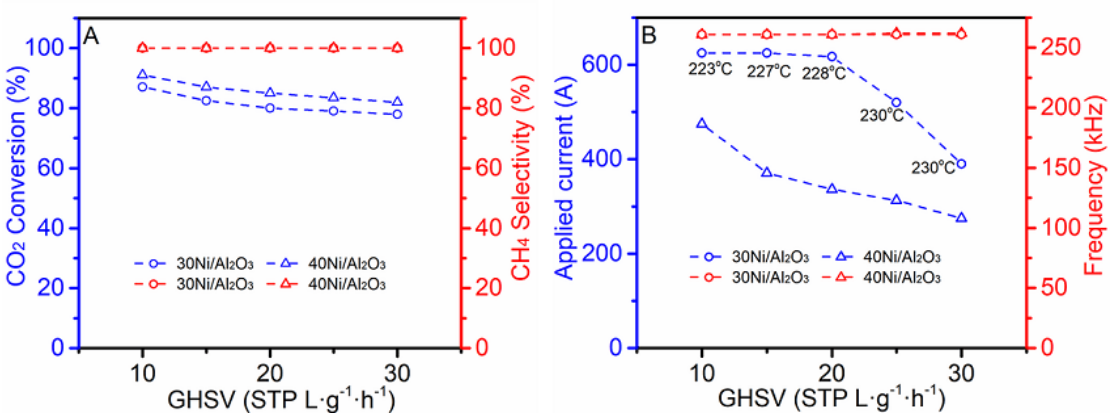

Fig. 4. CO_2 conversion and CH_4 selectivity as a function of GHSV (STP) (A) and the corresponding applied current (B) under IH mode. Reaction conditions: 0.4 g catalyst, H_2-to-CO_2 molar ratio of 4, 230 °C and 0.1 MPa.

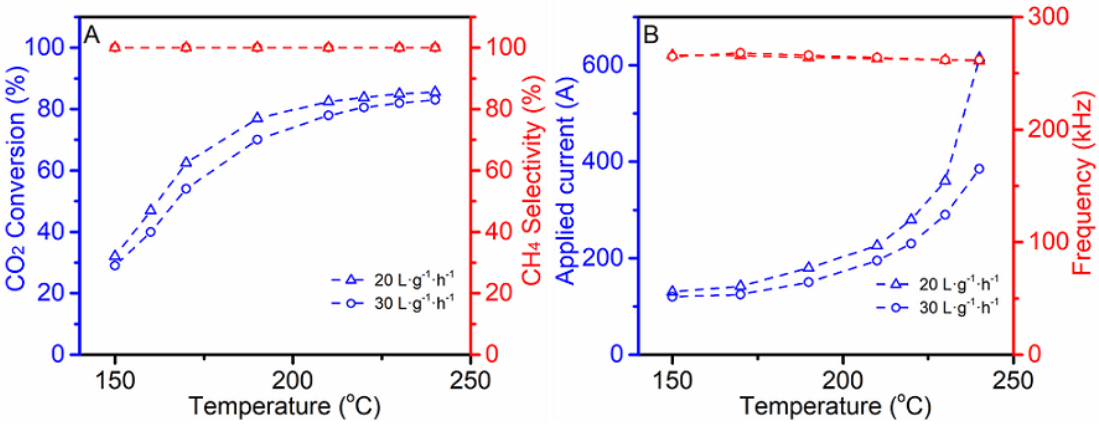

Fig. 5. CO_2 conversion and CH_4 selectivity as a function of reaction temperature (A) and corresponding applied current and frequency (B) with different GHSV (STP) = 20 $L \cdot g_{cat.}^{-1} \cdot h^{-1}$ and 30 $L \cdot g_{cat.}^{-1} \cdot h^{-1}$ under IH mode on the $40Ni/Al_2O_3$ catalyst. Reaction conditions: 0.4 g catalyst, H_2-to-CO_2 ratio (v./v.) of 4 and 0.1 MPa.

Catalytic performance of the $30Ni/Al_2O_3$ and $40Ni/Al_2O_3$ catalysts as a function of reaction temperature, in the range of 150 to 240 °C, was further investigated under different GHSV (**Fig. 5** and **Fig. S6**). Notably, appreciable CO_2 conversions can be achieved already at 150 °C, taken into account the high GHSV used. The CO_2 conversion displays significant improvement when the reaction temperature increases from 150 to 210 °C, indicating that the catalytic activity of the catalyst was remarkably affected by the reaction temperature at this period, which is generally attributed to the kinetic control [46]. For temperatures higher than 210 °C, CO_2 conversion only slightly increases due to the exothermic nature of the methanation reaction and the thermodynamic limitation under the test conditions [26, 46, 51]. When GHSV was increased from 20 $L \cdot g_{cat.}^{-1} \cdot h^{-1}$ to 30 $L \cdot g_{cat.}^{-1} \cdot h^{-1}$, a slight decrease of CO_2 conversion was observed. This result can be ascribed to an oversaturation of the catalyst active sites.

At 230 °C, at the steady-state conditions, CO_2 conversion reaches 85% with a CH_4 selectivity almost 100%. As far as we known, such a result ranks among the highest reported in the literature for methanation systems operating at low temperatures and it is certainly the highest among nickel-based catalysts, as listed in **Table S2**. In general, high CO_2 conversion (> 80%) are achieved at relatively high temperature (around 350 °C) on Al_2O_3 supported Ni-based catalysts operating under traditional thermal heating m. Under such severe conditions the formation of CO is unavoidable due to the side "reverse water gas shift (RWGS) reaction" whose occurrence can affect the process

selectivity [51-53]. In contrast to that, high CO_2 hydrogenation can be performed with IH mode at relatively low temperature where the occurrence of undesired side reactions is largely mitigated. Consequently, the CH_4 selectivity can be significantly improved, and overall system risks and operational costs are greatly reduced.

The influence of the H_2-to-CO_2 ratio on the performance of our catalytic systems has also been studied under IH mode. **Fig. 6** shows the CO_2 conversion and CH_4 selectivity of the Ni/Al_2O_3 catalysts with 30 and 40 wt.% nickel loading at different H_2-to-CO_2 ratio and under different GHSVs. Increasing the H_2-to-CO_2 ratio translates into an increase of CO_2 conversion. Over a H_2-to-CO_2 ratio of 6 the catalysts conversions substantially lie on a plateau value due to thermodynamic and kinetic limitation of the methanation reaction under the test conditions [46, 51, 54]. Anyway, CO_2 conversions as high as 98% and 94% are obtained with $40Ni/Al_2O_3$ catalyst at 230 ºC with a H_2-to-CO_2 ratio of 8 and a GHSV of 20 $L \cdot g_{cat.}^{-1} \cdot h^{-1}$ and 30 $L \cdot g_{cat.}^{-1} \cdot h^{-1}$, respectively. For all these issues, the CH_4 selectivity remained constantly at 100%. These results are rather close or even meet the target of high CO_2 conversion requirements in the PtG technical chain, where a high concentration of CH_4 is needed for the direct injection of the produced synthetic gas into the natural gas distribution grids [12, 53]. However, it is worthy to note that the CO_2 conversion is relatively high even a lower stoichiometric H_2-to-CO_2 ratios. These results can be directly attributed to the high intrinsic activity of the catalyst under a heating set-up (IH) where heat is directly (and almost exclusively) targeted where it is needed for the process to occur.

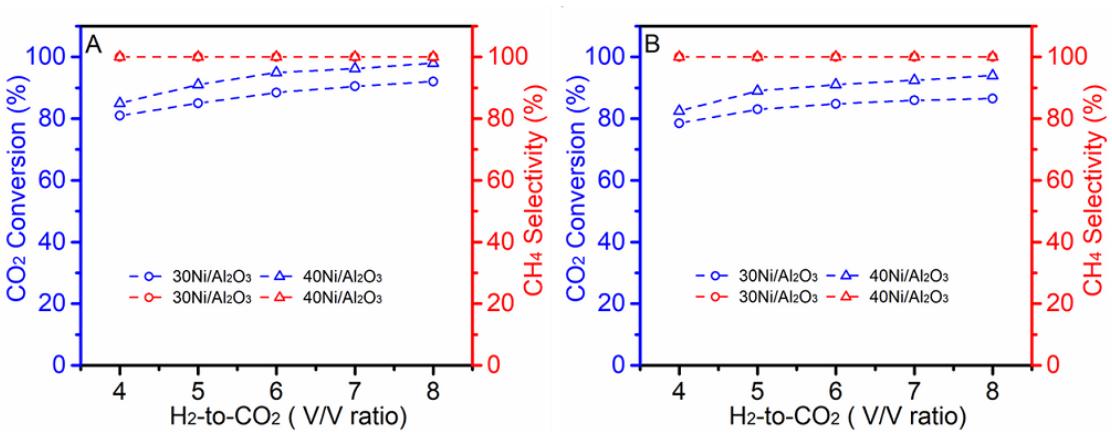

Fig. 6. CO_2 conversion and CH_4 selectivity as a function of H_2-to-CO_2 ratio (v./v.) with different GHSV (STP) = 20 $L \cdot g_{cat.}^{-1} \cdot h^{-1}$ (A) and 30 $L \cdot g_{cat.}^{-1} \cdot h^{-1}$ (B) under IH mode. Reaction conditions: 0.4 g catalyst, 230 ºC and 0.1 MPa.

For the sake of completeness, the catalytic activity of 40Ni/Al_2O_3 was additionally investigated under classical JH mode, hence by providing heat to the system using an external oven. For these trials, the system was stabilized at each target temperature for 30 min. (with a temperature fluctuation ≤ 1 °C), prior that the reaction mixture was fed into the reactor and come in contact with the catalyst. CO_2 conversions and CH_4 selectivity at different reaction temperatures are shown in **Fig. 7A**. With the increase of the reaction temperature, the catalytic activity was increased, which is in accordance with previous early reports on the topic [55-57]. Under the test conditions, CH_4 selectivity constantly lies on 100% all over the temperature range. In order to measure the temperature gap between the oven and the catalyst bed, a second thermocouple was installed inside the latter. For reaction temperatures ≤ 220 °C the catalyst temperature remains quite similar to that of the oven. Under these conditions a relatively moderate CO_2 conversion was observed, *i.e.* up to 12% at 220 °C. However, when the oven temperature was increased to 230 °C a sharp temperature runaway was recorded inside the catalyst bed, *i.e.* 274 °C. The temperature gap (between the oven and the catalyst bed) rises as a function of the temperature applied to the oven and confirms that (using JH) a large temperature runaway inside the catalytic bed occurs. A CO_2 conversion of 85% is reached when the temperature inside the catalyst bed is close to 270-290 °C compared to 230 °C with IH. The difference between the oven set temperature and the catalyst bed temperature remains almost stable which confirms that the extra heat provided by the reaction exothermicity remains constant under these experimental conditions.

For better understanding this phenomenon and its consequences in the methanation reaction operated under JH mode, a new configuration setup was arranged and the measurement of the catalyst bed temperature was accomplished directly with the thermocouple used for the oven temperature control. The system was first stabilized at 220 °C under He for 40 min (with the temperature fluctuation ≤ 1 °C), then the reaction mixture was introduced into the reactor at different GHSVs. The catalyst bed temperature was recorded until it went back to the initial base temperature and the results are displayed in **Fig. 7B**. According to the results the catalyst internal bed temperature suddenly increases in few minutes after that the reactants feed was admitted into the reactor, *i.e.* 40 °C with a GHSV of 20 $L \cdot g_{cat.}^{-1} \cdot h^{-1}$ and 60 °C with a

GHSV of 30 $L \cdot g_{cat.}^{-1} \cdot h^{-1}$; similar phenomena have been widely observed in recent studies on CO_2 methanation [26, 58-60]. Such temperatures runaway can be responsible of several drawbacks related safety issues and catalysts stability on time. Indeed, it can cause the sintering of the catalyst activate phase, thereby reducing the catalyst life and increasing the cost of industrial operation in the long runs [12, 61]. Moreover, with JH mode the time requested by the system to regulate the target reactor temperature remains extremely long (it may require tens of minutes or even hours to return back to the initial set reaction temperature (Fig. 7B). On the other hand, it should be stressed that during the evaluation of the same catalyst under IH mode, the maximum temperature fluctuation between the set temperature and the real detected temperature was (constantly) less than 5 °C at the high CO_2 conversions and it was quickly stabilized at the target temperature within one or two minutes thanks to the high efficiency of the IH to regulate any reaction temperature runaway.

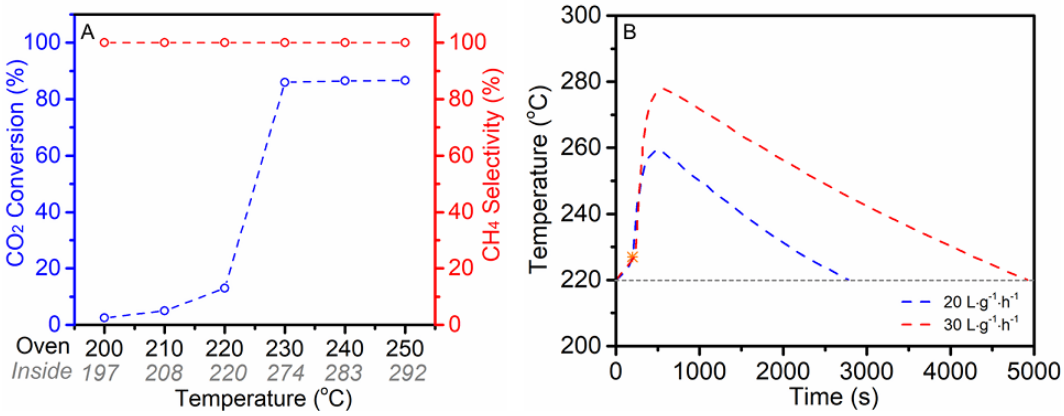

Fig. 7. CO_2 methanation performance under conversional thermal heating by external furnace with GHSV (STP) of 20 $L \cdot g_{cat.}^{-1} \cdot h^{-1}$ (A) and temperature runaway phenomena inside the catalyst bed and the low inertia of the JH to regulate the temperature runaway (B). Reaction conditions: 0.4 g catalyst, 1 atm. H_2 to CO_2 ratio (v/v) of 4.

The superior CO_2 methanation activity obtained under IH mode under markedly low operational temperatures using Ni-based catalyst can be ascribed to the highly efficient regulation of the target temperature at the catalytic bed. Indeed, the efficient electromagnetic energy conversion of large Ni NPs along with the heat contribution coming from the process exothermicity, make possible to perform the process efficiently already at low temperature. Moreover, the poor thermally conductive character of the Al_2O_3 support, mitigate the heat dissipation and allows Ni NPs to

harvest and store heat also from the process exothermicity, to be spent in turn for running the methanation reaction. By this way "functional hot-spots" are generated and exploited for catalysis purposes. At the same time the local and fast control exerted by IH on the catalyst target temperature, prevents any undesired temperature runaway and allows the whole process to occur under "virtually" isothermal conditions.

Therefore, the exploitation of IH technology in a highly exothermic process like methanation reaction is, does not simply imply a more convenient energy balance for the process but rather it allows a more favorable control of the target temperature at the catalyst bed and reduces the occurrence of side processes related to the reagent decomposition in the process [35]. The superior CO_2 methanation activity at such low catalyst bed temperature obtained under IH mode on the Ni-based catalyst is directly linked to the higher surface temperature of Ni NPs on the alumina support. However, this aspect has not been totally unveiled so far because the determination of NPs' temperature remains a challenging task [62-64]. Recent report by Chaudret and co-workers [65] on the hydrodeoxygenation (HDO) process at low pressure and temperature compared to the traditional process pointed out that local heat on the magnetic particles lead to the generation of much higher local temperatures on the particles and thus, create microscopic gaseous atmosphere around the active centers for operating the reaction while the macroscopic medium remain at mild conditions. Moreover, it has been reported by Donphai et al. that magnetic field could directly facilitate the adsorption of CO_2 molecules over the surface of magnetized catalyst and obviously decrease the apparent activation energy, thereby, significantly increasing the CO_2 hydrogenation activity for the production of methanol [66].

For catalysis operated under JH mode both the active phase and the support are classically heated by convection/conduction paths delivered by the oven. When operated under IH, heat is generated at the metal active sites only, while keeping the support at relatively low temperature. In addition, the high inertia response of the JH mode is unable to allow a rapid temperature regulation leading to the formation of large temperature runaway inside the catalyst bed once the reaction reach to a moderate conversion, which are detrimental for the whole catalytic process and catalyst stability.

The stability performance of $40Ni/Al_2O_3$ catalyst has been conducted under IH mode, and the results are displayed in **Fig. 8**. The catalyst was also evaluated under transient operational conditions to simulate discontinuous supply of reactants, hence by cycling the process with successive off/on switching of reactants (*i.e.* CO_2) and

temperature. After 60 h on stream and 10 start/stop cycles, the catalyst maintains is performance almost unchanged thus indicating that this system is a good candidate for fast and dynamic operational conditions in the methanation reaction. A TPO experiment was conducted to check the coke deposition on the surface of the spent catalyst. As exhibited in **Fig. S7**, no obvious carbon deposits were observed, which confirms the high ability of the system towards the undesired generation of coke deposits. This superior stability and coke resistance can be ascribed to the followings: (1) the overall relatively low reaction temperature (210 ºC), at which the formation of carbon deposits and RWGS reactions are unlikely to occur [51, 60]; (2) the rapid moderating ability and uniform heating capability of the IH setup along with the enhanced heat transfer ability by sufficient nickel loading, enabling precise control of the overall catalyst bed temperature with no obvious temperature gradient and serious temperature runaway inside the catalyst bed, which has been evidenced to be beneficial for carbon deposition [67-69]; (3) the thermal resistance of the support and the interaction between the support and active species to some extent work as "brakes", effectively suppress the migration and agglomeration of Ni NPs (as revealed in **Fig. 9** and illustrated in **Fig. S8**).

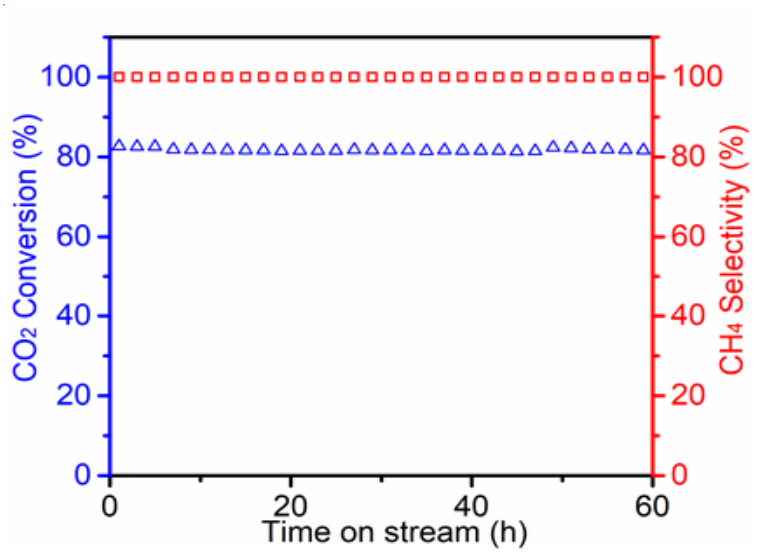

Fig. 8. Stability evaluation of 40Ni/Al_2O_3 catalyst with IH mode. Reaction conditions: 0.4 g catalyst, GHSV (STP) = 20 $L \cdot g_{cat.}^{-1} \cdot h^{-1}$, 210 ºC, H_2-to-CO_2 ratio (v/v) of 4 and 0.1 MPa.

The representative TEM micrographs of the fresh and spent 40Ni/Al_2O_3 catalysts are presented in **Fig. 9**. The Ni NPs were relatively well dispersed on the alumina

surface. After long term test, the Ni NPs size distribution is slightly increased compared to the spent one. This has also been evidenced by the almost similar XRD diffraction patterns of the fresh and spent catalysts (**Fig. S9**). Such slight Ni particle size increase could be attributed to the overheating of the Ni NPs by the electromagnetic IH which could induce some small Ni NPs sintering. However, one should notice that if sintering has occurred the effect is not dramatic as the Ni NPs particle size remains quite close to that of the fresh catalyst.

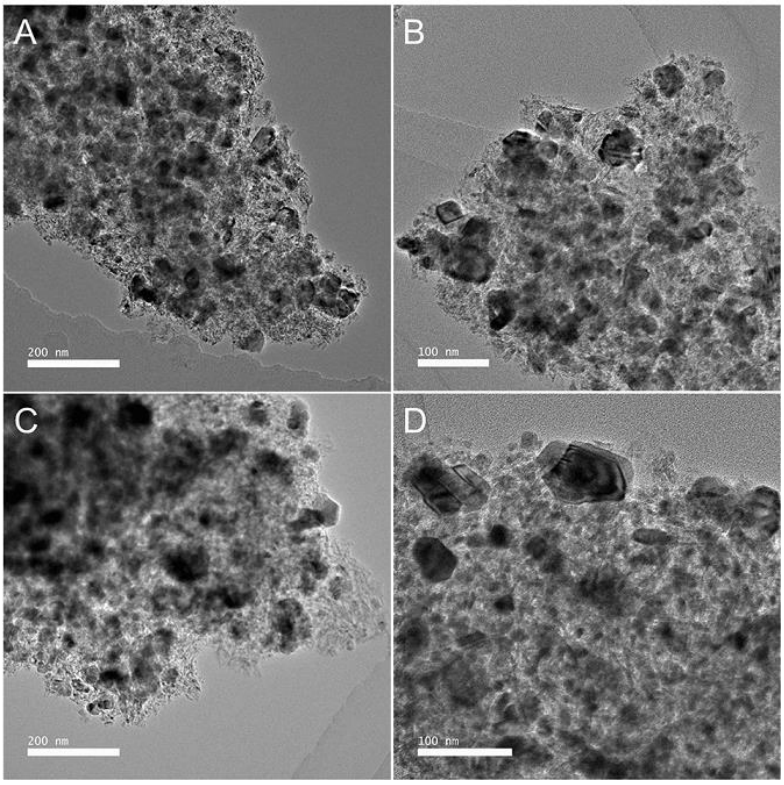

Fig. 9. TEM images of the fresh (A, B) and spent (C, D) 40Ni/Al_2O_3 catalyst.

4.2.4 Conclusion

In summary, we have reported an efficient continuous-flow process with superior CO_2 methanation performance at relatively low temperatures through the combination of active metal susceptors (*i.e.* Ni NPs) deposited on an electrically and thermally non-conductive support (Al_2O_3). High CO_2 conversion up to 82% with 100% of CH_4 selectivity was accomplished under IH mode already at 210 °C and relatively high GHSVs (20 $L \cdot g_{cat.}^{-1} \cdot h^{-1}$). Such a catalytic scheme allows to perform the process efficiently with activity, selectivity and catalyst stability on time that ranks among the highest reported in the literature up to now for related systems operating under classical

JH modes. The excellent performance of such a catalytic scheme can be attributed to the followings: (1) IH allows heating to occur selectively where it is needed; (2) the synergistic effect of nickel active sites with the rapid temperature control of IH on the catalyst that allow the catalyst to work efficiently and maintain a long-term stability.

It is expected that such research could open new perspectives for the design of highly efficient catalytic system from both catalyst design and heat management sides, especially for the low-temperature CO_2 hydrogenation. The unique properties of IH setup can be employed for enhancing other exothermic or endothermic processes. The optimization of such a heating technology for the CO_2 methanation is currently underway in our laboratories.

Reference

[1] International Energy Agency (IEA), *World Energy Balances 2019*, https://webstore.iea.org/download/direct/2710?fileName=World_Energy_Balances_2019_Overview.pdf.

[2] International Energy Agency (IEA), *CO_2 Emissions from Fuel Combustion 2018*, https://webstore.iea.org/download/direct/1082?fileName=CO2_Emissions_from_Fuel_Combustion_2018_Overview.pdf.

[3] S. J. Davis, K. Caldeira, H. D. Matthews. *Science*, 2010, 329(5997): 1330-1333.

[4] W. D. Nordhaus. *J. Econ. Lit.*, 2007, 45(3): 686-702.

[5] O. Ellabban, H. Abu-Rub, F. Blaabjerg. *Renew. Sust. Energy Rev.*, 2014, 39: 748-764.

[6] H. Lund. *Energy*, 2007, 32(6): 912-919.

[7] I. M. Bugaje. *Renew. Sust. Energy Rev.*, 2006, 10(6): 603-612.

[8] Eurostat (European statistics), Statistics Explained, Renewable energy statistics, https://ec.europa.eu/eurostat/statistics-explained/index.php/Renewable_energy_statistics.

[9] M. Jentsch, T. Trost, M. Sterner. *Energy Procedia*, 2014, 46: 254-261.

[10] M. Bailera, P. Lisbona, L. M. Romeo, S. Espatolero. *Renew. Sust. Energy Rev.*, 2017, 69: 292-312.

[11] M. Qadrdan, M. Abeysekera, M. Chaudry, J. Wu, N. Jenkins. *Int. J. Hydrogen Energy*, 2015, 40(17): 5763-5775.

[12] M. Götz, J. Lefebvre, F. Mörs, A. M. Koch, F. Graf, S. Bajohr, R. Reimert, T. Kolb. *Renew. Energy*, 2016, 85: 1371-1390.

[13] J. Ma, Q. Li, M. Kühn, N. Nakaten. *Renew. Sust. Energy Rev.*, 2018, 97: 478-496.

[14] S. Clegg, P. Mancarella. *IEEE Trans. Sust. Energy*, 2015, 6(4): 1234-1244.

[15] A. Lewandowska-Bernat, U. Desideri. *Energy Procedia*, 2017, 105: 4569-4574.

[16] S. McDonagh, R. O'Shea, D. M. Wall, J. P. Deane, J. D. Murphy. *Appl. Energy*, 2018, 215: 444-456.

[17] P. Collet, E. Flottes, A. Favre, L. Raynal, H. Pierre, S. Capela, C. Peregrina. *Appl. Energy*, 2017, 192: 282-295.

[18] G. Guandalini, S. Campanari, M. C. Romano. *Appl. Energy*, 2015, 147: 117-130.

[19] S. Schiebahn, T. Grube, M. Robinius, V. Tietze, B. Kumar, D. Stolten. Int. J.

Hydrogen Energy, 2015, 40(12): 4285-4294.

[20] W. Wang, S. Wang, X. Ma, J. Gong. *Chem. Soc. Rev.*, 2011, 40(7): 3703-3727.

[21] M. A. A. Aziz, A. A. Jalil, S. Triwahyono, A. Ahmad. *Green Chem.*, 2015, 17(5): 2647-2663.

[22] M. Younas, L. Loong Kong, M. J. Bashir, H. Nadeem, A. Shehzad, S. Sethupathi. *Energy Fuels*, 2016, 30(11): 8815-8831.

[23] G. A. Mills, F. W. Steffgen. *Catal. Rev.*, 1974, 8(1): 159-210.

[24] M. Frey, T. Romero, A. C. Roger, D. Edouard. *Catal. Today*, 2016, 273: 83-90.

[25] R. Try, A. Bengaouer, P. Baurens, C. Jallut. *AIChE J.*, 2018, 64(2): 468-480.

[26] S. Ratchahat, M. Sudoh, Y. Suzuki, W. Kawasaki, R. Watanabe, C. Fukuhara. *J. CO_2 Util.*, 2018, 24: 210-219.

[27] Y. Li, Q. Zhang, R. Chai, G. Zhao, Y. Liu, Y. Lu, F. Cao. *AIChE J.*, 2015, 61(12): 4323-4331.

[28] S. Rönsch, J. Schneider, S. Matthischke, M. Schlüter, M. Götz, J. Lefebvre, P. Prabhakaran, S. Bajohr. *Fuel*, 2016, 166: 276-296.

[29] S. Ceylan, L. Coutable, J. Wegner, A. Kirschning. *Chem. Eur. J.*, 2011, 17(6): 1884-1893.

[30] O. Lucía, P. Maussion, E. J. Dede, J. M. Burdío. *IEEE Trans. Ind. Electron.*, 2013, 61(5): 2509-2520.

[31] W. Wang, G. Tuci, C. Duong-Viet, Y. Liu, A. Rossin, L. Luconi, J. M. Nhut, L. Nguyen-Dinh, C. Pham-Huu, G. Giambastiani. *ACS Catal.*, 2019, 9: 7921-7935.

[32] F. Varsano, M. Bellusci, A. La Barbera, M. Petrecca, M. Albino, C. Sangregorio. *Int. J. Hydrogen Energy*, 2019, 44(38): 21037-21044.

[33] C. Wu, F. Li, W. Chen, C. P. Veeramalai, P. C. Ooi, T. Guo. *Sci. Rep.*, 2015, 5: 9034.

[34] W. Wang, C. Duong-Viet, Z. Xu, H. Ba, G. Tuci, G. Giambastiani, Y. Liu, T. Truong-Huu, J. M. Nhut, C. Pham-Huu. *Catal. Today*, 2019, in press, Doi: 10.1016/j.cattod.2019.02.050.

[35] M. Thommes, K. Kaneko, A. V. Neimark, J. P. Olivier, F. Rodriguez-Reinoso, J. Rouquerol, K. S. Sing. *Pure Appl. Chem.*, 2015, 87(9-10): 1051-1069.

[36] K. S. Sing. D. H. Everett, R. A. W. Haul, L. Moscou, R. A. Pierotti, J. Rouquerol, T. Siemieniewska. *Pure Appl. Chem.*, 1985, 57(4): 603-619.

[37] K. Zhao, W. Wang, Z. Li. *J. CO_2 Util.*, 2016, 16: 236-244.

[38] T. A. Le, M. S. Kim, S. H. Lee, T. W. Kim, E. D. Park. *Catal. Today*, 2017, 293:

89-96.

[39] J. Ashok, M. L. Ang, S. Kawi. *Catal. Today*, 2017, 281: 304-311.

[40] G. Zhou, H. Liu, K. Cui, H. Xie, Z. Jiao, G. Zhang, K. Xiong, X. Zheng. *Int. J. Hydrogen Energy*, 2017, 42(25): 16108-16117.

[41] J. Sun, Y. Wang, H. Zou, X. Guo, Z. J. Wang. *J. Energy Chem.*, 2019, 29: 3-7.

[42] D. Beierlein, D. Häussermann, M. Pfeifer, T. Schwarz, K. Stöwe, Y. Traa, E. Klemm. *Appl. Catal. B: Environ.*, 2019, 247: 200-219.

[43] X. Guo, Z. Peng, M. Hu, C. Zuo, A. Traitangwong, V. Meeyoo, C. Li, S. Zhang. *Ind. Eng. Chem. Res.*, 2018, 57(28): 9102-9111.

[44] J. Lin, C. Ma, Q. Wang, Y. Xu, G. Ma, J. Wang, H. Wang, C. Dong, C. Zhang, M. Ding. *Appl. Catal. B: Environ.*, 2019, 243: 262-272.

[45] W. Wang, W. Chu, N. Wang, W. Yang, C. Jiang. *Int. J. Hydrogen Energy*, 2016, 41(2): 967-975.

[46] G. Garbarino, C. Wang, T. Cavattoni, E. Finocchio, P. Riani, M. Flytzani-Stephanopoulos, G. Busca. *Appl. Catal. B: Environ.*, 2019, 248: 286-297.

[47] J. Li, Y. Zhou, X. Xiao, W. Wang, N. Wang, W. Qian, W. Chu. *ACS Appl. Mater. Interfaces*, 2018, 10(48): 41224-41236.

[48] F. Ocampo, B. Louis, L. Kiwi-Minsker, A. C. Roger. *Appl. Catal. A: Gen.*, 2011, 392(1-2): 36-44.

[49] F. Wang, S. He, H. Chen, B. Wang, L. Zheng, M. Wei, D. G. Evans, X. Duan. *J. Am. Chem. Soc.*, 2016, 138(19): 6298-6305.

[50] A. Quindimil, U. De-La-Torre, B. Pereda-Ayo, A. Davó-Quiñonero, E. Bailón-García, D. Lozano-Castelló, J. A. González-Marcos, A. Bueno-López, J. R. González-Velasco. *Catal. Today*, 2019, in press, Doi: 10.1016/j.cattod.2019.06.027.

[51] J. Gao, Y. Wang, Y. Ping, D. Hu, G. Xu, F. Gu, F. Su. *RSC Adv.*, 2012, 2(6): 2358-2368.

[52] G. Garbarino, P. Riani, L. Magistri, G. Busca. *Int. J. Hydrogen Energy*, 2014, 39(22): 11557-11565.

[53] S. Abate, K. Barbera, E. Giglio, F. Deorsola, S. Bensaid, S. Perathoner, R. Pirone, G. Centi. *Ind. Eng. Chem. Res.*, 2016, 55(30): 8299-8308.

[54] S. Abello, C. Berrueco, F. Gispert-Guirado, D. Montane. *Catal. Sci. Technol.*, 2016, 6(7): 2305-2317.

[55] G. Garbarino, D. Bellotti, P. Riani, L. Magistri, G. Busca. *Int. J Hydrogen*

Energy, 2015, 40(30): 9171-9182.

[56] W. Wang, C. Duong-Viet, H. Ba, W. Baaziz, G. Tuci, S. Caporali, L. Nguyen-Dinh, O. Ersen, G. Giambastiani, C. Pham-Huu. *ACS Appl. Energy Mater.*, 2019, 2(2): 1111-1120.

[57] Y. Zhan, Y. Wang, D. Gu, C. Chen, L. Jiang, K. Takehira. *Appl. Surf. Sci.*, 2018, 459: 74-79.

[58] D. Schlereth, O. Hinrichsen. *Chem. Eng. Res. Des.*, 2014, 92(4): 702-712.

[59] C. Schüler, M. Wolf, O. Hinrichsen. *J. CO_2 Util.*, 2018, 25: 158-169.

[60] A. Vita, C. Italiano, L. Pino, P. Frontera, M. Ferraro, V. Antonucci. *Appl. Catal. B: Environ.*, 2018, 226: 384-395.

[61] J. R. Rostrup-Nielsen, K. Pedersen, J. Sehested. *Appl. Catal. A: Gen.*, 2007, 330: 134-138.

[62] C. Niether, S. Faure, A. Bordet, J. Deseure, M. Chatenet, J. Carrey, B. Chaudret, A. Rouet. *Nat. Energy*, 2018, 3(6): 476-483.

[63] S. Ceylan, T. Klande, C. Vogt, C. Friese, A. Kirschning. *Synlett*, 2010, 13: 2009-2013.

[64] S. R. Chaudhuri, J. Hartwig, L. Kupracz, T. Kodanek, J. Wegner, A. Kirschning. *Adv. Synth. Catal.*, 2014, 356(17): 3530-3538

[65] J. M. Asensio, A. B. Miguel, P. F. Fazzini, P. W. van Leeuwen, B. Chaudret. *Angew. Chem. Int. Ed.*, 2019, 58: 11306-11310.

[66] W. Donphai, N. Piriyawate, T. Witoon, P. Jantaratana, V. Varabuntoonvit, M. Chareonpanich. *J. CO_2 Util.*, 2016, 16: 204-211.

[67] P. D. Muley, C. Henkel, K. K. Abdollahi, D. Boldor. *Energy Fuels*, 2015, 29(11): 7375-7385.

[68] Y. Liu, P. Gao, N. Cherkasov, E. V. Rebrov. *RSC Adv.*, 2016, 6(103): 100997-101007.

[69] S. Danaci, L. Protasova, J. Lefevere, L. Bedel, R. Guilet, P. Marty. *Catal. Today*, 2016, 273: 234-243.

Supporting Information

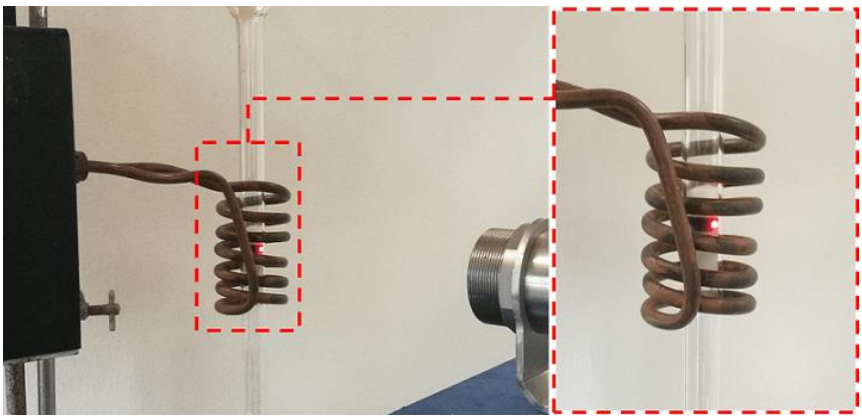

Fig. S1. Quartz tubular reactor placed inside the coils of the inductive heater along with the laser pyrometer for the real time control of the temperature inside the catalyst bed

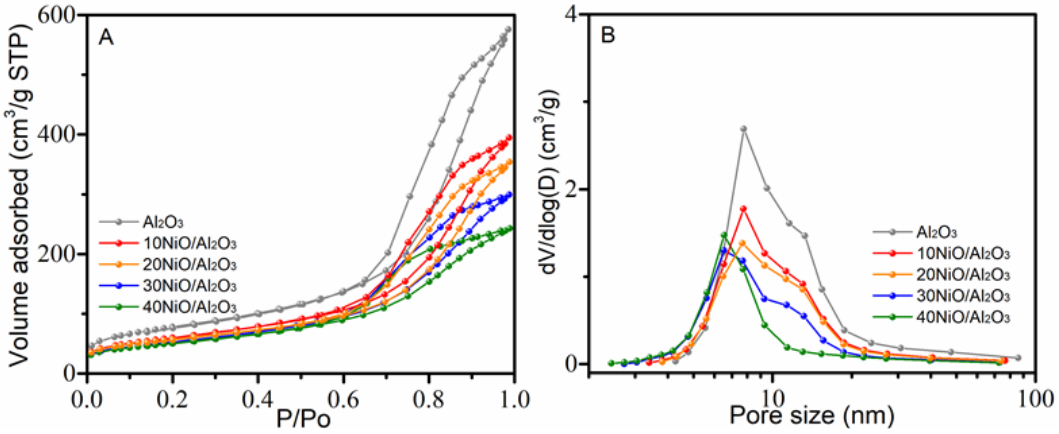

Fig. S2. N_2 adsorption-desorption isotherms (A) and pore size distributions (B) of the support and catalysts before reduction.

These samples exhibited similar type IV physisorption isotherms according to the IUPAC classification, indicating the typical characteristic of the mesoporous materials. With the increase of Ni loading, the hysteresis loop gradually shifts from the H_3 type for the A_2O_3 support to H_4 type for 40Ni/Al_2O_3, reflecting a gradual narrowing process of the catalyst pore structure [1, 2].

Table S1 - Textural properties of the samples.

Samples	SSA[a] $m^2 \cdot g^{-1}$	PV[b] $cm^3 \cdot g^{-1}$ STP	PD[c] nm
Al_2O_3	279	0.951	9.96
$10NiO/Al_2O_3$	216	0.641	9.29
$20NiO/Al_2O_3$	205	0.570	9.34
$30NiO/Al_2O_3$	190	0.486	8.12
$40NiO/Al_2O_3$	181	0.390	7.27

[a] Calculated by the BET equation.

[b] BJH desorption pore volume between 1.7 nm and 300 nm.

[c] BJH desorption average pore diameter.

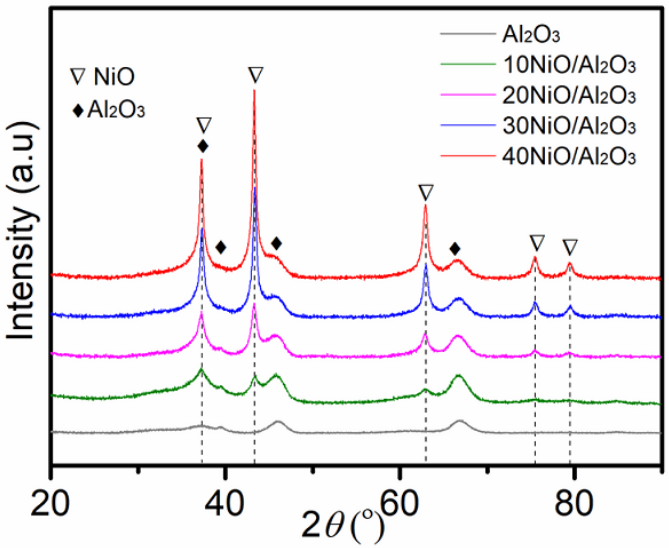

Fig. S3. XRD patterns of the support and the catalysts after calcination.

The XRD patterns of the support and the nickel doped catalyst after calcination in Air are shown in **Fig. S3**. The sharp diffraction peak located at 2θ = 37.2°, 43.3°, 62.9°, 75.4° and 79.4° were assigned to the (111), (200), (220), (311) and (222) crystal plans of nickel oxide, indicating high crystalline degree of nickel oxide [ICDD PDF#65-5745] [3, 4]. With the increase of nickel content, the size of NiO could be increased, and subsequently the intensity of the corresponding diffraction peaks was greatly enhanced. On the contrary, the increasing coverage of nickel species on the surface of the support and then leads to the decrease of the diffraction peak intensity of alumina.

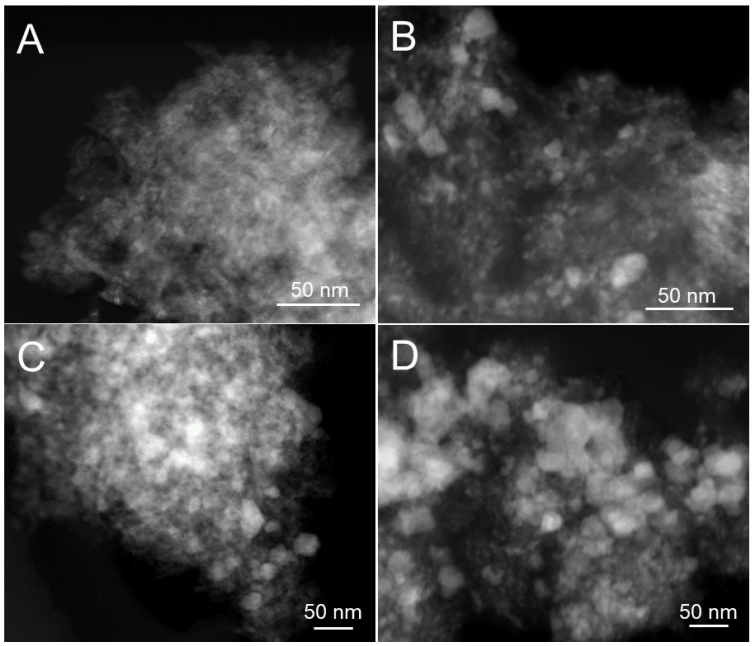

Fig. S4. STEM images of the nickel species on the surface of the reduced catalysts: (A) 10Ni/Al_2O_3; (B) 20Ni/Al_2O_3; (C) 30Ni/Al_2O_3; (D) 40Ni/Al_2O_3.

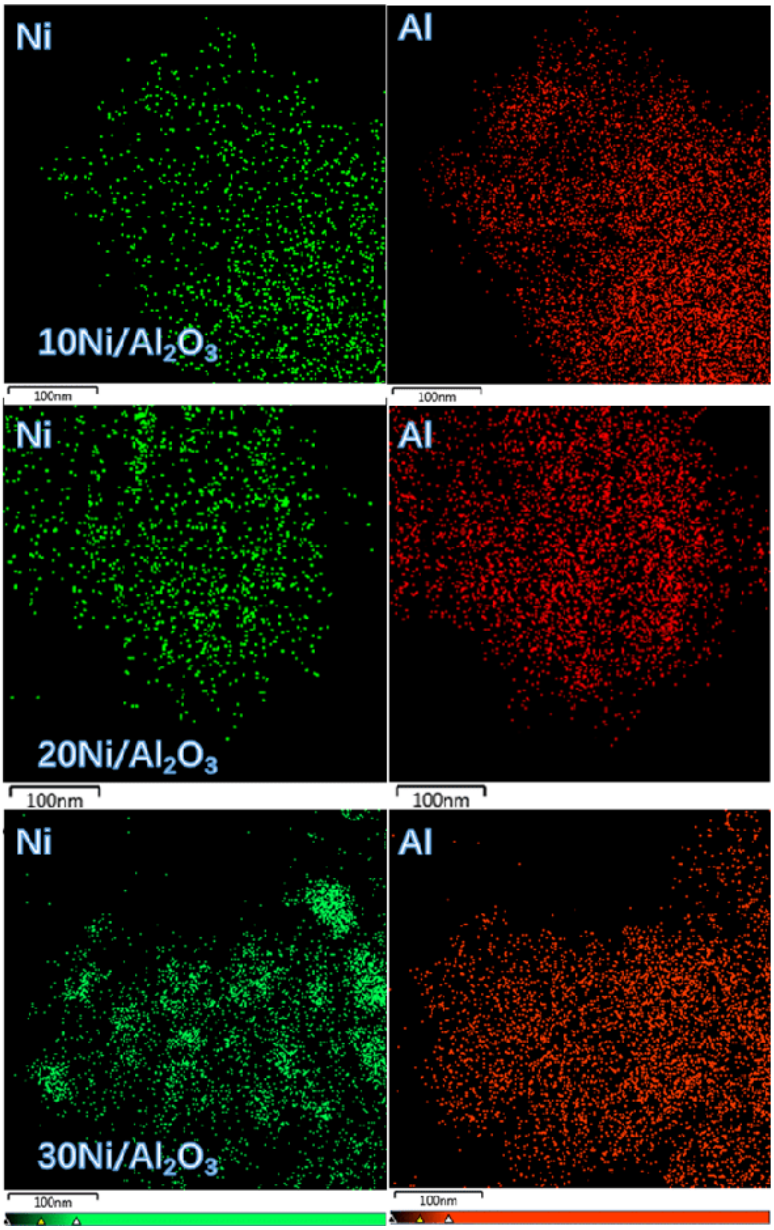

Fig. S5. Elements mapping of the reduced catalysts with different nickel loading.

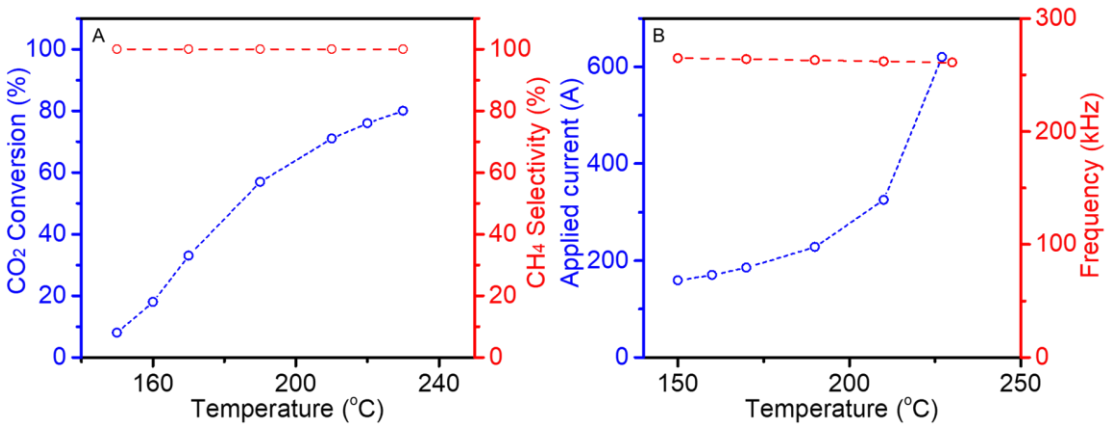

Fig. S6. CO_2 conversion and CH_4 selectivity as a function of reaction temperature (A) and corresponding applied current and frequency (B) under IH mode on the $30Ni/Al_2O_3$ catalyst. Reaction conditions: 0.4 g catalyst, GHSV (STP) = 20 $L \cdot g_{cat.}^{-1} \cdot h^{-1}$, H_2-to-CO_2 ratio (v./v.) of 4 and 1 atm.

Table S2. Specific rate expressed in terms of $mol_{CH4} \cdot g_{Ni}^{-1} \cdot h^{-1}$ on the different catalysts systems reported in the literatures.

Entry	(Ni wt.%) [a] Catalyst [b] [Catalyst., mg] [c]	Reaction temp. (°C)	Flow rate ($mL \cdot min^{-1}$)	Gas mixture CO_2:H_2:Inert ($mL \cdot min^{-1}$)	H_2/CO_2 v/v ratio	GHSV ($mL \cdot g^{-1} \cdot h^{-1}$)	X_{CO2} (%)	S_{CH4} (%)	Specific rate ($mol_{CH_4} \cdot g_{Ni}^{-1} \cdot h^{-1}$)	Ref.
1[d]	(40) Ni/Al_2O_3 [400]	230	200	40:160:0	4	30,000	82	100	0.54	This work
2[d]	(40) Ni/Al_2O_3 [400]	230	200	28.57:171.42:0	6	30,000	91	100	0.43	
3[d]	(40) Ni/Al_2O_3 [400]	210	133.35	26.67:106.68:0	4	20,000	82.5	100	0.36	
4[d]	(40) Ni/Al_2O_3 [400]	210	133.35	19.05:114.3:0	6	20,000	95	100	0.29	
5	(15) NiMn350 [100]	230	50	10:40:0	4	30,000	15	100	0.27	5
6	(10) OMA-10Ni8Ca [100]	230	25	5:20:0	4	15,000	18	96	0.23	6
7[e]	(16.6) $17Ni/Al_2O_3$ [300]	230	300	30:120:150	4	60,000	10	98.5	0.16	7
8	(12)12Ni4.5Ce/CNT [100]	230	50	10:40:0	4	30,000	8	97	0.17	8
9	(12) Ni-Ac-La/SiC [200]	230	31	10:21:0	2.1	9,300	14	100	0.16	9
8[e]	(10.7) Ni/N-CNT [200]	230	200	20:80:100	4	60,000	4	100	0.10	10
9[e]	(18.9) $Ni/H\text{-}Al_2O_3(400)$ [1000]	230	40	6:24:10	4	2,400	45	> 99	0.04	11
10	(58) $Ni_{0.8}Ce_{0.2}O_x$ [100]	230	100	1:50:49	50	60,000	100	100	0.05	12
11	(20) $20Ni/Al_2O_3\text{-}ZrO_2$-1.0 [500]	230	50	10:40:0	4	6,000	40	100	0.11	13
12	(10) MA-10Ni3Pr [100]	230	25	5:20:0	4	15,000	15	96.3	0.19	14
13[e]	(8.68) Ni/ZrO_2-P [50]	230	50	8:32:10	4	60,000	6	100	0.30	15
14	(10) NCS [50]	230	37.5	3.75:15:18.75	4	45,000	13	100	0.26	16
15	(10) Ni/CZ-AE [150]	230	50	4:16:30	4	20,000	28	99.8	0.20	17
16	(10) Ni/Si [200]	230	80	10:40:30	4	15,000	6	98.5	0.08	18
17	(78) $Ni\text{-}Al_2O_3$-HT [40]	230	50	9:36:5	4	75,000	12	98.5	0.09	19
18[e]	(14.8) Ni/TiO_2-DP [1000]	230	40	6:24:10	4	2,400	63	100	0.07	20
19	(10) Ni@MOF-5 [200]	230	25	3:12:10	4	7,500	9	100	0.04	21
20[f]	(10) Ni/CeO_2 [300]	230	70	7:28:35	4	14,000	30	100	0.19	22
21	(40) $40Ni\text{-}Nb_2O_5$-700 [1000]	230	12.5	2.5:10:0	4	750	37	> 99	0.01	23
22	(30) $3Ru\text{-}30Ni/Ce_{0.9}Zr_{0.1}O_2$ [1000]	230	40	8:32:0	4	2,400	98.2	100	< 0.07	24
23	(15) Ni/Al_2O_3-S [100]	230	100	20:80:0	4	60,000	0	0	0	25
24	(5) 5Ni-0.5Ru(80-20) [150]	230	55	9:36:10	4	22,000	0	0	0	26

[a] wt.% of Ni loading in the catalyst. [b] catalyst acronym. [c] mg of catalyst used in CO_2 methanation. [d] 30 wt.% theoretical loading. [e] determined by inductively coupled plasma-atomic emission spectroscopy (ICP-AES). [f] segment-type catalyst with gap distance of 15 mm.

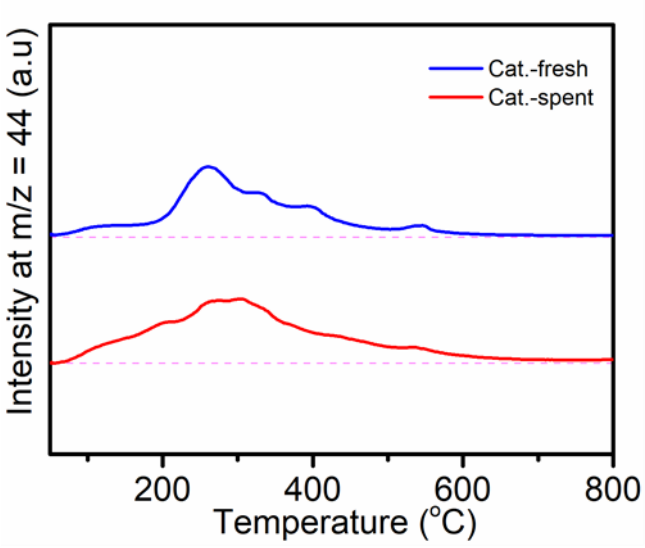

Fig. S7. TPO profiles of the 40Ni/Al_2O_3 catalyst before and after long term test.

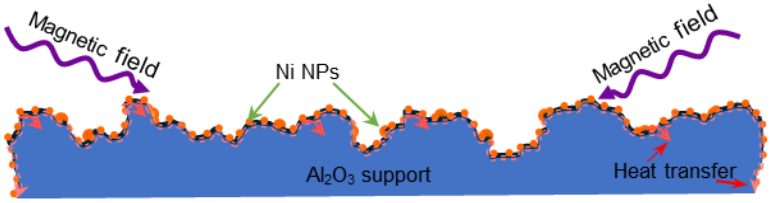

Fig. S8. Illustration of the heating process under IH mode.

Sufficient amount of nickel loading, on the one hand, promotes the formation of more small adjacent nickel particles on the surface of the carrier, forming a denser layer with more nickel species, on the other hand, it will cause the aggregation of some small nickel particles, forming large particles on the surface of the support. Therefore, the catalysts with high nickel loadings process wide particle size distribution range. As a consequence, the thermal and electrical conductivity of the catalysts can be greatly enhanced, increasing the opportunity for the catalysts to be electromagnetically heated up, and is expected to be benefited for the overall catalytic performance.

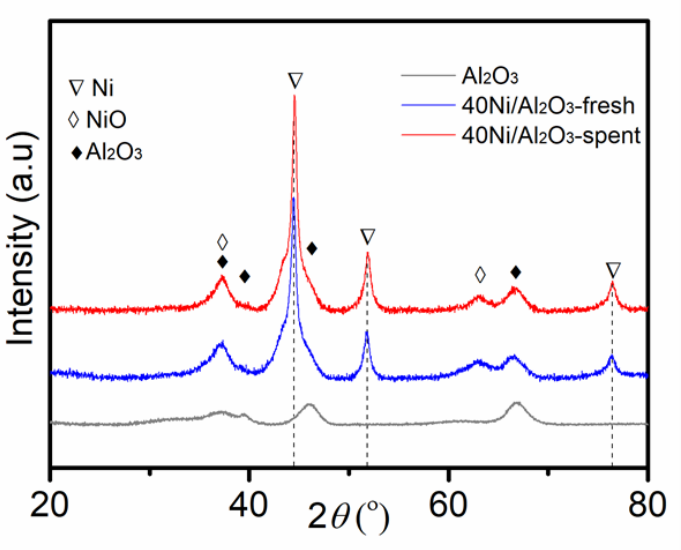

Fig. S9. XRD patterns of the catalyst before and after long term test.

Reference

[1] M. Thommes, K. Kaneko, A. V. Neimark, J. P. Olivier, F. Rodriguez-Reinoso, J. Rouquerol, K. S. Sing. *Pure Appl. Chem.*, 2015, 87(9-10): 1051-1069.

[2] K. S. Sing. D. H. Everett, R. A. W. Haul, L. Moscou, R. A. Pierotti, J. Rouquerol, T. Siemieniewska. *Pure Appl. Chem.*, 1985, 57(4): 603-619.

[3] K. Zhao, W, Wang, Z. Li. *J CO_2 Util.*, 2016, 16: 236-244.

[4] F. Ocampo, B. Louis, A. C. Roger. *Appl. Catal. A: Gen.*, 2009, 369(1-2): 90-96.

[5] J. Li, Y. Zhou, X. Xiao, W. Wang, N. Wang, W. Qian, W. Chu. *ACS Appl. Mater. Interfaces*, 2018, 10(48): 41224-41236.

[6] L. Xu, H. Yang, M. Chen, F. Wang, D. Nie, L. Qi, X. Lian, H. Chen, M. Wu. *J. CO_2 Util.*, 2017, 21: 200-210.

[7] B. Mutz, M. Belimov, W. Wang, P. Sprenger, M. A. Serrer, D. Wang, P. Pfeifer, W. Kleist, J. D. Grunwaldt. *ACS Catal.*, 2017, 7(10): 6802-6814.

[8] W. Wang, W. Chu, N. Wang, W. Yang, C. Jiang. *Int. J. Hydrogen Energy*, 2016, 41(2): 967-975.

[9] L. Li, J. Zheng, Y. Liu, W. Wang, Q. Huang, W. Chu. *ChemistrySelect*, 2017, 2(13): 3750-3757.

[10] W. Wang, C. Duong-Viet, H. Ba, W. Baaziz, G. Tuci, S. Caporali, L. Nguyen-Dinh, O. Ersen, G. Giambastiani, C. Pham-Huu. *ACS Appl. Energy Mater.*, 2019, 2(2): 1111-1120.

[11] S. He, C. Li, H. Chen, D. Su, B. Zhang, X. Cao, B. Wang, M. Wei, D. G. Evans, X. Duan. *Chem. Mater.*, 2013, 25(7): 1040-1046.

[12] T. A. Le, M. S. Kim, S. H. Lee, T. W. Kim, E. D. Park. *Catal. Today*, 2017, 293: 89-96.

[13] J. Lin, C. Ma, Q. Wang, Y. Xu, G. Ma, J. Wang, H. Wang, C. Dong, C. Zhang, M. Ding. *Appl. Catal. B: Environ.*, 2019, 243: 262-272.

[14] L. Xu, F. Wang, M. Chen, D. Nie, X. Lian, Z. Lu, H. Chen, K. Zhang, P. Ge. *Int. J. Hydrogen Energy*, 2017, 42(23): 15523-15539.

[15] X. Jia, X. Zhang, N. Rui, X. Hu, C. J. Liu. *Appl. Catal. B: Environ.*, 2019, 244: 159-169.

[16] G. Zhou, H. Liu, K. Cui, H. Xie, Z. Jiao, G. Zhang, K. Xiong, X. Zheng. *Int. J. Hydrogen Energy*, 2017, 42(25): 16108-16117.

[17] J. Ashok, M. L. Ang, S. Kawi. *Catal. Today*, 2017, 281: 304-311.

[18] M. Guo, G. Lu. *Catal. Commun.*, 2014, 54: 55-60.

[19] L. He, Q. Lin, Y. Liu, Y. Huang. *J. Energy Chem.*, 2014, 23(5): 587-592.

[20] J. Liu, C. Li, F. Wang, S. He, H. Chen, Y. Zhao, M. Wei, D. G. Evans, X. Duan. *Catal. Sci. Technol.*, 2013, 3(10): 2627-2633.

[21] W. Zhen, B. Li, G. Lu, J. Ma. *Chem. Commun.*, 2015, 51(9): 1728-1731.

[22] S. Ratchahat, M. Sudoh, Y. Suzuki, W. Kawasaki, R. Watanabe, C. Fukuhara. *J. CO_2 Util.*, 2018, 24: 210-219.

[23] E. S. Gnanakumar, N. Chandran, I. V. Kozhevnikov, A. Grau-Atienza, E. V. R. Fernández, A. Sepulveda-Escribano, N. R. Shiju. *Chem. Eng. Sci.*, 2019, 194: 2-9.

[24] X. Shang, D. Deng, X. Wang, W. Xuan, X. Zou, W. Ding, X. Lu. *Int. J. Hydrogen Energy*, 2018, 43(14): 7179-7189.

[25] J. Sun, Y. Wang, H. Zou, X. Guo, Z. J. Wang. *J. Energy Chem.*, 2019, 29, 3-7.

[26] F. Ocampo, B. Louis, L. Kiwi-Minsker, A. C. Roger. *Appl. Catal. A: Gen.*, 2011, 392(1-2): 36-44.

Chapter 5

Conclusions and perspectives

5.1 Conclusions

The steadily increase of the world population along with an ever deeply industrially-driven economy for a great number of developing countries translates into an increasing demand for energy supply, mostly from fossil sources, which are at the origin of environment degradation and represents a threat for human society, *i.e.* global warming and its resulting consequences [1, 2]. In the last decades large efforts have been devoted to the implementation of renewable energy sources (RES) to mitigate or reduce the global warming and their consequences [3, 4]. The large implementation of RES goes alongside with the development of large scale and efficient energy storage systems along with new infrastructural technologies suitable to cope with the high volatility of selected RES and their intermittent nature. The development of highly efficient electrochemical devices for energy conversion and storage (*i.e.* solar cells and supercapacitors) together with the development of integrated chemical energy conversion and storage strategies, such as Power-to-Gas (PtG), are highly promising solutions towards a sustainable energy mix scheme for the future [5, 6].

The thesis focuses on the investigation of two technologies for the electrochemical and chemical energy conversion and storage, *i.e.* the development of highly-performing and cost-effective carbon materials for energy storage applications (high-performance supercapacitor electrodes) and metal-based composites as highly efficient and robust catalysts for CO_2 methanation. For the latter process, we have also highlighted how the adoption of innovative heating schemes (from classical joule heating to electromagnetic inductive heating) can be largely beneficial to the process performance, including catalyst stability on run and transformation energetics.

5.1.1 Electrochemical storage device based on supercapacitor

The work describes the preparation of two different types of porous carbon materials with diverse morphologies featured by relatively high specific surface area (SSA) and highly open-cell structure, synthesized by modified KOH chemical activation of different biomass sources, *i.e.* waste fig fruit or sugar, and their subsequently application as highly performing electrodes in supercapacitors.

In the first part of this section, porous carbon foam structures originated from waste fig-fruit raw materials using KOH chemical activation are described. The amount of KOH, the calcination temperature, and the carbon precursors (different part of fig

fruit) have been found to have great influence on the structure of the final products. The optimized hierarchical porous carbon material exhibited SSA higher than 2000 $m^2 \cdot g^{-1}$ with plenty of interconnected micro-, meso- and macropores, which could significantly improve the overall accessible surface area as well as ion diffusion rate. Therefore, supercapacitor electrode based on such material displayed superior specific capacitance of 340 and 217 $F \cdot g^{-1}$ in aqueous electrolyte at a current density of 0.5 and 20 $A \cdot g^{-1}$, respectively, along with high stability.

In the second part of this section, a robust few-layer graphene-like structures have been prepared by a modified chemical activation procedure starting from costless sugar/salt mixtures. Thermal annealing followed by chemical activation and salts washing steps, left behind carbon material featured by highly accessible and non-stackable few-layer graphene-like nanosheets. The as-prepared C-samples ensure high ion-accessible surface area and low ion transport resistance, two key features for the fabrication of effective supercapacitors. Electrochemical capacitors based on the as-prepared materials have shown markedly high specific capacitance values, particularly at high current densities, along with excellent capacitance retentions upon thousands of cycles and increasing charge-discharge rates. Selected sample from this series exhibited high specific capacitance (312 and 234 F g^{-1} at 0.5 and 50 A g^{-1}, respectively, in 0.5 M H_2SO_4), particularly at high current density values, along with excellent cycling stability and specific capacitance retention for increasing charge-discharge rates.

In summary, the biomass derived carbon materials, *i.e.* carbon foam and graphene-like carbon nanosheets, displayed superior capacitance in a three-electrode system under test conditions, indicating that these carbon materials were suitable candidates for high capacitance supercapacitors. We can also state that KOH chemical activation is an efficient approach to fabricate high porosity carbon structure materials with exceptional electrochemical performance from natural resources. The calcination temperature, the amount of KOH versus fruit and the way it is added have a significant influence on the morphology and textural properties of the final carbon structures, consequently affecting their ultimate electrochemical performance.

5.1.2 Chemical energy storage through CO_2 methanation process

We have approached this study with the aim at preparing highly efficient, robust and selective catalysts for CO_2 methanation while developing a new reactor scheme

based on an unconventional heating mode. All the synthesized catalysts demonstrate significantly improved catalytic performance for CO_2 methanation under IH mode compared with that under classical heating approach, indicating the overwhelming advantages of the IH approach.

In the first part of this work we described the CO_2 methanation based on nickel nanoparticles (Ni NPs) decorated on electrically conductive and macroscopically shaped oxidized carbon-felt disks (OCF), heated at the target reaction temperature by electromagnetic induction (IH). At odds with the more classical external heat sources (based on contact heat conduction), IH has allowed the electromagnetic energy to be directly converted by the susceptor (OCF) into heat to be transferred to the catalyst active sites (Ni NPs). Inductive heating (IH) of Ni/OCF gave CO_2 conversion (X_{CO2}) up to 74% and CH_4 selectivity (S_{CH4}) close to 97% at 320 °C, showing an excellent control of the catalyst stability under forced dynamic operational conditions.

Indeed, the combination of a thermally conductive susceptor (OCF) along with the fast temperature regulation capability of IH system allowed to prevent the generation of serious local hot spots within the catalyst bed, hence ensuring high stability to the catalyst in a highly exothermic process. The fast temperature regulation ability of IH setup allowed to operate the process under virtually isothermal conditions even when reagents were discontinuously fed into the reactor: a fast temperature control not generally possible under traditional Joule heating conditions due to the higher thermal inertia of the system. Ni/OCF showed an excellent stability upon IH when forced dynamic operational conditions were applied (reaction temperature, GHSV and reagents loads). In a model trial, dynamic operational modes were expressly forced in the system as to mimic the process discontinuity under conditions close to those operated in real plants. Accordingly, several and sequential start/stop cycles were run, including changes in the target reaction temperature and GHSV, thus unveiling the extremely high stability of Ni/OCF under harsh experimental conditions. Finally, a long-term experiment (> 80 h) has been used to confirm the stability of the catalyst after several hours on stream. TEM analyses of the exhaust Ni/OCF had finally rule out the occurrence of any appreciable NPs sintering throughout the process due to the advantages of IH mode.

In a second part of this work, γ-Al_2O_3 support decorated with high nickel loading as metal active phase was evaluated for the catalytic and highly efficient CO_2 methanation under IH. For this catalyst, metal nanoparticles were directly employed as

both susceptor for the conversion of electromagnetic energy into heat and active phases for hydrogen activation. With such a scheme, high CO_2 methanation performance and almost complete methane selectivity were already obtained under very moderate reaction temperatures, as low as 210 °C. The superior CO_2 methanation of Ni/Al_2O_3 catalyst already at low temperatures, was ascribed to the highly efficient heating of the local Ni NPs by IH. Indeed, the efficient electromagnetic energy conversion of large Ni NPs (basically due to eddy currents dissipation phenomenon) along with the heat contribution coming from the process exothermicity, made possible to perform the process efficiently already at low temperature and within a highly energy-saving scheme. Moreover, the poor thermally conductive character of the Al_2O_3 support, mitigated the heat dissipation, thus allowing Ni NPs to harvest and store heat also from the exothermic process, to be spent in turn for running the methanation reaction. By this way "functional hot-spots" are generated and exploited for catalysis purposes. At the same time the local and fast control exerted by IH on the catalyst target temperature, prevents any undesired temperature runaway and allows the whole process to occur under "virtually" isothermal conditions. Such results are of high interest as low temperature, *i.e.* ca < 200 °C, CO_2 conversion has been fixed as future goal for CO_2 methanation process. Moreover, NPs passivation by the generation of coke deposition were unlikely to occur due to the efficient heat management within the process ensured by IH.

In summary, the extremely fast power regulation capacity of IH system allows an almost real time control and balance of any undesired and sudden temperature changes at the catalyst bed. As a matter of fact, temperature fluctuations, frequently encountered in real systems, can be finely controlled if not definitively suppressed. Therefore, the system can be operated under dynamic conditions and the temperature runaway phenomena inside the catalyst bed can be significant suppressed compared that with classical electrical furnace heating.

5.2 Perspectives

The research work presented in this thesis fits well with a series of urgent and timely issues related to energy conversion and storage. In the light of the different results obtained some milestones can be fixed as to trace out future perspectives and developments in the field:

(i) KOH activation process applied to other carbon-based materials can be pursued with the aim of modifying their porosity and accessibility hence to find ever newer materials for application in the field of electrochemical storage or as functional supports for catalytic transformations.

(ii) The in-depth investigation of inherent potentialities of IH for the generation of local high temperatures on metal nanoparticles can open the way to the exploitation of this technology in low-temperature and highly performing CO_2 methanation reactions.

(iii) The exploitation of IH for other catalytic processes [7], *i.e.* Fischer-Tropsch synthesis, selective oxidation, where the gradient temperature control could be of high interest to prevent selectivity lost or catalyst deactivation phenomena can have largely beneficial effects on the improvement of processes efficiency and catalysts stability on time.

Reference

[1] Z. Gao, Y. Zhang, N. Song, X. Li. *Mater. Res. Lett.*, 2017, 5(2), 69-88.

[2] I. Dincer. *Renew. Sust. Energy Rev.*, 2000, 4(2), 157-175.

[3] G. H. Brundtland. United Nations. Oxford University Press, 1987, ISBN: 019282080X.

[4] I. M. Bugaje. *Renew. Sust. Energy Rev.*, 2006, 10(6), 603-612.

[5] L. Dai, D. W. Chang, J.-B. Baek, W. Lu. *Small*, 2012, 8(8), 1130-1166.

[6] M. Götz, J. Lefebvre, F. Mörs, A. M. Koch, F. Graf, S. Bajohr, R. Reimert, T. Kolb. *Renew. Energy*, 2016, 85, 1371-1390.

[7] W. Wang, G. Tuci, C. Duong-Viet, Y. Liu, A. Rossin, L. Luconi, J. M. Nhut, L. Nguyen-Dinh, C. Pham-Huu, G. Giambastiani. Induction Heating: An Enabling Technology for the Heat Management in Catalytic Processes. *ACS Catal.*, 2019, 9(9): 7921-7935.

Annex

Publications and Communications

Publications

[1] **W. Wang**, G. Tuci, C. Duong-Viet, Y. Liu, A. Rossin, L. Luconi, J.-M. Nhut, C. Pham-Huu, G. Giambastiani. Induction Heating: An Enabling Technology for the Heat Management in Catalytic Processes. *ACS Catal.*, 2019, 9(9), 7921-7935.

[2] **W. Wang**, C. Duong-Viet, Z. Xu, H. Ba, G. Tuci, G. Giambastiani, Y. Liu, T. Truong-Huu, J.-M. Nhut, C. Pham-Huu. CO_2 methanation under dynamic operational mode using nickel nanoparticles decorated carbon felt (Ni/OCF) combined with inductive heating. *Catal. Today*, 2019, in press.

[3] **W. Wang**, C. Duong-Viet, H. Ba, W. Baaziz, G. Tuci, S. Caporali, L. Nguyen-Dinh, O. Ersen, G. Giambastiani, C. Pham-Huu. Nickel Nanoparticles Decorated Nitrogen-Doped Carbon Nanotubes (Ni/N-CNT); a Robust Catalyst for the Efficient and Selective CO_2 Methanation, *ACS Appl. Energy Mater.*, 2019, 2(2), 1111-1120.

[4] H. Ba[1], **W. Wang**[1], G. Tuci, S. Pronkin, C. Weinberg, L. Nguyen-Dinh, G. Giambastiani, C. Pham-Huu. Tridimensional few-layer graphene-like structures from sugar-salt mixtures as high-performance supercapacitor electrodes. *Mater. Today Energy*, 2018, 10: 118-125.

[5] H. Ba[1], **W. Wang**[1], S. Pronkin, T. Romero, W. Baaziz, L. Nguyen-Dinh, W. Chu, O. Ersen, C. Pham-Huu. Biosourced Foam-Like Activated Carbon Materials as High-Performance Supercapacitors. *Adv. Sustain. Sys.,* 2018, 2(2): 1700123.

[6] H. Ba, Y. Liu, **W. Wang**, C. Duong-Viet, V. Papaefthimiou, L. Nguyen-Dinh, G. Tuci, G. Giambastiani, C. Pham-Huu. Carbon felt monoliths coated with a highly hydrophobic mesoporous carbon phase for the continuous oil sorption/filtration from water. *Adv. Sustainable Syst.*, 2018, 2(7): 1800040.

[7] J. Li, Y. Zhou, X. Xiao, **W. Wang**, N. Wang, W. Qian, W. Chu. Regulation of Ni–CNT Interaction on Mn-Promoted Nickel Nanocatalysts Supported on Oxygenated CNTs for CO_2 Selective Hydrogenation. *ACS Appl. Mater. Inter.*, 2018, 10(48): 41224-41236. (Master)

[8] L. Li, J. Zheng, Y. Liu, **W. Wang**, Q. Huang, W. Chu. Impacts of SiC Carrier and Nickel Precursor of NiLa/support Catalysts for CO_2 Selective Hydrogenation to Synthetic Natural Gas (SNG). *ChemistrySelect*, 2017, 2(13): 3750-3757. (Master)

[9] H. Lu, C. Jiang, Z. Ding, **W. Wang**, W. Chu, Y. Feng. Effects of ultrasonic impregnation combined with calcination in N_2 atmosphere on the property of

Co_3O_4/CeO_2 composites for catalytic methane combustion. *J. Energy Chem.*, 2016, 25(3): 387-392. (Master)

[10] **W. Wang**, W. Chu, N. Wang, W. Yang, C. Jiang. Mesoporous nickel catalyst supported on multi-walled carbon nanotubes for carbon dioxide methanation. *Int. J. Hydrogen Energy*, 2016, 41(2): 967-975. (Master)

[11] **W. Wang**, Z. Xu, Z. Guo, C. Jiang, W. Chu. Layered double hydroxide and related catalysts for hydrogen production and a biorefinery. *Chin. J. Catal.*, 2015, 36(2): 139-147. (Master)

Communications

[1] CarboCat - VIII: 8th International Symposium on Carbon for Catalysis, 26-29, 06, 2018, Porto, Portugal

Nickel nanoparticles decorated nitrogen doped carbon nanotubes as an efficient catalyst for CO_2 methanation.

Poster & Oral Communication. Best Poster Award.

[2] International Conference Catalysis for Renewable Sources: Fuel, Energy, Chemicals, 02-06, 09, 2019, Crete, Greece

Enhanced catalytic performance for CO_2 methanation powered by induction heating. Presentation (20 minutes).

Wei WANG

Matériaux à base de carbone pour la conversion et le stockage d'énergie électrochimique et chimique

Résumé

La conversion et le stockage de l'énergie ont toujours été les deux problèmes critiques de la société humaine. Dans la présente thèse, nous nous concentrons sur le développement de matériaux carbonés durables pour le stockage d'énergie électrochimique (supercondensateurs) et des catalyseurs au nickel supportés pour la conversion et le stockage d'énergie chimique (méthanation de CO_2). Deux structures de carbone différentes dérivées de la biomasse (mousse de carbone hiérarchisée et feuille nanométrique de carbone de type graphène) ont été développées pour les applications en supercondensateurs. Parallèlement, un catalyseur à base de nickel supporté sur du carbone (Ni/OCF) a été mis au point pour la méthanation du CO_2 avec une performance catalytique améliorée grâce au chauffage inductif (IH). La capacité de régulation rapide du système IH pour éviter le problème d'emballement de la température a également été étudiée à l'aide d'un catalyseur au nickel sur support d'alumine.

Mots-clés: matériaux carbonés; supercondensateur; méthanation de CO_2; chauffage par induction

Abstract

Energy conversion and storage have always been the two critical issues for human society. In this thesis, we focus on the development of sustainable carbon materials for effective electrochemical energy storage, especially for supercapacitors, and supported nickel catalysts for chemical energy conversion and storage, mainly on CO_2 methanation. Two different biomass derived carbon structures, *i.e.* hierarchical carbon foam and graphene-like carbon nanosheets, have been synthesized and applied for supercapacitor. Exceptional electrochemical performances have been obtained. Meanwhile, nickel decorated macroscopic carbon catalyst (Ni/OCF) has been developed for CO_2 methanation with enhanced catalytic performance powered by electromagnetic induction heating (IH). The rapid regulation capability of IH system to jugulate the problem of temperature runaway has also been investigated in the last part using powdered alumina supported nickel catalyst for this exothermic reaction.

Keywords: Carbon materials; Supercapacitor; CO_2 methanation; Induction heating